

NONINVASIVE SENSING TECHNIQUES 2012

GUEST EDITORS: FRANCESCO SOLDOVIERI, JEAN DUMOULIN, NICOLA MASINI, RAFFAELE SOLIMENE,
AND ERICA UTSI





Noninvasive Sensing Techniques 2012

International Journal of Geophysics

Noninvasive Sensing Techniques 2012

Guest Editors: Francesco Soldovieri, Jean Dumoulin,
Nicola Masini, Raffaele Solimene, and Erica Utsi



Copyright © 2012 Hindawi Publishing Corporation. All rights reserved.

This is a special issue published in "International Journal of Geophysics." All articles are open access articles distributed under the Creative Commons Attribution License, which permits unrestricted use, distribution, and reproduction in any medium, provided the original work is properly cited.

Editorial Board

Andrea Bizzarri, Italy
Jean-Pierre Burg, Switzerland
John F. Cassidy, Canada
Ping Chang, USA
Yun-tai Chen, China
Gordon Cooper, South Africa
Robin Crockett, UK
Gary Egbert, USA
Semih Ergintav, Turkey
Fabrizio Galadini, Italy
Marek Grad, Poland
Hans-Gert Kahle, Switzerland

Masao Kanamitsu, USA
Shuichi Kodaira, Japan
Libo Liu, China
Francisco Luzon Martinez, Spain
Zdenek Martinec, Czech Republic
Philip Meredith, UK
Steve Milan, UK
Marco Mucciarelli, Italy
Michael Nicolls, USA
Salvatore Piro, Italy
Ruey-Juin Rau, Taiwan
Wouter Schellart, Australia

Joerg Schleicher, Brazil
Sheng-Rong Song, Taiwan
Alexey Stovas, Norway
Sándor Szalai, Hungary
P. Talwani, USA
Robert Tenzer, New Zealand
Rudolf A. Treumann, Germany
Filippos Vallianatos, Greece
Petr Vaníček, Canada
Michael S. Zhdanov, USA
Sergej Zilitinkevich, Finland

Contents

Noninvasive Sensing Techniques 2012, Francesco Soldovieri, Jean Dumoulin, Nicola Masini, Raffaele Solimene, and Erica Utsi
Volume 2012, Article ID 817357, 2 pages

A “Non-Invasive” Technique for Qualifying the Reinforced Concrete Structure, Antonella Guida, Antonello Pagliuca, and Alessandro Tranquillino Minerva
Volume 2012, Article ID 659612, 9 pages

Rapid Mapping and Deformation Analysis over Cultural Heritage and Rural Sites Based on Persistent Scatterer Interferometry, D. Tapete and F. Cigna
Volume 2012, Article ID 618609, 19 pages

Geophysical Surveys at Khirbat Faynan, an Ancient Mound Site in Southern Jordan, Alexandre Novo, Matthew L. Vincent, and Thomas E. Levy
Volume 2012, Article ID 432823, 8 pages

Multitemporal High-Resolution Satellite Images for the Study and Monitoring of an Ancient Mesopotamian City and its Surrounding Landscape: The Case of Ur, Giacomo Di Giacomo and Giuseppe Scardozzi
Volume 2012, Article ID 716296, 14 pages

Pseudo 3D Imaging of Dielectric and Magnetic Anomalies from GPR Data, Raffaele Persico, Sergio Negri, Francesco Soldovieri, and Elena Pettinelli
Volume 2012, Article ID 512789, 5 pages

Accounting for Antenna in Half-Space Fresnel Coefficient Estimation, A. D’Alterio and R. Solimene
Volume 2012, Article ID 138458, 11 pages

Antipodal Vivaldi Antenna for Water Pipe Sensor and Telemetry, Giuseppe Ruvio, Domenico Gaetano, Max J. Ammann, and Patrick McEvoy
Volume 2012, Article ID 916176, 8 pages

Entropy-Based Clutter Rejection for Intrawall Diagnostics, Raffaele Solimene and Antonietta D’Alterio
Volume 2012, Article ID 418084, 7 pages

Ground-Penetrating Radar Investigations along Hajipur Fault: Himalayan Frontal Thrust—Attempt to Identify Near Subsurface Displacement, NW Himalaya, India, Javed N. Malik, Ashutosh Kumar, Sravanthi Satuluri, Bishuddhakshya Puhan, and Asmita Mohanty
Volume 2012, Article ID 608269, 7 pages

Analysis and Interpretation of the Field and Laboratory Geophysical Measurements of Black-Sand Beach Deposits, East Rosetta, Egypt, Mohamed A. El-Sadek, Ahmed A. Ammar, and Sayed A. Elkhateeb
Volume 2012, Article ID 435216, 10 pages

Editorial

Noninvasive Sensing Techniques 2012

**Francesco Soldovieri,¹ Jean Dumoulin,² Nicola Masini,³
Raffaele Solimene,⁴ and Erica Utsi⁵**

¹ *Istituto per il Rilevamento Elettromagnetico dell'Ambiente, Consiglio Nazionale delle Ricerche, Via Diocleziano 328, 80 124 Napoli, Italy*

² *Monitoring, Assessment and Computational Science Department (MACS), French Institute of Science and Technology for Transport, Development and Networks (IFSTTAR), Route de Bouaye, CS4, 44344 Bouguenais, France*

³ *Istituto per i Beni Archeologici e Monumentali, Consiglio Nazionale delle Ricerche, C. da S. Loja, 85050 Tito Scalco, Italy*

⁴ *Dipartimento di Ingegneria dell'Informazione, Seconda Università di Napoli, Via Roma 29, 81031 Aversa, Italy*

⁵ *Utsi Electronics Ltd., Cambridge CB22 7NZ, UK*

Correspondence should be addressed to Francesco Soldovieri, soldovieri.f@irea.cnr.it

Received 5 August 2012; Accepted 5 August 2012

Copyright © 2012 Francesco Soldovieri et al. This is an open access article distributed under the Creative Commons Attribution License, which permits unrestricted use, distribution, and reproduction in any medium, provided the original work is properly cited.

The preservation of both the cultural heritage and modern civil and critical infrastructures is a matter of transnational concern worldwide not only in areas subject to natural disasters but also, for example, in the name of health and safety where such structures continue in regular use. Structural preservation relies uniquely on our ability to monitor accurately and form reliable diagnoses of the current condition of built structures both in terms of their material composition and any deterioration to date. These same diagnostics give us the capability to monitor over time even where such structures are not apparently at unusual levels of risk. They also allow us to manage any necessary work before and after major crisis events such as, for example, earthquakes, landslides, or floods.

This special issue of the International Journal of Geophysics focuses on noninvasive sensing techniques which form the principal method of monitoring cultural heritage and civil engineering infrastructures in order to define its current condition and ensure its preservation now and into the future.

The papers included in this issue fall into two main categories.

The first of these is the development of innovative analysis methods in order to improve the understanding and interpretation of the results of noninvasive investigations with the aim of improving the diagnostic abilities. Three of the ten papers form this category.

In their first contribution, A. D'Alterio and R. Solimene report on a new method regarding the possibility to estimate the electromagnetic parameters of a structure starting from ground penetrating radar (GPR) measurements. They extend their previous work on characterising the signal responses from the ground surface to include antenna characteristics and achieve this by taking measurements from multiple offset positions and using multiple polarisation configurations.

In their second contribution, R. Solimene and A. D'Alterio develop a method of highlighting targets embedded within a masonry wall by eliminating background clutter from GPR traces. They do this by developing a windowing strategy based on an entropy measure of temporal traces "similarity." As a result, the visibility of the targeted objects is strongly improved.

The third paper in this category deals with the development of methods of data interpretation. R. Persico demonstrate the application of a data processing method based on the Born approximation to GPR data in order to improve the detectability and geometry estimation of buried targets with both electrical and magnetic characteristics. The results are compared with the more traditional processing method of migration.

The second main category and the one into which the majority of the papers fall is that of practical applications of noninvasive investigative techniques to a wide variety of

historical monuments and other natural resources. The techniques used in these studies are extremely wide ranging and are a good illustration of the resources available to evaluate heritage buildings, culturally sensitive structures as well as their environmental contexts. They include electromagnetic induction (EMI), electrical resistivity tomography (ERT), ground penetrating radar (GPR), magnetic susceptibility, synthetic aperture radar interferometry, the use of high-resolution satellite imaging, sonic, and mechanical methods.

A. Novo et al. apply a suite of geophysical techniques (notably EMI and ERT) to the investigation of an ancient mound, Khirbat Faynan, in Southern Jordan in order to define the archaeological remains. Although they did not apply GPR due to the surface conditions, they include this in their appraisal of the work done to date and their recommendations for future potential investigations.

Turning to a more environmental context, M. A. El-Sadek et al. used a range of primarily magnetic methods to investigate and identify the locations of beach-alluvial deposits of the Koam Mashaal area of East Rosetta in Egypt, demonstrating the usefulness of these methods for this type of mapping investigation.

Ground penetrating radar was used by J. N. Malik et al. within an earthquake zone, the Hajipur Fault in North West Himalaya, India, to identify a suitable trenching site and to investigate the geometry of the fault plane. A series of 2-dimensional data profiles were combined to form an image of the fault plane in 3 dimensions.

D. Tapete and F. Cigna applied a procedure based on the application of Persistent Scatterer Interferometry to Synthetic Aperture Radar repeated passages for a multi-spatial/temporal hazard assessment of cultural heritage sites in Tuscany, in Italy, in areas critically affected by landslides. From their analyses at these sites, they developed a rapid mapping and deformation analysis intended to aid in preservation of critically endangered historical sites.

The ancient city of Ur in Mesopotamia (modern day Iraq) was investigated by G. Di Giacomo and G. Scardozzi using multitemporal high-resolution satellite images in order to analyse the structure and composition of this world heritage site. The results show the correlation of data from excavation and remote monitoring over a lengthy time period and point the way to a potential method for a long-term monitoring.

Moving into a more modern context, albeit concerning buildings of cultural and historical interest, A. Guida et al. applied ultrasound and mechanical investigation techniques to a historic building composed of reinforced concrete mixed with stone. They found that combining the results of the two methods provided an efficient method of evaluating the building and a basis on which to preserve and transform it for future use (ultimately the best method of ensuring future preservation).

Finally, in a category of its own, one paper deals with the application of developing technology. Vivaldi antennas are not new but are more traditionally applied to microwave applications. G. Ruvio et al. applied the use of Vivaldi antennas to monitor the water content of polyvinyl chloride pipes and communicate this data to an external gateway. They

illustrate the operational characteristics of these antennas with a number of relevant tests.

The common theme of all of these papers is the application of a wide range of geophysical techniques to the problems of assessing and monitoring structures of historical, cultural and social importance without causing further damage to the structures themselves or triggering damaging external environmental effects.

*Francesco Soldovieri
Jean Dumoulin
Nicola Masini
Raffaele Solimene
Erica Utsi*

Research Article

A “Non-Invasive” Technique for Qualifying the Reinforced Concrete Structure

Antonella Guida, Antonello Pagliuca, and Alessandro Tranquillino Minerva

*Department of European and Mediterranean Cultures, School of Architecture, University of Basilicata,
Via Lazazzera, 75100 Matera, Italy*

Correspondence should be addressed to Antonella Guida, arch.antonellaguida@gmail.com

Received 21 March 2012; Revised 4 June 2012; Accepted 30 June 2012

Academic Editor: Raffaele Solimene

Copyright © 2012 Antonella Guida et al. This is an open access article distributed under the Creative Commons Attribution License, which permits unrestricted use, distribution, and reproduction in any medium, provided the original work is properly cited.

In recent years, a lot of studies on built heritage emphasize the need to use appropriate techniques to evaluate the current condition of the structure before designing an intervention. The research focuses on the restoration of reinforced concrete buildings that begin to show signs of decay and deterioration. To verify the state of a building, it's possible to use the “destructive” methods (that require a local removal of material) and “nondestructive” tests. The combined results from different “nondestructive” tests are very interesting instruments to assess the concrete strength. This methodological approach can help to reduce the possible errors when using the sclerometer and ultrasonic tests separately; in this way, the combined method called “SonReb” (SONic + REBound) was developed. This paper would highlight the importance with respect to cultural heritage buildings and on the studied structure and contribute to developed engineering strategies to maintenance and restoration. The above-defined methodology has been tested on a postwar building which is located in Gravina in Puglia (Italy): the “Centrone” theatre; it was built using a mixed structure, that is, reinforced concrete and bearing masonry built of local stone. The building was used until the 1990s and now is abandoned. The analysis and qualification of the masonry structures of built heritage show how this approach is useful for classifying the pathological events on each building and to implement the innovative solutions to improve the durability of a restoration intervention.

1. Introduction

In the last decades, the architectural heritage of the modern movement seems to be more at risk than during any other period. This built inheritance embodies the dynamic spirit of the industrial age. At the end of the 1980s, many modern masterpieces had already been demolished or changed beyond recognition. This was mainly due to the fact that many were not considered to be elements of heritage that their original functions have substantially changed and that their technological innovations have not always endured long-term stresses.

A thorough research of built heritage enables understanding of the evolution of design philosophies and underlying cultural meanings and messages, artistic and functional qualities, and engineering achievements. A detailed knowledge of building materials, construction techniques, environmental services, external impacts, and internal impacts

of use or disuse assist in identifying the problems affecting buildings and defining a methodological approach for interventions.

The research objective is to provide new qualitative information on the strength of reinforced concrete structures of a building by using innovative, non-invasive testing techniques. The case of study is the “Centrone” theatre in Gravina in Puglia (Italy).

The confluence of the local architectural styles (vernacular and academic) and the emerging aesthetic of reinforced concrete is explored to outline the context that influenced the building design.

The research methodology includes (a) the context in which the buildings were designed, (b) their history, (c) building technologies used, (d) non-invasive testing of the reinforced concrete structures, (e) the analysis of the test results, and (f) the conclusions.

Testing methods could be “destructive”, as they require a local removal of material, or “nondestructive”, that is, they do not affect the structure. A sclerometer test, an ultrasonic test and their combined use, called SonReb (*SONic* + *REBound*), are “nondestructive” tests on reinforced concrete. The combined tests are a very useful method for assessing the concrete strength and to reduce the possibility of errors that can happen if the tests are not combined, as it has been noticed that the humidity content of a structural element can influence the sclerometer index and the ultrasound speed [1]. The combined method requires shorter time to obtain the results.

2. A “Critical” Approach to Building Restoration

The conservation intervention on a historic building, regardless of its architectural and/or artistic value, is generally more appropriate if information on its construction, evolution to date, materials, construction techniques, and structure is available. The conservation of built heritage highlights different issues such as the vast number of buildings needing attention and the urgency of cases that have to be resolved with limited economic resources and time.

To undertake a suitable intervention, three questions have to be answered: whether, where, and how to restore. The fourth question could be added, in which the economic aspect dominates: when to restore. To be able to respond adequately to these questions, it is necessary to proceed by developing specifications step by step, starting from a detailed knowledge of the entire building, the level and causes of degradation, and by finishing with the “operational” description of the proposed interventions.

Within the preliminary data acquisition phase, the direct survey of the building characteristics and condition and the mapping of any noticed changes are accompanied by the research on the project documentation and the events that have affected the structure during its construction and throughout the building life.

These approaches, often coupled with normative models which translate living conditions into objective parameters and standards, hinder the interventions such as a “simple” maintenance or a restoration or produce the result that is not logically related to the structural, typological, functional, and technological characteristics of the artefacts.

An “appropriate” restoration should plan the reuse of built heritage and aim to achieve building performance comparable to new buildings. The reuse interventions should be integrated with the conservation and not imposed.

The above methodology highlights how the approach could be helpful for the classification of pathological events within a building and for the application of innovative solutions to increase the durability of restoration interventions.

3. The Investigative Techniques for Concrete

The investigative techniques for concrete are also classified in two defined macrocategories (“destructive” and “non-destructive”). The former are based on the extraction of

concrete samples to undertake compressive tests and represent the most reliable instrument for assessing the mechanical properties of concrete. The second investigative typology, the nondestructive tests, can be further subdivided in: really “nondestructive” investigations and “partially destructive” investigations. The latter include (a) the penetration test with a Windsor gun (ASTM C 83) which enables the identification of compressive resistance of concrete by measuring the depth of penetration of the special metal pins projected with a Windsor gun into concrete, (b) the extraction test (pull-out) (UNI 10157:1992-ASTM C 900-06) which enables the assessment of compressive resistance of concrete by measuring the force used by a hydraulic jack for extracting a special plug inserted into concrete.

The really nondestructive investigations include, among others, (a) endoscopy that enables a direct observation of form and appearance of an investigated object, (b) thermography that assists in recognising potential structural anomalies by using the capacity of materials to transfer heat, (c) magnetometry which enables localising metal bars in reinforced concrete, (d) the Ground Penetrating Radar (GPR), especially with regard the investigation of the internal reinforcement bars, (e) measurement of the electric potential of concrete which enables defining the level of corrosion of metal reinforcements in concrete, (f) ultrasound investigation that allows qualitative assessment of the concrete resistance by using the capacity of the concrete components to transfer ultrasound waves, (g) sclerometric tests that assess the concrete resistance by reading the bounce results, and finally, (h) so-called “SonReb” (*SONic* + *REBound*) that enables assessing the concrete resistance by combining the speed of ultrasound waves and the index of surface bounce through a synergic use of the two previous investigations.

3.1. The “SonReb” Method for Determining the Resistance of Concrete. The SonReb method, as mentioned above, allows a qualitative determination of the concrete resistance [2] through the cross-examination of the values of the speed of ultrasound waves and the values of sclerometric bounce. This investigation method is standardised by RILEM Recommendations [3] 43 CND-EN 13791:2007, the EC regulation 1-2010 UNI EN 12504-2:2001, ASTM C597, UNI EN 12504-4:2005, the Test Report CUR 69, the standards UNI 7997, UNI 9524 and UNI 83308.

This method is used for assessing the resistance of concrete, enabling the elimination of errors, at least partly, that appear when the two investigation methods are separately applied. This method, in fact, allows reducing the errors made when the sclerometric and ultrasound tests are undertaken separately [4].

It has been noticed, for example, that the humidity content leads to an underestimation of the sclerometric index and in an inversely proportional way leads to an overestimation of the ultrasound speed; similarly, the sclerometric index rises in a directly proportional way to the increase of the age of concrete [1], while the ultrasound speed decreases in an inversely proportional way to it [5].

In fact, the risk that can come up in the separate use of sclerometric and/or ultrasound tests is related, for example,

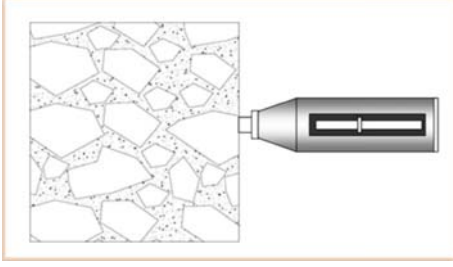


FIGURE 1: Sclerometer beats against a large piece of aggregate.

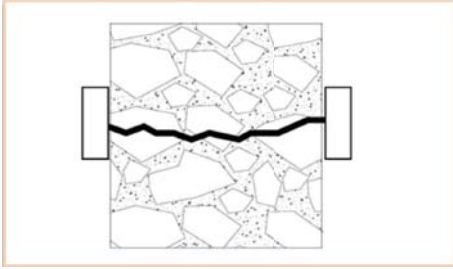


FIGURE 2: Ultrasound equipment: the impulse transmission.

to the chance nature of the position of aggregates in relation to the external surface of an investigated component; the sclerometer can easily beat against a large piece of aggregate, probably obtaining a higher value of the bounce index S in relation to the one returned when the blow is executed on a homogenous concrete surface (Figure 1).

Again as an example, the ultrasound test (Figure 2) can equally be affected by the chance nature of the disposition of aggregates in a cement mix when the gaps between the aggregates are arranged in the way that induces the rise of the void index; in this case, the speed of wave spread V decreases in relation to the value that would be obtained when the wave spreads through an area of “homogenous” concrete.

The application of the “SonReb” method asks for the appraisal [6] of local values of the ultrasound speed V and of the bounce index S from which it is possible to obtain the resistance of concrete R_c through expressions such as:

$$R_{c,\text{sonReb}} = a \cdot S^b \cdot V^c. \quad (\text{a})$$

In the scientific literature this formula has assumed different forms, each one expressing the experiments undertaken directly on site or in a laboratory on standardised samples.

For example:

(i) Gasparik [7] (1992)

$$R_{c,2} = 8,06 \cdot 10^{-8} \cdot S^{1,246} \cdot V^{1,85}, \quad (\text{b})$$

(ii) RILEM (1993) [2], NDT 4

$$R_{c,1} = 9,27 \cdot 10^{-11} \cdot S^{1,4} \cdot V^{2,6}, \quad (\text{c})$$

(iii) Di Leo and Pascale [6] (1994)

$$R_{c,3} = 1,2 \cdot 10^{-9} \cdot S^{1,058} \cdot V^{2,446}, \quad (\text{d})$$

in which:

- (i) R_c is the resistance of a cube under compression [N/mm²];
- (ii) S is the sclerometric index;
- (iii) V is the ultrasound speed [m/s].

The formula (c) depicts the correlation curve applied in the investigated case studies. In (c) R_c is expressed in MPa and the ultrasound speed in m/s; this relationship is related to a standard concrete whose properties are described in RILEM 43-CND. When a different type of concrete is employed the following relationship is applicable [8]:

$$R_{\text{sonReb}} = R'_{\text{sonReb}} \cdot (C_c \cdot C_d \cdot C_a \cdot C_f \cdot C_p \cdot C_m), \quad (1)$$

where R'_{sonReb} is the value obtained from (1), while C_c (cement type), C_d (cement content), C_a (aggregate types), C_f (proportions of fines), C_p (maximum aggregate size), and C_m (errors) are coefficients of influence that permit the extension of (b) to the cases of a nonstandard concrete (as defined above).

Hence, if the concrete has the same characteristics as the one whose experimental curves are available, the graph directly provides the estimated resistance of concrete. Otherwise, as usually happens, when the concrete has a different composition from the one presented by the curve, the corrective coefficients, that take into account the type of cement and the related dosage, the nature and dimensions of aggregates, and the potential additives need to be applied to obtain an approximately true estimate of the concrete resistance [1].

It is evident that the above equations could not have universal validity except for the fact that the values of S and V depend on the characteristics of concrete, even when the specific indications on the limitations of applicability are missing.

However, a qualitative appraisal of the resistance of concrete can be made even by using the graphs (Figure 3) which show a series of isoresistance curves in the plane V - S (obtained from the above analytic expressions) and which refer to the tests undertaken on standardised samples in a laboratory.

Although it appears absolutely necessary to analyse a wider range of cases, the above methodological investigation approach, based on the comparative analysis of the two described test campaigns, suggests several important considerations regarding the modality of investigation and the interpretation of results, demonstrating the need for establishing general investigation criteria: more than defining in a strict manner the number of tests that should be undertaken, it would be necessary to preset the level of significance to be achieved.

4. The Case of Study: “Centrone” Theatre in Gravina in Puglia (Italy)

The above-defined methodology has been tested on a postwar building which is located in Gravina in Puglia

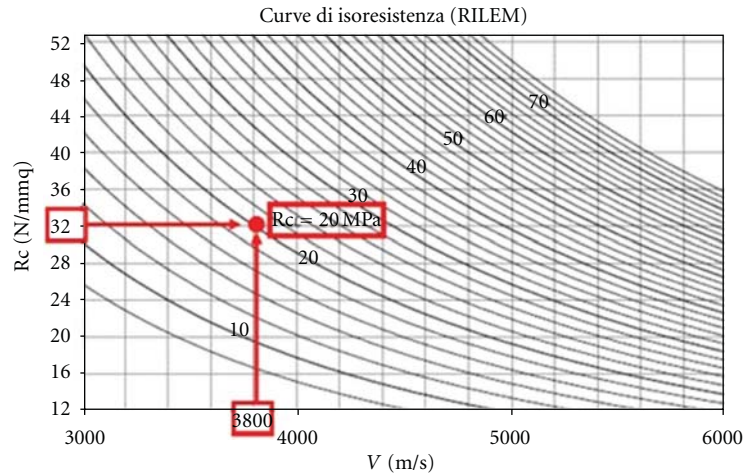


FIGURE 3: Example of iso-resistance curves—RILEM NDT 4 recommendations.



FIGURE 4: Historical image of vault construction.



FIGURE 5: Historical image of iron trusses.

(Italy): the “Centrone” theatre; it was built using a mixed structure, that is, reinforced concrete and bearing masonry built of local stone.

The building is not very old, but it is very interesting for the local civic history; in fact, it represents different values. Values that are set in different reels from the life of the building and revolved the surrounding environment in which it is inserted.

Historical value related to the historical development of the building and to the importance that it has in terms of expression of the local civic history; social value that is related to the social development of the city; cultural value that is related to the cultural growth of society; value of identity that has the building in terms of physics and metaphysics belong to a place then; but not least; the economic value related to the ability to reuse the building readapting it to new needs.

The building was built between 1946 and 1948; the foundations were built on pillars and vaults (Figure 4) and the pitched roof using iron trusses (Figure 5).

The building is a rectangular block (Figure 6), developed on three levels and covered using plaster and stone; the main façade is symmetrical, tripartite and follows the ground inclination; in the opposite side, the building shows two projecting polygonal elements realized using the local stone.

In the central part of the building; approximately 10 m wide; is located the entrance, highlighted by the massive



FIGURE 6: The “Centrone” theatre in Gravina in Puglia (Italy).

presence of two Doric columns that support a loggia. The building is organized in different spaces: the central part, where at ground floor there are the foyer entrance and ticket office, while on the first floor there is the Room “Italy” (Figure 7) that contains 110 seats; at second floor there are three flats for the managers of the theatre. The mail hall contains the stalls with 800 seats (a big space 32.5 m long and 21 m wide); it is partly covered by a balcony (at the first level) with 300 seats and a gallery on the second level with 300 seats.

The pathologies that interest the building are not particularly serious, since it does not affect in any way the



FIGURE 7: The room “Italy” on the first floor of the theatre.

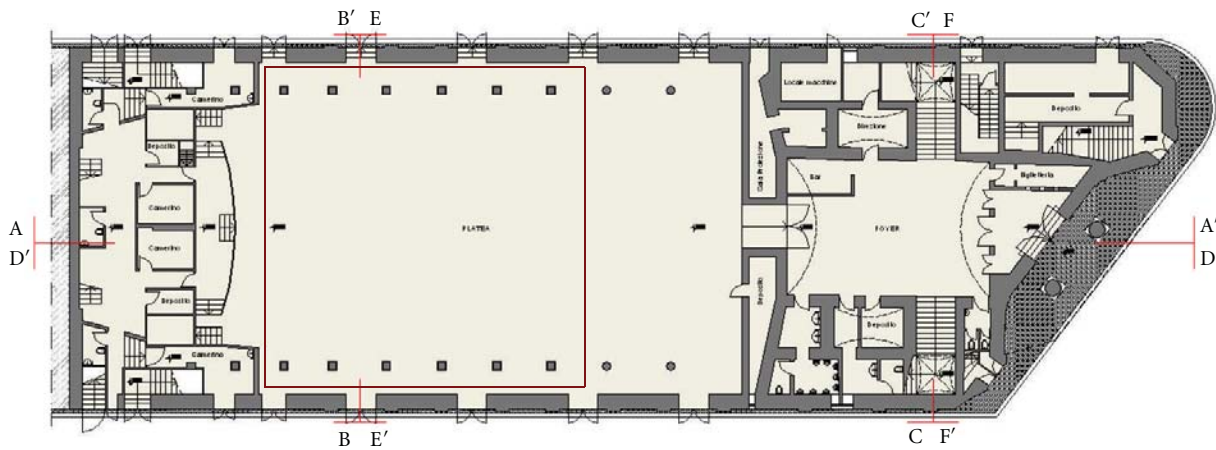


FIGURE 8: The specification of the location of the investigation points.

static system of structure and are easily solvable with non-invasive interventions. Inside are not detectable serious and manifest diseases, except for some water infiltrations from the roof that are determined as chromatic alterations and plaster detachment.

The condition of the pillars is generally acceptable, since they do not show obvious pathologies; however, you should note that some have a bad state of preservation of the plaster due to moisture that caused severe swelling, internal cavities and an evident surface lack of homogeneity.

4.1. On-Site Tests: Formulation. Essential elements for the organisation of an investigation campaign are the selection of the components that will be examined (which have to be representative of the whole structure), the investigation methodology that will be used, and the number and location of the investigation points; these requirements, in fact, are fundamental to guarantee a certain level of “reliability” of the obtained results and a “trustworthiness” with regard

to the qualitative indications related to the characteristics of the material. In the case of the “Centrone” theatre, the identification of the components to be investigated was made by selecting the structural components which make the internal core of the load-bearing structure for two reasons: (1) because they enable to investigate a concrete in the state of “natural aging” (i.e., without considering the aggressive atmospheric agents which could have modified the condition of the material) and (2) for easiness of selecting the testing points. The structure of the whole building consists of a dual typology of structural components: those inserted in the external fabric (therefore difficult to investigate) and those located within the building.

The selection of the location of the investigation points (Figure 8) was random (with the aim to guarantee the representativeness of the investigation for the entire structure); in addition, “homogenous” areas [1] (which have the same characteristics) were noted and considered by making the obtained results “qualitative” and representative for all the

TABLE 1: The value of rebound index.

Structural element		Sclerometer value										Average value
Element code	Size [cm]	Rebound value										
P1 Dx T	43 × 43	27	28	26	29	25	25	31	26	28	28	28
P2 Dx T	43 × 43	34	38	36	42	40	36	37	38	41	38	38
P3 Dx T	43 × 43	32	33	30	31	32	32	34	31	31	31	32
P4 Dx T	43 × 43	35	33	34	30	36	34	34	34	36	38	38
P5 Dx T	43 × 43	35	33	34	34	33	32	35	37	34	34	34
P6 Dx T	43 × 43	35	37	38	38	36	34	35	38	36	36	36
P1 Sx T	43 × 43	41	37	45	47	37	38	42	39	40	41	41
P2 Sx T	43 × 43	43	42	42	40	44	42	46	44	44	40	43
P3 Sx T	43 × 43	34	34	37	35	34	33	34	32	36	35	34
P4 Sx T	43 × 43	32	28	32	32	34	34	34	34	30	32	32
P5 Sx T	43 × 43	30	28	28	32	30	28	32	32	30	30	30
P6 Sx T	43 × 43	34	35	34	36	35	37	38	35	38	35	36
P1 Dx I p	43 × 43	23	21	21	22	22	25	25	26	24	22	23
P2 Dx I p	43 × 43	33	32	33	32	30	30	30	33	31	30	31
P3 Dx I p	43 × 43	37	40	38	41	43	38	38	38	41	38	39
P4 Dx I p	43 × 43	38	38	38	38	37	39	37	38	39	39	38
P5 Dx I p	43 × 43	37	39	35	38	37	38	38	40	38	40	38
P6 Dx I p	43 × 43	36	38	37	37	38	38	37	38	36	38	37
P1 Sx I p	43 × 43	26	22	24	22	24	20	23	22	22	22	23
P2 Sx I p	43 × 43	40	41	37	40	40	39	38	38	37	38	39
P3 Sx I p	43 × 43	40	37	35	37	36	35	35	35	35	35	36
P4 Sx I p	43 × 43	35	35	35	37	35	37	36	38	36	38	36
P5 Sx I p	43 × 43	40	40	37	35	36	35	38	36	36	36	37
P6 Sx I p	43 × 43	36	38	36	38	38	38	40	40	38	38	38

components that show the same characteristics; a further condition is that the selected surfaces do not show any obvious condition of degradation. The methodology used to undertake the tests was exclusively selected in terms of the possibility to undertake the tests. Regarding the sclerometric tests, they were undertaken by placing the instrument always orthogonally in relation to the investigated surface; the preference was given to the direct method of investigation. The considered reference (in terms of the number of tests with the aim to guarantee the reliability of the results) for the investigation campaign was taken from the framework of the Italian investigation procedures.

4.2. On-Site Tests: Analysis and Results. Sclerometer tests were carried out following the directions contained in UNI EN 12504-2 (2001). The instrument used is the concrete GEI model. On each pillar identified, it was carried out 10 measurements (Table 1) of the value of rebound (for each test, ten values were taken, from which the average value was considered as illustrative).

Three different areas were selected for each investigated component; at 0.70 m, at 1.40 m, and at 2.10 m from the floor. This selection, in fact, was motivated by the need to investigate the columns at the points of major stress (base and middle), having assumed (1) a uniform distribution of

the loads and imposed loads (due to the homogenous structure) and (2) a homogenous condition of the loads (there are no visible cracks to induce any different considerations).

Ultrasonic tests were carried out according to the UNI EN 12504-4 (2005). Ultrasonic equipment used is the DSP model of Ultrasonic UTD 1004. On each pillar identified, it was carried out 10 measurements (Table 2) of the value of rebound (for each test ten values were taken, from which the average value was considered as illustrative).

These data were compared with the method “SonReb” (Tables 3, 4, 5, and 6) to improve—as said before—the qualitative interpretation of results; the analysis showed satisfactory results of the state of concrete condition, as well as the importance to compare the ultrasonic and sclerometer tests.

The obtained results show a significant homogeneity of values measured at each investigated level; more precisely, the sclerometric tests show an average value (of the ten measurements made at each point) of the bounce index uniformly distributed on the surfaces; whereas, the ultrasound tests returned average values of the ultrasound between a minimum value of 3050 m/s² and a maximum value of 3660 m/s². Comparing the results by using the method SonReb, the obtained values of the concrete resistance are from a minimum value of 18 MPa to a maximum value of

TABLE 2: The value of ultrasonic speed.

P1 Sx T average ultrasonic speed: 2862,9 m/s						
Height: 0,70 m Size 0,46 × 0,46	X direction	2039	2036	2035	2038	2041
	Y direction	2032	2034	2045	2048	2029
Height: 1,40 m Size 0,43 × 0,43	X direction	3656	3669	3686	3676	3664
	Y direction	3668	3672	3675	3663	3665
Height: 2,10 m Size 0,40 × 0,40	X direction	2043	2041	2042	2045	2046
	Y direction	2049	2068	2061	2043	2048
Height: 2,10 m Size 0,40 × 0,40	X direction	3665	3681	3687	3690	3684
	Y direction	3689	3676	3679	3695	3700
Height: 2,10 m Size 0,40 × 0,40	X direction	2052	2045	2049	2046	2048
	Y direction	2058	2060	2039	2059	2056
Height: 2,10 m Size 0,40 × 0,40	X direction	3685	3684	3682	3679	3669
	Y direction	3689	3694	3692	3686	3696
P1 Dx T average ultrasonic speed: 2873,2 m/s						
Height: 0,70 m Size 0,46 × 0,46	X direction	3367	3355	3362	3360	3355
	Y direction	3394	3397	3389	3362	3392
Height: 1,40 m Size 0,43 × 0,43	X direction	2520	2521	2531	2513	2512
	Y direction	2515	2510	2533	2511	2525
Height: 1,40 m Size 0,43 × 0,43	X direction	3250	3257	3260	3252	3247
	Y direction	3302	3315	3333	3341	3348
Height: 2,10 m Size 0,40 × 0,40	X direction	2490	2499	2510	2512	2505
	Y direction	2496	2493	2495	2491	2510
Height: 2,10 m Size 0,40 × 0,40	X direction	3322	3320	3333	3327	3325
	Y direction	3139	3152	3134	3152	3157
Height: 2,10 m Size 0,40 × 0,40	X direction	2526	2516	2545	2544	2558
	Y direction	2556	2559	2562	2568	2564
P6 Sx T average ultrasonic speed: 2134,1 m/s						
Height: 0,70 m Size 0,46 × 0,46	X direction	2160	2084	2053	2016	2066
	Y direction	2161	2016	2103	2105	2150
Height: 1,40 m Size 0,43 × 0,43	X direction	2160	2154	2111	2102	2013
	Y direction	2163	2136	2165	2130	2122
Height: 1,40 m Size 0,43 × 0,43	X direction	2160	2136	2165	2154	2155
	Y direction	2155	2153	2151	2160	2165
Height: 2,10 m Size 0,40 × 0,40	X direction	2152	2154	2150	2153	2103
	Y direction	2100	2155	2015	2140	2150
Height: 2,10 m Size 0,40 × 0,40	X direction	2150	2099	2088	2066	2200
	Y direction	2035	2150	2156	2171	2015
Height: 2,10 m Size 0,40 × 0,40	X direction	2030	2105	2145	2144	2014
	Y direction	2156	2148	2154	2148	2154
P6 Dx T average ultrasonic speed: 2560,9 m/s						
Height: 0,70 m Size 0,46 × 0,46	X direction	2562	2563	2545	2568	2567
	Y direction	2575	2574	2586	2544	2578
Height: 1,40 m Size 0,43 × 0,43	X direction	2543	2546	2566	2564	2568
	Y direction	2545	2544	2543	2549	2548
Height: 1,40 m Size 0,43 × 0,43	X direction	2566	2531	2533	2540	2545
	Y direction	2562	2545	2565	2555	2551
Height: 1,40 m Size 0,43 × 0,43	X direction	2556	2565	2559	2557	2549
	Y direction	2552	2553	2545	2551	2553

TABLE 2: Continued.

		P6 Dx T average ultrasonic speed: 2560,9 m/s				
Height: 2,10 m Size 0,40 × 0,40	X direction	2565	2596	2586	2567	2568
	Y direction	2564	2572	2575	2574	2573
		2564	2561	2563	2559	2568
		2567	2586	2584	2583	2569
		P1 Sx I p average ultrasonic speed: 2582,0 m/s				
Height: 0,70 m Size 0,46 × 0,46	X direction	1899	2130	2156	2102	2105
	Y direction	2111	2182	2221	2310	2229
		3200	3180	3196	3102	3104
		3016	3038	3086	3048	3062
Height: 1,40 m Size 0,43 × 0,43	X direction	1700	1750	1890	1806	1830
	Y direction	1834	1905	1942	1972	1973
		3109	3140	3149	3131	3158
		3160	3263	3264	3285	3189
Height: 2,10 m Size 0,40 × 0,40	X direction	2005	2103	1999	2150	2015
	Y direction	2060	2160	2163	2184	2150
		3005	3158	3139	3190	3100
		3089	3048	3069	3099	3105
		P1 Dx I p average ultrasonic speed: 3006,5 m/s				
Height: 0,70 m Size 0,46 × 0,46	X direction	3000	3002	3005	3019	2993
	Y direction	3010	3015	3019	2921	2996
		3012	3015	3018	3016	3018
		3001	3021	3029	3028	3020
Height: 1,40 m Size 0,43 × 0,43	X direction	3000	3052	3013	3002	3015
	Y direction	2999	3050	3015	3016	3019
		2996	3047	3036	3033	3031
		3002	3052	3035	3063	3043
Height: 2,10 m Size 0,40 × 0,40	X direction	2899	2915	3005	3001	3045
	Y direction	3015	3062	3036	3035	3046
		3051	3015	3063	3026	3033
		3018	3017	3021	3012	3026

TABLE 3: Left side pillar (Sx): Ground floor.

Pillar	Average rebound value	Average ultrasonic speed
P1 Sx T	41	2862,9
P2 Sx T	43	3297,1
P3 Sx T	34	3345,3
P4 Sx T	32	3181,2
P5 Sx T	30	3192,1
P6 Sx T	36	2134,1

TABLE 4: Right side pillar (Dx): Ground floor.

Pillar	Average rebound value	Average ultrasonic speed
P1 Dx T	28	2873,2
P2 Dx T	38	3103,6
P3 Dx T	32	3199,3
P4 Dx T	38	3313,2
P5 Dx T	34	3082,1
P6 Dx T	36	2560,9

22 MPa, that take in a significant consideration the contribution of the covered concrete conditions.

5. Conclusions

The tests carried out are the basis of a diagnostic project that is possible to implement and monitor to guarantee

a deeper knowledge, with the goal of attaining a level of thorough understanding aimed at the “preservation and improvement” of a building.

The recovery project, that takes particular care in the methodological application of the diagnostic phase, cannot leave out of consideration the necessity of a careful and timely monitoring of building conditions.

TABLE 5: Left side pillar (Sx): First floor.

Pillar	Average rebound value	Average ultrasonic speed
P1 Sx I p	23	2582,0
P2 Sx I p	39	3476,1
P3 Sx I p	36	3358,2
P4 Sx I p	36	3319,6
P5 Sx I p	37	3450,3
P6 Sx I p	38	3346,1

TABLE 6: Right side pillar (Dx): First floor.

Pillar	Average rebound value	Average ultrasonic speed
P1 Dx I p	23	3006,5
P2 Dx I p	31	3210,2
P3 Dx I p	39	3120,9
P4 Dx I p	38	3204,6
P5 Dx I p	38	3098,1
P6 Dx I p	37	3301,5

The carried out tests are the first and simplest analysis for a qualitative assessment; it is necessary to classify the structure regarding the following consolidation procedures. The recovery and conservation project, as well as an “indispensable” transformation of an old building, must be in that evaluations, of feasibility and suitability, both economic and practice which is the basis for a “suitable choice” of recovery intervention, that permit to annul the “cancellation” of the Built Heritage.

References

- [1] A. Masi, *La Stima della Resistenza del Calcestruzzo in situ Mediante Prove Distruttive e non Distruttive*, Il Giornale delle Prove non Distruttive Monitoraggio Diagnostica no. 1, 2005.
- [2] RILEM Draft Recommendation, 43-CND. Combined non-destructive testing of concrete. Draft recommendation for in situ concrete strength determination by combined non-destructive methods. Materials and Structures no. 26, 1993.
- [3] RILEM (The International Union of Testing and Research Laboratories for Materials and Structures) is an organisation which enables exchanges through an international network of testing engineers, researchers, academics, educators and practitioners.
- [4] F. Braga, M. Dolce, A. Masi, and D. Nigro, *Valutazione delle Caratteristiche Meccaniche dei Calcestruzzi di Bassa Resistenza Mediante Prove non Distruttive*, L'Industria Italiana del Cemento no. 3, 1992.
- [5] P. Bocca and S. Cianfrone, “Le prove non distruttive sulle costruzioni: una metodologia combinata,” L'Industria Italiana del Cemento no. 6, 1986.
- [6] A. Di Leo and G. Pascale, *Prove Non Distruttive Sulle Costruzioni in Cemento Armato*, Convegno Sistema Qualità e Prove non Distruttive per l'affidabilità e la Sicurezza delle Strutture Civili, Bologna, Italy, 1994.
- [7] J. Gasparik, *Prove Non Distruttive Nell'edilizia*, Università di Brescia, 1992.
- [8] R. Giochetti and L. Lacquaniti, *Controlli non Distruttivi su Impalcati da Ponte in Calcestruzzo Armato*, Nota Tecnica 04, Università degli Studi di Ancona, Facoltà di Ingegneria, Istituto di Scienza e Tecnica delle Costruzioni, 1980.

Research Article

Rapid Mapping and Deformation Analysis over Cultural Heritage and Rural Sites Based on Persistent Scatterer Interferometry

D. Tapete¹ and F. Cigna²

¹Department of Earth Sciences, University of Florence, Via G. La Pira 4, 50121 Florence, Italy

²British Geological Survey, Natural Environment Research Council, Nicker Hill, Keyworth, Nottingham NG12 5GG, UK

Correspondence should be addressed to D. Tapete, deodato.tapete@gmail.com

Received 23 May 2012; Accepted 3 July 2012

Academic Editor: Francesco Soldovieri

Copyright © 2012 D. Tapete and F. Cigna. This is an open access article distributed under the Creative Commons Attribution License, which permits unrestricted use, distribution, and reproduction in any medium, provided the original work is properly cited.

We propose an easy-to-use procedure of “PSI-based rapid mapping and deformation analysis,” to effectively exploit Persistent Scatterer Interferometry (PSI) for multispatial/temporal hazard assessment of cultural heritage and rural sites, update the condition report at the scale of entire site and single building, and address the conservation strategies. Advantages and drawbacks of the methodology are critically discussed based on feasibility tests performed over Pitigliano and Bivigliano, respectively, located in Southern and Northern Tuscany, Italy, and representative of hilltop historic towns and countryside settlements chronically affected by natural hazards. We radar-interpreted ERS-1/2 (1992–2000) and ENVISAT (2003–2010) datasets, already processed, respectively with the Permanent Scatterers (PSs) and Persistent Scatterers Pairs (PSPs) techniques, and assigned the levels of conservation criticality for both the sites. The PSI analysis allowed the zoning of the most unstable sectors of Pitigliano and showed a good agreement with the most updated hazard assessment of the cliff. The reconstruction of past/recent deformation patterns over Bivigliano confirmed the criticality for the Church of San Romolo, supporting the hypothesis of a correlation with local landslide phenomena, as also perceived from the annual motions observed over the entire site, where several landslide bodies are mapped.

1. Introduction

One of the main challenges in conducting a technological transfer process consists in communicating developments and achievements of science to the potential stakeholders, to effectively contribute to the building and strengthening of their capabilities in the use of new technologies for the specific fields of application. This issue is currently particularly relevant in the perspective of spreading and encouraging the use of satellite radar data for deformation analyses, not only in geological and environmental applications but also in the management and conservation of built heritage in cultural and rural sites.

In this regard, in the last decades, the standard approach of Synthetic Aperture Radar Interferometry (InSAR) [1, 2] has increasingly found successful implementation in ground motions monitoring and deformation analyses at multiple scales, mainly relating to natural hazard events [3–6], geological processes [7, 8], and human-induced phenomena

[9, 10]. But a significant improvement, especially for analyses over urbanized areas, infrastructure, and human settlements [11–14], has been achieved with the multi-interferogram approaches referred to as Persistent Scatterer Interferometry (PSI). The latter are actually performed by means of different algorithms (among which those developed by different authors [15–19]), which share the common feature of providing point wise information regarding displacements of reflective targets recognized as Persistent Scatterer (PS) throughout long data stacks of processed SAR images.

Hence, the PSI approaches are nowadays validated techniques which can allow a quantitative estimation of the degree of (in)stability of an entire region, an enclosed sector and even single clusters of buildings/elements on the ground to be performed, with a temporal reconstruction up to 1992 in case of availability of ERS-1/2 satellite imagery. This actually corresponds to the so-called back monitoring, as firstly defined by Cigna et al. [12] and specifically adapted to structural monitoring and early stage warning of cultural

heritage sites by Tapete et al. [20]. The demonstration that PSI data can support the preventive diagnosis of monuments and historical buildings induces to consider such techniques as potential routine tools to monitor and assess the stability and, more generally, the condition over time, to be used by heritage bodies, superintendences, public administrations in charge of cultural heritage management, conservators, and practitioners.

A further chance for that is currently offered by the increasing number of projects and acquisition programmes at regional, national, and, sometimes, transnational level, which are aimed at the creation of databases containing processed PSI data thought to be finally used by public bodies, local authorities, and a wide spectrum of stakeholders and end-users, in their ordinary activities of land and urban environment planning and management. We can here cite, for instance, the ESA GMES project TerraFirma [21] and the Seventh Framework Programme EU project PanGeo [22], as well as the Extraordinary Plan of Environmental Remote Sensing (EPRS-E), that is, the Italian project established between the Italian Ministry of Environment Territory and Sea (METS), Chairperson of the Council of Ministers Department of Civil Protection and the Ministry of Defense in agreement with the Regions and Autonomous Provinces, to acquire, process, and periodically update PSI data over the whole Italian territory for environmental and civil protection activities [23].

Although such initiatives are frequently designed for other uses than application on cultural heritage sites, it cannot exclude that this typology of PSI data can constitute a precious reservoir of information for the preservation of monuments and historic centres, as also recently suggested by Trigila et al. [24] for landslide risk assessment in cultural heritage sites.

The present work is specifically aimed at proposing a simple and easy-to-use methodology to exploit PSI data for rapid mapping and deformation analysis over hilltop historic centres and rural sites, based on the results of feasibility tests performed on two case studies located in Tuscany, Central Italy. The latter were purposely selected as examples of real-world situations and related analytical issues that potential end-users (e.g., superintendence officers, conservators) might have to tackle, especially if they have to radar-interpret PSI data not necessarily processed to be used for cultural heritage applications or to be focused over a particular area of interest at an appropriate scale of analysis. Under this perspective, ERS-1/2 (1992–2000) and ENVISAT (2003–2010) PSI data, already processed in the framework of the EPRS-E project [23] by means of, respectively, the PSInSAR technique [16] and PSP-DIFSAR approach (Persistent Scatterers Pairs-Differential InSAR; [15]), were radar-interpreted as they are, without any further processing. The results of these site-specific analyses are here presented to critically discuss the potentials and limits of such PSI-based deformation analysis, in terms of real usefulness for preventive diagnosis of cultural heritage and land management in rural environments.

2. PSI-Based Procedure of Preventive Diagnosis

2.1. PSI Techniques. Superficial deformation affecting the area covered by the processed radar imagery (Area Of Interest (AOI)) acquired by means of space-borne SAR sensors can be detected after a PSI processing, since the employed algorithms allow the identification of natural/artificial reflectors on the ground. The latter keep their dielectric properties quite constant over the monitoring period and, consequently, act as permanent reflectors (Persistent Scatterer—(PS)) with respect to the microwave wavelengths generated and sent by the active satellite sensors. For each identified PS, the multi-interferogram processing of long data stacks of SAR images covering the AOI highlights the occurrence of changes in its spatial position along the Line Of Sight (LOS) of the satellite and provides an estimate, over time, of the LOS component of the real displacement vector, which geometrically describes the deformation of the point wise target.

The final output of such PSI processing consists of a distribution, over the AOI, of clusters and/or isolated PS; for each of them the following parameters and information are retrieved:

- (i) longitude and latitude coordinates, associated with the height (h) and related standard deviation (SD_h);
- (ii) estimate along the LOS of the yearly deformation rate (V_{LOS}), usually expressed in mm/yr, and related standard deviation ($SD_{V_{LOS}}$);
- (iii) deformation time series, where the single values of LOS displacements (expressed in mm) estimated according to the sampling frequency of the satellite are plotted versus the monitoring interval;
- (iv) PS coherence, that is, one of the quality parameters, together with the LOS velocity and height deviation standards, usually employed to evaluate the informational content of each PS estimate. Its dimensionless value, ranging between 0 and 1, gives a measure of how much the single time series fits with the deformation model used for the PSI processing.

Different authors [25, 26] have demonstrated that the PS usually corresponds to boulders and outcrops within natural contexts, man-made structures and infrastructure in built-up areas. In this regard, monuments, architectural elements with prominent and multiangular shape (e.g., pillars, towers, spires), archaeological structures (e.g., pinnacles, columns, ruins), and findings scattered on the ground (e.g., column drums, fallen architraves) can generate PS after PSI processing. This evidence has been recently confirmed by the results of different site-specific analyses, such as those discussed elsewhere [13, 20, 27, 28].

The papers [19, 27] also provide an extended theoretical discussion of the basic principles of the PSI processing (particularly the PSInSAR technique [16], used for the PSI processing of the radar data here analyzed) with specific reference to cultural heritage contexts, as well as schematic examples of the deterioration processes which can be monitored (e.g., land subsidence, masonry toppling,

crack opening, collapses). The wide spectrum of detectable phenomena is evidently coupled by intrinsic pros and cons. If on one hand the PSI techniques can be successfully exploited for different typologies of instability processes, on the other hand the retrieved estimates only give information about the superficial effects of deterioration and instability phenomena which might be actually attributed to different triggering causes. Hence, solid background knowledge of the AOI and on-site inspections are frequently the key elements to achieve a correct radar interpretation of the PSI data.

Nevertheless, the last decade of PSI applications on environmental, geological, and urban topics confirms the reliability of these techniques, especially in terms of interoperability with conventional field observations and investigations [29, *cum biblio*]. This property is evidently essential for the purposes of a rapid mapping based on PSI data, like that proposed in this paper, which starts from an evaluation, carried out remotely, of the conservation issues affecting the built heritage over the AOI, as preparatory action to the execution of targeted and tailored terrestrial surveys.

2.2. PSI-Based Rapid Mapping. With the term “PSI-based rapid mapping” we mean the methodology and related final product to assess the (in)stability conditions over the AOI and reconstruct their past and/or recent evolution, by means of a multispatial and temporal analysis of PSI data which uses the LOS velocity estimates and the associated directions of movement (towards or away from the satellite) as reliable satellite evidences of “conservation criticalities.” In particular, the latter term refers to natural and/or human-induced factors, conditions, and dynamics which can bring to the triggering of deterioration processes and more generally to key areas of concern for the conservation of the AOI.

The main objective of a PSI-based rapid mapping is the production of a map (updated as much as possible, dependently on the last SAR image of the processed data stacks) of the deformation patterns recognized after the PSI processing, which are likely to be related to recent, ongoing, or, even, upcoming deterioration phenomena. This map is expected to preventively highlight the unstable sectors of a monument, archaeological site, historic centre, or rural settlement rather than the stable ones (“preventive diagnosis”), thereby becoming a practical guiding tool for the selective zoning of the critical areas, where the execution of surveys and stabilization interventions is found as a priority.

The proposed procedure (Figure 1) is aimed at the extraction of the maximum amount of information in terms of deformation estimates, especially in cases of already existing PSI data, which were not processed with the main purpose of being used for cultural heritage applications. In doing that, the sequence of the different phases constituting the methodology is thought to avoid both under- and overestimation of the identified PS, as well as possible misinterpretation of those PSs which are actually pertinent to unrelated elements on the ground, located close to the objects of interest.

In this regard, the first step is the “background phase.” It is specifically dedicated to the collection and review of

all the existing information about the AOI and its heritage, to build a background knowledge which should address the subsequent multispatial and temporal analysis of the PSI data.

Before running through the “rapid mapping phase”, which is the core of the PSI-based procedure of preventive diagnosis, SAR imagery to process and the deformation model to employ for the PSI processing are to be carefully selected (a specific focus on this issue can be found in [20]). This intermediate step is not tackled in the present paper, since we here consider the case of rapid mapping and deformation analysis carried out on already available and processed multiplatform PSI data. Nevertheless, it is worth mentioning that the choice of the processing parameters can significantly influence the obtained PSI data and, consequently, the reliability of the analysis. Indeed, they might have nonnegligible implications on the actual capability of monitoring deformation at the scale of single building/monument, as well as very localized small-area phenomena, as properly suggested by Colesanti and Wasowski [30].

During the rapid mapping phase, each of the employed PS datasets is progressively analyzed in terms of velocity, spatial distribution, and temporal frame.

The first evaluation concerns the LOS velocity distribution of the PS identified over the AOI. This initial assessment gives a rough idea of the overall stability of the AOI, although it is to be considered only a preliminary impression of the deformation pattern(s) to be confirmed during the subsequent phases. According to the sensitivity of the PSI techniques, the threshold commonly chosen as “interval of relative stability” is fixed at $V_{LOS} = \pm 1.5$ mm/yr (where negative values correspond to LOS displacements away from the satellite, while the positive ones towards the satellite).

It means that PSs with value of -1.5 mm/yr $\leq V_{LOS} \leq +1.5$ mm/yr are classified as relatively stable, pending the verification that any displacement trend or acceleration/deceleration(s) are recognizable within their respective time series. An area apparently stable might have been affected by deformation in the past. At the opposite, high values of V_{LOS} can correspond to LOS displacements with acceleration(s) concentrated in temporal intervals limited within the whole monitoring period, which might have consequently influenced the entire PS deformation time series.

Prior to a temporal evaluation of the detected deformation, the PS spatial distribution is analyzed with regard to the location of the site/monuments, to highlight if significant deformation has taken place in correspondence with elements of cultural/civil value, their surroundings, and/or their foundation substratum. In relation to the spatial configuration of the PS clusters, the detected deformation can be distinguished into three main typologies, following the classification proposed in the papers [20, 28]—“macropattern,” “micropattern,” and “localized deformation” (Figure 2).

A macropattern is frequently found over areas affected by natural and/or anthropogenic phenomena active at large scale, in some cases at regional scale. An example is provided

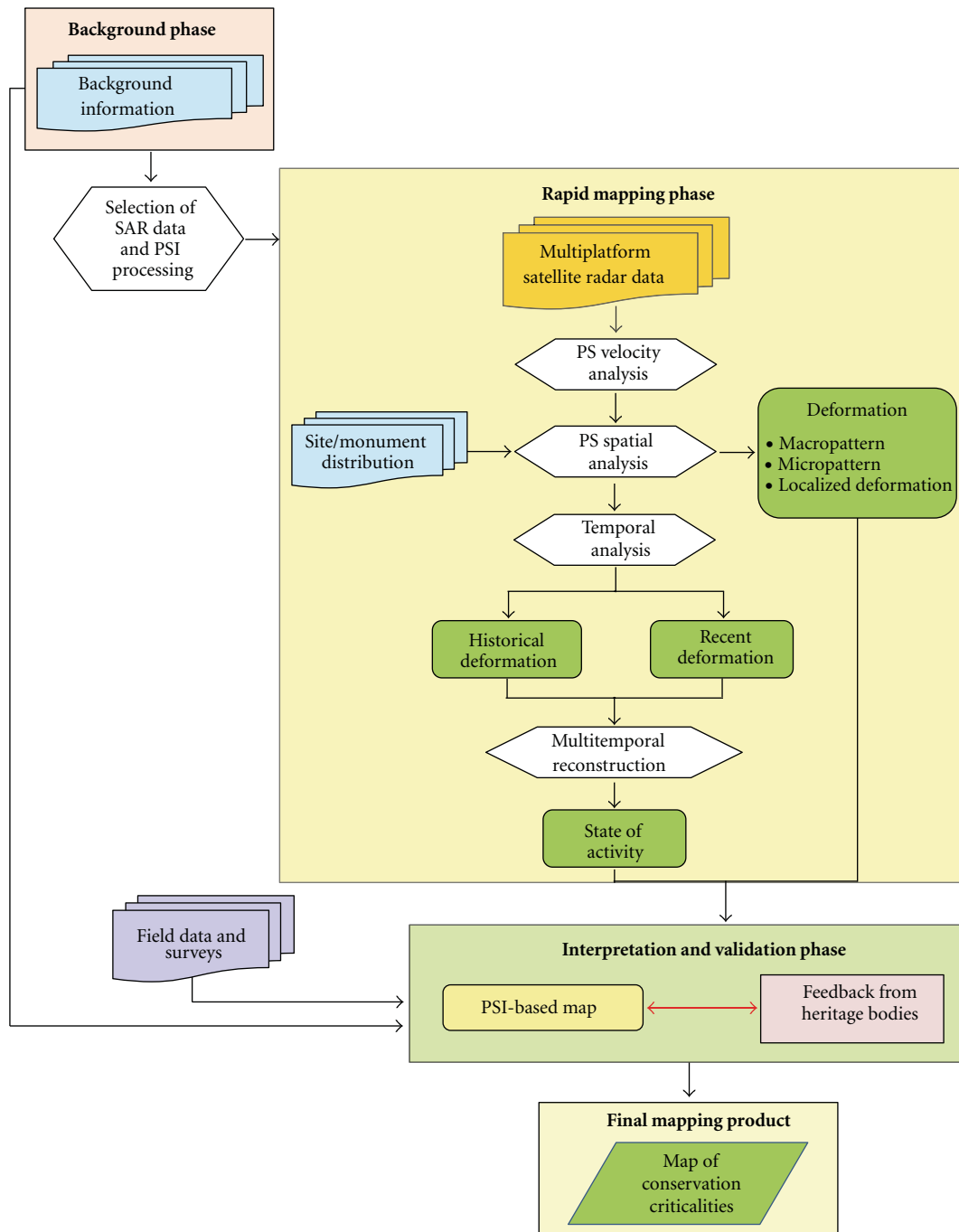


FIGURE 1: Procedure of PSI-based rapid mapping and deformation analysis to retrieve the map of conservation criticalities over cultural heritage and rural sites.

by the subsidence movements observed over recent alluvial deposits of the Tiber river, centre of Rome (Italy), which might have implications for the conservation of urban monuments like the Aurelian Walls (Figure 2(a)). Deformation macropatterns may also affect human settlements, such as in the case of Torrita di Siena, Tuscany (Italy), where a large portion of the town shows LOS displacements away from the satellite (Figure 2(b)). Differently, micropatterns are usually much less extended and typically mark single portions of

a site/monument (Figure 2(c), with a zoomed aerial view of Fortezza da Basso, centre of Florence, Italy), likely over buildings located on unstable ground or structural weakness points.

While small clusters of PSs (at least two/three PSs) can identify a micropattern, especially if they show common LOS displacement trends over the same time interval, isolated PS can be referred to localized deformation (Figure 2(c), PS in the yellow circle). The major issue during the interpretation

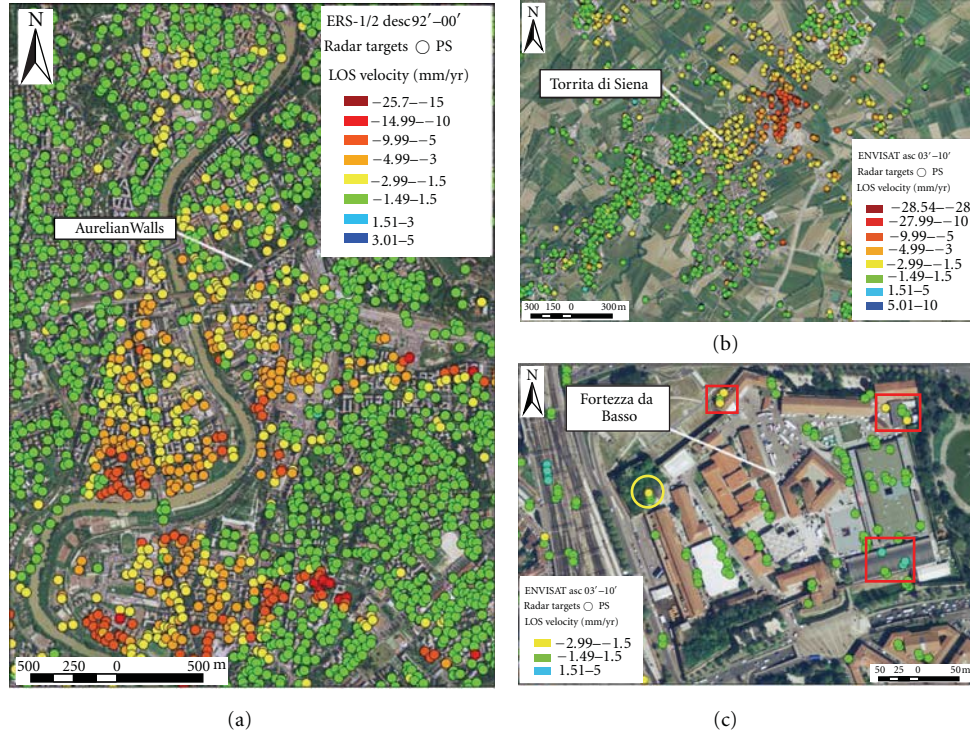


FIGURE 2: PSI-based deterioration patterns classifiable as macropattern ((a)-(b)); micropattern (i.e., the PS clusters within the red squares in (c)); localized deformation (i.e., the single PS within the yellow circle in (c)).

of such localized deformation concerns the reliability of their informational value. The comparison between their coordinates and height value and the spatial distribution of the built heritage, as well as the knowledge of the local AOI topography, significantly facilitates the attribution of single PS to objects of interest rather than neighbouring unrelated elements (e.g., light poles, infrastructure, public bins). Once the PS has been correctly spatially located, its value in terms of detected deformation is to be carefully assessed in the context of a multitemporal PSI analysis, before classifying it as an occasional displacement event or a negligible deformation estimate.

In this regard, the temporal analysis of multiplatform PS datasets covering distinct and subsequent temporal intervals of observation allows the reconstruction of the evolution of the detected deformation in time, although the different acquisition geometries which characterize the employed satellites still remain a technical constraint to achieve a perfect comparison between multi-platform deformation estimates. Nevertheless, the persistence of deformation over a same area, monument, or architectural element, throughout the different analyzed datasets (i.e., from historical data to recent ones), is generally a reliable indicator of ongoing deterioration processes. Frequently, the analysis of more recent PSI data permits the operators to better and more correctly radar-interpret PS belonging to older datasets, and further confirmation can be retrieved by means of field surveys.

As main outcome of the multitemporal analysis, the state of activity of a deformation is assessed. Regarding

the historical data, the absence of any previous PSI-based classification implies that the areas found as subjected to deformation can be classified as follows:

- (i) absence of PSI data \rightarrow N.C. (i.e., not classifiable);
- (ii) single or clusters of PS with $-1.5 \text{ mm/yr} \leq V_{\text{LOS}} \leq +1.5 \text{ mm/yr}$ (independently of the PS spatial distribution) \rightarrow stable;
- (iii) single or clusters of PS with V_{LOS} exceeding the stability threshold, that is, $V_{\text{LOS}} \leq -1.5 \text{ mm/yr}$ or $V_{\text{LOS}} \geq +1.5 \text{ mm/yr} \rightarrow$ active.

In the latter case, the definition of the state of activity is coupled with the assessment of the typology of deformation pattern (i.e., macropattern, micropattern or localized deformation).

This type of classification is also employed in those cases where the rapid mapping is performed only based on single-platform PSI data (e.g., PS obtained after multi-interferogram processing of ERS-1/2 radar imagery rather than ENVISAT one). The nonavailability of other platform PS datasets should always be avoided, since it leads to a partial evaluation of the deformational behaviour over the AOI. Nevertheless, it is not rare that, due to economic reasons and/or gaps in the satellite archives, the rapid mapping over the AOI can be carried out with a limited number of PS datasets. Furthermore, even if both the ascending and descending geometries of a same satellite are available, any difference in spatial resolution (e.g., Standard Beam Mode rather than Fine Beam Mode in the case of

Classification based on historical versus recent PSI data			
State of activity	LOS velocity	Spatial distribution	Level of conservation criticality
Active	Intensified	More extended	
Active	Intensified	Stable	
Active	Intensified	Reduced	
Active	Less intense	More extended	
Active	Less intense	Stable	
Active	Less intense	Reduced	
Stabilized	—	—	
Stable	—	—	

FIGURE 3: Scale of conservation criticality based on multi-temporal analysis of historical and recent PSI data. Increasing level of conservation criticality is associated to deformation, which worsen in terms of state of activity, intensity (LOS velocity— V_{LOS}) and/or spatial distribution (i.e., typology of deformation pattern).

RADARSAT-1/2 data stacks) or type of processing can affect the quality of the radar interpretation.

Conversely, when comparing recent PSI data with the historical ones, the following aspects should be taken into account:

- (i) if new deformation is detected where no PSs were identified in the previous dataset(s);
- (ii) if a previously detected phenomenon is still present and, in such a case, if it is still active or not;
- (iii) if the deformation has changed its intensity or not;
- (iv) if the new PS spatial distribution still belongs or not to the same class of deformation pattern typology.

According to the previously listed elements, a level of conservation criticality can be assigned, following the scale of progressive alert and priority shown in Figure 3.

The maximum level is attributed to deformation which is found as intensified (i.e., $V_r \geq V_h$, where V_h is the LOS velocity estimated in the historical PSI data and V_r in the recent ones) and becomes more spatially extended (e.g., localized deformation changed into micropattern or micropattern changed into macropattern) from the historical data to the recent ones. Similarly, if a new deformation not previously mapped is identified, worse typologies of deformation pattern will be classified with higher alert levels.

On the contrary, if the more updated PSI data record lower yearly deformation rates (i.e., $V_r \leq V_h$), an accurate detailed analysis of the deformation time series is highly suggested, in addition to the mere comparison between the two LOS velocity values. Also, following such a cautionary and conservative approach (similar to that currently employed in PSI-based updating of landslide inventories; [28]), the execution of on-site inspections and feedback from the heritage bodies can provide, during the “interpretation and validation phase,” further evidence to classify a sector of the AOI as stabilized (Figure 1).

If no changes occurred over the area, this sector can be classified as stable with a relatively high degree of confidence. Conversely, the absence of PSs over previously moving areas does not necessarily mean that these sectors are now stable. Especially when comparing multiplatform PS datasets, the difference of both the acquisition geometry and temporal period of observation is to be carefully considered. Deformation that was observed and estimated by one satellite at a certain time according to its acquisition geometry might not have been appreciated by another satellite. Lack of PS is evidently an intrinsic weakness of such a type of rapid mapping.

2.3. Map of Conservation Criticalities. The output of the rapid mapping phase is a “PSI-based map” which shows the location, extent, and distribution of the unstable areas of a site and critical sectors of a monument, dependently on the scale and purposes of the analysis. This map is, at the same time, a guide for the execution of targeted on-site checks rather than extensive and expensive surveys and a tool to be validated by the ground truth collected during the inspections themselves.

Indeed, the latter, combined with the background knowledge and the feedback from the heritage bodies (and, more generally, from all the keepers of the cultural and civil elements of interest subjected to deformation during the observation temporal interval) can help to confirm the satellite evidences reported in the PSI-based map. Also, a reliable and strong correlation between the detected deformation and the deterioration phenomena observable on the exposed surfaces can be found, thereby retrieving essential elements to propose a robust interpretation of the analyzed PSI data.

The multilayering analysis of (i) the local natural and/or human-induced factors of deterioration, (ii) the multitemporal deformation estimates detected from satellite, and (iii) the information of the past/recent history of the AOI

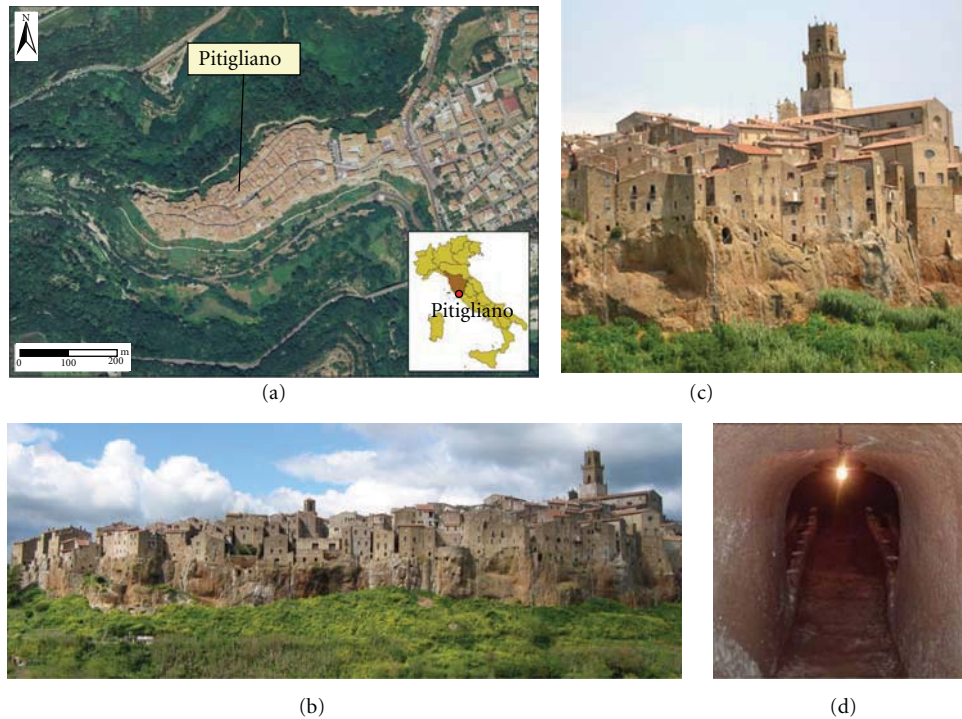


FIGURE 4: (a) Aerial view of the Pitigliano cliff, Southern Tuscany and (b) a detail of the southern side. The built heritage along the cliff edge is exposed to rock mass instability mechanisms (c), while an additional hazard can derive from inner collapses of the cavities cut in the tuff substratum underneath the buildings ((d); photo by M. Capretti).

finally translates into a same mapping product, called map of conservation criticalities. This actually represents the final output of the process of rapid mapping and deformation analysis, and it is expected to provide an inventory map in support of the condition reporting of the site/monument of interest. Its degree of updating is evidently strictly dependent on the temporal coverage of the analyzed PSI data. The map of conservation criticalities can be ideally updated, as soon as new satellite acquisitions and more recent PS datasets are added to the previous analysis.

3. Feasibility Tests

3.1. Sites Selection, PSI Data, and Rationale. The applicability of the proposed methodology was evaluated by means of feasibility tests carried out on two case studies located in Tuscany, Central Italy, which were purposely selected to be representative of the following typologies of cultural heritage and countryside settlements: (i) hilltop historic towns and (ii) rural sites.

The first category allows the discussion of the conservation issues concerning architectural heritage built at the top of unstable rock masses, whose instability mechanisms can progressively cause structural damages to the monuments located along the edge, even their collapse and consequent disappearance. In these terms, the case of the historic centre of Pitigliano, Southern Tuscany (Figure 4) is a quite demonstrative example of sites where the built heritage potentially at risk is distributed along the entire cliff edge

and is exposed to rock mass instability mechanisms, as well as cavities collapse.

For the second category of cultural heritage, the countryside settlement of Bivigliano, north of Florence (Figure 5), was selected, since its cultural, landscape, and built heritage and related conservation issues well exemplify situations of land management quite common over the Italian territory.

These feasibility tests were thought not only to provide a multiple validation of the usefulness of the PSI-based methodology and techniques employed on different contexts of application but also to demonstrate the potential range of stakeholders and end-users who can be interested in the use of PSI data, especially if the latter are made available in the framework of acquisition and processing programmes at local, regional, or national scale.

In this perspective, we exploited the deformation estimates of the previously cited EPRS-E database [23], obtained after PSI processing of C-band data of ENVISAT and ERS-1/2 satellites of the European Space Agency. ENVISAT images, acquired with wavelength (λ) of 5.63 cm and nominal revisiting time of 35 days, were processed with the PSP-DIFSAR approach (Persistent Scatterers Pairs-Differential InSAR; [15]), while ERS-1/2 images, acquired with $\lambda = 5.66$ cm and the same nominal revisiting time as ENVISAT satellite, were processed with the PSInSAR technique [16]. Details about the processing parameters, as well as accuracy and error bars of these PSI estimates, are reported in [31], while the main characteristics of the analyzed PS datasets with specific regard to each test site are summarized in Table 1.

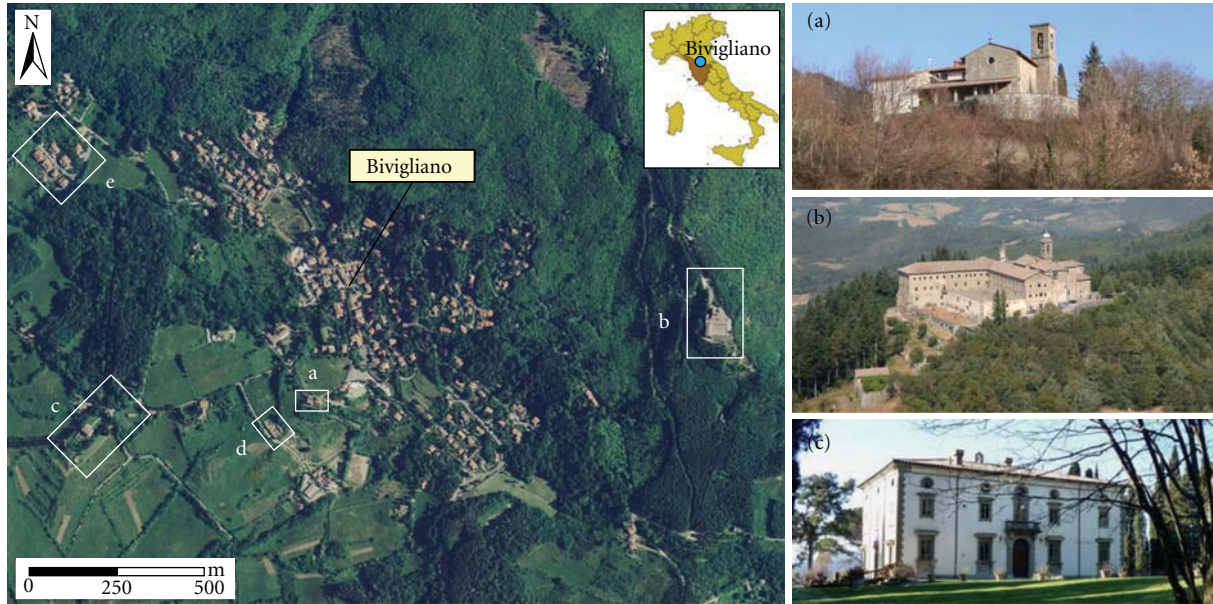


FIGURE 5: Aerial view of the countryside settlement of Bivigliano, Northern Tuscany, with location of the main historic heritage: (a) Church of San Romolo; (b) Convent of Monte Senario; (c) Villa Pozzolini. Further elements of interest for the present feasibility test are (d) the modern cemetery and (e) the area of the local craftsmen (Marroneto).

TABLE 1: Main characteristics of the analyzed datasets; Asc: ascending; Desc: descending. PS density was calculated with regard to the extent of the AOI, which was equal to 0.11 km² for the Pitigliano cliff and 1.73 km² for the territory of Bivigliano.

Site	Data stack	Orbit	Repeat cycle (days)	Time interval	N. images	Processing technique	Total N. PS	PS density (PS km ⁻²)
Pitigliano	ERS-1/2	Desc	35	10/05/1992 13/12/2000	60	PSInSAR	44	400
	ENVISAT	Asc	35	16/10/2003 27/05/2010	34	PSP-DIFSAR	159	1446
	ENVISAT	Desc	35	07/05/2003 09/06/2010	51	PSP-DIFSAR	193	1775
Bivigliano	ERS-1/2	Desc	35	24/04/1992 27/11/2000	79	PSInSAR	145	84
	ENVISAT	Asc	35	16/10/2003 27/05/2010	35	PSP-DIFSAR	130	75
	ENVISAT	Desc	35	10/02/2003 28/06/2010	35	PSP-DIFSAR	504	291

As previously mentioned, these PSI data were radar-interpreted as they are, without any further processing. The rationale behind this technical choice was the possibility to simulate real-world situations that any public administration officer or stakeholder might have to tackle, when exploiting this type of data for applications of rapid mapping and deformation analysis, dealing with both their advantages and shortcomings.

3.2. Hilltop Historic Sites: Pitigliano, Southern Tuscany (Italy). The historic centre of Pitigliano developed through centuries over a flat slab at the top of 25-metre-thick plateau of Pleistocene tuffs, with a present elevation of about 310 m a.s.l. and approximately oriented along the E-W direction (Figures 4(a)-4(b)). The geological sequence

which constitutes the cliff is the result of an intense volcanic activity, mainly related to the volcanic complexes located in the northern Latium [32, 33], and the rock formations originated from the corresponding phases of pyroclastic deposits. Referring to Canuti et al. [34] and Fanti et al. [35] for a detailed geological setting of the Pitigliano cliff, it is here worth mentioning that the welded tuffs belonging to the Sorano/Grotte di Castro Formation represent the substratum underneath the historical buildings. These tuffs were also extensively cut and excavated in depth since Etruscan times, thereby creating a huge network of subterranean caves and corridors, which is actually a sort of “second town” and, at the same time, a source of instability issues due to inner collapses (Figure 4(d)).

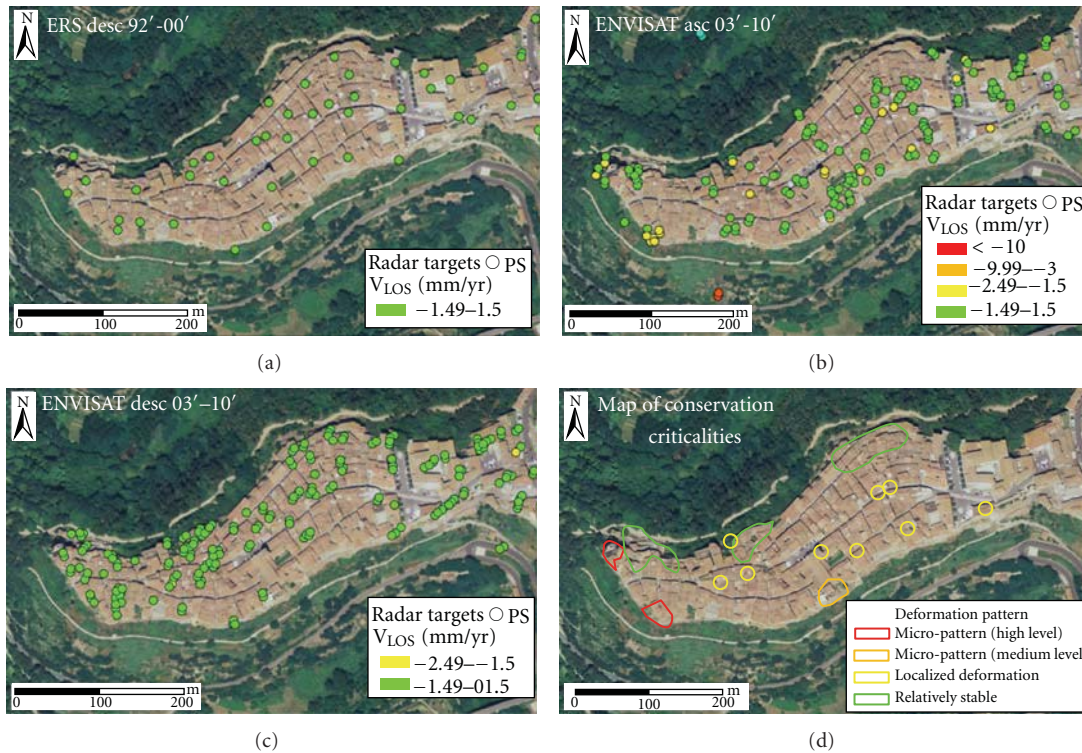


FIGURE 6: PS spatial distribution and related V_{LOS} field over the Pitigliano cliff for the datasets: (a) ERS descending (1992–2000); (b) ENVISAT ascending (2003–2010); (c) ENVISAT descending (2003–2010). The PSI-based rapid mapping led to draw a map of the conservation criticalities (d), which reports the zoning of the unstable sectors and localized deformation, distinguished from the relatively stable areas.

In addition to this factor of criticality, the built heritage of Pitigliano located along the cliff edges is chronically affected by the instability mechanisms of the exposed rock surfaces, due to a combination of several weathering processes, such as chemical alteration, erosion, cryoclastism, and crack patterns opening, which progressively create the conditions for the triggering of rock falls and toppling events (Figure 4(c)). Hence, the continuous geomorphologic evolution of the cliff can be nowadays recognized as one of the main threats for the preservation of the Pitigliano heritage [35].

PSI data were specifically radar-interpreted to perform a zoning of the sectors along the cliff edges classifiable as potentially critical. At the same time, detailed time series analysis was exploited to verify if the unstable PSs identified over the historical buildings located within the town centre could highlight the occurrence of sudden displacements, to be correlated to potential collapses of subterranean cavities or predisposing conditions for near future collapses.

Despite the relevant number of the processed SAR images, the PSInSAR processing of the ERS-1/2 descending (1992–2000) data stack led to the identification of a reduced set of PSs (Table 1), whose spatial distribution does not homogeneously cover the historic centre (Figure 6(a)). Although this result partially makes the deformation analysis less spatially representative over the different sectors of the town, the ERS data are sufficient to confirm the absence, in the period 1992–2000, of deformation macropatterns

referable to instability phenomena extended to the entire site. Indeed, all the ERS descending PSs show values of V_{LOS} not exceeding the stability threshold (± 1.5 mm/yr). This first impression of relative stability is supported by the detailed analysis of the PS time series, which in few cases highlight a slight tendency of the LOS displacements to movements going towards the satellite, only occasionally with $V_{LOS} > +1$ mm/yr. In the absence of the corresponding ascending dataset, very low level of conservation criticality can be assigned over the whole historic centre for the period (1992–2000).

Passing to the more recent data, that is, the ENVISAT (2003–2010) ones, a significant increase in the total number of PS is immediately appreciable in both the ascending and descending datasets (Table 1), although their respective PS spatial distribution shows some lack over certain sectors of the town, reflecting the different acquisition geometry of the processed SAR images (Figures 6(b)–6(c)). Particularly, the ascending dataset mainly covers the central-southern parts of the town (Figure 6(b)), while the descending one results in being better distributed over the central-northern sectors (Figure 6(c)).

Being aware that the two datasets are not perfectly temporally overlapped (October 2003–May 2010 for the ascending data, May 2003–June 2010 for the descending ones), the integrated analysis of the deformation estimates highlights the presence of two micropatterns, with downwards LOS

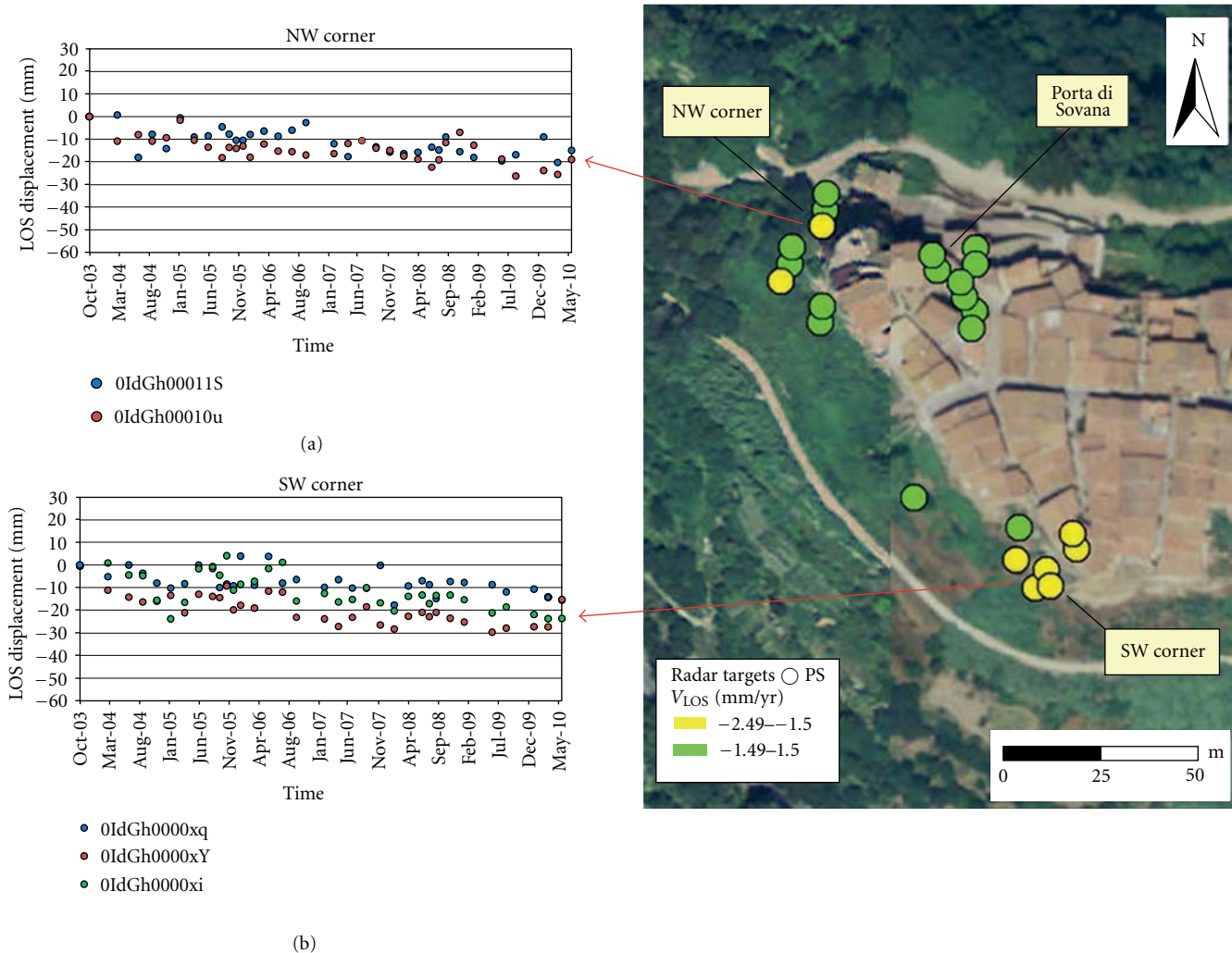


FIGURE 7: Spatial distribution and related V_{LOS} field for the ENVISAT ascending (2003–2010) dataset over the western side of the Pitigliano cliff. Deformation micropatterns are identified over the north-western and south-western corners of the cliff, with downwards moving PS, whose time series are reported, respectively, in the plots (a) and (b).

displacements in the ascending data, concentrated, respectively, over the north-western and south-western corners of the cliff (Figures 6(b), 6(d), and 7).

The PS cluster over the north-western corner is characterized by two PS ENVISAT ascending (2003–2010) with V_{LOS} up to -2.1 mm/yr (Figure 7), whose time series show displacement trends progressively going away from the satellite, especially since March 2005 (Figure 7(a)). Slight tendency to downwards movements is also recognizable within the time series of neighbouring PSs, which appear stable as their V_{LOS} only occasionally exceed the value of -1 mm/yr. The presence of several deformation estimates which share similar displacement trends induces to assign a medium-high level of conservation criticality to the buildings located on the north-western corner of the cliff.

On the other hand, there is no doubt to classify the built-up area on the south-western corner as highly critical (Figures 6(d) and 7), due to the significant number of downwards moving PS ENVISAT ascending (2003–2010) concentrated

over the buildings and along the slope; the intensity of the detected deformation (V_{LOS} up to -2.9 mm/yr); the persistence, throughout the monitoring period, of a displacement trend progressively going away from the satellite (Figure 7(b)); the value of the estimated total LOS displacement (up to -25 mm over approximately seven years). Also, the time series of the PS located, respectively, along the slope, close to the cliff edge and over the buildings show similar LOS displacement trends (Figure 7(b)).

The priority level to assign to these two sectors, as assessed based on the PSI data, is further appreciable if compared with the relative stability that both the ascending and descending ENVISAT datasets show over other sectors of the cliff, such as the area of Porta di Sovana, located just few metres from the north-western corner, along the northern edge (Figures 6(d) and 7). Here, the detailed analysis of PS time series completely excludes the occurrence of clear deformation trends potentially associable to instability processes active in the period 2003–2010.



FIGURE 8: Detailed view of the south-western corner of the Pitigliano cliff. Close examination of the rock surfaces highlights the boundaries of rock wedges underneath the masonry walls.

As further element to strengthen the relevance of these satellite findings in the perspective of an effective early stage warning of near future instability, it is to be mentioned that both the sectors classified as unstable belong to a portion of the Pitigliano town which was historically damaged by progressive retreat of the cliff likely due to rock falls. As reported by Fanti et al. [35], a recent archive-based research comparing historical maps and old photographs has clarified that the western side of the cliff is nowadays completely modified from the past, and several buildings totally disappeared.

The high level of conservation criticality of both the sectors is also confirmed by the hazard assessment performed by Canuti and Fanti [36] and recently published by Fanti et al. [35] as 3D quantitative kinematic analysis directly performed on high detailed terrestrial laser scanning survey of the cliff. Based on these data and direct observations on the rock surfaces (Figure 8), the mechanisms known as “wedge failure,” “flexural block toppling,” and, secondarily, “toppling” are the highest probable for the south-western corner, while the flexural toppling is predominant for the north-western corner. In these terms, the persistence, throughout the monitoring period, of LOS displacements going away from the satellite in the ascending geometry leads not to exclude the hypothesis of tilting movements of the exposed elements as a consequence of active rock mass instability.

A second level of priority seems reasonable to be attributed to localized deformation, which was detected over single buildings located along the southern side of the cliff (orange micropattern in Figures 6(d) and 9). The similarity in terms of LOS displacement trend between a downwards moving PS with V_{LOS} up to -1.7 mm/yr and two PSs

apparently stable suggests the presence of a more extended deformation pattern (Figure 9(b)). In particular, mutually comparable records of LOS displacements are recognizable within all the respective PS time series, especially since February 2007.

Differently, the ENVISAT ascending (2003–2010) dataset does not show particular evidence of instability processes for the northern cliff side, except for a localized deformation found over an enclosed sector of buildings in the central part of the northern edge (yellow circle in Figure 6(d)). Although the poor coverage of this dataset along the northern side does not allow a complete deformation analysis to be performed, the corresponding descending data show relatively stable PS time series and suggest a quite relative stability in the period 2003–2010 (Figures 6(c)–6(d)).

Interestingly, over several buildings within the town centre, the time series of downwards moving PS ENVISAT ascending (2003–2010) do not reveal the occurrence of significant accelerations. No evidences of sudden displacements due to cavities collapses are found (Figures 6(b) and 9). Indeed, most of the PS time series are characterized by LOS displacement trends progressively going away from the satellite, with V_{LOS} up to -2.2 mm/yr (Figure 9(a)). If on one hand this evidence does not give proof about past/recent instability events, on the other hand it is not to be excluded that further SAR acquisitions after the last updating of the analyzed PSI data (i.e., May 2010) could confirm the evolution of these progressive displacement trends. Hence, on-site checks and terrestrial surveys, performed also within the subterranean cavities underneath the buildings, seem to be a necessary step to validate and correctly interpret the data.

Similar considerations are also valid for the time series of the single downwards moving PS identified in the ENVISAT descending data (2003–2010) in the middle of the town centre (Figure 6(c)).

3.3. Rural Sites: Bivigliano, Northern Tuscany (Italy). Sited 20 km north of Florence in the municipal territory of Vaglia, the countryside settlement of Bivigliano is mainly built along the western slope of the mountain called Monte Senario (Figure 5). Geologically, the site is founded on Holocene colluvial sediments overlying the bedrock constituted by the Monte Senario Sandstones Formation, that is, Middle-Lower Eocene feldspathic-quartz sandstones containing coarse quartz pebbles, mica, phyllite, and calcareous material. In terms of historic and artistic heritage, since medieval times the parish church (Figure 5(a)) based in Bivigliano was a landmark for the social life of all the territory and, starting from the XIII century, it was flanked by the neighbouring Convent of Monte Senario (Figure 5(b)). Despite this ancient origin (the name “Bivigliano” derives from a member of the Medici family, already powerful in the Medieval-Renaissance Florence), the current urban arrangement of Bivigliano was strongly influenced by the recent history. The village was a renowned place for holidays since the end of the XIX century and flourished with a significant urban development phase in the decades 1900–1950s. In this period, for instance, the

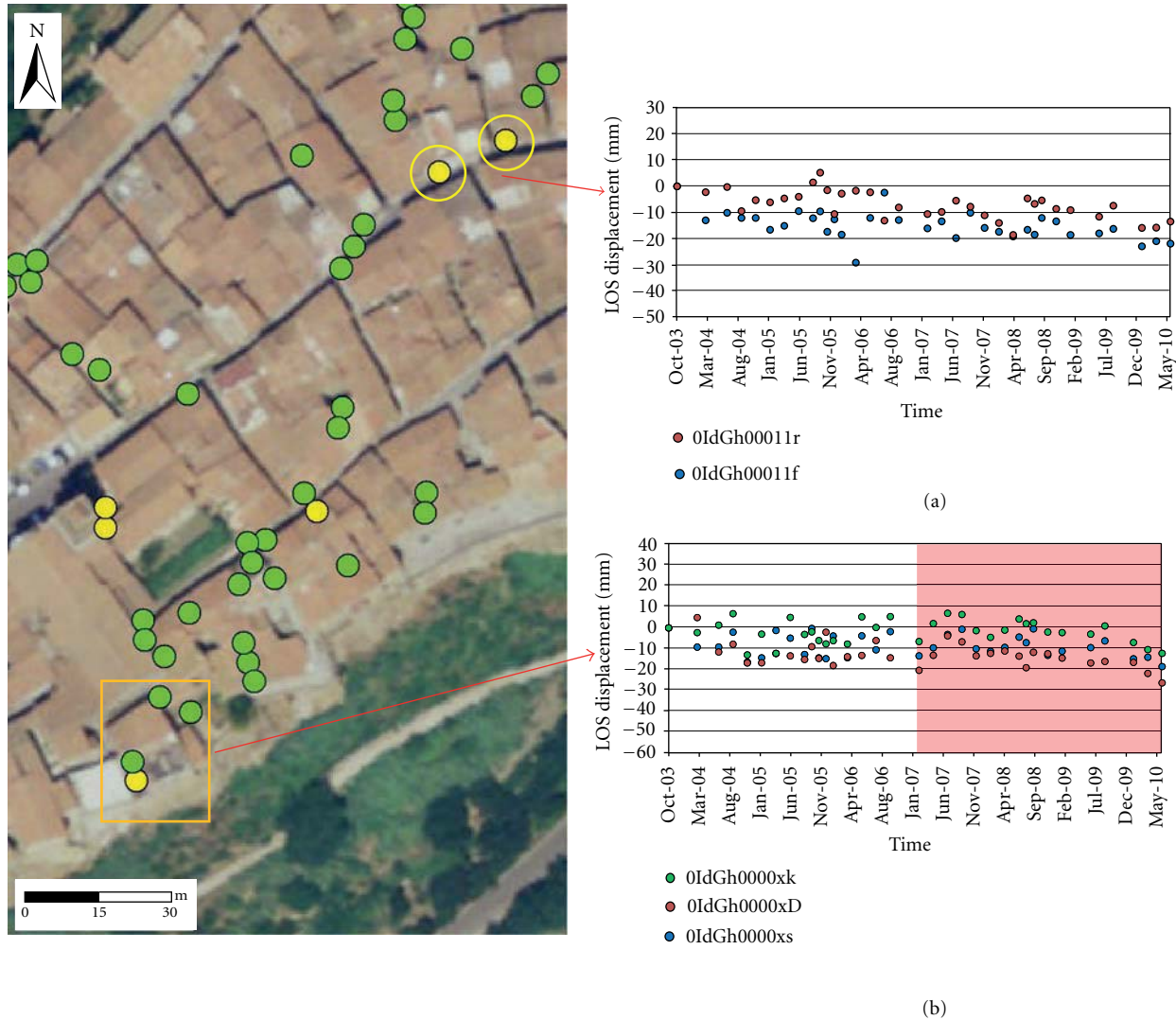


FIGURE 9: Spatial distribution and related V_{LOS} field for the ENVISAT ascending (2003–2010) dataset over the central-eastern part of the Pitigliano town centre. Localized deformation is identified over some buildings, with downwards moving PS showing a progressive LOS displacement trend away from the satellite (a), while one downwards moving PS and some apparently stable PSs located close to the cliff edge share a common LOS displacement trend, especially since February 2007 (b).

road still connecting the village with the Monte Senario convent was cut along the slope. Among the built heritage of Bivigliano are to be mentioned the Church of San Romolo (Figure 5(a)), the late XVI century noble residency called Villa Pozzolini (or “Villa di Bivigliano”; Figure 5(c)), and the Monte Senario convent itself (Figure 5(b)). All these historical evidences are still inserted within a landscape context, which is nowadays one of the main features to be preserved.

Nevertheless, effective strategies of land management have to tackle the landslide susceptibility of the territory, as testified from different historical records of terrain motions and ground instability, such as the “landslide of Bivigliano” mentioned in a document and which occurred in 1729 [37]. Indeed, several landslide bodies are also reported in the Regional Geological Map (*Carta Geologica Regionale*

(CGR)) Sheet 263120 scale 1:10,000 (Figure 10), as well as in the Italian Landslide Inventory (*Inventario Fenomeni Franosi in Italia* (IFFI)) produced by the Italian Institute for Environmental Protection and Research in 2007. Due to landslipping, in modern times the old cemetery of the village was moved to the present place (area d in Figure 5).

In light of these conservation issues, the feasibility test was aimed at exploiting the PSI data to assess the evolution of the condition for the main monuments and historical buildings of Bivigliano since 1992, within the broader environmental context and related deformation patterns.

At the scale of entire site, the multitemporal analysis of the PS spatial distribution of both the ERS and ENVISAT datasets highlights the persistence, from the historical period (1992–2000) to the recent one (2003–2010), of an extended deformation macropattern covering most of the residential

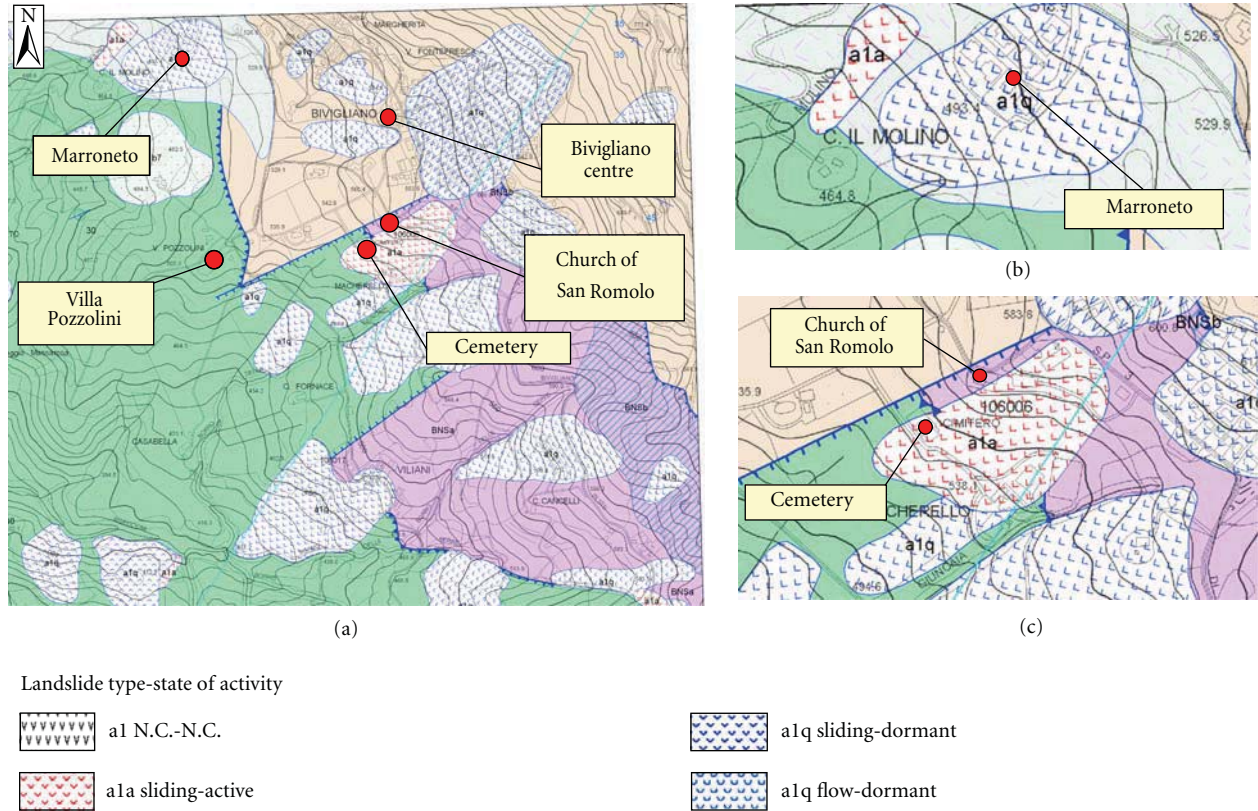


FIGURE 10: (a) Detail of the Regional Geological Map Sheet 263120 scale 1 : 10,000 over the Bivigliano territory, with the landslide inventory reporting several landslide bodies, among which: (b) dormant slide over Marroneto; (c) active slide close to the church and including the cemetery.

sectors of Bivigliano, with LOS displacement field mainly characterized by movements going away from the satellite (Figure 11). This deformation macropattern is clearly detected in both ERS descending (1992–2000) and ENVISAT descending (2003–2010) datasets (Figures 11(a) and 11(c)), while in the ENVISAT ascending (2003–2010) dataset only few and isolated PSs show V_{LOS} exceeding the stability threshold (± 1.5 mm/yr; Figure 11(b)).

In particular, for the ERS descending (1992–2000) data, the modal value (i.e., the value that occurs most frequently) of coherence is 0.73, with 35% of the identified MP assuming coherence values ≥ 0.80 . The associated V_{LOS} field spans from -8.8 to -0.5 mm/yr, with a V_{LOS} modal value of -2.2 mm/yr. On the other hand, the ENVISAT descending (2003–2010) data, here used as recent dataset, shows coherence modal value of 0.76, with 25% of the identified PS assuming coherence values ≥ 0.78 . The associated V_{LOS} field ranges from -4.7 to -1.2 mm/yr, with a V_{LOS} modal value of -1.0 mm/yr.

These simple statistics confirm the impression of a less concentrated and intense deformation macropattern covering the settlement during the period 2003–2010, than the corresponding one observed in the historical data (1992–2000). Nevertheless, both the datasets suggest a potential correlation between the spatial distribution of most of the identified PS clusters and the presence of landslide bodies,

especially if considering the boundaries and extent of the landslide phenomena mapped in the previously mentioned CGR scale 1:10,000 (Figures 10 and 11). At the same time, the PS spatial distribution of the ERS and ENVISAT descending data opens to the need of an accurate updating of the knowledge basis about the current state of activity of the already mapped landslide phenomena. Such analysis will clarify whether the deformation detected from the satellite can be attributed only to natural hazards or also to human-induced impacts (e.g., water pumping).

In these terms, it is quite interesting to note the persistence of a deformation micropattern since 1992 over the peripheral area of Bivigliano called Marroneto (Figures 11 and 12), historically occupied by the local craftsmen and located north-west of the main residential quarter (area (e) in Figure 5). Here, the CGR reports the presence of a huge landslide body classified as “dormant slide” (“*frana di scorrimento quiescente*”; Figure 10(b)).

Over there, the ERS descending (1992–2000) data show a concentrated micropattern consisting of four downwards moving PS (Figure 12(a)), with V_{LOS} up to -5.1 mm/yr and a linear displacement trend progressively going away from the satellite, reaching a total value of LOS displacement up to -50 mm over approximately eight years (Figure 12(d)). Not less severe is the corresponding micropattern observable in the ENVISAT descending (2003–2010) data (Figure 12(c)).

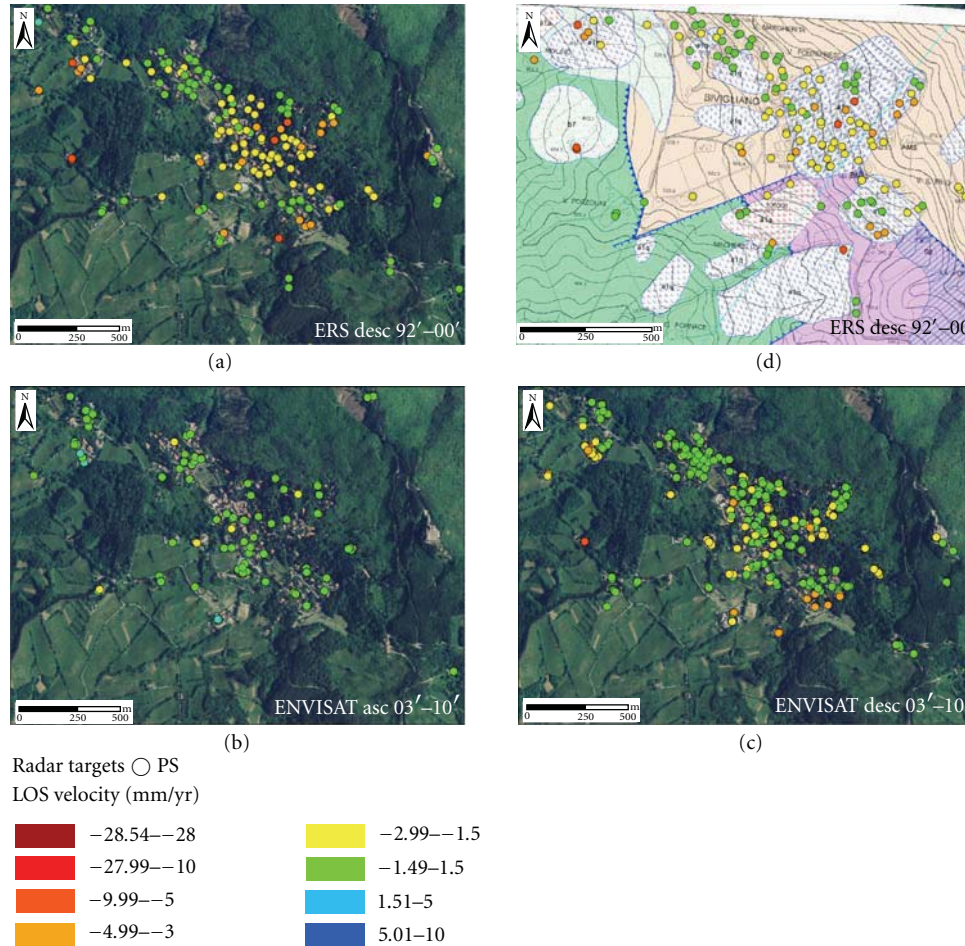


FIGURE 11: PS spatial distribution and related V_{LOS} field over the Bivigliano territory for the datasets: (a) ERS descending (1992–2000); (b) ENVISAT ascending (2003–2010); (c) ENVISAT descending (2003–2010). Superimposition of PS datasets over the landslide inventory (see Figure 10) suggests a potential correlation with the distribution and extent of the mapped landslides, as perceivable observing the ERS data (d).

Nineteen downwards moving PSs were identified over the whole area, with V_{LOS} ranging from -5.3 to -1.5 mm/yr, and modal value of -3.7 mm/yr. All the PS time series share the same LOS displacement trend, which progressively goes away from the satellite throughout the monitoring period (Figure 12(f)), with a progression not as linear as that found in the time series of the historical ERS descending data (Figure 12(d)). The total LOS displacement reaches up to -45 mm over about seven years. Correspondingly, despite the reduced number of the identified PS, the ENVISAT ascending (2003–2010) dataset shows a localized micropattern consisting of two isolated upwards moving PSs (Figure 12(b)), with V_{LOS} of $+1.8$ mm/yr and LOS displacement trends characterized by an annual seasonal component of about 5 mm (Figure 12(e)).

Passing to the scale of single building, the ancient and modern built heritage of Bivigliano is characterized by differential conditions in terms of PSI-based levels of conservation criticality. The worst situation was found for the Church of San Romolo (Figure 13). Although it is only a single PS not surrounded by other deformation estimates,

the downwards moving PS ERS descending (1992–2000) identified over the bell tower of the church (Figure 13(a)) assumes a particular relevance, especially if analyzed in integration with the more recent PSI data (Figure 13(c)). This PS shows a V_{LOS} of -2.2 mm/yr and an approximately linear LOS displacement trend progressively going away from the satellite until March 1999 (Figure 13(b)).

While a lack of PS characterizes the ENVISAT ascending (2003–2010) dataset, a clear deformation micropattern affects the entire complex of the church in the corresponding descending (2003–2010) dataset (despite the shift in the PS georeferencing; Figure 13(c)). All the five identified PSs, including the one which appears stable, share a common LOS displacement trend going progressively away from the satellite, with V_{LOS} reaching the maximum value of -2.7 mm/yr and a total LOS displacement up to -20 mm over approximately seven years (Figure 13(d)). These satellite evidences confirm a high level of conservation criticality for the entire architectural complex.

Indeed, the recent history of the church and on-site inspections provide a strong validation of the analyzed PSI

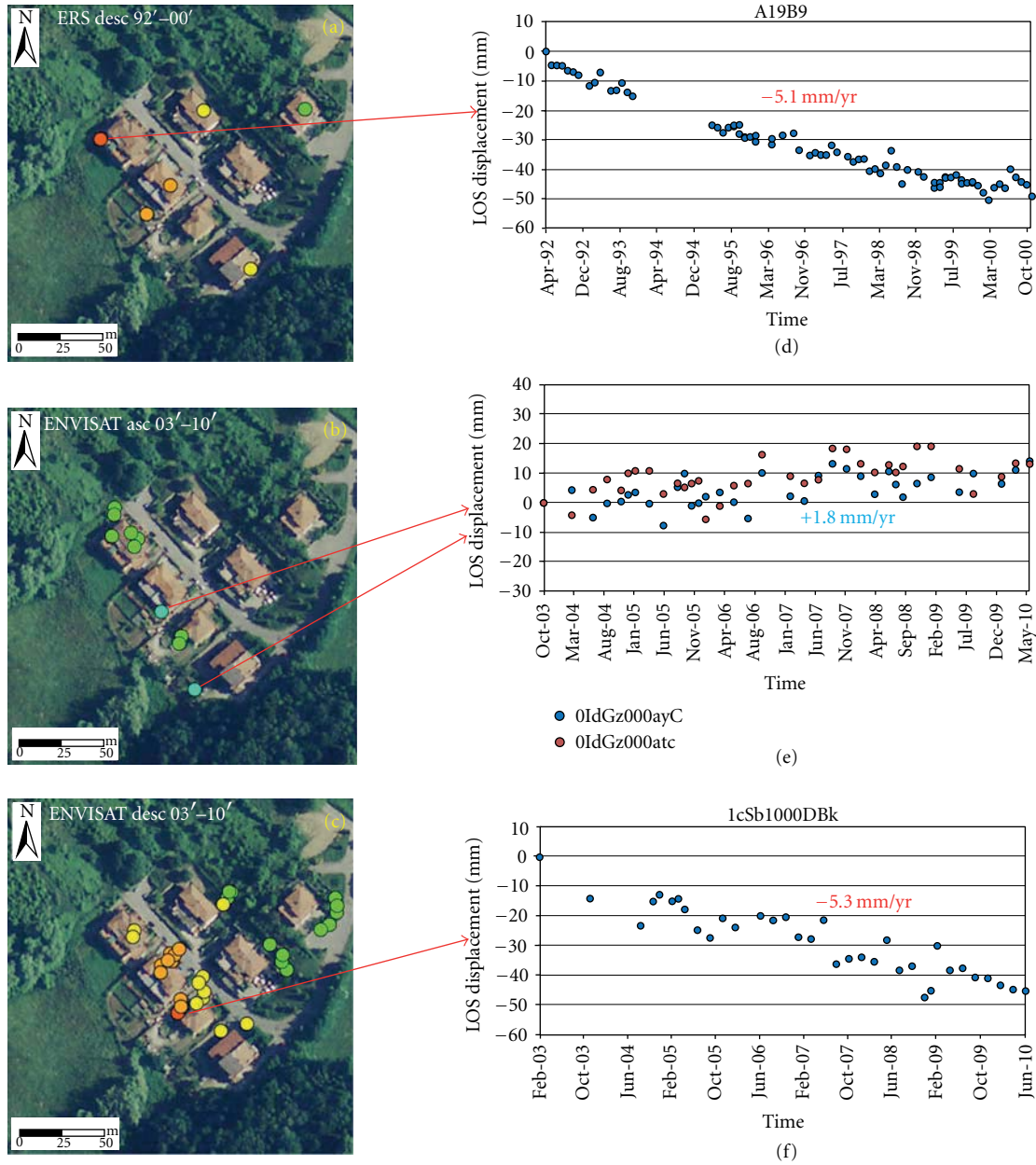


FIGURE 12: PS spatial distribution and related V_{LOS} field over Marroneto for the datasets: (a) ERS descending (1992–2000); (b) ENVISAT ascending (2003–2010); (c) ENVISAT descending (2003–2010), associated to examples of time series representative of the respective LOS displacement trends ((d)–(f)).

data. During the monitoring period (1992–2010), several interventions of stabilization and consolidation were carried out by the local authorities and heritage bodies. Particularly, substantial repairs were carried out between 1990s and 2000s on the containing wall, which supports and protects the substratum on which the church is founded.

Nevertheless, new cracks recently opened and currently cross over the pavement in front of the main entrance of the church. Also, new fissures progressively developed on the brick floor inside the church, starting from the main entrance and reaching the middle of the nave and the southern wall,

as well as huge cracks which run on both the exterior and interior façades (Figure 13(f)).

Curiously, looking at the landslide inventory reported in the CGR, the boundary of an “active slide” (“*frana di scorrimento attiva*”) runs close to the church but does not include it (Figure 10(c) and red dashed line in Figure 13(a) and 13(c)). Based on the PSI data and ground truth, it seems reasonable to propose a modification of the landslide boundaries, to be extended also to the area of the church. Execution of detailed ground investigations might be preparatory to the design of appropriate consolidation

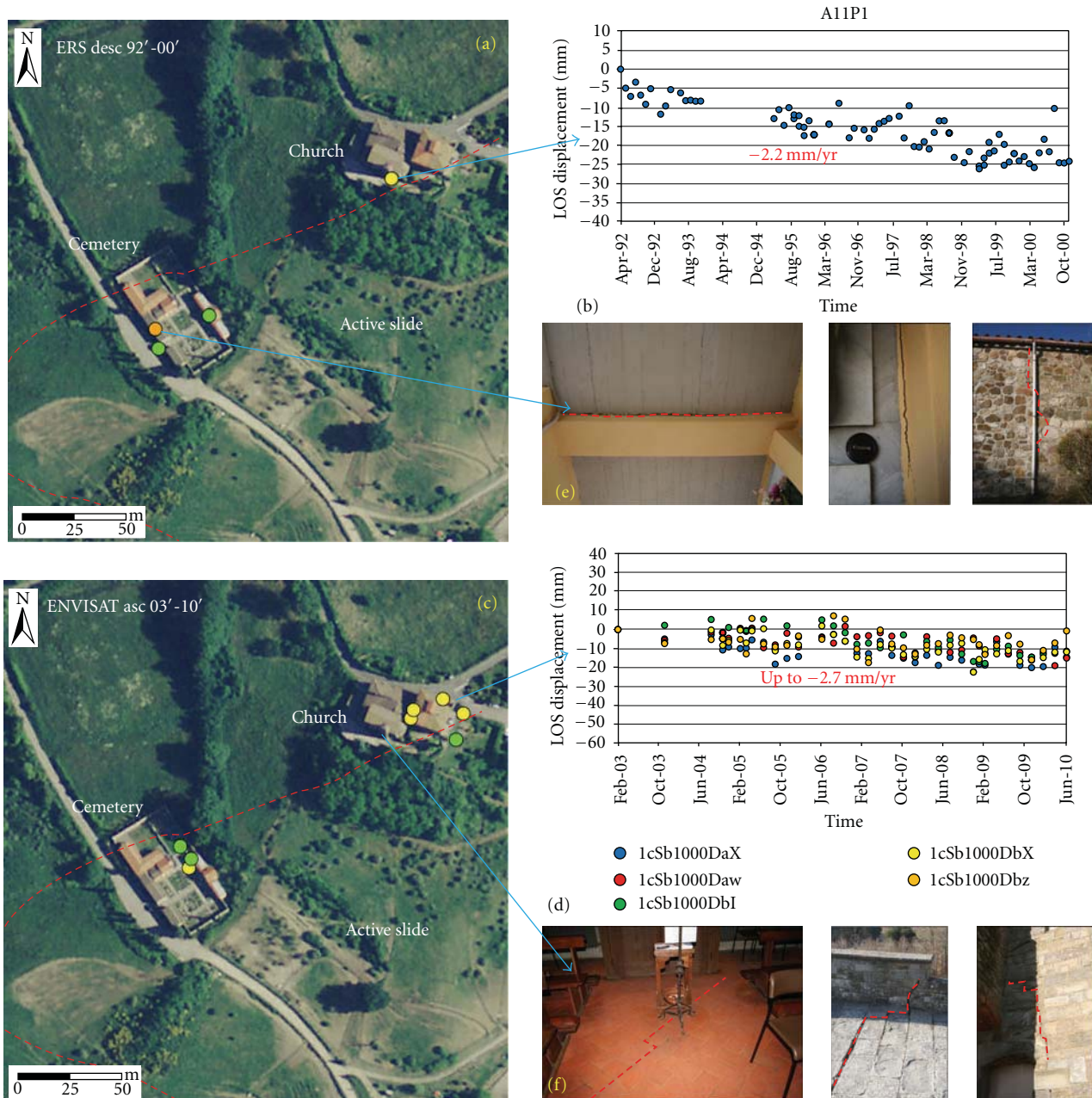


FIGURE 13: PS spatial distribution and related V_{LOS} field over the Church of San Romolo and the cemetery for the datasets: (a) ERS descending (1992–2000) with (b) a single downwards moving PS in correspondence with the bell tower; (c) ENVISAT descending (2003–2010), with several downwards moving PSs sharing a common LOS displacement trend (d). Severe crack patterns affect the exterior and interior wall surfaces and floor of both the cemetery (e) and the church of San Romolo (f). The red dashed line in (a) and (c) marks the boundary of an active slide mapped in the inventory of the CGR (cf. Figure 10).

works, at the level of both the unstable ground and the deteriorated structures.

The same active slide actually includes most of the modern cemetery, located south of the church, along the slope (Figure 10(c)). Again, the ERS descending (1992–2000) and ENVISAT descending (2003–2010) datasets suggest the presence of superficial deformations which might be the effects of landsliding phenomena and consequent structural instability of the masonries (Figure 13(a) and 13(c)). A single

PS with a linear LOS displacement trend going away from the satellite shows a V_{LOS} of -3.5 mm/yr, and it is coupled with an apparently stable PS. The latter is characterized by a phase of downwards movements until May 1999, followed by an upwards phase till November 2000. Both the PSs are located over the southern wall of the cemetery (Figure 13(a)).

Differently from the ENVISAT ascending (2003–2010) data where a lack of PS affects most of the area of the cemetery, the corresponding ENVISAT descending data

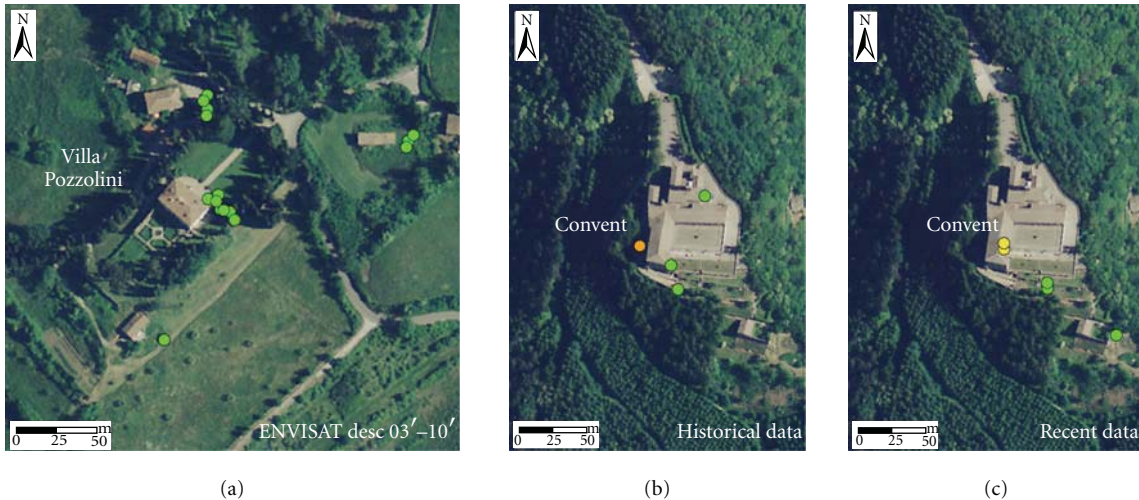


FIGURE 14: (a) Spatial distribution and related V_{LOS} field of the ENVISAT descending (2003–2010) dataset confirm a relative stability for Villa Pozzolini and surroundings, while the comparison between (b) historical data (ERS descending 1992–2000) and (c) recent ones (ENVISAT descending 2003–2010) over the Convent of Monte Senario highlights the persistence of localized deformation over the southern part of the complex.

highlight a slight tendency to downwards LOS displacements throughout the monitoring period within the time series of all the three identified PSs.

Although the reduced number of the identified PS and their spatial configuration lead to consider them only localized deformation, a stronger evidence to validate these satellite findings can be retrieved from on-site checks. The crack pattern survey over the concrete and stone-faced masonries of both the southern and northern walls highlights a good agreement between the spatial distribution of the fissures and the PS positions (Figure 13(e)). The cracks mainly developed in correspondence with the conjunction of masonries related to different phases of construction, that is, the weakest structural points on which active landslide events can have higher impacts.

Conversely, low levels of conservation criticalities are to be assigned to the monumental complexes of Villa Pozzolini and the Convent of Monte Senario (Figure 14). In the first case, all the three analyzed PS datasets show a quite relative stability over the Villa, as well as for the surrounding buildings and the homestead in front of the Villa which belong to the estate. This is particularly observable in the ENVISAT descending (2003–2010) dataset, which is the most completed one in terms of PS spatial distribution (Figure 14(a)). Nevertheless, this dataset clearly exemplifies the issue that sometimes an operator could find, that is, the error in the PS georeferencing and consequent shift of the PS with respect to the orthophoto used as visual reference. In this case, the shift is very easily appreciable by comparing the spatial configuration of the identified PS clusters and the geometry of the buildings to which the PSs are reasonably to be referred.

Similarly, no relevant deformation patterns are detected over the Convent of Monte Senario, except for one single PS ERS descending (1992–2000) with V_{LOS} of -3.4 mm/yr and an almost constant linear trend throughout the monitoring

period, reaching a total LOS displacement of -40 mm over eight years (Figure 14(b)). The impression that this deformation is to be recognized as a localized deformation is confirmed by the persistence of downwards LOS displacements also within the time series of two PS ENVISAT descending (2003–2010), located over the southern part of the convent (Figure 14(c)). These PSs share a common LOS displacement trend progressively going away from the satellite and reach a total LOS displacement of about -15 mm over eight years, associated to a V_{LOS} of, respectively, -2.5 and -2.2 mm/yr.

4. Conclusions

The methodology of rapid mapping and deformation analysis proposed here has the potential to become a routine tool to be increasingly employed by the practitioners and heritage bodies, in support of the ordinary activities of noninvasive diagnosis and preservation of cultural heritage, both concentrated within enclosed areas (e.g., historic centres) and spread within urban and rural environments. The implementation of PSI-based analyses is also expected to be more and more complementary to the activities of built heritage management, in the framework of broader strategies of land planning.

The feasibility tests discussed in this paper confirm these potentials of the PSI techniques, especially for the purposes of preventive diagnosis, thanks to the capability of detecting superficial deformation as indicators of ongoing deterioration phenomena, or even evolving processes which might develop into severer instability events. Such diagnostic feature is further enriched by the possibility of back monitoring the displacement field of the AOI up to 1992 with the ERS-1/2 imagery, thereby reconstructing the deformational behaviour of the observed phenomena during a sufficiently long period of observation.

Nevertheless, some drawbacks can arise, such as the lack of PS over the AOI while passing from a dataset to another, especially if the analyzed datasets are acquired from different satellite platforms. The reduced number of identified PSs over the elements of major interest and even the total absence of deformation estimates, respectively, limit and inhibit the execution of a reliable and complete deformation analysis. Frequently, the deformational behaviour is actually assessed based on one of the two acquisition geometries (ascending or descending), and, consequently, the retrieved information can be only referred to the LOS component of the real displacement vector which represents the deformation affecting the radar targets. This issue is only partially solvable by refining the processing setting and better focusing the scale of analysis, but not always significant improvements are achieved. Certainly, the installation of corner reflectors over the AOI and in correspondence with the buildings to monitor is a feasible solution but requires additional costs, is not retroactive before the date of installation, and implies issues in terms of landscape impacts on the monuments.

Although the PSI data radar-interpreted here were not formerly processed for cultural heritage applications, both the feasibility tests of rapid mapping provide interesting results, showing a good agreement between the satellite evidences and the ground truth, as well as the information retrieved from previous research (case of Pitigliano) and existing mapping products (case of Bivigliano). With reference to this second case, the PSI data also demonstrated their potential to provide informational elements to update the background knowledge, suggesting, for instance, a review of the landslide inventory.

In terms of selective analysis of differential conditions, the PSI data over Pitigliano led to zone the most unstable sectors of the built-up areas along the cliff edges, while those covering the territory of Bivigliano allowed localized criticalities to be identified over some historical buildings rather than others, within the broader context of deformation patterns detected at the scale of entire site.

In light of the good results retrieved on ERS-1/2 and ENVISAT data stacks at medium spatial resolution and monthly sampling, further advances in such PSI-based feasibility tests are represented by experiments on PS obtained from the PSI processing of SAR imagery characterized by higher spatial and temporal resolutions.

Undoubtedly, the collection of ground truth and the integration with ancillary data and background information still remain essential elements, without which the radar interpretation of the PSI data might be affected by misinterpretation risks, especially in relation to the distinction between related and unrelated PSs (the latter correspond to PS actually not attributable to radar targets belonging to the element of interest). In this regard, the high level of agreement between the satellite evidences and other source data found during the two feasibility tests encourages the implementation of the experimented PSI techniques, also in the perspective of addressing the execution of terrestrial survey activities and the planning of targeted mitigation works, with consequent benefits in terms of cost effectiveness and sustainability.

Acknowledgments

PSI data were processed in the framework of the Extraordinary Plan of Environmental Remote Sensing (EPRS-E) project and made available through the WMS service of the Italian Ministry of Environment, Territory and Sea. Access to the Regional Geological Map (*Carta Geologica Regionale* (CGR)) Sheet 263120 scale 1:10,000 was performed through the Geoportale of Lamma Consorzio (<http://geoportale.lamma.rete.toscana.it/>).

References

- [1] D. Massonnet and K. L. Feigl, "Radar interferometry and its application to changes in the earth's surface," *Reviews of Geophysics*, vol. 36, no. 4, pp. 441–500, 1998.
- [2] P. A. Rosen, S. Hensley, I. R. Joughin et al., "Synthetic aperture radar Interferometry," *Proceedings of the IEEE*, vol. 88, no. 3, pp. 333–382, 2000.
- [3] D. Massonnet, K. Feigl, M. Rossi, and F. Adragna, "Radar interferometric mapping of deformation in the year after the Landers earthquake," *Nature*, vol. 369, no. 6477, pp. 227–230, 1994.
- [4] C. Squarzoni, C. Delacourt, and P. Allemand, "Nine years of spatial and temporal evolution of the La Valette landslide observed by SAR interferometry," *Engineering Geology*, vol. 68, no. 1-2, pp. 53–66, 2003.
- [5] A. M. Goudarzi, T. Woldai, and V. A. Tolpekin, "Surface deformation caused by April 6th 2009 earthquake in L'Aquila (Italy): a comparative analysis from ENVISAT ASAR, ALOS PALSAR and ASTER," *International Journal of Applied Earth Observation and Geoinformation*, vol. 13, no. 5, pp. 801–811, 2011.
- [6] S. Bianchini, F. Cigna, G. Righini, C. Proietti, and N. Casagli, "Landslide HotSpot mapping by means of persistent scatterer interferometry," *Environmental Earth Sciences*. In press.
- [7] H. Rott and T. Nagler, "The contribution of radar interferometry to the assessment of landslide hazards," *Advances in Space Research*, vol. 37, no. 4, pp. 710–719, 2006.
- [8] F. Gutiérrez, J. P. Galve, P. Lucha, C. Castañeda, J. Bonachea, and J. Guerrero, "Integrating geomorphological mapping, trenching, InSAR and GPR for the identification and characterization of sinkholes: a review and application in the mantled evaporite karst of the Ebro Valley (NE Spain)," *Geomorphology*, vol. 134, no. 1-2, pp. 144–156, 2011.
- [9] S. Stramondo, F. Bozzano, F. Marra et al., "Subsidence induced by urbanisation in the city of Rome detected by advanced InSAR technique and geotechnical investigations," *Remote Sensing of Environment*, vol. 112, no. 6, pp. 3160–3172, 2008.
- [10] F. Cigna, B. Osmanoglu, E. Cabral-Cano et al., "Monitoring land subsidence and its induced geological hazard with synthetic aperture radar interferometry: a case study in Morelia, Mexico," *Remote Sensing of Environment*, vol. 117, pp. 146–161, 2012.
- [11] M. Crosetto, O. Monserrat, and G. Herrera, "Urban applications of persistent scatterer interferometry," *Radar Remote Sensing of Urban Areas, Remote Sensing and Digital Image Processing*, vol. 15, pp. 233–248, 2010.
- [12] F. Cigna, C. Del Ventisette, V. Liguori, and N. Casagli, "Advanced radar-interpretation of InSAR time series for mapping and characterization of geological processes," *Natural Hazards and Earth System Science*, vol. 11, no. 3, pp. 865–881, 2011.

- [13] G. Gigli, W. Frodella, F. Mugnai et al., “Instability mechanisms affecting cultural heritage sites in the Maltese Archipelago,” *Natural Hazards and Earth System Sciences*, vol. 12, no. 6, pp. 1883–1903, 2012.
- [14] P. Teatini, L. Tosi, T. Strozzi et al., “Resolving land subsidence within the Venice Lagoon by persistent scatterer SAR interferometry,” *Physics and Chemistry of the Earth, Parts A/B/C*, vol. 40–41, pp. 72–79, 2012.
- [15] M. Costantini, A. Iodice, L. Magnapane, and L. Pietranera, “Monitoring terrain movements by means of sparse SAR differential interferometric measurements,” in *Proceedings of the International Geoscience and Remote Sensing Symposium (IGARSS’00)*, pp. 3225–3227, Honolulu, Hawaii, USA, July 2000.
- [16] A. Ferretti, C. Prati, and F. Rocca, “Permanent scatterers in SAR interferometry,” *IEEE Transactions on Geoscience and Remote Sensing*, vol. 39, no. 1, pp. 8–20, 2001.
- [17] A. Ferretti, A. Fumagalli, F. Novali, C. Prati, F. Rocca, and A. Rucci, “A new algorithm for processing interferometric data-stacks: SqueeSAR,” *IEEE Transactions on Geoscience and Remote Sensing*, vol. 49, no. 9, pp. 3460–3470, 2011.
- [18] C. Werner, U. Wegmüller, T. Strozzi, and A. Wiesmann, “Interferometric point target analysis for deformation mapping,” in *Proceedings of the IGARSS: Learning From Earth’s Shapes and Colours*, pp. 4362–4364, Toulouse, France, July 2003.
- [19] A. Hooper, H. Zebker, P. Segall, and B. Kampes, “A new method for measuring deformation on volcanoes and other natural terrains using InSAR persistent scatterers,” *Geophysical Research Letters*, vol. 31, no. 23, Article ID L23611, 5 pages, 2004.
- [20] D. Tapete, R. Fanti, R. Cecchi, P. Petrangeli, and N. Casagli, “Satellite radar interferometry for monitoring and early-stage warning of structural instability in archaeological sites,” *Journal of Geophysics and Engineering*, vol. 9, pp. S10–S25, 2012.
- [21] The TerraFirma Atlas, “Terrain-motion across Europe. A compendium of results produced by the European space agency GMES service element project TerraFirma 2003–2009,” 94 pages, June 2009, <http://esamultimedia.esa.int/multimedia/publications/TerraFirmaAtlas/pageflip.html>.
- [22] L. Bateson, M. Cuevas, M. Crosetto, F. Cigna, and M. Schijf, D3. 5: PanGeo Production Manual Version 1, 2012, http://www.pangeoproject.eu/sites/default/files/pangeo_other/D3.5_PanGeo_Production_Manual_v1_of_2nd_April_2012.pdf.
- [23] National Geoportal, “Extraordinary plan of environmental remote sensing,” 2012, http://www.pcn.minambiente.it/GN/progetto_pst.php?lan=en.
- [24] A. Trigila, C. Cacace, C. Iadanza, S. Del Conte, D. Spizzichino, and S. Cespa, “Cultural heritage, landslide risk and remote sensing in Italy,” in *The Second World Landslide Forum—Abstract Book*, F. Catani, C. Margottini, A. Trigila, and C. Iadanza, Eds., p. 603, FAO, Rome, Italy, 2011, ISPRa, WLF2-2011-0397.
- [25] G. Savio, A. Ferretti, F. Novali, S. Musazzi, C. Prati, and F. Rocca, “PSInSAR validation by means of a blind experiment using dihedral reflectors,” in *Proceedings of FRINGE 2005 Workshop*, pp. 1–6, Frascati, Italy, December 2005.
- [26] D. Perissin and A. Ferretti, “Urban-target recognition by means of repeated spaceborne SAR images,” *IEEE Transactions on Geoscience and Remote Sensing*, vol. 45, no. 12, pp. 4043–4058, 2007.
- [27] G. Zeni, M. Bonano, F. Casu et al., “Long-term deformation analysis of historical buildings through the advanced SBAS-DInSAR technique: the case study of the city of Rome, Italy,” *Journal of Geophysics and Engineering*, vol. 8, no. 3, pp. S1–S12, 2011.
- [28] D. Tapete and F. Cigna, “Site-specific analysis of deformation patterns on archaeological heritage by satellite radar interferometry,” in *20th International Materials Research Congress, Symposium 8 Cultural Heritage and Archaeological Issues in Materials Science*, vol. 1374 of *MRS Proceedings*, Cambridge University Press, 2012.
- [29] F. Cigna, S. Bianchini, and N. Casagli, “How to assess landslide activity and intensity with persistent scatterer interferometry (PSI): the PSI-based matrix approach,” *Landslides*. In press.
- [30] C. Colesanti and J. Wasowski, “Investigating landslides with space-borne synthetic aperture radar (SAR) interferometry,” *Engineering Geology*, vol. 88, no. 3–4, pp. 173–199, 2006.
- [31] National Geoportal, “Progetto persistent scatterers interferometry,” 2012, http://www.pcn.minambiente.it/GN/progetto_psi.php?lan=en.
- [32] L. Vezzoli, “Stratigraphy of the latera volcanic complex: proposals for a new nomenclature,” *Periodico di Mineralogia*, vol. 56, no. 2–3, pp. 89–110, 1987.
- [33] S. Conticelli, L. Francalanci, P. Manetti, and A. Peccerillo, “Evolution of Latera Volcano, Vulturnian district (central Italy): stratigraphical and petrological data,” *Periodico di Mineralogia*, vol. 56, no. 2–3, pp. 175–199, 1987.
- [34] P. Canuti, N. Casagli, R. Fanti, A. Iotti, E. Pecchioni, and A. P. Santo, “Rock weathering and failure of the “Tomba della Sirena” in the Etruscan necropolis of Sovana (Italy),” *Journal of Cultural Heritage*, vol. 5, no. 3, pp. 323–330, 2004.
- [35] R. Fanti, G. Gigli, L. Lombardi, D. Tapete, and P. Canuti, “Terrestrial laser scanning for rockfall stability analysis in the cultural heritage site of Pitigliano (Italy),” *Landslides*. In press.
- [36] P. Canuti and R. Fanti, “The instability of Pitigliano’s cliff: the role of the anthropic cavities, the geotechnical studies and the monitoring system,” in *Conservation and Sustainable Development of the Tuff Towns. An Exploration of Pitigliano*, World Monuments Fund Publication, Civita di Bagnoregio, Italy, 2007, http://www.wmf.org/sites/default/files/wmf_publication/tuff_canuti-en.pdf.
- [37] Archivio Galilei 18 ins. 1, Memorie per Pratolino Frana di Bivigliano dell’agosto 1729.

Research Article

Geophysical Surveys at Khirbat Faynan, an Ancient Mound Site in Southern Jordan

Alexandre Novo,¹ Matthew L. Vincent,² and Thomas E. Levy²

¹ *Geostudi Astier, via A. Nicolodi 48, 57121 Livorno, Italy*

² *Department of Anthropology & California Institute for Telecommunications and Information Technology (Calit2), University of California, San Diego, CA 92093, USA*

Correspondence should be addressed to Alexandre Novo, novo@geoastier.it

Received 16 April 2012; Accepted 4 July 2012

Academic Editor: Nicola Masini

Copyright © 2012 Alexandre Novo et al. This is an open access article distributed under the Creative Commons Attribution License, which permits unrestricted use, distribution, and reproduction in any medium, provided the original work is properly cited.

Faynan in Jordan contains the largest copper ore resource zone in the southern Levant (Israel, Jordan, Palestinian territories, Lebanon, Syria, and the Sinai Peninsula). Located 50 km southeast of the Dead Sea, it is home to one of the world's best-preserved ancient mining and metallurgy districts encompassing an area of ca. 400 km². During the past three decades, archaeologists have carried out numerous excavations and surveys recording hundreds of mines and sites related to metallurgical activities that span the past 10 millennia. Khirbat Faynan (Biblical Punon), is situated in the main Faynan Valley and is the largest (ca. 15 ha) settlement site in the region and has remained unexcavated until 2011. As Jordan's most southern mound site with indications of widespread ancient architecture, we employed a suite of noninvasive geophysical survey methods to identify areas suitable for excavation. Earlier geophysical surveys were carried out in the Faynan region by our team in the late 1990s when only EMI (electromagnetic induction) proved successful, but with relatively poor resolution. As reported here, by 2011, improvements in data processing software and 3D ERT (electrical resistivity tomography) sampling protocols made it possible to greatly improve the application of noninvasive geophysical surveying in this hyperarid zone.

1. Introduction

Improvements in processing software and sampling protocols for shallow geophysical prospecting make it a key tool for initiating archaeological exploration. In terms of research design, geophysics have increasingly become an essential part of the methodology for planning archaeological excavation in a number of unexplored regions around the world [1, 2]. As part of a long-term archaeological study of the role of mining and metallurgy in the evolution of societies from the Neolithic period (ca. 8000 BC–6000 BC) to Islamic times (7th c. CE–early 20th c. CE) in Jordan's Faynan copper ore district, the University of California, San Diego (UCSD) Edom Lowlands Regional Archaeology Project (ELRAP) conducted intensive systematic surveys and large-scale excavations at sites spanning all these periods. From 2002–2010, the primary research focus was on the formative Iron Age (ca. 1200–500 BCE) when the first historical state-level

societies evolved in this part of the eastern Mediterranean and the ancient Near East's first industrial revolution took place. Large-scale excavations were carried out at Khirbat en-Nahas (ca. 10 hectares), the largest copper ore processing and smelting site in the region (cf. [3]), smaller production sites [4], fortresses [5], mining complexes [6], and other sites making it possible to reconstruct the Iron Age "metallurgical landscape" of this natural resource zone [7]. While it was possible to reconstruct the network of ore exploitation, processing, and manufacture, the location and nature of political and economic center remains a mystery. Based on previous surveys and research in the main Wadi Faynan valley, more researchers believe that a large (ca. 15 hectares) ancient mound site called Khirbat Faynan (known as Punon in the Hebrew Bible and Phaino in late Roman/Byzantine texts) may have been that center during the Iron Age [8]. In 2011, the UCSD ELRAP team initiated the first multiyear large-scale excavation project at this site, the most southern ancient

mound site in Jordan. To initially tackle the excavation of this site, a geophysical survey was carried out that helped guide the selection of the first excavation at the site.

Khirbat Faynan (Figure 1) is a multiperiod site located where Wadi Dana and Wadi Ghuwayr meet (becoming Wadi Faynan) in the hyperarid Saharo-Arabian vegetation zone [9]. The site has a significant amount of well-preserved Roman and Byzantine ruins still visible. Previously, the Deutsches Bergbau Museum under Andreas Hauptman and the Council for British Research in the Levant (CBRL) under Graeme Barker and colleagues surveyed the site [8, 10]. To facilitate a Paleoenvironmental study in the region, a small sounding was made north of the site behind a large wall structure called the “Barrage” [11, 12]. The site’s prominent position next to the convergence of the two previously mentioned wadis sets it apart in the landscape, and it is easy to postulate that it controlled the agricultural field systems to the north and west, and access to the road leading from the copper-ore-rich lowlands to the highland plateau to the east. While many have suggested the role of the “Khirbat” in the region, there still lacks archaeological evidence to fully support these postulations. The 2011 ELRAP expedition was codirected by Thomas Levy and Mohammad Najjar to begin to answer questions concerning the socioeconomic function of the site during the Iron Age. With several significant periods of occupation, it will require several seasons of excavation to fully articulate and understand the site. As part of this expedition, a geophysical survey of the site and its immediate surroundings was conducted in order to create a geological profile of the tell (Arabic: ancient mound site) and identify primary candidates for excavation.

Full characterization of archaeological sites by conventional archaeological techniques can take years. Moreover, drilling and excavations, the most often applied methods for archaeological assessment, are ground disturbing. Therefore, nondestructive geophysical techniques have been used to detect and map underground features in a fast and noninvasive manner [13–16]. Among these techniques and based on previous results in the same area [17], we decided to use EMI (electromagnetic induction) and ERT (electrical resistivity tomography). Electromagnetic techniques have been used for archaeological investigations of different sites [18, 19], including places with similar conditions in the Middle East [20, 21]. Similarly, resistivity surveying has commonly used in noninvasive archaeological prospection [22, 23]. ERT is quite popular in archaeological investigations [24–27]. The success of the method depends on the difference between the resistivity properties of the potential archaeological targets (walls, roads, buildings, etc.) and the surrounding environment [25]. In recent years, 3D ERT is being increasingly used because it provides a three-dimensional view of the subsoil resistivity. Besides, this technology is considered well-suited for mapping Near Eastern tell sites [28].

The combination of EMI and ERT methods provides a flexible approach for planning archaeological excavations [29]. Our aim was to survey buried structures, especially Iron Age ones, around the site. This paper shows the preliminary results of our archaeogeophysical investigations at Khirbat Faynan undertaken in 2011. After a brief description of the



FIGURE 1: Aerial view of Khirbat Faynan looking east showing the excavation trench and excavators. Geophysical surveys were made around the entire site. Scale, note that the trench is 40 m in length from west to east. Arrow indicates the location of 3D ERT survey (photo, UCSD Levantine Archaeology Lab).



FIGURE 2: Operator follows the string to ensure straight profiles on the slopes of the site of Khirbat Faynan, Jordan. The instrument (photo, M. L. Vincent, UCSD Levantine Archaeology Lab) is kept at a constant distance from the ground surface.

area and past results of the ongoing project, we describe our survey strategies and data processing methods and offer an overview of our findings to date.

2. Methodologies

Conditions around the site of Khirbat Faynan make some of the more successful techniques such as GPR (Ground Penetrating Radar) nearly impossible to employ. The ground surface is generally covered with debris from earlier occupation that would have to be cleared before any survey could take place. The process of clearing rocks would not only be expensive in terms of time required to complete such a task, but would also be potentially invasive as it might put at risk exposed architecture which is not always immediately visible among the rock debris. It was decided that the next best options were EMI and ERT, both being well suited for the difficult terrain. These techniques allow for the characterization of the subsoil as well as the ability to detect anomalies that could be associated with buried structures or artifacts.

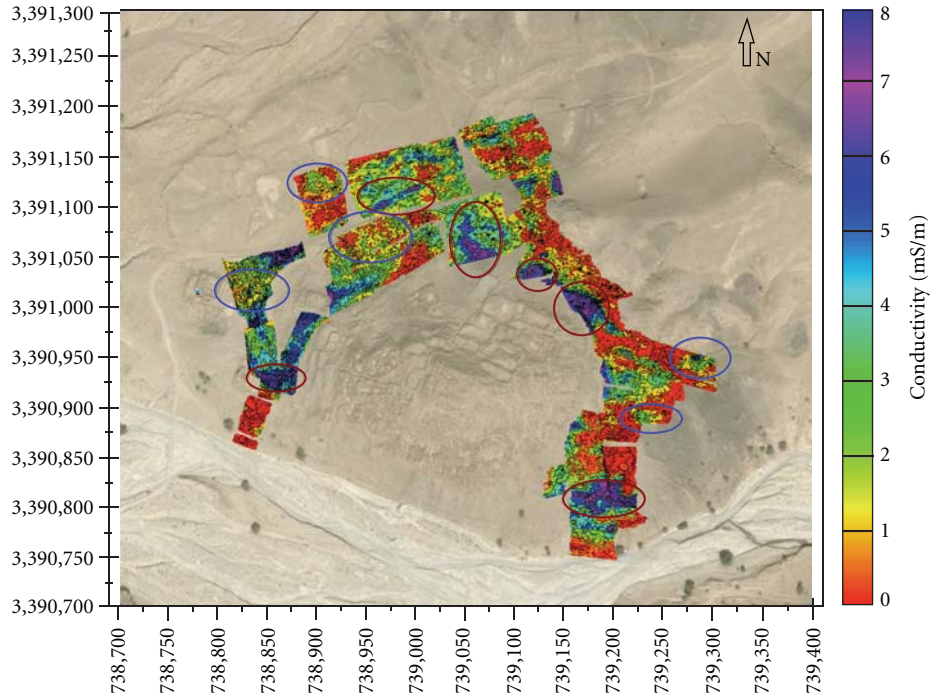


FIGURE 3: EMI data acquired at Khirbat Faynan. While numerous ancient walls can be seen on the surface of this site with Google Earth, the geophysics survey aimed at identifying subsurface features suitable for excavation. Blue color ellipses show interesting areas of low conductivity. Brown color ellipses indicate areas of high conductivity that might be related to past human activity. The site measures approximately 270×640 meters.

We first used EMI, requiring no direct contact with the ground surface, which allowed us to survey large areas quickly even with the difficult terrain. We then selected locations to perform ERT dipole-dipole profiles across the site in order to obtain vertical cross sections of the first 5 meters depth. These data were inverted to obtain 2D electrical images. Finally, we selected an appropriate place to perform a high-resolution 3D mesh. The 3D electrical image obtained from these data was used to decide the location of the season's excavation.

2.1. EMI Equipment and Discussion. Among many applications, electromagnetic induction instruments are used for near-surface archaeological investigations, the detection of buried structures, such as building foundations as well as for the detection of highly conductive metallic objects. EMI was, therefore, used in this study to attempt to locate buried remains of past human activity in the lower flat areas of Khirbat.

The system used in this campaign is a Profiler EMP-400 (GSSI, USA) that is a digital, portable, multifrequency electromagnetic induction sensor. The system bandwidth extends from 1 kHz to 16 kHz. The system collects three different frequencies simultaneously. The in-phase and quadrature components of the induced secondary field as well as the apparent conductivity are collected and stored for each reading along with a time stamp. GPS data, in the form of a NMEA string, were also recorded for every line.

The system sensor electronics are controlled via a wireless Bluetooth communications interface. The system user interface and data storage are incorporated into a TDS RECON-400 personal digital assistant (PDA) provided with the system. This instrument is easy to use in the field, and the operator can cover several hectares in a week (Figure 2). Due to extremely rough topography, some areas were not scanned.

We studied an area of approximately 6 ha. The system was calibrated every day before starting the data acquisition. Data were collected in rectangular grids of parallel lines spaced 1 m apart. After marking the grid corners, two measuring tapes were placed in the shorter pair of parallel sides of the grid for measuring the 1 m spacing between the two survey tapes to mark the exact profile location. The surveyor precisely followed a string in order to ensure straight profiles. For data acquisition consistency, the same person collected all EMI datasets. Field system calibration was a crucial requirement for every survey grid because of extreme temperature changes during data acquisition as well as variable topography across the site.

After collection, data were sent to Geostudi Astier (Livorno, Italy) for processing. First, data trajectories were corrected for spurious GPS points in order to properly align the profiles. Therefore, and second, the data were gridded in MVS/EVS (CTech, USA) using the Kriging algorithm [30]. Finally, the processed results were then sent back to us to be incorporated in the project's geodatabase [31]. The rapid

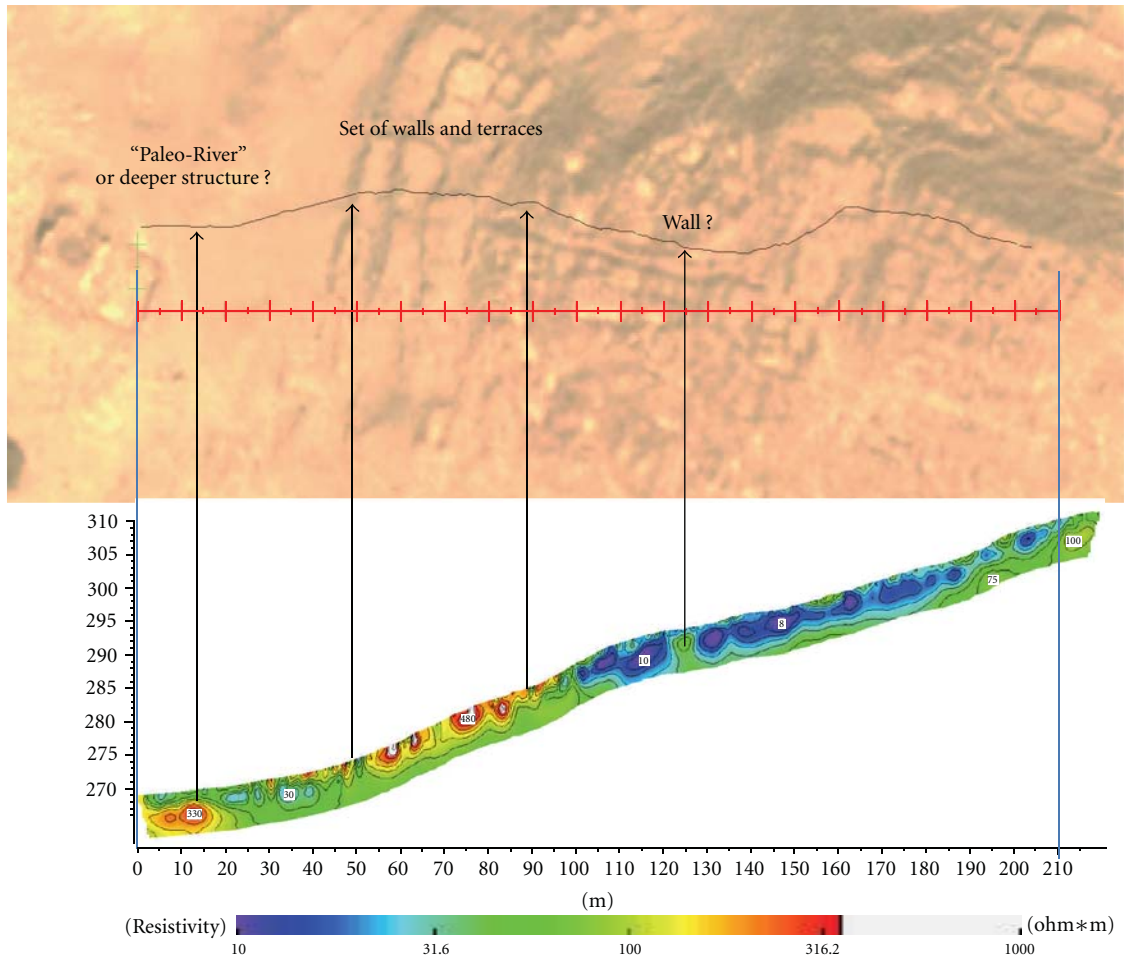


FIGURE 4: 2D ERT line in the west side of the ancient mound.

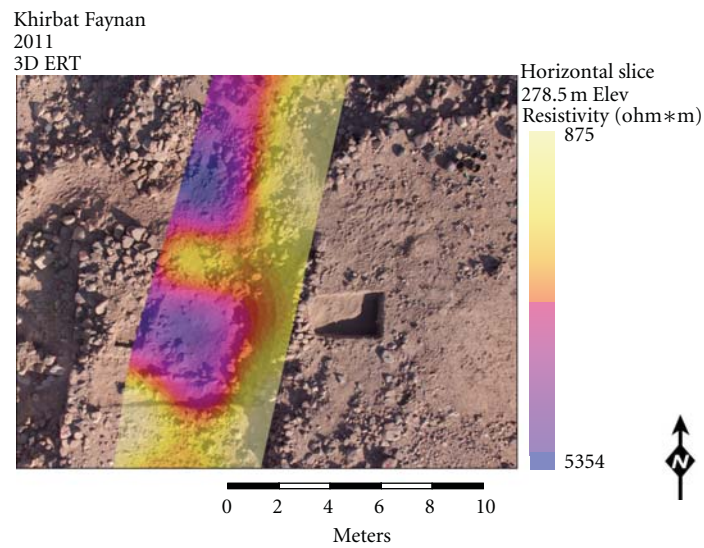


FIGURE 5: Semitransparent horizontal ERT slice at 1 m depth, overlaid on top of an aerial image of the excavation.

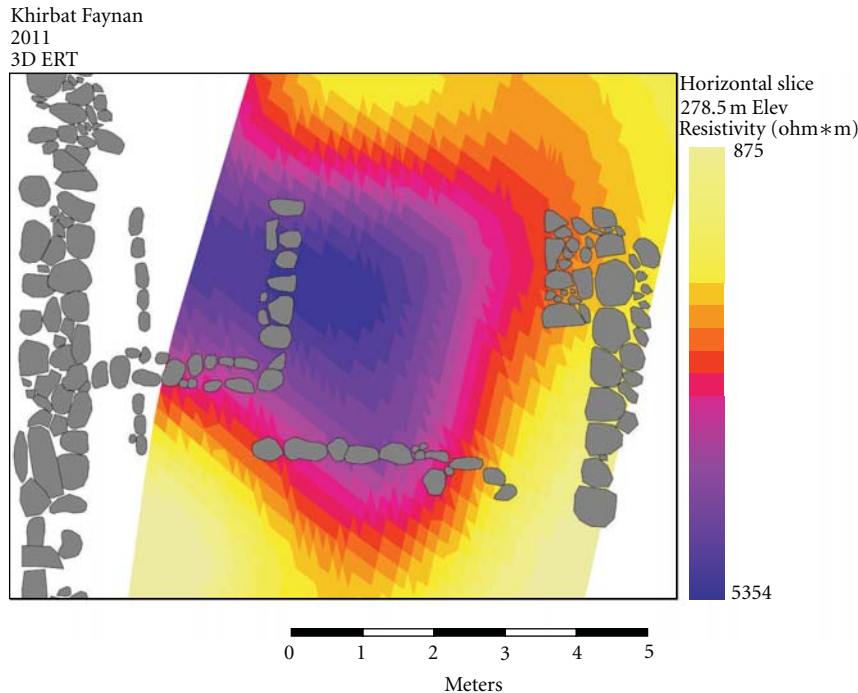


FIGURE 6: Walls found during the excavation superimposed on a horizontal ERT slice at 1 m depth.

processing allowed for minor adjustments to be made in the survey planning, prioritizing areas with greater potential and leaving areas where there was clearly no subsurface cultural remains.

2.2. ERT Equipment and Discussion. We used a Syscal Pro resistivimeter (Iris Instruments, France) with 48 electrodes spaced by 0.5 meters. Four different sets of 2D ERT lines (24 electrodes at 1 m separation each) were collected over 4 sides (north, south, east, and west) of the Khirbat Faynan mound. The main objective was to obtain vertical sections up to 6 meters along the mound in order to investigate the different layers and distinguish cultural from natural layers.

Additionally, a small 3D ERT survey was collected in order to facilitate excavation. The 3D ERT survey used a set of parallel 2D profiles with a separation of 0.5 m among electrodes. The surveyed area of 24 m × 5 m included 6 ERT profiles. Both dipole-dipole and Wenner arrays were performed.

Data acquisition proved to be particularly challenging due to the extremely dry soil, preventing electrical conductivity, and abundance of rocks under the surface, impeding easy introduction of the metal stakes into the ground. While the later was not easily overcome, the former was improved through a mixture of water, clay, and salt producing a remarkably conductive medium which could be poured over each electrode.

After collection, data were sent to Geostudi Astier (Livorno, Italy) for inversion using ERTLab software (Multi-Phase Technologies LLC, USA and Geostudi Astier srl, Italy)

and generation of final maps within the software MVS/EVS (CTech, USA) and ArcMap 10 (ESRI, USA). The main purpose of the 3D ERT survey was to delineate buried stonewalls to guide archaeological excavations.

In our processing, full three-dimensional inversions of apparent resistivities are performed using a specific customized tool, derived from the ERTLab 3D inversion software, which uses a finite-element (FEM) approach to model the subsoil by adopting mesh of hexahedrons to correctly incorporate terrain topography [32]. Throughout the inversion iterations, the effect of non-Gaussian noise is appropriately managed using a robust data weighting algorithm [33, 34].

This past season, new benchmarks were placed around and on top of the tell with an RTK GPS system to ensure precise control of the surveying. Unlike EMI, the ERT has no self-georeferencing system. Therefore, the ERT was georeferenced using a reflectorless total station, which could measure the precise position of the stakes with or without a prism. Each individual line was shot in its entirety in order to provide redundancy when the lines were then matched up during the postprocessing. Since GIS has been a major component of the ELRAP field recording system since 1999 [35], there was already an infrastructure in place to relate the geophysical data with the archaeological data. As part of this recording system, daily aerial photographs are taken documenting the position of significant architectural features. Each photograph can be correlated with the daily elevations to know exactly what the elevations of the exposed layers are. This enabled us to lay the 3D ERT slices that corresponded to each aerial photograph's elevation in order to study the relationship of the geophysics with the archaeological record.

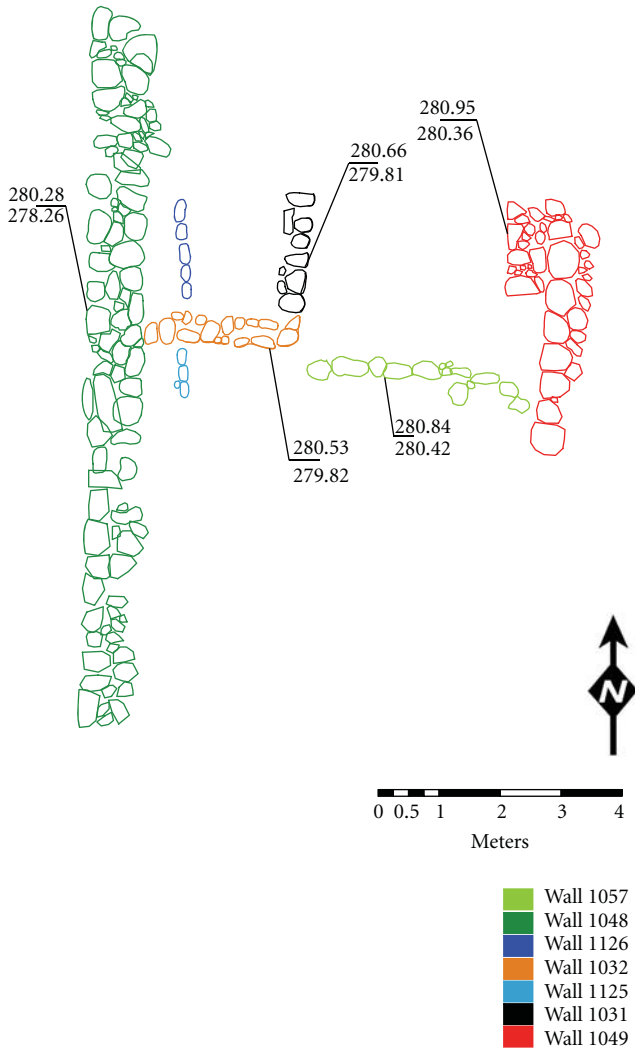


FIGURE 7: Ground truth, archaeological plan of the excavated walls detected using the 3D ERT geophysics.

3. Discussion

No features suggesting buried structures appeared in the lower-frequency EMI data. For this reason, EMI results presented here are for the higher (15 kHz) operating frequency (Figure 3). The most interesting areas, likely related to past human activity, have been highlighted. Some of them show clear linear patterns, other show areas with very high conductivity values (magenta and blue color) which might indicate the presence of accumulated metallurgic production materials. Unfortunately, in some areas, the presence of many pieces of slag covering the surface might have affected the EMI data due to its high sensitivity to metals. Thus, areas with higher conductivity may indicate just places of high concentration of slag covering the surface. However, other areas present subtle features of lower values (green and yellow colors) that may represent walls. As discussed by Witten [17], who worked in similar conditions, buried walls can appear as low values in the EMI data.

Past surveys in the area have included EMI and GPR, but ERT had not yet been employed. The 2D lines have enabled us to characterize the mound and we now have a better idea of the overall archaeological record. While the 2D does not give us a precise picture of the archaeology, it does at least suggest possible depths of archaeological depositions (Figure 4). Because of the lack of ERT performed in the area, it was felt that a ground truthing should be conducted in addition to the survey to correlate the results with the archaeological record. Half of square 16–56 was excavated, an area representing over half of the 3D ERT. The 3D volume showed what were most likely buried walls underneath the surface (see Figures 5 and 6). On the other hand, the ERT sections and volumes have shown that the very low-conductivity values, between 0 and 1 mS/m, match well with areas where the resistivity is higher than 1000 Ohm·m. Therefore, the ERT sections were used also to verify and calibrate properly the conductivity value in a condition that is typically not favorable for EM induction instruments.

The most significant correlation can be found between walls 1032 and 1057 (Figure 7). Because the lines went from north to south, the east-west walls seem to be the most visible in the data. In other words, every wall crossed is more visible than those running parallel to the survey lines. Wall 1032 was the closer of the two walls to the surface and was also more substantial than wall 1057 which had less preservation, these two factors together likely account for the stronger area of resistivity around wall 1032.

The GIS centric system of archaeological recording employed by the ELRAP team [35] allowed us to closely compare the archaeology with the geophysical survey. We were able to drape the appropriate ERT slices with the corresponding exposures at precise elevations. This allowed us to both compare the results of the excavation alongside the geophysics as well as predict what was coming next through the same sort of comparison. The final results were a series of images (see Figures 5 and 6) that show both the archaeology and the geophysics, with the later overlaid over the former. This further highlights the need for accurate georeferencing in geophysical survey, something which was central in our data collection.

4. Conclusion

The EMI data give us a general idea of what might be interesting to look at in detail in subsequent seasons in the lower area of the site. Future geophysical surveys should focus on the use of 3D GPR to locate more structures and accurately delineate those suggested by the EMI maps. The use of mobile multicoil EMI systems is also being considered due to their high lateral spatial resolution with accurate vertical measurements [36]. 3D GPR provides high-resolution volumetric data [14, 37, 38]. However, in order to use a GPR system in this area, rocks will have to be cleared from the study surface beforehand. Considering the quantity of rocks strewn about the surface, this will be a difficult task. On the other hand, the high-precision 3D ERT is potentially one of the more useful survey methods for such difficult terrain as

a rock-strewn tell. The time required to clean the surface of rocks as well as sort out what was tumble and what was part of existing architecture, would have proved far too costly to make it a viable technique for wide-area surveys. Indeed, the 3D ERT is still expensive in terms of human hours required to employ it; however, the technique is much less disturbing with high potential for excellent results.

The results from this season's work suggest that 3D ERT is a useful method for geophysical survey in difficult conditions that prevent the use of GPR. However, future work should include continued 3D ERT survey to conduct further correlation between the data and the archaeological record. Likewise, continued use of EMI can be helpful in revealing promising areas for more precise geophysical survey. With newer instruments, EMI is continuing to increase in precision and could potentially become one of the more useful tools as precision becomes more like that of ERT or GPR. Until such a time, however, EMI surveys like ours do not appear to offer much beyond that of general characterization of subsurface features. Southern Jordan continues to be an ideal place for testing geophysical survey techniques in difficult and harsh environments. The two techniques employed at Khirbat Faynan both resulted in success, each in their own way. We found that EMI helped to guide us towards the regions that we wanted to investigate further with higher-precision survey tools. This saved us countless hours considering the difficulty of employing the ERT versus that of EMI. Ultimately, the two tools together offered the best geophysical kit for our environment.

Acknowledgments

The authors are grateful to the Department of Antiquities (DOA) of Jordan for its help and interest in the 2011 ELRAP expedition. In particular, Jehad Haroun, Khalil Hamdan, Qutaiba al-Dasouqi, and especially Abdelrahim Al Dwikat and Zouhair Zoubi who served as DOA representatives to our project. Thanks also to Barbara Porter (director) and Christopher Tuttle (associate director) of the American Center of Oriental Research (ACOR), Amman, for their help and support. Members of most of the Bedouin tribes from the Qurayqira/Faynan villages worked on the project. Funding for this project came from: Research Opportunities (CSRO) Grant program; NSF grant EAR-Geophysics, 09-539; National Geographic Society (Grant no. 8974-11), the Jerome and Miram Katzin Family Foundation, and the Norma and Reuben Kershaw Family Foundation. M. Vincent was supported by the National Science Foundation IGERT (Integrative Graduate Education and Research): Training, Research and Education in Engineering for Cultural Heritage Diagnostics (NSF 0966375), where T. E. Levy serves as co-PI. A special thanks to Ramesh Rao, director, Calit2 San Diego Division for his support of the ELRAP expedition. They deeply appreciate the hard work carried out by the undergraduate students enrolled in the UCSD Middle East Archaeology Field School that forms part of the ELRAP research endeavor. The 2011 ELRAP expedition was directed by T. E. Levy and Mohammand Najjar. They thank M. Najjar

for his collegiality and interaction in the field. Thanks also to Gianfranco Morelli, Geostudi Astier, for help with data processing.

References

- [1] R. Slatt, W. C. King, J. Molyneux et al., "Tribute to Dr. Alan Witten," *Earth Scientist*, pp. 9–23, 2005.
- [2] A. J. Witten, *Handbook of Geophysics and Archaeology*, Equinox Pub, 2006.
- [3] T. E. Levy, T. Higham, C. B. Ramsey et al., "High-precision radiocarbon dating and historical biblical archaeology in southern Jordan," *Proceedings of the National Academy of Sciences of the United States of America*, vol. 105, no. 43, pp. 16460–16465, 2008.
- [4] E. Ben-Yosef, T. E. Levy, T. Higham, M. Najjar, and L. Tauxe, "The beginning of Iron Age copper production in the southern Levant: new evidence from Khirbat al-Jariya, Faynan, Jordan," *Antiquity*, vol. 84, no. 325, pp. 724–746, 2010.
- [5] E. Ben-Yosef, T. E. Levy, and M. Najjar, "Rās al-Miyāh fortresses: new discoveries at one of the gateways to the iron age copper production district of Faynan, Jordan," pp. 832–841, 2009.
- [6] E. Ben-Yosef, T. E. Levy, and M. Najjar, "New iron age coppermine fields discovered in southern Jordan," *Near Eastern Archaeology*, vol. 72, no. 2, pp. 98–101, 2009.
- [7] T. E. Levy, E. Ben-Yosef, and M. Najjar, "New perspectives on iron age copper production and society in the Faynan Region, Jordan," in *Eastern Mediterranean Metallurgy and Metalwork in the Second Millennium BC*, V. Kassianidou, Ed., Oxbow Books, Oxford, UK, 2012.
- [8] G. Barker, D. D. Gilbertson, and D. J. Mattingly, *Archaeology and Desertification: The Wadi Faynan Landscape Survey, Southern Jordan*, Oxbow, 2007.
- [9] C. E. Cordova, *Millennial Landscape Change in Jordan: Geoarchaeology and Cultural Ecology*, The University of Arizona Press, 2007.
- [10] A. Hauptmann, *The Archaeometallurgy of Copper: Evidence from Faynan, Jordan*, Springer, 2007.
- [11] J. P. Grattan, D. D. Gilbertson, and C. O. Hunt, "The local and global dimensions of metalliferous pollution derived from a reconstruction of an eight thousand year record of copper smelting and mining at a desert-mountain frontier in southern Jordan," *Journal of Archaeological Science*, vol. 34, no. 1, pp. 83–110, 2007.
- [12] C. O. Hunt, D. D. Gilbertson, and H. A. El-Rishi, "An 8000-year history of landscape, climate, and copper exploitation in the Middle East: the Wadi Faynan and the Wadi Dana National Reserve in southern Jordan," *Journal of Archaeological Science*, vol. 34, no. 8, pp. 1306–1338, 2007.
- [13] B. W. Bevan, "Geophysical exploration for archaeology: an introduction to geophysical exploration," Midwest Archaeological Center Special Report 1, U.S. Department of the Interior, National Park Service, Lincoln, Neb, USA, 1998.
- [14] L. B. Conyers and D. Goodman, *Ground-Penetrating Radar: An Introduction for Archaeologists*, AltaMira Press, 1997.
- [15] C. Gaffney, "Detecting trends in the prediction of the buried past: a review of geophysical techniques in archaeology," *Archaeometry*, vol. 50, no. 2, pp. 313–336, 2008.
- [16] K. L. Kvamme, "Geophysical surveys as landscape archaeology," *American Antiquity*, vol. 68, no. 3, pp. 435–457, 2003.

- [17] A. J. Witten, T. E. Levy, R. B. Adams, and I. Won, "Geophysical surveys in the Jebel Hamrat Fidan, Jordan," *Geoarchaeology*, vol. 15, no. 2, pp. 135–150, 2000.
- [18] D. Simpson, A. Lehouck, M. Van Meirvenne, J. Bourgeois, E. Thoen, and J. Vervloet, "Geoarchaeological prospection of a medieval manor in the Dutch polders using an electromagnetic induction sensor in combination with soil augerings," *Geoarchaeology*, vol. 23, no. 2, pp. 305–319, 2008.
- [19] A. Tabbagh, "Applications and advantages of the Slingram electromagnetic method for archaeological prospecting," *Geophysics*, vol. 51, no. 3, pp. 576–584, 1986.
- [20] B. Frohlich and W. J. Lancaster, "Electromagnetic surveying in current Middle Eastern archaeology: application and evaluation.," *Geophysics*, vol. 51, no. 7, pp. 1414–1425, 1986.
- [21] A. Witten, G. Calvert, B. Witten, and T. Levy, "Magnetic and electromagnetic induction studies at archaeological sites in Southwestern Jordan," *Journal of Environmental and Engineering Geophysics*, vol. 8, no. 3, pp. 209–215, 2003.
- [22] M. Dabas, A. Hesse, and J. Tabbagh, "Experimental resistivity survey at Wroxeter archaeological site with a fast and light recording device," *Archaeological Prospection*, vol. 7, no. 2, pp. 107–118, 2000.
- [23] I. Scollar, A. Tabbagh, A. Hesse, and I. Herzog, *Archaeological Prospecting and Remote Sensing*, Cambridge University Press, Cambridge, UK, 1990.
- [24] M. Drahor, M. Berge, and Ö. Caner, "Integrated geophysical surveys for the subsurface mapping of buried structures under and surrounding of the Agios Voukolos Church in Izmir, Turkey," *Journal of Archaeological Science*, vol. 38, no. 9, pp. 2231–2242, 2001.
- [25] S. Negri, G. Leucci, and F. Mazzone, "High resolution 3D ERT to help GPR data interpretation for researching archaeological items in a geologically complex subsurface," *Journal of Applied Geophysics*, vol. 65, no. 3-4, pp. 111–120, 2008.
- [26] G. N. Tsokas, P. I. Tsourlos, G. Vargemezis, and M. Novack, "Non-destructive electrical resistivity tomography for indoor investigation: the case of Kapnikarea Church in Athens," *Archaeological Prospection*, vol. 15, no. 1, pp. 47–61, 2008.
- [27] P. I. Tsourlos and G. N. Tsokas, "Non-destructive electrical resistivity tomography survey at the South Walls of the Acropolis of Athens," *Archaeological Prospection*, vol. 18, no. 3, pp. 173–186, 2011.
- [28] J. Casana, J. T. Herrmann, and A. Fogel, "Deep subsurface geophysical prospection at Tell Qarqur, Syria," *Archaeological Prospection*, vol. 15, no. 3, pp. 207–225, 2008.
- [29] A. Osella, M. de la Vega, and E. Lascano, "3D electrical imaging of an archaeological site using electrical and electromagnetic methods," *Geophysics*, vol. 70, no. 4, pp. G101–G107, 2005.
- [30] G. Matheron, "Principles of geostatistics," *Economic Geology*, vol. 58, no. 8, pp. 1246–1266, 1963.
- [31] T. E. Levy, M. Najjar, A. D. Gidding et al., "The 2011 Edom Lowlands Regional Archaeology Project (ELRAP): Excavations and Surveys in the Faynan Copper Ore District, Jordan," *Annual of the Department of Antiquities of Jordan*.
- [32] Z. Bing and S. A. Greenhalgh, "Finite element three-dimensional direct current resistivity modelling: accuracy and efficiency considerations," *Geophysical Journal International*, vol. 145, no. 3, pp. 679–688, 2001.
- [33] D. J. LaBrecque, M. Miletto, W. Daily, A. Ramirez, and E. Owen, "The effects of noise on Occam's inversion of resistivity tomography data," *Geophysics*, vol. 61, no. 2, pp. 538–548, 1996.
- [34] G. Morelli and D. J. Labrecque, "Advances in ERT inverse modeling," *European Journal of Environmental and Engineering Geophysics*, vol. 1, no. 2, pp. 171–186, 1996.
- [35] T. Levy, V. Petrovic, T. Wypych et al., *On-Site Digital Archaeology 3.0 and Cyber-Archaeology: Into the Future of the Past—New Developments, Delivery and the Creation of a Data Avalanche*, Introduction to Cyber-Archaeology, Archaeopress, Oxford, UK, 2010.
- [36] P. De Smedt, M. Van Meirvenne, E. Meerschman et al., "Reconstructing palaeochannel morphology with a mobile multicoil electromagnetic induction sensor," *Geomorphology*, vol. 130, no. 3-4, pp. 136–141, 2011.
- [37] J. Leckebusch, "Ground-penetrating radar: a modern three-dimensional prospection method," *Archaeological Prospection*, vol. 10, no. 4, pp. 213–240, 2003.
- [38] A. Novo, M. Grasmueck, D. Viggiano, and H. Lorenzo, "3D GPR in archaeology: what can be gained from dense data acquisition and processing," in *Proceedings of the 12th International Conference on Ground Penetrating Radar*, pp. 16–19, 2008.

Research Article

Multitemporal High-Resolution Satellite Images for the Study and Monitoring of an Ancient Mesopotamian City and its Surrounding Landscape: The Case of Ur

Giacomo Di Giacomo and Giuseppe Scardozi

*Istituto per i Beni Archeologici e Monumentali (IBAM), Consiglio Nazionale delle Ricerche (CNR),
Strada per Monteroni c/o Campus Universitario, 73100 Lecce, Italy*

Correspondence should be addressed to Giuseppe Scardozi, g.scardozi@ibam.cnr.it

Received 7 February 2012; Revised 9 June 2012; Accepted 24 June 2012

Academic Editor: Nicola Masini

Copyright © 2012 G. Di Giacomo and G. Scardozi. This is an open access article distributed under the Creative Commons Attribution License, which permits unrestricted use, distribution, and reproduction in any medium, provided the original work is properly cited.

The paper concerns the use of multitemporal high-resolution satellite images for the study of the ancient city of Ur, in southern Mesopotamia, inaccessible to scholars from 2003. The acquired dataset is composed by two Gambit KH-7 (1966) and one Corona KH-4B (1968) declassified spy space photos and by few images taken by the recent satellites for civilian use QuickBird-2 (2002, 2004, 2007), Ikonos-2 (2008), and WorldView-1 (2008). The processing of all these images and the integration with ASTER and SRTM DEMs allowed the acquisition of new data about the topographical layout of the city and its monuments and ancient roads; the georeferencing of all archaeological remains and traces visible on the images allowed the upgrade of the archaeological map of Ur. The research also provided important data concerning the reconstruction of the surrounding landscape, where a lot of traces of old channels and riverbeds of the Euphrates were identified in areas much modified and altered during the last decades by urbanization and agricultural works. Moreover, the multitemporal images allowed the monitoring of the conservation of the archaeological area, particularly before and after second Gulf War.

1. Introduction

The research activity concerning Ur was gained in the context of the “Virtual Museum of Iraq” Project, promoted by the Italian Ministry of Foreign Affairs and carried out by the National Research Council (CNR) of Italy. The project was designed to the construction of a Virtual Museum of the ancient civilizations that flourished in the territory of modern Iraq; the result was a rich website (<http://www.virtualmuseumiraq.cnr.it/>), free to the general public, based on the archaeological collection of one of the most important museums in the world. In fact, in 2003, during the 2nd Gulf War, the National Museum of Baghdad has been looted, stripping it of a priceless collection of cultural artefacts that are important historical treasures not only for Iraqi people but also for all humanity. The “Virtual Museum of Iraq” Project explored different new integrated digital technologies for virtual heritage, particularly focusing

on the use of image-based 3D modelling and satellite remote sensed data [1–7]. Specifically, the present work concerns the case of the ancient city of Ur, in southern Mesopotamia (Figure 1), that is exemplificative of the contribution of high-resolution satellite images for the reconstruction of the ancient topography and the monitoring of the site.

2. Methodology: The Research Activity concerning Ur in the “Virtual Museum of Iraq” Project

In the “Virtual Museum of Iraq” Project, the activities of the Institute for Archaeological and Monumental Heritage (IBAM-CNR) were focused on the realization of 3D reconstruction of settlements, monuments, and objects of the most important archaeological Iraqi sites and on the contextualization of finds stored into the Baghdad Museum,

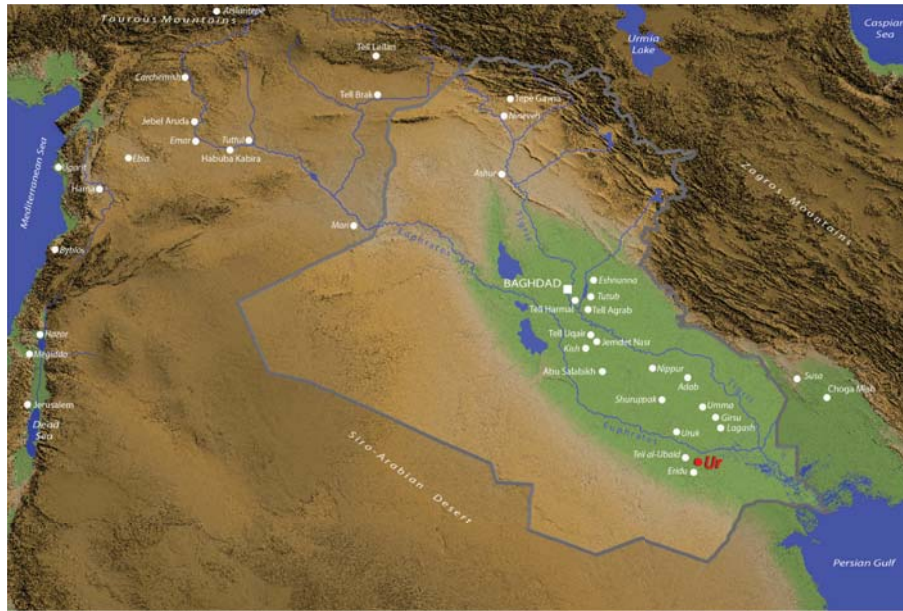


FIGURE 1: Ur in the southern Mesopotamia (Digital Elevation Model processed from the Shuttle Radar Topography Mission).

linking them to their sites of provenance. This process of contextualization enables the “visitors” of the Virtual Museum to view the original territorial contexts of the finds and it was implemented on three temporal levels: the ancient times, the moment of the discovery, and modern times. The virtual reconstructions, including those based on excavation photos, yield excellent results for the first two levels. Concerning the third temporal level, allowing a virtual visit to the place of provenance in its current situation, the photographic images, both aerial and from the ground, allow the user to view the archaeological areas with a very high detail. Considerable problems arise, however, in situations where the contexts are not easily accessible and adequate photographic documentation is not available. This is the case of much ancient cities and settlements of Iraq; generally, only few terrestrial images and some oblique aerial photographs of small sectors of the archaeological areas are available, together with some documents (graphic and photographic) of the excavations. An important contribution to the resolution of this problem, as well as to the recovery of documentation that serves to complement any photographic material that may be available, has been provided by high-resolution satellite images.

For each chronological section of the Virtual Museum, two or three archaeological sites more representative were chosen; they were documented by cataloguing the most significant monuments in order to provide the “visitors” of the Virtual Museum with a complete image of the characteristics of the contexts where the artefacts were found. In particular, the ancient city of Ur was chosen both for the Sumerian and the Neo-Babylonian “Halls” of the Museum.

In the section “Archaeological Sites” of the Iraq Virtual Museum, the contribution of high-resolution multitemporal satellite images was very important. First of all, the images were used to document the modern situation of ancient sites

and for monitoring their conditions before and after the first and second Gulf War. These images make it possible to observe and document the archaeological areas as they are today, both as a substitute for a real visit (currently impossible) and in preparation for a future visit. The detailed examination of these images also constitutes an important opportunity to acquire new data about the topographical layout of the sites and their principal monuments [8, 9]. Moreover, satellite orthoimages were used for the production of new archaeological map of the ancient sites investigated in the research project [10].

In the case of Ur, we have a rich data set, starting from three panchromatic photos taken in the 1960s by the United States reconnaissance satellites Gambit KH-7 (1966; one vertical and one oblique, with a ground geometric resolution of 0.6 m) and Corona KH-4B (1968; ground geometric resolution of about 1.83 m). The documentation of the USA spy satellites covers the entire site and its surroundings; it is a fundamental tool for archaeological research, very useful when old aerial photos are scarce. In fact, thanks to their high geometric resolution, they allow the examination in detail of ancient urban areas and territories that later are changed or also partially destroyed; so, it is possible to detect and examine ancient structures, paleoenvironmental elements, and archaeological traces of buried features not yet visible [11].

The satellite documentation of the 1960s was augmented by the use of five high-resolution images taken between 2002 and 2008 by the commercial satellites QuickBird-2 (2002, 2004, 2007; *Standard Ortho-ready* products), Ikonos-2 (2008; *Carterra Geo Ortho kit* product), and WorldView-1 (2008; *Standard Ortho-ready* product). These images constitute an up-to-date documentation, very useful for the study and presentation of the archaeological site, through which it is possible also to compare with the aerial photos taken by



FIGURE 2: The new general plan of Ur (drawn up by F. Ghio): 1: City Wall; 2: North Harbour; 3: Palace of Ennigaldi-Nanna; 4: Harbour Temple; 5: Houses on City Wall; 6: Kassite Fort; 7: enclosure of the Sacred Area in the neo-Babylonian period; 8: enclosure of the Sacred Area during the 3rd Dynasty; 9: Nanna Court; 10: Etemenniguru; 11: Ziggurat; 12: Nanna Temple; 13: Boat Shrine; 14: Ningal Temple; 15: Giparku; 16: Edublamakh; 17: Ganunmakh; 18: Ekhursag; 19: Mausolea of the 3rd Dynasty; 20: Royal Graves; 21: Nimintabba Temple; 22: Houses (EM District); 23: West Harbour; 24: Houses (AH District); 25: neo-Babylonian Houses; 26: Enki Temple.

Royal Air Force pilots during the main excavations of Ur in 1930s. The high geometric, spectral, and radiometric resolutions of the recent satellite images allowed the detailed analysis of the archaeological site; particularly, their very high ground geometric resolution (between 1 and 0.5 m in panchromatic mode; between 4 and 2.40 m in multispectral mode) makes them similar, in terms of definition, to vertical aerial photographs on a middle scale that in the case of Ur are scarce. The images made it possible to obtain a detailed view from above of the current state of the ancient remains and their layouts, given the possibility of noticing even quite small details; they enabled us to identify elements that are not easily perceptible on the ground and to recognize the traces of structures that are still buried or have become buried again

since their original excavation. Moreover, it is also possible to identify some paleoenvironmental features [12–18].

Very useful in the study of the site was also the integration of the images with ASTER and SRTM DEMs, from which were also extracted the contour lines of the new archaeological map of Ur elaborated during the research (Figure 2). The 3D models of the terrain show the tell of Ur, composed from successive stratifications, that rises approximately 20 m above the surrounding plain. The DEMs also allowed the 3D visualization of the site and its surroundings, and they made it possible to associate the archaeological traces and anomalies to the morphology of the ground thanks to the draping of the satellite images on the models (see Figure 7).

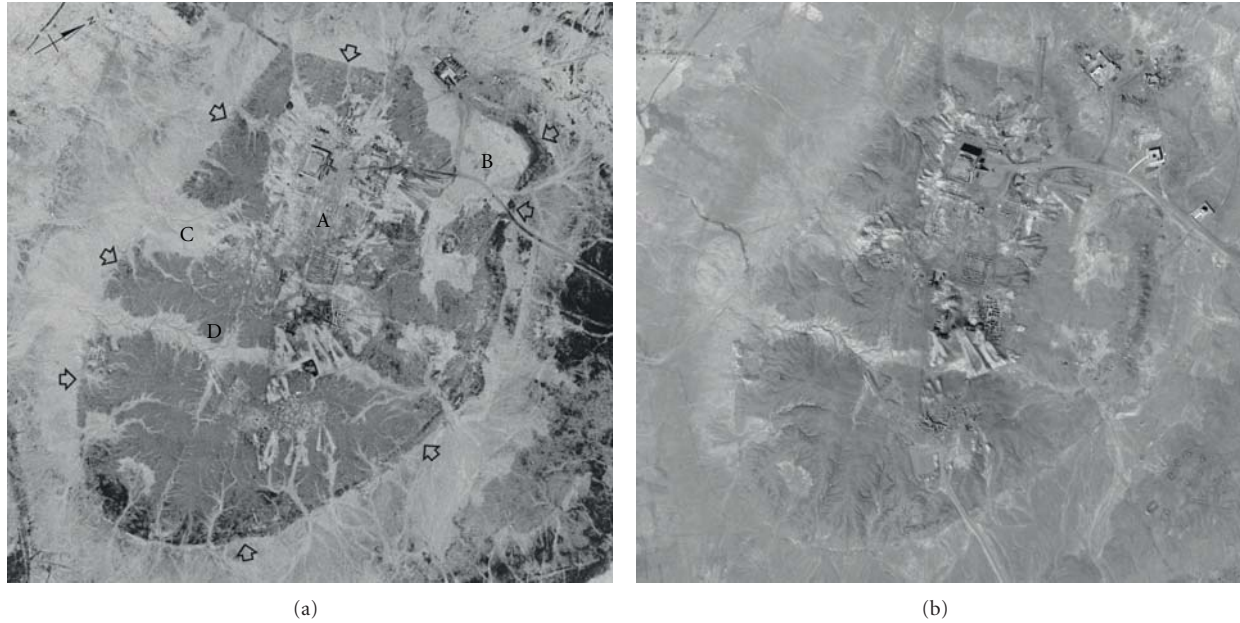


FIGURE 3: The hill of Ur in a Gambit KH-7 photograph taken in April 1966 and in a WorldView-1 image acquired in March 2008: A: the sacred area with the Ziggurat and the other main monuments; B: the North Harbour; C: the West Harbour, a depression that probably corresponds to an ancient channel. The arrows indicate traces and remains of the city walls.

3. Data Set

The data set used in this research is very detailed and covers a time span ranging from 1966 to 2008. Technical developments in the fields of electronics, optics, and space engineering of the last 50 years have made a substantial contribution to the study of the archaeological site of Ur, allowing multitemporal analysis, using historical images taken by spy satellites during the 1960s, and then multispectral investigation, thanks to the images of modern satellites for civilian use.

The oldest images coming from the historical archives of the USGS (United States Geological Service-<http://www.usgs.gov/>) provide datasets of declassified images from spy satellites constellation Corona and Gambit. The Corona program was the first United States strategic reconnaissance satellites project operated by the Central Intelligence Agency in cooperation with US Air Force. The Corona satellites were originally used for photographic surveillance of the Soviet Union (USSR) and of China, but during the operational phase satellites acquired images of many other areas of the world. The Corona program began in June 1959 and ended in May 1972. Satellite series were designated KH-1, KH-2, KH-3, KH-4, KH-4A, and KH-4B; KH is an acronym for “Key Hole” and the incrementing number indicates changes in the instrumentation (e.g., the camera type). 144 Corona satellites were launched and 102 of them returned usable photographs.

The altitude of these satellites was 165 to 460 kilometers above the surface of the Earth, so the cameras could acquire images with a ground resolution down to 7.5 meters; satellites used special 70 millimeter film with 60-centimeters

focal length cameras. The two KH-4A and KH-4B systems improved this resolution to 2.75 m and 1.8 m, respectively, because they operated at lower orbital altitudes. The KH-4 satellites used two panoramic cameras with 30-degree separation angle to produce stereoscopic imagery; in particular, the KH-4B system used two convergent rotating panoramic (black and white) cameras to record dual images of specific areas on the Earth with ground resolution of about 1.83 m and focal length of 60 centimetres and a Dual Improved Stellar Index Camera for target location identification and assistance in mapping. During 16 successful missions (from September 1967 to May 1972) it has produced 188,000 frames: an image taken on May 4, 1968, was used for this work, but this is not the oldest image available.

In fact, the dataset also includes two images taken in 1966 from a satellite of Gambit KH-7 series. The KH-7 was the first satellite for high-quality reconnaissance images. The system was designed to work with Corona program to take higher resolution images of a smaller area and the operational phase started in July 1963 and ended in June 1967. Gambit KH-7 successfully returned film on 34 of 38 missions and the usable images came from 30 missions. Satellites returned a total of 19,000 frames, with an initial ground resolution of 1.2 m; by 1966, best resolution improved to 0.6 m. These satellites, equipped with a Kodak advanced lens drive scanning Optical Bar camera system with its forward rotating primary mirror and folding optics capable of creating images on large format on a 9 inch wide, provided key cartographic information for large-scale (1 : 50,000) maps for US Department of Defense; priority targets for systems included Soviet and Chinese nuclear installations, but photos of other areas were taken. Most of the imagery from the KH-7 satellites was declassified



FIGURE 4: The territory of Ur (A) in a Gambit KH-7 photograph taken in April 1966: the traces of a paleoriver bed of the Euphrates (B) and the present river bed (C) are visible.

in 2002, and one oblique taken in February 18, 1966 and one vertical taken in April 23, 1966 (Figures 3 and 4; see also Figure 9) are part of the data set used for the research concerning Ur. In particular, the vertical image, as all the images acquired at nadir on the later KH-7 missions, can be compared favourably with the best commercial systems like Ikonos-2, QuickBird-2, and WorldView-1.

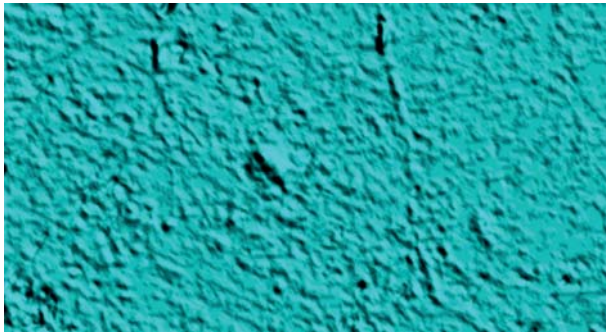
Ikonos-2 is a commercial earth observation satellite, owned by GeoEye, and was the first to collect publicly available high-resolution imagery at 1 m in panchromatic mode and 4 m in multispectral mode (<http://www.geoeye.com/>). Ikonos-2 was launched in 2001 and imagery began being sold on January 1, 2000. Ikonos-2 is the first next-generation commercial satellite, capable of acquiring images in stereo-mode, by rotating the camera along track; this satellite uses telemetry to transfer data to the ground and to receive navigation data from remote control center. The system, based on a fully digital image acquisition, has a primary mirror aperture of 0.7 m and a folded optical focal length of 10 m using 5 mirrors. The detectors at the focal plane include a panchromatic and a multispectral sensor, with 13500 pixels and 3375 pixels, respectively (cross-track). The sensor collects data with a 11-bit (0–2047) sensitivity that are delivered in an unsigned 16-bit (0–65535) data format. Sometimes data are rescaled down to 8 bit (0–255) to decrease file size, but this causes a loss of data. Ikonos-2 revisit time is 3 to 5 days for off-nadir and 144 days for true-nadir. An image taken by Ikonos-2 on August 9, 2008 was used for this work.

QuickBird-2 is another high-resolution commercial earth observation satellite, owned by DigitalGlobe and launched in 2001 (<http://www.digitalglobe.com/>). Until 2007

it has been the platform that has taken Earth images with the best geometric resolution; in fact the system collects 61-centimeter class panchromatic and 2.5-meter multispectral data over a large field of view with rapid target selection. QuickBird-2 was equipped with a sensor implemented by Ball Aerospace and Technologies Corporation, named Ball Global Imaging System 2000 (BGIS 2000), designed to be an agile, stable, and highly accurate Earth remote sensing platform. The imaging system returns 11-bit digital high resolution imagery from space, with 23 meters of horizontal accuracy. The operational orbit of the satellite is set to an altitude of 450 km with 98 degree sun synchronous inclination. Revisit frequency is 1 to 3.5 days depending on latitude. In the research concerning Ur three Quickbird-2 images were used; they were taken on February 27, 2002, on April 04, 2004, and on March 20, 2007.

WorldView-1, another satellite of DigitalGlobe company, was successfully launched on September 18, 2007. It was equipped with only a panchromatic imaging system, which can acquire half-meter resolution imagery with a dynamic range of 11 bit per pixel. Operating at an altitude of 496 kilometers, WorldView-1 has an average revisit time of 1.7 days and is capable of collecting up to 750,000 square kilometers per day of half-meter imagery. The satellite is also equipped with state-of-the-art geolocation capabilities and exhibits stunning agility with rapid targeting and efficient in-track stereo collection. Only one image, captured by this satellite on March 10, 2008, was used for the case study concerning Ur (Figure 3).

These eight images taken over 40 years from different satellites, with different characteristics and in different seasons, make up the data set that was used for this case study.



(a)



(b)



(c)

FIGURE 5: The hill of Ur in ASTER (a) and SRTM (b) DEMs; contour lines (c) extracted from the SRTM DEM, draped with the QuickBird-2 panchromatic image of 2004.

Depending on the type of the image, it was possible to perform various analyses and processing, from georeferencing, reading, and interpretation of the older images to the application of algorithms for postprocessing of the digital images taken by modern satellites.

4. Data Processing

In this case study, and also during all activities of the “Virtual Museum of Iraq” Project, the analysis of satellite images represented an opportunity to acquire new data on the ancient topography of the archaeological sites that were examined. This documentation was very important specifically for

contexts that have been studied many years ago or that are characterized by a history of the research centered mainly on individual complexes, monuments, or wealth of finds. In addition, these studies have often not interested the general layout of the settlement. However, it is important to specify that in the analysis of remote sensing data verification on the ground of presences, traces, and anomalies is fundamental; it is in order to clarify their real pertinence to archaeological elements, their interpretation and, if possible, also their dating, avoiding misunderstandings and mistakes. But in the study cases of the project, the ground control with a survey of the sites was impossible, so we could often formulate only hypotheses and the only comparison was with published studies.

The preliminary data processing has been the developing of three-dimensional models of the area of Ur (Figure 5), starting from the radar data taken by the Shuttle Radar Topography Mission and from an optical stereo pair taken by the radiometer ASTER (Advanced Spaceborne Thermal Emission and Reflection) of the Terra satellite; this stereo pair was already processed by the data center of Land Processes (LP) of Distributed Active Archive Centers (DAAC), which is a part of NASA’s Earth Observing System Data and Information System (EOSDIS).

The Shuttle Radar Topography Mission (SRTM) obtained elevation data on a near-global scale to generate the most complete high-resolution digital topographic database of Earth. SRTM consisted of a specially modified radar system that flew onboard the Space Shuttle during an 11-day mission in February of 2000. SRTM is an international project spearheaded by the National Geospatial-Intelligence Agency (NGA) and NASA. The processing method of SRTM data is divided in three stages: the first processing stage involves importing and merging the 1-degree tiles into continuous elevational surfaces in ArcGRID format. The second process fills small holes iteratively and the cleaning of the surface to reduce pits and peaks. The third stage then interpolates through the holes using a range of methods. The method used is based on the size of the hole and the landform that surrounds it. In the processing Arc/Info AML model was used. The final product is a shape file that contains three-dimensional data of Earth surface that can be used as a Digital Elevation Model to extract contours.

Instead the ASTER Digital Elevation Model product is generated using bands 3N (nadir-viewing) and 3B (backward-viewing) of an ASTER Level-1A image acquired in the Visible Near Infrared (VNIR). The VNIR subsystem of ASTER includes two independent telescopes that facilitate the generation of stereoscopic data. There is a time lag of approximately one minute between the acquisition of the nadir and backward images. Starting in early summer of 2006, LP DAAC has implemented a new production software for efficiently creating quality DEMs starting from the ASTER stereo pairs [19, 20]. Based on an automated stereocorrelation method, the new software generates a relative DEM without any ground control points (GCPs). It utilizes the ephemeris and altitude data derived from both the ASTER instrument and the Terra spacecraft platform. The ASTER DEM is a single-band product with 30-meters

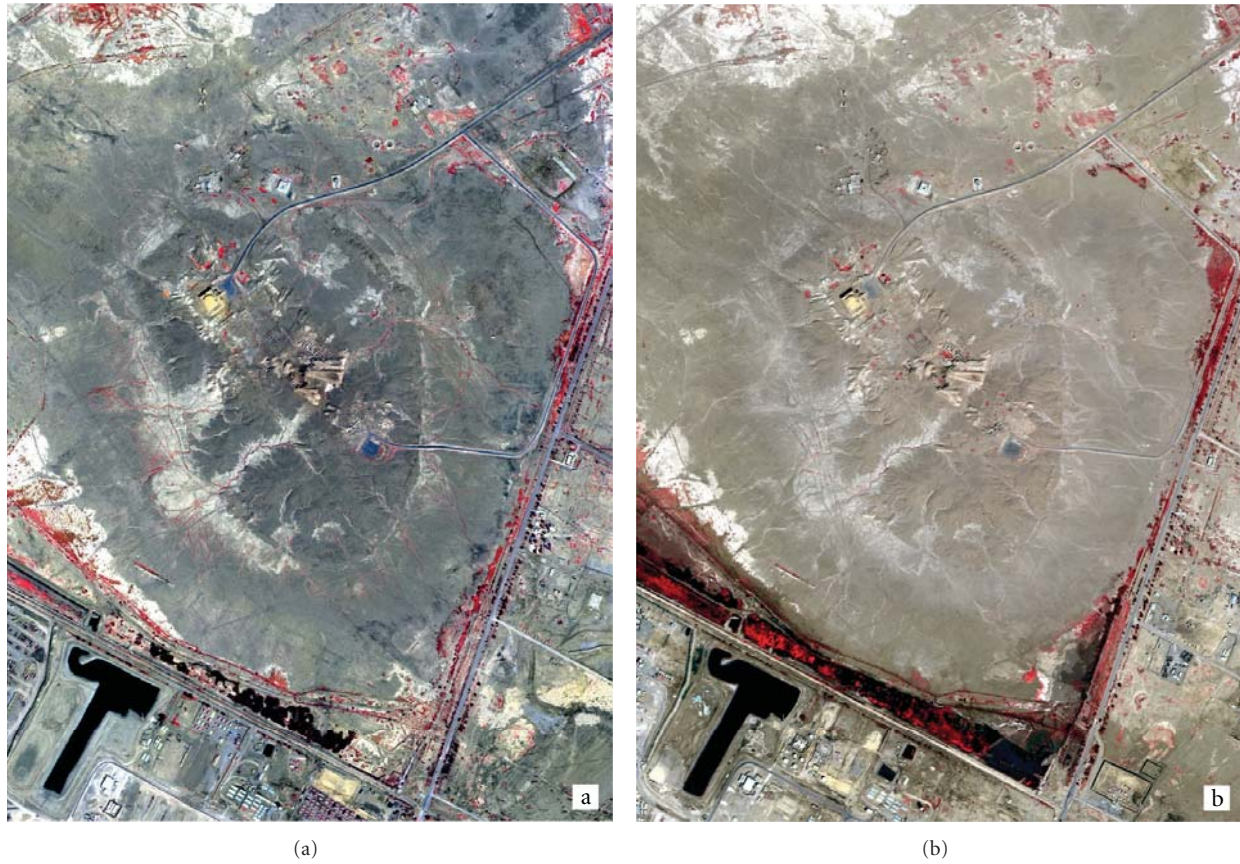


FIGURE 6: Ur in a pan-sharpened QuickBird-2 image of April 2004 (colour composite RGB bands 4-3-1) and in a pan-sharpened QuickBird-2 image of March 2007 (colour composite RGB bands 4-3-2).

horizontal postings that is geodetically referenced to the UTM coordinate system and referenced to the Earth's geoid using the EGM96 geopotential model.

Both the ASTER DEM and the SRTM DEM were alternatively used to orthorectify satellite images through the Rational Polynomial Coefficients released by the satellite company: Rational Polynomial satellite sensor models are simpler empirical mathematical models relating image space (line and column position) to latitude, longitude, and surface elevation. The name Rational Polynomial derives from the fact that the model is expressed as the ratio of two cubic polynomial expressions. Actually, a single image involves two such rational polynomials, one for computing line position and one for the column position. The coefficients of these two rational polynomials are computed by the satellite company from the satellite's orbital position and orientation and the rigorous physical sensor model.

The aberrations on the images caused by satellite absolute position at taking time has been reduced (as much as possible in the absence of Ground Control Points) using three-dimensional models SRTM and ASTER in association with ortho-rectifying algorithms implemented in software like ENVI or PCI Geomatica. So it was possible to upgrade the archaeological plan of the site and to create an up-to-date vector documentation.

Once georeferenced and geometrically corrected, image processing was carried out on some satellite images,

panchromatic and multispectral, acquired from Ikonos-2 and QuickBird-2 platforms. In particular, work was oriented in two directions: on the one side, we proceeded to elaborate the multispectral bands and to produce high-resolution colour images from the fusion with panchromatic images through various algorithms of pan-sharpening; on the other side, the georeferencing and orthorectification of panchromatic images for cartographic purposes were carried out. The multispectral processing of the images and the subsequent analysis of data from the near infrared and from the bands of the visible spectrum, was taken up in successive steps: the first phase of the work is consisted in the fusion of the different bands forming the data set of a raw satellite image. In fact the sensors of commercial satellites QuickBird-2 and Ikonos-2 acquire at the same time the same image in two different geometric resolutions: the panchromatic ones can reach a resolution at nadir of about 0.60 and 0.80 m, while the multispectral ones can reach a resolution between 2.40 and 3.20 m. The acquisition in multispectral mode for this type of satellites is in turn subdivided in four bands of the spectrum: red, green, blue (bands of the spectrum visible to the naked eye), and near infra-red (NIR-spectrum invisible to the naked eye). The images with different geometric resolution do not allow their direct overlay, unless an appropriate breakdown of the pixels is carried out, and a resampling through several algorithms: the most performance for images analysis aimed to the archaeological

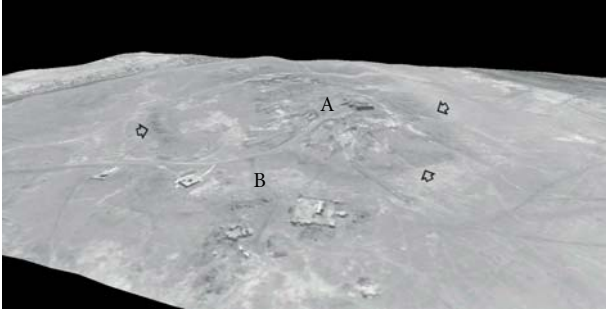


FIGURE 7: The QuickBird-2 panchromatic image of April 2004 draped on the DEM based on SRTM data: a view from the north, with the Ziggurat on the top of the hill (A), and the North Harbour area (B); the arrows indicate traces and remains of the city walls.

research were those of Zhang, implemented in the PCI Geomatica software, and the Gram-Schmidt algorithm, implemented in ENVI [21]. Using these algorithms it is possible to obtain high-resolution images (between 0.70 and 1 m) in the four bands acquired by QuickBird-2 and Ikonos-2 sensors (Figure 6; see also Figures 10–11 and 13).

The orderly overlaying of the single bands thus allows to visualize the image in true colours or in false colours, highlighting each time the different types of anomalies: for example, the use of red and near infra-red bands resulted being the most suitable to spot the anomalies and traces that are an outcome of vegetation growth. In fact, in the visible spectrum the red wavelength is very sensitive to the energy absorbed by chlorophyll during photosynthesis, while in the near infra-red the energy released by the internal structure of the leaves is highlighted. These data were also analyzed by dedicated software like PCI Geomatica 10.0 and ENVI 4.7 that implements algorithms for image enhancement like for example, the NDVI, useful for analyzing the growth rate, of vegetation in a defined area [22]; these are interpreted in order to acquire new data on the potential presence of buried structures that have affected vegetation growth.

The availability of modern satellite images with high geometric resolution represents a tool with enormous potential for the study of ancient urban and territorial contexts. These images provide plan views and, together with the photos of the 1960s spy satellites, make a complete multitemporal documentation of the archaeological areas. The manual vectorization of all archaeological remains and traces visible in the multi-temporal remote sensing data so allowed the creation of a new archaeological map (see Figure 2), ready for input in a GIS, with new data on the ancient topography of the site, monuments, and roads; in the map, the contour lines were extracted from the DEM based on SRTM and ASTER data. In addition, the three-dimensional models were used, together with QuickBird-2 panchromatic image of April 2004, to create a realistic 3D image of the ancient area, as it now appears (Figure 7).

5. Ancient Topography of the Site and Monitoring of the Archaeological Area

The processing and visual analysis of all acquired photos and satellite images available were very important for the study of Ur due to the inaccessibility of the archaeological area for scholars and the unavailability of vertical aerial photos and cartographies. This remote-sensed documentation allowed the acquisition of new data about the topographical layout of the city and its monuments, the ancient road network, and the paleoenvironmental context; these data are critical for the reconstruction of the historic landscape in which the settlement was located. In fact, a lot of traces and anomalies linked to archaeological and paleoenvironmental features were identified [1, 2]. In particular, the satellite images taken in winter and early spring, as most of those used in this study, are very useful for the visual photo-interpretation; in fact in these periods the more humid climate allows some types of traces (crop marks and damp marks) to be better visible, while in southern Iraq summer and early autumn are too dry and the archaeological traces are scarce clear. Furthermore, the draping of satellite images on DEMs (together with the only oblique image and in which the scarce air-photo available) highlighted the anomalies due to microrelief and allowed to connect the traces with the morphology of the site.

The integration of the documentation from old excavations and the remote-sensed data allowed the update of the archaeological map of Ur (see Figure 2), where all ancient remains and traces visible in the satellite images (orthorectified using the SRTM DEM and the Rational Polynomial Coefficients) were georeferenced. From the new digital archaeological map of Ur it is also possible to extract diachronic maps that document the historical development of the city during its main phases (Figure 8): (i) the Sumerian period, from the 1st to the 3rd Dynasty; (ii) the Isin and Larsa Dynasties; (iii) the Kassite period; (iv) the Neo-Babylonian age.

First of all, satellite images provide plan views of the entire archaeological area of Ur, very useful for a site where excavations were focused only on single monumental complexes or buildings and in which the studies had not interested the general layout of the settlement; they make available a complete image of the site, where different monuments and archaeological areas are together integrated and correctly localized. So, it is possible to understand the mutual relationships between various sectors of the urban area and different buildings.

In particular, it is possible to see the whole perimeter of the city with its circuit of walls and the position, plan, and reciprocal relationships of the buildings that were excavated between 1919 and 1934 (see Figure 3). In the highest part of the tell, the sacred area with the Ziggurat and the other main monuments are visible, while at the northern end and in the south-eastern part of the city it is possible to distinguish the depressions corresponding to the two harbours, today silted up. It is important also to note the presence of another depression stretching southwards from the northern harbour and passing to the east of the sacred area; it then curves towards the south-west, terminating



FIGURE 8: Maps of the main phases of Ur: (a) the Sumerian period, from the 1st to the 3rd Dynasty; (b) the Isin and Larsa Dynasties; (c) the Kassite period; (d) the Neo-Babylonian age.

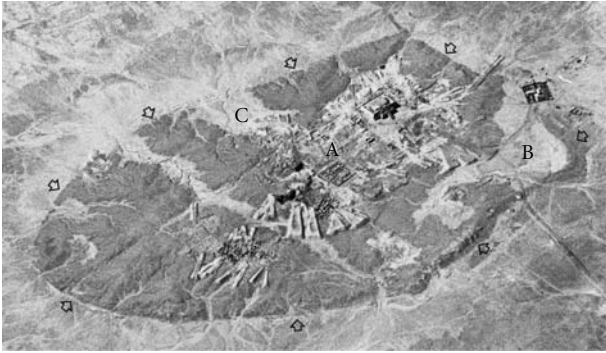


FIGURE 9: An oblique view of Tell al Muqayyar (Ur) in a Gambit KH-7 photograph acquired in February 1966: A: the sacred area on the top of the hill; B: the North Harbour; C: the West Harbour. The arrows indicate traces and remains of the city walls.



FIGURE 10: Traces and remains of the Palace of Ennigaldi-Nanna (A), of few houses built against the city walls (B), and of the Kassite Fort (C) in a pan-sharpened QuickBird-2 image of February 2002 (colour composite RGB bands 3-2-1).

to the south of the south-western harbour: this depression probably corresponds to the channel that crossed the city from the northern harbour and which was built or restored by Hammurabi. The remains and traces of the defensive city walls were also well visible in a Gambit KH-7 oblique photo of February 1966 (Figure 9) that shows very well the morphology of the site.

In the Northern part of the urban area, the satellite images show in detail the depression corresponding to the main harbour of Ur, which, besides being buried, is also partially covered by some modern constructions; particularly in the Gambit KH-7 vertical photo of April 1966, it is even possible to make out a few traces of the inner edge of the northern and south-western docks. Further south may be seen the remains and traces of the Palace of Ennigaldi-Nanna, today partly reburied after its excavation (Figure 10). The scant remains of the so-called Harbour Temple are visible immediately to the south. In the north-eastern sector of Ur, the satellite images show quite clearly the traces of the



FIGURE 11: Traces of structures and streets between the Neo-Babylonian Houses (A) and the Enki Temple (B) in a pan-sharpened QuickBird-2 image of February 2002 (colour composite RGB bands 3-2-1): the arrows indicate buried streets and walls along their sides, while the circle highlights buried structures (maybe other Neo-Babylonian houses).

fortifications, only partially excavated. Also visible are the scant remains and traces of a few houses built against the walls and of the quadrangular Kassite Fort, which stood in this stretch of the fortifications.

In the south-eastern sector of the city, satellite images clearly show the path of the walls; the scarce traces of the small Temple of Enki and the remains of the so-called AH Quarter are visible nearby (Figure 11). The last residential complex dates back to the period of the Isin and Larsa dynasties; the view from above shows the plan of the restored area, with the houses built up against each other and separated by narrow winding streets. Traces of the structures, partly reburied after the excavations, of another residential district, dateable to the Neo-Babylonian period, are visible to the south-west; the houses were inserted in a regular urban layout, marked by broad straight roads. The satellite image makes it possible to identify even traces of buried or semiexposed structures, identifiable with other houses and parallel streets: so, it is possible to integrate the excavation areas, showing how the regular urban planning of the Neo-Babylonian period concerned a broad section of the south-eastern part of Ur.

In the central sector of the city, it is possible to read the entire plan of the monumental sacred area and verify the preservation of the buildings excavated in 1920s and 1930s. The Ziggurat dominates this area, also thanks to its impressive visual impact, which is made even more evident by the modern restoration; on the other hand, traces of the Etemenniguru are scarce. The remains of the Edublamakh, the Ganunmakh, the Giparku, and the Hekhursag are clearly visible, while only some structures pertaining to the so-called Court of Nanna are preserved. It is possible to observe the structures and the traces of two other excavated monuments, the Temple of Nimin-Tabba and the so-called EM District, a



FIGURE 12: Ur (A) and the surrounding territory in a Corona KH-4B photo of May 1968: a lot of traces (B) of the paleoriver bed of the Euphrates are visible.

residential sector poorly conserved and dateable to the Isin-Larsa period. The broad pit resulting from the excavation of the so-called Royal Cemetery Clearly is visible to the south of the Hekhursag; the necropolis is characterized by the presence of numerous burials of high dignitaries and kings of Ur.

The remote-sensed documentation also provided important data concerning the reconstruction of the landscape surrounding Ur, where a lot of traces of old channels and paleoriver beds of the Euphrates were identified in areas much modified and altered during the last decades by urbanization and agricultural works. For this reason, the high-resolution USA reconnaissance photographs taken in 1966 by Gambit KH-7, which document the region of Nasiriyah, are very useful (see also Figure 4). In particular, they show the traces of a paleo-river bed of the Euphrates to the south-west, to the south, and to the south-east of the hill where the city was built; in fact, in ancient times the bed of the river ran near Ur, that, how we have seen, had two harbours and was an important trading centre. So, the Gambit image documents the paleohydrology of the area, in a territory that today is partially modified and altered by modern structures and above all by the military base and the airport built about 500 m south-west of the ancient city, exactly over the paleoriver bed, which was visible also in the Corona KH-4B image of 1968 (Figures 12 and 13). The oblique Gambit KH-7 photo, taken from the east in 1966, shows the modern route of the Euphrates, very far from the ancient city (Figure 14).

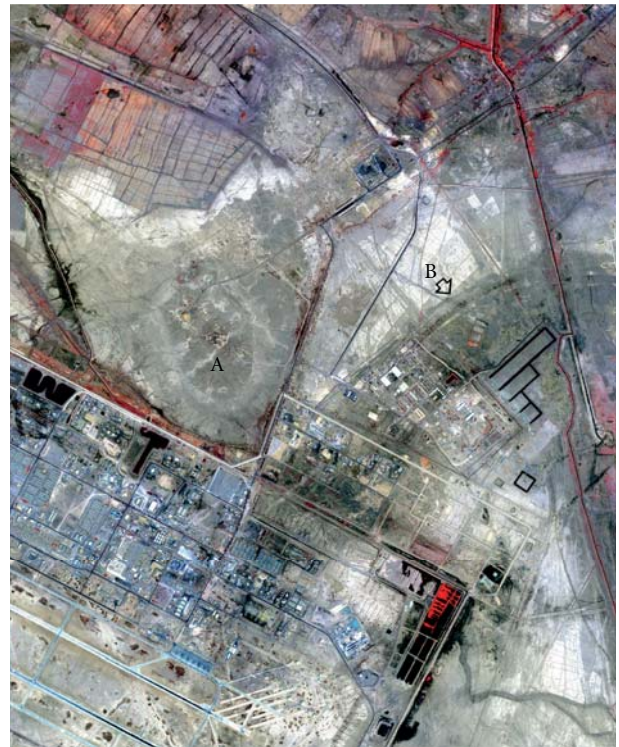


FIGURE 13: Ur (A) and the surrounding territory in a pan-sharpened Ikonos-2 image of 2008 (colour composite RGB bands 4-3-2): only some traces (B) of the paleo river bed of the Euphrates are visible.



FIGURE 14: Gambit KH-7 oblique photo of 1966: A: Ur; B: paleo river bed of the Euphrates; C: present river bed of the Euphrates; D: Nasiriyah.



(a)



(b)

FIGURE 15: The area of the North Harbour in a Gambit KH-7 photo of 1966 (a) and in the WorldView-1 image of 2008 (b): the arrows show the traces and remains of the northern and north-eastern docks.

Lastly, the multitemporal satellite images allowed the monitoring of the conservation of archaeological area during the last four decades and particularly before and after second Gulf War. In fact, in time of war, satellite images provided a crucial and invaluable tool for monitoring archaeological sites as well as their preservation or damage. Moreover, for a documentation of the situation before the first Gulf War and to study the area in a period chronological nearer the times of the archaeological excavations, the photos taken from the United States reconnaissance satellites are very useful. For example, the comparison between the vertical Gambit KH-7 image of 1966 and the WorldView-1 image of 2008 shows that during the 1960s some buildings and structures excavated between 1919 and 1934 were better preserved than

today (see Figure 3): the Palace of Ennigaldi-Nanna and the nearby residence of the high priestess of Nanna/Sin, the quadrangular Kassite fortress, the so-called AH Quarter and the North Harbour (Figure 15).

6. Conclusions

Through this experience, we could appreciate, one more time, the usefulness of historical and recent satellite images for remote analysis of archaeological sites. The potential of such data in research studies becomes even more evident when one considers that the revisit time of the last built satellites has further lowered: this feature allows not only to

acquire information programming also the time of taking the image (useful for example to analyze the shadows and calculate the height above ground of archaeological evidence) but also to implement systems for remote monitoring of archaeological sites. The completeness of the data set available for the study of Ur also made it possible not only to create an archaeological map in which all the evidence brought to light by the excavations and the visible traces are displayed in their correct relation to each other but also to contextualize the surrounding area, also reconstructed by using old satellite images. The analysis of historical and recent images, together with the availability of altimetric data acquired by SRTM mission and ASTER images, has helped to achieve a much more accurate and precise classification of the entire archaeological area, as well as to simplify the presentation of data, which are now easily understandable to nonspecialists, who may visit the site of the Virtual Museum of Iraq (<http://www.virtualmuseumiraq.cnr.it/>), while for a viewing of the maps created ad hoc for three other ancient centers of Iraq (Hatra, Khorsabad, and Seleucia), they can see the “Ancient cities of Mesopotamia” webGIS [7].

Acknowledgments

The “Virtual Museum of Iraq” Project was coordinated by Dr. Massimo Cultraro of the CNR-IBAM. The work concerning the satellite remote-sensed data was carried out by Drs. Laura Castrianni, Imma Ditaranto, Fabrizio Ghio, Giuseppe Pellino, Iliaria Miccoli, and Veronica Randino in the Ancient Topography, Archaeology and Remote Sensing Laboratory of the CNR-IBAM. The work concerning the 3D reconstruction was directed by Dr. Francesco Gabellone and carried out by Ivan Ferrari, Francesco Giuri, and Massimo Limoncelli in the Information Technologies Laboratory of the CNR-IBAM. The present work was made in strict cooperation between the authors; Sections 1, 2, and 5 are written by Giuseppe Scardozi, while Giacomo Di Giacomo is the author of Sections 3, 4, and 6.

References

- [1] F. Gabellone and G. Scardozi, “Integrated technologies for the reconstructive study of Mesopotamian cultural heritage: the cases of Ur, Uruk and Nimrud,” in *Proceedings of the International Congress on Cultural Heritage and New Technologies, Workshop 11 “Archäologie und Computer”*, pp. 1–46, Vienna, Austria, October 2006.
- [2] F. Gabellone and G. Scardozi, “From the object to the territory: image-based technologies and remote sensing for the reconstruction of ancient contexts,” *Archeologia e Calcolatori*, supplement 1, pp. 123–142, 2007.
- [3] M. Cultraro, F. Gabellone, and G. Scardozi, “Integrated methodologies and technologies for the reconstructive study of Dur-Sharrukin (Iraq),” in *Proceedings of the 21st International Symposium on AntiCIPAting the Future of the Cultural Past (CIPA ’07)*, vol. 1, pp. 253–258, Athens, Greece, 2007.
- [4] M. Cultraro, F. Gabellone, and G. Scardozi, “From remote sensing to 3D modelling and virtual reconstructions of the Iraqi archaeological sites: the case of Hatra,” in *Proceedings of the 1st International Workshop on Remote Sensing for Archaeology and Cultural Heritage Management*, R. Lasaponara and N. Masini, Eds., pp. 239–242, Rome, Italy, 2008.
- [5] M. Cultraro, F. Gabellone, and G. Scardozi, “The virtual musealization of archaeological sites: between documentation and communication,” in *Proceedings of the Workshop on 3D Virtual Reconstruction and Visualization of Complex Architectures*, pp. 1–6, Trento, Italy, February 2009.
- [6] M. Cultraro, F. Gabellone, and G. Scardozi, “The virtual musealization of archaeological sites: between documentation and communication,” in *Proceedings of 14th International Congress on Cultural Heritage and New Technologies*, pp. 294–308, Vienna, Austria, November 2009.
- [7] G. Di Giacomo and G. Scardozi, “Un webGIS per la conoscenza delle antiche città della Mesopotamia,” in *Proceedings of the 2nd Congreso Internacional de Arqueología e Informática Gráfica, Patrimonio e Innovación*, pp. 135–139, Seville, Spain, 2010.
- [8] G. Scardozi, “Multitemporal satellite high resolution images for the knowledge and the monitoring of the Iraqi archaeological sites: the case of Seleucia on the Tigris,” *European Journal of Applied Remote Sensing*, vol. 45, no. 4, pp. 143–160, 2009.
- [9] G. Scardozi, “Multitemporal satellite images for knowledge of the assyrian capital cities and for monitoring landscape transformations in the upper course of tigris river,” *International Journal of Geophysics*, vol. 2011, Article ID 917306, 17 pages, 2011.
- [10] G. Scardozi, “The contribution of high resolution satellite images to the production of base-maps and cartographies for archaeological research in Turkey and Iraq,” in *Remote Sensing for Environmental Monitoring, GIS Applications, and Geology IX*, vol. 7478 of *Proceedings of SPIE*, pp. 1–12, Berlin, Germany, September 2009.
- [11] G. Scardozi, “Old high resolution satellite images for landscape archaeology: case studies from Turkey and Iraq,” in *Remote Sensing for Environmental Monitoring, GIS Applications, and Geology*, vol. 7110/03 of *Proceedings of SPIE*, pp. 1–14, Cardiff, UK, September 2008.
- [12] G. Bitelli and V. A. Girelli, “Metrical use of declassified satellite imagery for an area of archaeological interest in Turkey,” *Journal of Cultural Heritage*, vol. 10, supplement 1, pp. e35–e40, 2009.
- [13] A. Beck, G. Philip, M. Abdulkarim, and D. Donoghue, “Evaluation of Corona and Ikonos high resolution satellite imagery for archaeological prospection in western Syria,” *Antiquity*, vol. 81, no. 311, pp. 161–175, 2007.
- [14] J. Casana and J. Cothren, “Stereo analysis, DEM extraction and orthorectification of CORONA satellite imagery: archaeological applications from the Near East,” *Antiquity*, vol. 82, no. 317, pp. 732–749, 2008.
- [15] N. Galiatsatos, D. N. M. Donoghue, and G. Philip, “High resolution elevation data derived from stereoscopic CORONA imagery with minimal ground control: an approach using Ikonos and SRTM data,” *Photogrammetric Engineering and Remote Sensing*, vol. 74, no. 9, pp. 1093–1106, 2008.
- [16] M. Jahjah, C. Olivieri, A. Invernizzi, and R. Parapetti, “Archaeological remote sensing application pre-post war situation of Babylon archaeological site-Iraq,” *Acta Astronautica*, vol. 61, no. 1–6, pp. 121–130, 2007.
- [17] R. Goossens, A. De Wulf, J. Bourgeois, W. Gheyle, and T. Willems, “Satellite imagery and archaeology: the example of CORONA in the Altai Mountains,” *Journal of Archaeological Science*, vol. 33, no. 6, pp. 745–755, 2006.

- [18] J. A. Ur, "Sennacherib's northern Assyrian canals: new insights from satellite imagery and aerial photography," *Iraq*, vol. 67, pp. 317–345, 2005.
- [19] T. Toutin, "Three-dimensional topographic mapping with ASTER stereo data in rugged topography," *IEEE Transactions on Geoscience and Remote Sensing*, vol. 40, no. 10, pp. 2241–2247, 2002.
- [20] T. Toutin, "ASTER DEMs for geomatic and geoscientific applications: a review," *International Journal of Remote Sensing*, vol. 29, no. 7, pp. 1855–1875, 2008.
- [21] R. Lasaponara and N. Masini, "Pan-sharpening techniques to enhance archaeological marks: an overview," in *Satellite Remote Sensing. A New Tool for Archaeology*, R. Lasaponara and N. Masini, Eds., pp. 87–109, Springer, 2012.
- [22] R. Lasaponara, N. Masini, and " , "Image enhancement, feature extraction and geospatial analysis in an archaeological perspective," in *Satellite Remote Sensing. A New Tool For Archaeology*, R. Lasaponara and N. Masini, Eds., pp. 17–63, Springer, 2012.

Research Article

Pseudo 3D Imaging of Dielectric and Magnetic Anomalies from GPR Data

Raffaele Persico,¹ Sergio Negri,² Francesco Soldovieri,³ and Elena Pettinelli⁴

¹*Institute for Archaeological and Monumental Heritage (IBAM), CNR, 73100 Lecce, Italy*

²*Department of Biological and Environmental Sciences and Technologies, University of Salento, 73100 Lecce, Italy*

³*Institute for Electromagnetic Sensing of the Environment (IREA), CNR, 80124 Naples, Italy*

⁴*Department of Physics, Roma Tre University, 00146 Roma, Italy*

Correspondence should be addressed to Francesco Soldovieri, soldovieri.f@irea.cnr.it

Received 12 March 2012; Accepted 25 June 2012

Academic Editor: Nicola Masini

Copyright © 2012 Raffaele Persico et al. This is an open access article distributed under the Creative Commons Attribution License, which permits unrestricted use, distribution, and reproduction in any medium, provided the original work is properly cited.

This paper deals with the reconstruction of buried targets exhibiting both dielectric and magnetic characteristics, starting from GPR data collected at the interface air/soil. The problem is tackled under the Born approximation. In particular, two-dimensional migration and linear inversion results will be compared versus experimental data and three-dimensional representations of the reconstructions achieved from both methods will be shown.

1. Introduction

GPR data processing has been historically focused on dielectric anomalies [1, 2], whereas the magnetic properties of the targets and of the embedding medium are customarily neglected. Recently, it has been outlined that the anomalies and/or the background scenario can exhibit magnetic properties, even in the radio-frequency and microwave range [3–9].

For this reason, in previous papers [10, 11] the problem of the estimation of dielectric and magnetic anomalies has been theoretically studied. It has been worked out that, at least within a 2D linear inversion model, based on the Born approximation and specifically referred to common offset GPR prospecting, the magnetic nature of the targets is not retrievable in absence of a priori information. Therefore, if one is interested in discriminating whether the targets have or not magnetic properties, either a more complicated model (where nonlinear effects and/or polarization effects are accounted for) or further measurements (i.e., not only GPR data) are useful. The theoretical demonstration passes through a long series of mathematical passages and will not be repeated here. In [12], experimental data with magnetic

targets have been gathered and processed for the first time. In that occasion, however, only four B-scans on the targets were gathered.

In this paper, we present reconstruction results by considering a measurement survey on a more complete grid in order to achieve pseudo 3D reconstructions with a specific focus on the depth slices. In particular, we have made use of a tank filled with sand, which was relatively wet at the time of the first measurements (exploited in [12]) but was quite drier when we have gathered the data shown here.

The paper is organised as follows. In Section 2 we present the generalized two-dimensional scalar scattering equations, relative to dielectric and magnetic objects embedded in a dielectric and magnetic (possibly lossy) soil. In Section 3, we briefly resume the theoretical discussion about the expected effects of the possible magnetic properties of the buried object on the reconstruction. In Section 4 the experimental case is shown. Conclusions follow.

2. Formulation of the Problem

The reference scenario is composed by two half spaces, with the interface air/soil at $z = 0$, according to Figure 1. The

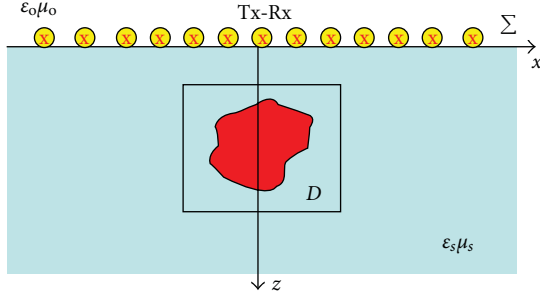


FIGURE 1: Geometry of the problem.

upper medium is built of air (assimilated to vacuum space), and the lower one shows an equivalent dielectric permittivity ϵ_s and magnetic permeability μ_s , both possibly complex to account for losses.

As source, we consider a filamentary electric current I_o invariant along the y -axis. The measurement configuration is a common offset B-scan with a fixed offset Δ between source and receiver. The source moves along the air-soil interface within the observation domain $\Sigma = [-x_M, x_M]$. The targets are enclosed in the investigation domain $D = [-a, a] \times [z_{\min}, z_{\min} + 2b]$, where a is the semiextent along the x -axis; z_{\min} and b are the minimum depth and the extent of the investigation domain, along the z -axis, respectively.

The problem can be recast in terms of the dielectric and magnetic contrast functions, respectively, defined as

$$\begin{aligned}\chi_e(x, z) &= \frac{\epsilon(x, z) - \epsilon_s}{\epsilon_s}, \\ \chi_m(x, z) &= \frac{\mu(x, z) - \mu_s}{\mu_s},\end{aligned}\quad (1)$$

where $\epsilon(x, z)$ is the equivalent dielectric permittivity and $\mu(x, z)$ is the equivalent magnetic permeability within the investigation domain D , respectively. The contrast functions in (1) account for the targets as ‘‘anomalies’’ with respect to the background scenario.

The scattering equations worked out are expressed as follows:

$$E = E_{\text{inc}} + k_s^2 \iint_D \left[\frac{1}{k_s^2} \nabla' G_i \cdot \nabla' E \frac{\chi_m}{1 + \chi_m} + G_i E \chi_e \right] dx' dz', \quad (2)$$

$$E_s = k_s^2 \iint_D \left[\frac{1}{k_s^2} \nabla' G_e \cdot \nabla' E \frac{\chi_m}{1 + \chi_m} + G_e E \chi_e \right] dx' dz'. \quad (3)$$

Equations (2) and (3) extend the classical two-dimensional scattering equations [1, 2] because of the magnetic terms. In particular, (2) accounts for the electromagnetic field inside the investigation domain, whereas (3) accounts for the scattered field, that is, the datum of our problem. Accordingly, in (2) and (3) $G_i(x, z, x', z')$ and $G_e(x, z, x', z')$ are the internal and external Green’s function. The gradient symbols are primed because they refer to x' and z' meant with respect to the primed couple of variables (the spatial

variables defined in the investigation domain D). Moreover, E and E_{inc} are the (y -directed) internal and incident electric fields, whereas E_s is the (y -directed) scattered field. The dot symbol in (2) and (3) stands for ‘‘scalar products,’’ and, finally, k_o and k_s are the wavenumbers in the air and in the soil.

3. Diffraction Tomography Relationships

Diffraction tomography (DT) provides well-known [13] approximate linear algebraic relationships between the spectra of the contrast and the one of the scattered field. We resume here the extension of the DT relationships to the more general case with both dielectric and magnetic anomalies; this analysis is discussed in detail in [11, 12].

The analysis is based on the following assumptions:

$$E(x, z) \approx E_{\text{inc}}, \quad (4)$$

$$\nabla E(x, z) \approx \nabla E_{\text{inc}}.$$

Equations (4) stem from the Born approximation in presence of both dielectric and magnetic anomalies. Under the above assumptions, we can rewrite (3) as

$$E_s \approx k_s^2 \iint_D \left[\frac{1}{k_s^2} \nabla' G_e \nabla' E_{\text{inc}} \chi_{m1} + G_e E_{\text{inc}} \chi_e \right] dx' dz', \quad (5)$$

where

$$\chi_{m1} \equiv \frac{\chi_m}{1 + \chi_m} \quad (6)$$

is a ‘‘derived’’ magnetic contrast function.

Substituting in (5) the expressions of the external Green function and of the incident field due to a filamentary current (available, i.e., in [11]), the generalised DT relationship for dielectric and magnetic anomalies is then worked out as

$$\hat{E}_s(p) = f(p) \hat{\chi}_{e1}(\eta(p), \varsigma(p)) + f(p) \hat{\chi}_{m1}(\eta(p), \varsigma(p)), \quad (7)$$

where $\hat{E}_s(p)$ is the Fourier transform of the scattered field with respect to the abscissa x_s of the source point (variable along the observation line Σ), $\hat{\chi}_{e1}(\eta(p), \varsigma(p))$ is the double Fourier transform of the auxiliary function $\chi_{e1}(x', z') = \chi_e(x', z')/\sqrt{z'}$ with respect to x' and z' , and $\hat{\chi}_{m1}(\eta(p), \varsigma(p))$ is the double Fourier transform of the auxiliary function $\chi_{m1}(x', z') = \chi_{m1}(x', z')/\sqrt{z'}$. Both these transforms are calculated in the spectral point

$$\begin{aligned}\eta &= p, \\ \varsigma &= \sqrt{4k_s^2 - p^2}.\end{aligned}\quad (8)$$

The spectral weight and $f(p)$ is given by

$$\begin{aligned}f(p) &= \frac{jk_s^2 \sqrt{\pi} f I_o \mu_o^2 \mu_s \exp(j(\pi/4))}{(\mu_o k_{zs}(p/2) + \mu_s k_{zo}(p/2))^2} \sqrt{\frac{k_{zs}(p/2)^3}{(p/2)^2 + (k_{zs}(p/2))^2}} \\ &\quad \times \exp(-j\Delta(p/2)) \exp(j2k_{zo}(p/2)z_s),\end{aligned}\quad (9)$$

where f is the working frequency and $k_{zo,s} = \sqrt{k_{o,s}^2 - p^2}$.

The physical conclusion related to (9) is that a linear reconstruction will be substantially the same for dielectric and magnetic targets (we have a formal difference of the two object functions, but it is irrelevant), and in particular, any linear reconstruction will not be able to distinguish whether the focused target was dielectric or magnetic (or both) contrasted with the surrounding soil.

4. Experimental Tests

The experimental test has been performed in a box set up within the Laboratory of Applied Geophysics of the Department of Biological and Environmental Sciences and Technologies of the University of Salento. The box is a wooden container internally sized 1.5×1.18 square meters and high 90 cm from the floor of the tank. It has been filled up with sand up to the top.

Within this box, four targets have been buried. Two equal metallic sheets sized 20×25 square cm, and two equal polystyrene boxes, the first of which filled up with (dusted) magnetite and the second filled up with the same sand that fills the tank. The size of the box filled up with magnetite is $23 \times 16 \text{ cm}^2$, whereas that of the box filled with sand is $26 \times 18 \text{ cm}^2$. Both boxes are high 8.5 cm (actually their shape is not that of a perfect parallelepiped, because they are slightly larger at the central point of their height). The thickness of the polystyrene walls of the boxes is of the order of 4 mm. The box filled with sand is a reference about the negligibility of the polystyrene walls of the boxes. In particular, if the walls of the box are really negligible, this box should be almost transparent and we can be confident that the signal scattered by the box filled up with magnetite is not substantially ascribable to the content of the box and not to the container. The two metallic boxes also were markers, and in particular they have been placed in two different points at two different depths, so to have a check also about the degree of homogeneity of the sand. Figure 2 illustrates the plant, the position of the targets, and the grid of the B-scan lines. In particular, the transect between two adjacent B-scan lines was 10 cm.

The data have been gathered with a SIR-3000 system, manufactured by GSSI, by making use of an antenna with nominal peak frequency at 900 MHz, manufactured by IDS.

With regard to the characteristics of the magnetite, exploiting the model assessed in [14], we have estimated in the band of interest an average relative dielectric permittivity nearly equal to 11.8 and an average relative magnetic permeability about nearly to $2-j0.5$. By exploiting the metallic sheets we have evaluated that the sand is quite homogeneous and its relative permittivity can be assumed equal to 4. Moreover, we have assumed for the inversions a conductivity of the soil equal to 0.001 S/m .

We have performed both a standard processing based on the Kirchhoff migration (performed by means of the commercial software Reflexw 15) and a tomographic inversion of the data, based on the described inverse scattering model [11, 12]. We show the results at three constant depth slices, at the depth of about 40, 50, and 80 cm, that is, at the depth of the four targets (see Figures 3, 4, 5, 6, 7, and 8).

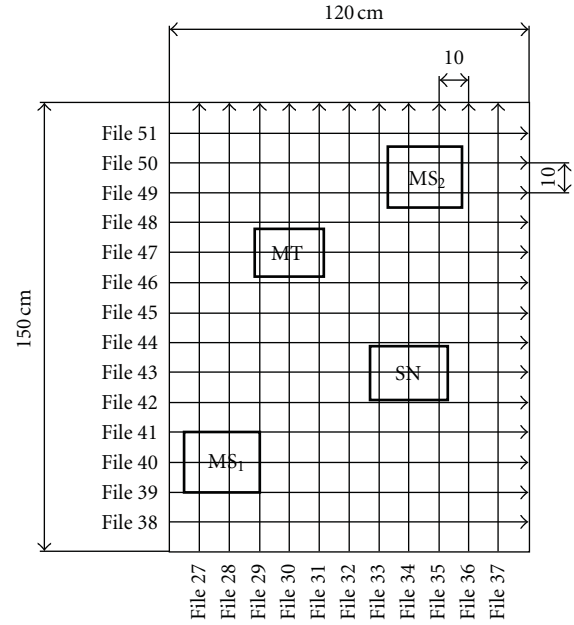


FIGURE 2: Plant of the box: the axes are in cm, the first metallic sheet (MS_1) is at the depth of 50 cm, the box filled up with magnetite (MT), and the box filled up with sand (SN) is at the depth of 41.5 cm (meant with respect to their top); the second metallic sheet (MS_2) is at the depth of 80 cm.

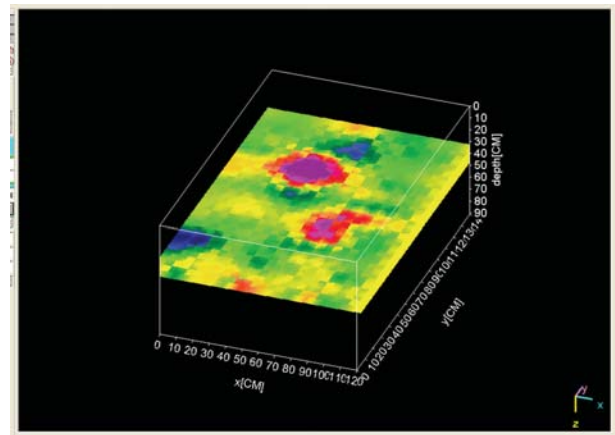


FIGURE 3: Constant depth at the depth of about 40 cm, achieved from migration.

For the inverse scattering algorithm, we have made use of an investigation domain 110 cm long (two investigation domains have been joined side by side for the long edge of the tank, with some correspondent to zero padding of the data); the discretization of the investigation domain has been performed by means of 45 Fourier harmonic functions along the abscissa and 37 step functions along the depth; the working frequency band (based on the spectrum of the data) ranged from 550 to 1250 MHz, sampled with a frequency step of 50 MHz. The spatial step of the data was 1 cm.

The comparison shows that the magnetic properties of one of the targets do not cause any particular effect in the

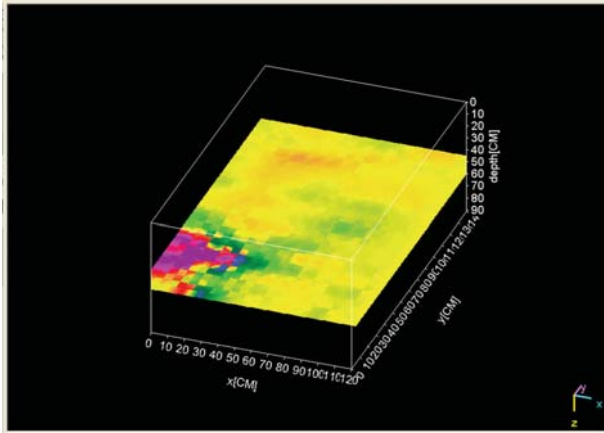


FIGURE 4: Constant depth slice at the depth of about 50 cm, achieved from migration.

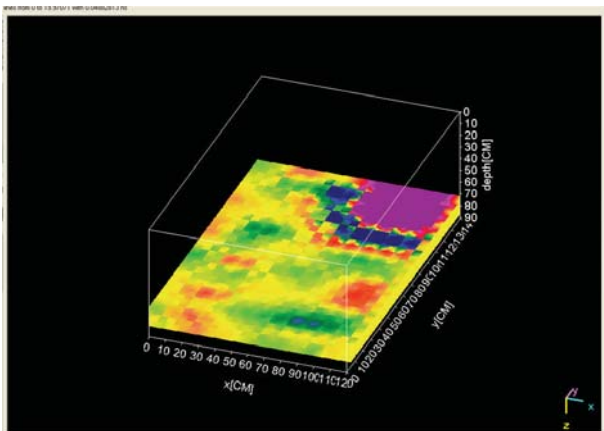


FIGURE 5: Constant depth slice at the depth of about 80 cm, achieved from migration.

reconstruction, either in the migrated or in the inverted data. In particular, we can see more evident “spots” regarding the two boxes within the migrated data (Figure 3) than in the inverted data (Figure 6). However, the size of the two boxes is better reproduced in the inverted data, which also show more clearly the difference of scattered energy between the box filled with sand and that filled with magnetite. In both cases we have artefact, due to the metallic sheets and the edge effects of the tank. Moreover, the inversion is affected by the fact that the box has been (for computational reasons) in two adjacent investigation domains, which causes the horizontal seam visible in the middle of Figures 6–8. Also the shallower metallic sheets seem slightly better localised in the inverted data. However, the comparison suggests that, when possible, both processing schemes are worth performing, since each of them has its intrinsic pros and cons. The metallic sheets are focused in a poorer way than the boxes: this is because both of them are close to the edges of the tank (so that a limited view angle problem arises for them). In particular, with regard to the deeper metallic sheet the problem of the limited view angle added to that of loss of resolution with the depth makes

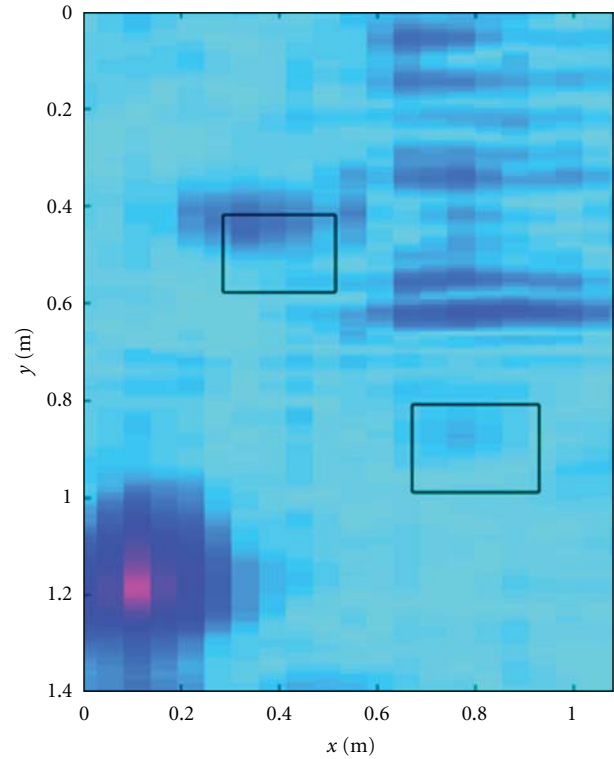


FIGURE 6: Constant depth slice at the depth of about 40 cm, achieved from inversion.

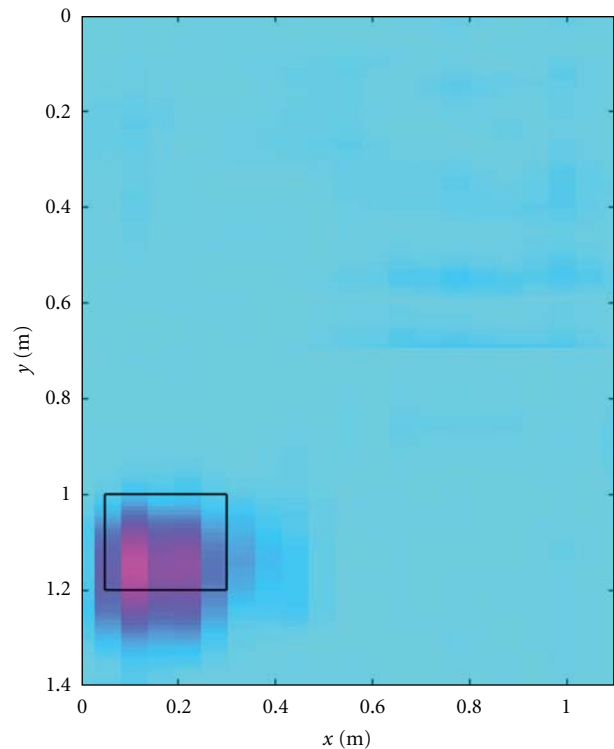


FIGURE 7: Constant depth slice at the depth of about 50 cm, achieved from inversion.

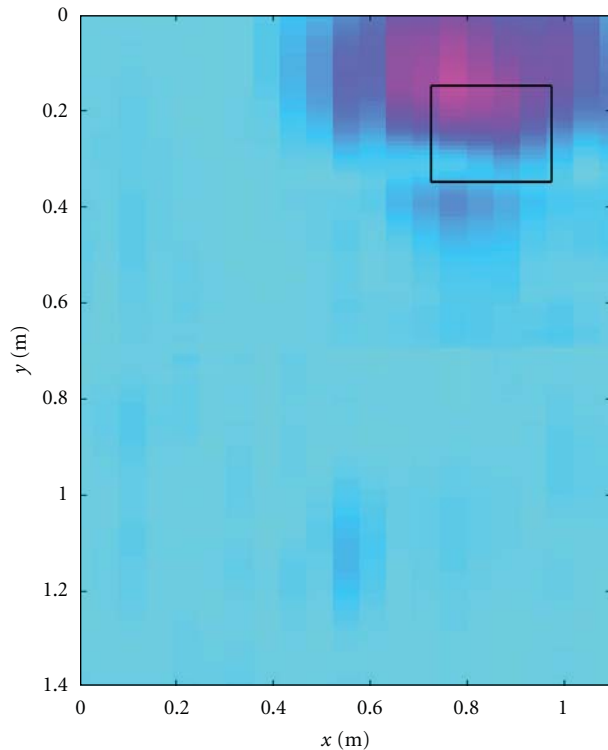


FIGURE 8: Constant depth slice at the depth of about 80 cm, achieved from inversion.

the achieved focussing poorer than the one achieved for the shallower targets, both migrating or inverting the data (see Figures 5 and 8).

5. Conclusions

In this paper we have dealt with the scattering from buried targets that can exhibit both a dielectric and a magnetic contrast with respect to the surrounding soil. We have reported a resume of theoretical considerations more deeply exposed elsewhere [11], or even inedited (but the space required to expose them in a full way would have been too long). We have shown some pseudo 3D reconstructions, achieved from experimental data. In future applications, therefore, we will try to measure magnetic properties of the soil or of the targets by other methods, exploiting, for example, TDR and GPR data and/or nonlinear processing; this activity could be of interest in Mars and other planets' exploration [8, 9].

Acknowledgment

The authors thank Dr. Antonia Tamborino for her collaboration.

References

[1] D. Colton and R. Kress, *Inverse Acoustic and Electromagnetic Scattering Theory*, Springer, 1992.

- [2] W. C. Chew, *Waves and Fields in Inhomogeneous Media*, IEEE Press, Piscataway, NJ, USA, 1995.
- [3] P. Chen, R. X. Wu, T. Zhao, F. Yang, and J. Q. Xiao, "Complex permittivity and permeability of metallic magnetic granular composites at microwave frequencies," *Journal of Physics D*, vol. 38, no. 14, pp. 2302–2305, 2005.
- [4] J. L. Young and C. M. Johnson, "A compact recursive trans-impedance Green's function for the inhomogeneous ferrite microwave circulator," *IEEE Transactions on Microwave Theory and Techniques*, vol. 52, no. 7, pp. 1751–1759, 2004.
- [5] G. Dural and M. I. Aksun, "Closed-form Green's functions for general sources and stratified media," *IEEE Transactions on Microwave Theory and Techniques*, vol. 43, no. 7, pp. 1545–1552, 1995.
- [6] J. B. Jarvis, M. D. Janezic, B. F. Riddle et al., *Measuring the Permittivity and Permeability of Lossy Materials: Solids, Liquids, Metals, Buildings Materials, and Negative-Index Materials*, NIST Technical Note 1536, 2004.
- [7] M. Nabighian, *Electromagnetic Methods in Applied Geophysics—Theory*, vol. 1, Society of Exploration Geophysics, 1987.
- [8] D. E. Stillman and G. R. Olhoeft, "Electromagnetic properties of martian analog minerals at radar frequencies and martian temperatures," in *Proceedings of the 37th Lunar and Planetary Science Conference*, 2006.
- [9] G. Picardi, J. J. Plaut, D. Biccari et al., "Radar soundings of the subsurface of Mars," *Science*, vol. 310, no. 5756, pp. 1925–1928, 2005.
- [10] R. Persico and F. Soldovieri, "Two dimensional inverse scattering from buried magnetic anomalies," *Annals of Geophysics*, vol. 51, no. 1, pp. 147–158, 2008.
- [11] R. Persico and F. Soldovieri, "Two-dimensional linear inverse scattering for dielectric and magnetic anomalies," *Near Surface Geophysics*, vol. 9, no. 3, pp. 287–295, 2011.
- [12] R. Persico, F. Soldovieri, S. Negri, and E. Pettinelli, "Dielectric and magnetic anomaly imaging from GPR data," in *Proceedings of the 13th International Conference on Ground Penetrating Radar (GPR '10)*, Lecce, Italy, June 2010.
- [13] W. Tabbara, B. Duchene, C. Pichot, D. Lesselier, L. Chommeloux, and N. Joachimowicz, "Diffraction tomography: contribution to the analysis of some applications in microwaves and ultrasonics," *Inverse Problems*, vol. 4, no. 2, pp. 305–331, 1988.
- [14] K. Klein and J. C. Santamarina, "Ferromagnetic inclusions in geomaterials: implications," *Journal of Geotechnical and Geoenvironmental Engineering*, vol. 126, no. 2, pp. 167–179, 2000.

Research Article

Accounting for Antenna in Half-Space Fresnel Coefficient Estimation

A. D'Alterio and R. Solimene

Dipartimento di Ingegneria dell'Informazione, Seconda Università di Napoli, Via Roma 29, 81031 Aversa, Italy

Correspondence should be addressed to A. D'Alterio, antonietta.dalterio@unina2.it

Received 27 April 2012; Accepted 14 June 2012

Academic Editor: Francesco Soldovieri

Copyright © 2012 A. D'Alterio and R. Solimene. This is an open access article distributed under the Creative Commons Attribution License, which permits unrestricted use, distribution, and reproduction in any medium, provided the original work is properly cited.

The problem of retrieving the Fresnel reflection coefficients of a half-space medium starting from measurements collected under a reflection mode multistatic configuration is dealt with. According to our previous results, reflection coefficient estimation is cast as the inversion of linear operator. However, here, we take a step ahead towards more realistic scenarios as the role of antennas (both transmitting and receiving) is embodied in the estimation procedure. Numerical results are presented to show the effectiveness of the method for different types of half-space media.

1. Introduction

Subsurface imaging problem is relevant in several applicative contexts that range from geophysical to civil engineering applications [1].

In this framework, regardless of the imaging algorithm one may want to use, the knowledge of soil parameters is necessary in order to obtain properly focused images and free from artifacts proliferation [2].

By contrast, in realistic scenarios, such parameters are generally unknown or, at best, known with some degree of uncertainty. Therefore, a soil parameter estimation procedure must be run before imaging.

Many procedures for estimating soil parameters are widespread in the literature. Reflectometry methods are very common [3]. There are methods which rely on fitting the moveout of hyperbolic diffraction pattern or measure travel time to a scatterer buried at known depth [4]. Other methods exploit different offset data and perform velocity or amplitude analysis to gather soil properties [5, 6]. Iterative imaging instead identifies soil parameters as those which return the more focalized reconstruction of a cooperative target [7]. Finally, further methods first retrieve reflection coefficient and then infer the soil properties by minimizing

a nonlinear cost function by using optimization procedure [8].

Most of the methods quoted above require far zone approximation, so that asymptotic ray approximation works and generally assume soil as a homogeneous (at least transversally) half space. Moreover, time domain data, equivalently multifrequency data, are employed. In particular, this requires dealing with a non-linear inversions when the reflection coefficient is used to infer soil properties [8]. As well known, non-linear inversion are generally computationally demanding and can suffer from reliability problems due to the occurrence of false solutions. In these cases, one can take advantage from a priori information about the soil which allows to reduce the number searched for unknowns. However, this entails that soil dispersive law must be a priori known.

Determining soil electromagnetic parameters is a mandatory step to achieve soil analysis in order to assess, for example, water content and in general material composition. However, this is not necessarily hold for imaging. Indeed, what is really needed to obtain properly focused image of buried scatterers is the relevant Green's function. Under half-space homogenous assumption for soil (which is an assumption commonly used, as can be argued from previous

references), Green's function can be directly determined from the half-space Fresnel reflection coefficients [9]. Of course, from the Fresnel coefficients soil properties can be inferred as well, but as said above this step is not required for imaging. However, it is remarked that following this new perspective requires to retrieve the reflection coefficients not only as a function of the time frequency but also as a function of the spatial frequencies (i.e., for different angles of incidence).

Recently, in [10] a new estimation method, which achieves such a task, was proposed. There, proximal GPR measurements, collected at different positions, were exploited to develop an estimation method based on multiview (multi-offset) information. Therefore, far-zone approximation were no longer necessary. More precisely, the problem is cast as the inversion of a linear integral operator linking the reflected field and the Fresnel reflection coefficients. When such a problem is solved, an estimation of the reflection coefficient is available for different angle of incidence but for a fixed-time frequency. Therefore, the procedure must be run for each adopted frequency. However, this inconvenient is not too critical, as to image shallowly buried scatterers the number of necessary frequency can be not so high [11, 12] and is traded off by the advantage that soil dispersive laws are not required.

The method presented in [10] was first developed and numerically validated by considering two-dimensional scalar cases. Then, the procedure was extended to three-dimensional cases where reflection coefficient is indeed a matrix. Therefore, in that cases the problem was cast as the inversion of a linear integral operator where the relevant unknowns (i.e., the Fresnel coefficients) appear embedded within a dyad. As shown in [13], depending on antennas' polarization, this gives rise to different strategies for achieving the solution.

However, in that contribution, reflected field measurements were considered as data, instead, in practical cases, what is actually measured is the voltage signal and not the field. Hence, the estimation scheme must account also for the role of the receiving antenna. This is just the further step towards a more realistic scenario done in this paper.

The plan of the paper is the following. In Section 2, we describe the adopted measurement configuration and introduce the problem mathematical formulation. In Section 3, the procedure for retrieving the Fresnel reflection coefficients is introduced, whereas in Section 4 numerical results are reported for different types of soil. Conclusions follow.

2. Geometry and Problem Formulation

The scattering problem depicted in Figure 1 is of concern.

The scenario consists of a two-layered medium separated by a planar interface at $z = 0$. The upper layer is assumed to be the free-space with ϵ_0 and μ_0 being its dielectric permittivity and magnetic permeability, respectively. The

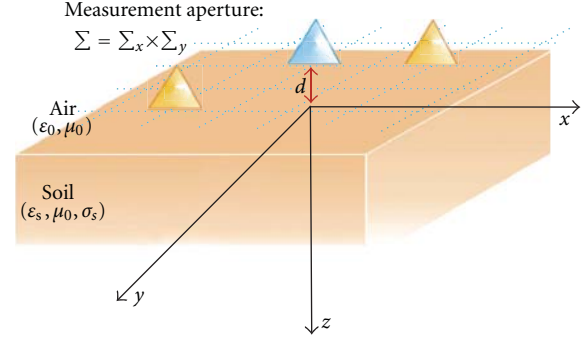


FIGURE 1: Geometry of the problem.

lower half-space is representative of the soil which is assumed nonmagnetic (i.e., its magnetic permeability is equal to the one of free space) and homogeneous with a relative dielectric permittivity and electric conductivity, denoted as ϵ_s and σ_s , respectively.

Accordingly, in the frequency domain the dielectric permittivity is actually a complex function which depends on the angular frequency ω and thus the relative equivalent permittivity is given by $\epsilon_{eq}(\omega) = \epsilon_s(\omega) - j\sigma_s/\omega$.

The transmitting antenna is located in the upper half-space at height d from the air/soil interface in $P = (x_s, y_s, -d)$. It is assumed that it is far enough so that the effect of the soil on the antenna radiation properties is negligible or a proper gating procedure, as suggested in [14], is employed before the estimation takes place.

We consider a multistatic measurement configuration where the reflected field is collected over a set of different positions taken over the observation domain $\Sigma = \Sigma_x \times \Sigma_y$ which is parallel to the air/soil interface and located at the same height as the source. $\Sigma_x = [-X_O, X_O]$ and $\Sigma_y = [-Y_O, Y_O]$ are the extent of the observation domain along the x - and y -axes, respectively.

As discussed in the Introduction, we aim at retrieving Fresnel reflection coefficients from reflected field measurements. Moreover, this must be achieved for all the relevant spatial harmonics as these are necessary for Green's function determination for a subsequent imaging stage.

Accordingly, it is natural to express the link between the reflected field, $\underline{E}_r(x_O, y_O, k_0)$, and the reflection coefficients, in terms of plane-wave spectrum notation, that is,

$$\begin{aligned} \underline{E}_r(x_O, y_O, k_0) &= \frac{1}{(2\pi)^2} \iint_D \underline{\Gamma}(k_x, k_y, k_0) \underline{f}_S(k_x, k_y, k_0) \\ &\quad \times \exp[-jk_x(x_O - x_s)] \exp[-jk_y(y_O - y_s)] \\ &\quad \times \exp(-j2k_z d) dk_x dk_y, \end{aligned} \quad (1)$$

where $\underline{\Gamma}(k_x, k_y, k_0)$ is the dyadic reflection coefficient at the air/soil interface [13]:

$$\underline{\Gamma}(k_x, k_y, k_0) = \begin{bmatrix} \left(\Gamma_{\text{TE}} \frac{k_y^2}{k_t^2} + \Gamma_{\text{TM}} \frac{k_x^2}{k_t^2} \right) & \left(\Gamma_{\text{TM}} \frac{k_x k_y}{k_t^2} - \Gamma_{\text{TE}} \frac{k_x k_y}{k_t^2} \right) & 0 \\ \left(\Gamma_{\text{TM}} \frac{k_x k_y}{k_t^2} - \Gamma_{\text{TE}} \frac{k_x k_y}{k_t^2} \right) & \left(\Gamma_{\text{TE}} \frac{k_x^2}{k_t^2} + \Gamma_{\text{TM}} \frac{k_y^2}{k_t^2} \right) & 0 \\ 0 & 0 & -\Gamma_{\text{TM}} \end{bmatrix} \quad (2)$$

Γ_{TE} and Γ_{TM} are the Fresnel reflection coefficients, $\underline{f}_S = (f_x, f_y, f_z)$ is the source plane-wave spectrum, k_x, k_y, k_z are the wavenumber components corresponding to x, y, z , respectively, and $k_t^2 = k_x^2 + k_y^2$. Finally, $k_0 = \omega \sqrt{\epsilon_0 \mu_0}$ is the free-space wavenumber.

Note that in (1) the spectral integration interval D corresponds to the minimum square enclosing the circle of radius k_0 which accounts for the so-called ‘‘visible domain.’’

Equation (1) represents the link to be inverted in order to retrieve reflection coefficients. In particular, it should be solved for Γ_{TE} and Γ_{TM} which appear embodied within $\underline{\Gamma}$.

A way to achieve such a task has been described in [13]. That paper reports promising results but has to be meant as a proof of principle. Indeed, the inversion of (1) relies on field measurements whereas what can be actually measured is antenna output voltage. In other words, the role of receiving antenna has to be accounted for and (1) properly modified.

To this end, here, a simple truncated waveguide is considered as transmitting and receiving antenna. In particular, the source point $x_s, y_s, -d$ and the observation point $x_o, y_o, -d$ correspond to the centre of the antenna apertures. For convenience, we also introduce a local reference frame x', y', z' (see Figure 2) to address points within the antenna aperture for each antenna position.

By neglecting finite aperture effects and by assuming that the guide is matched, then the field at the antenna terminal section $z' = 0$ (for each receiving antenna positions) is just the incoming field reflected by the soil $\underline{E}_r(x', y', 0)$.

Hence, we can write the ‘‘voltage’’ at $z' = 0$ associated to the waveguide fundamental mode as [15]

$$V_{10}^{\text{TE}}(0) = \iint_S \underline{E}_r(x', y', 0) \times \underline{h}_{10}^{\text{TE}} \cdot \hat{i}_{z'} dS \quad (3)$$

In particular, if the working frequency is properly chosen and L sufficiently greater than the wavelength (see Figure 2), this is the only relevant contribution at the reference plane in $z' = -L$ as high-order modes are in cutoff.

Accordingly, the voltage at the reference section writes as

$$V = V_{10}^{\text{TE}}(0) \exp(-ik'_z L), \quad (4)$$

where $k'_z = \sqrt{k_0^2 - (\pi/a)^2}$ being the z -component of the waveguide wavevector.

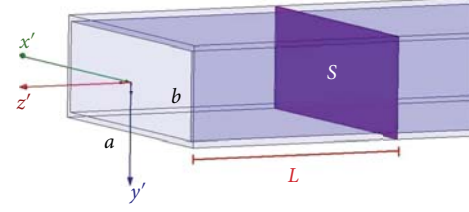


FIGURE 2: Truncated waveguide antenna.

Eventually, the relationship upon which the estimation procedure is based is obtained by inserting (1) in (4); that is

$$\begin{aligned} V(x_o, y_o, k_0) &= \exp(-ik'_z L) \\ &\times \iint_S \frac{1}{(2\pi)^2} \iint_D \underline{\Gamma}(k_x, k_y, k_0) \\ &\times \underline{f}_S(k_x, k_y, k_0) \times \underline{h}_{10}^{\text{TE}} \\ &\times \exp[-jk_x(x' + x_o - x_s)] \\ &\times \exp[-jk_y(y' + y_o - y_s)] \\ &\times \exp(-j2k_z d) dk_x dk_y dS. \end{aligned} \quad (5)$$

3. Estimation Procedure

In this section we introduce the procedure to estimate Γ_{TE} and Γ_{TM} (embedded in the coefficients of $\underline{\Gamma}$) starting from voltage measurements taken at a grid of points over Σ .

To this end, different inversion strategies can be employed to invert (5) and de-embed Γ_{TE} and Γ_{TM} from $\underline{\Gamma}$ [13]. Basically, by changing the polarization of the transmitting and/or the receiving antennas, a couple of linear integral equations are obtained whose solution gives two different parameters of the reflection matrix (2). Hence, from these two independent equations, the Fresnel coefficients are obtained.

Here, we adopt the strategy depicted in Figure 3. In particular, the two needed voltage measurements (for each observation point) are obtained by considering first the transmitting and receiving antennas polarized along the x -axis. Accordingly, (5) particularizes as

$$\begin{aligned} V_1(x_o, y_o, k_0) &= \frac{1}{(2\pi)^2} \sqrt{\frac{2}{ab}} \iint_D \Gamma_{11}(k_x, k_y, k_0) f_x^2(k_x, k_y, k_0) \\ &\times \exp[-jk_x(x_o - x_s)] \\ &\times \exp[-jk_y(y_o - y_s)] \exp(-j2k_z d) \\ &\times \exp(-jk'_z L) dk_x dk_y, \end{aligned} \quad (6)$$

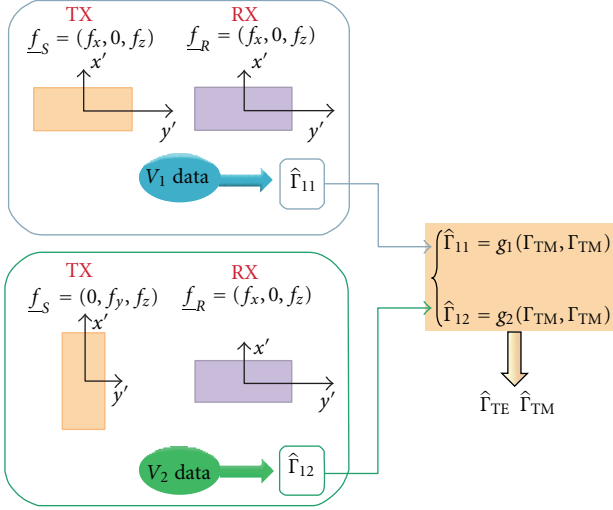


FIGURE 3: Illustrating the overall estimation procedure.

where we considered that $\underline{f}_S = \underline{f}_R = (f_x, 0, f_z)$, Γ_{11} is the (1,1) entry of $\underline{\Gamma}$, a and b are the guide transverse dimensions (with $a > b$), and $\underline{k}_t = (k_x, k_y, 0)$.

The second equation is obtained by rotating the transmitting antenna of 90 degrees so that it results to be polarized along the y -axis; that is, $\underline{f}_S = (0, f_y, f_z)$. In this case (5) becomes

$$\begin{aligned}
 V_2(x_O, y_O, k_0) &= \frac{1}{(2\pi)^2} \sqrt{\frac{2}{ab}} \iint_D \Gamma_{12}(k_x, k_y, k_0) f_x^2(k_x, k_y, k_0) \\
 &\quad \times \exp[-jk_x(x_O - x_S)] \\
 &\quad \times \exp[-jk_y(y_O - y_S)] \\
 &\quad \times \exp(-j2k_z d) \\
 &\quad \times \exp(-jk'_z L) dk_x dk_y,
 \end{aligned} \tag{7}$$

where now the term Γ_{12} of $\underline{\Gamma}$ is involved.

We have now a pair of integral equations whose inversion returns an estimation for $\Gamma_{11}(\cdot)$ and $\Gamma_{21}(\cdot)$, that is, $\hat{\Gamma}_{11}(\cdot)$ and $\hat{\Gamma}_{21}(\cdot)$, from which, according to (2), the Fresnel reflection coefficients can be obtained via algebraic relations as

$$\begin{aligned}
 \hat{\Gamma}_{TE}(k_x, k_y, k_0) &= \frac{\Gamma_1(k_x, k_y, k_0) - k_x^2 \Gamma_2(k_x, k_y, k_0)}{k_t^2}, \\
 \hat{\Gamma}_{TM}(k_x, k_y, k_0) &= \frac{\Gamma_1(k_x, k_y, k_0) + k_y^2 \Gamma_2(k_x, k_y, k_0)}{k_t^2},
 \end{aligned} \tag{8}$$

where $\Gamma_1(\cdot) = k_t^2 \hat{\Gamma}_{11}(\cdot)$, $\Gamma_2(\cdot) = (k_t^2/k_x k_y) \hat{\Gamma}_{21}(\cdot)$, $\hat{\Gamma}_{TE}(\cdot)$ and $\hat{\Gamma}_{TM}(\cdot)$ are the estimated Fresnel reflection coefficients.

In this plan, the inversion of the two integral equations (6) and (7) is crucial in order to get a reasonable reflection

coefficient estimations. In particular, since such operators are compact, the corresponding inversion is an ill-posed inverse problem [16]. Accordingly, a suitable inversion scheme has to be adopted to establish a proper compromise between accuracy and stability against uncertainties. To cope with this point, inversions are achieved by exploiting the truncated singular value decomposition (SVD) method [16]. Details concerning the singular value threshold N_T , the number of required measurements and unknown representation (to obtain discrete counterparts of (6) and (7)), and noise propagation can be found in [13]. Here, we report only the relevant equations. On denoting as $\{u_n, v_n, \sigma_n\}_{n=0}^{\infty}$ the singular system of one of the involved integral operators, where u_n , v_n , and σ_n are the n th left singular function, the n th right singular function, and the n th singular value, respectively, the corresponding solutions can be expressed as

$$\begin{aligned}
 \hat{\Gamma}_{11}(k_x, k_y, k_0) &= \sum_{n=0}^{N_T} \frac{\langle V_1, v_n \rangle}{\sigma_n} u_n, \\
 \hat{\Gamma}_{21}(k_x, k_y, k_0) &= \sum_{n=0}^{N_T} \frac{\langle V_2, v_n \rangle}{\sigma_n} u_n.
 \end{aligned} \tag{9}$$

We end this section by remarking that (8) allows to retrieve the Fresnel coefficient as a function of the spectral angular variables and for a fixed frequency. When more frequency are needed, as usually occurs during imaging, the procedure outlined above must be repeated for each adopted frequency.

4. Numerical Results

In this section, we report some numerical reconstructions obtained by exploiting synthetic data with the aim to assess the performance achievable by the estimation procedure. The source is located at $\underline{r}_S = (0, 0, -d)$, with $d = 0.1$ m, whereas receiving antenna span a grid of $N_x \times N_y = 20 \times 20$ points taken uniformly over the observation domain $\Sigma = [-X_O, X_O] \times [-Y_O, Y_O] = [-1, 1] \times [-1, 1] \text{ m}^2$ and a frequency $f = 1.5$ GHz is adopted.

The waveguide transverse dimensions are $a = 0.16$ m, $b = 0.08$ m whereas the reference plane is fixed at $h = 0.1$ m from the aperture.

We consider three kinds of soil addressed for convenience, in the following, as soil 1, soil 2, and soil 3. More in detail, soil 1 is characterized by $\epsilon_{\text{eq}} = 4\epsilon_0$, hence describes a nondissipative as well as nondispersive medium; soil 2 accounts for Ohmic losses, hence $\epsilon_{\text{eq}} = 4\epsilon_0 - j(0.1/\omega)$; finally soil 3 considers both Ohmic losses and dielectric hysteretic behaviours so that $\epsilon_{\text{eq}}(\omega)/\epsilon_0 = \epsilon_\infty - j(\sigma_S/\omega\epsilon_0) + ((\epsilon_S - \epsilon_\infty)/(1 + j\omega\tau_e))$ with $\epsilon_\infty = 4$, $\epsilon_S = 16$, $\sigma_S = 0.1$ S/m, and $\tau_e = 64$ ns. Moreover, in order to test the procedures for data corrupted by noise, some examples are obtained by adding, to both voltage data, a complex zero mean white Gaussian noise n so as to have a SNR = $20 \log(\|V_{1,2}\|/\|n\|) = 30$ dB.

The reconstructions corresponding to the three types of soil are reported in Figures 4 and 5, Figures 6 and 7, Figures 8 and 9, respectively. In those figures, for comparison purposes, beside being noiseless and noisy estimations also actual Fresnel reflection coefficients are shown.

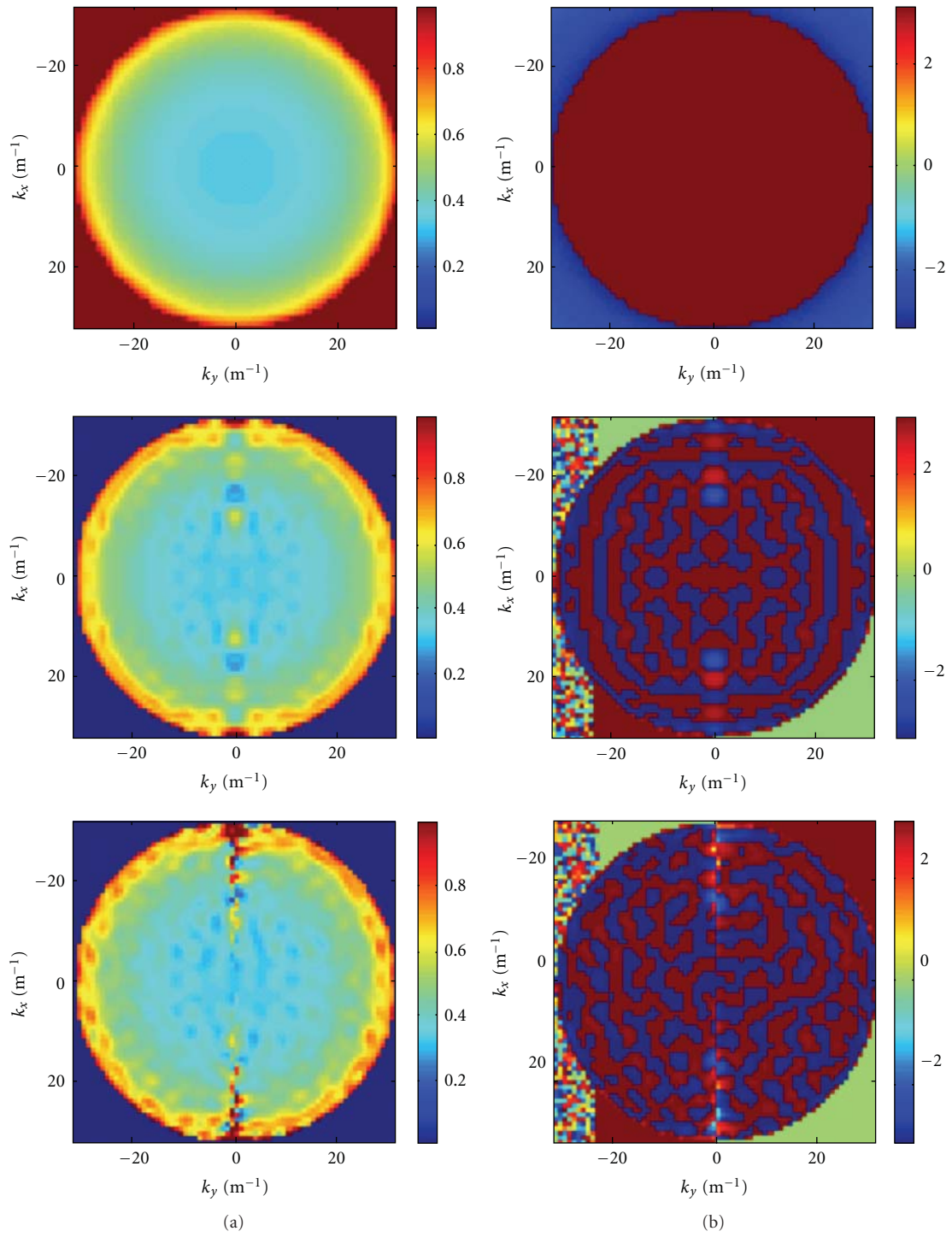


FIGURE 4: Soil 1. Amplitude (a) and phase (b) of Γ_{TE} . Top line: actual values; middle line: noiseless estimation; bottom line: noisy estimation.

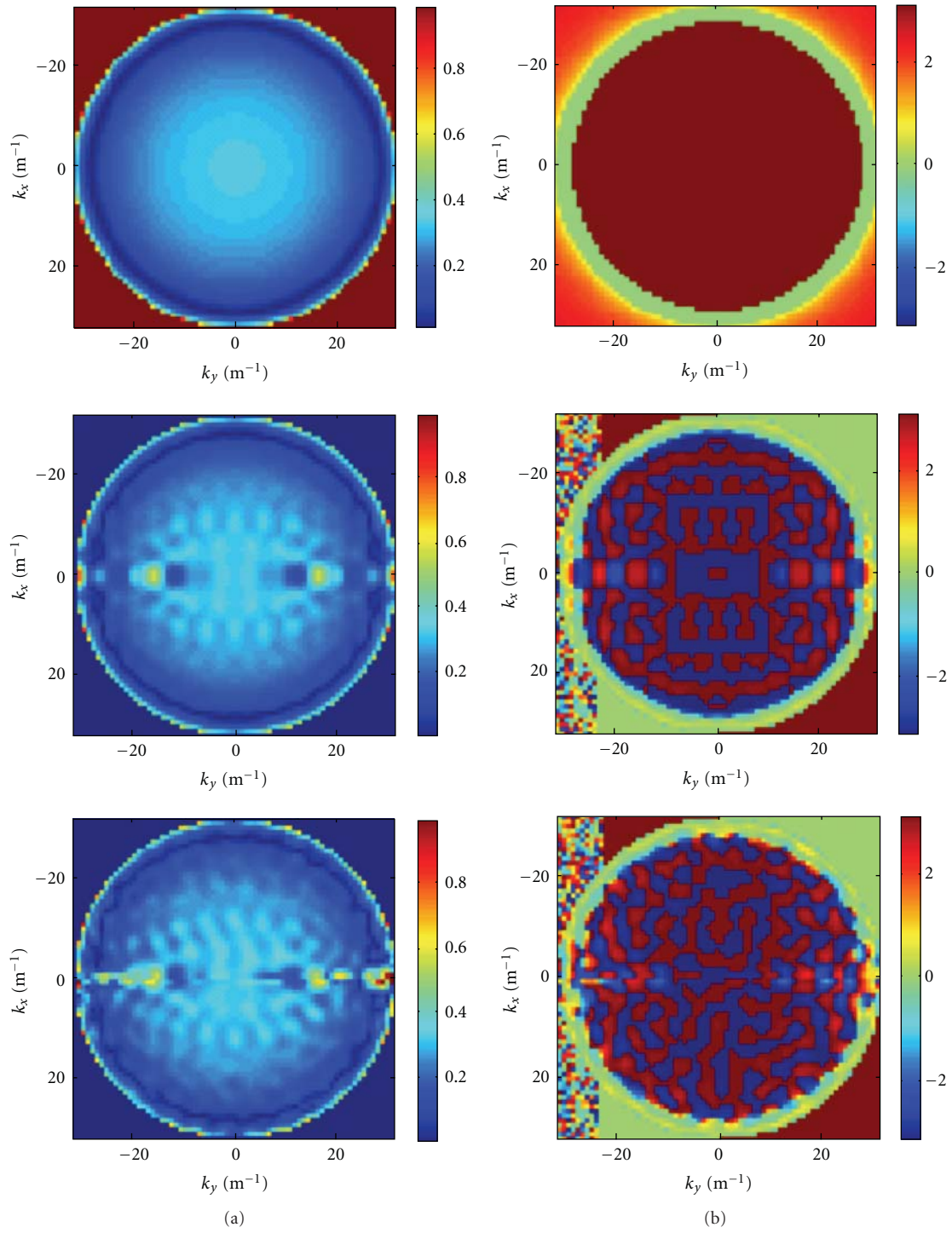


FIGURE 5: Soil 1. Amplitude (a) and phase (b) of Γ_{TM} . Top line: actual values; middle line: noiseless estimation; bottom line: noisy estimation.

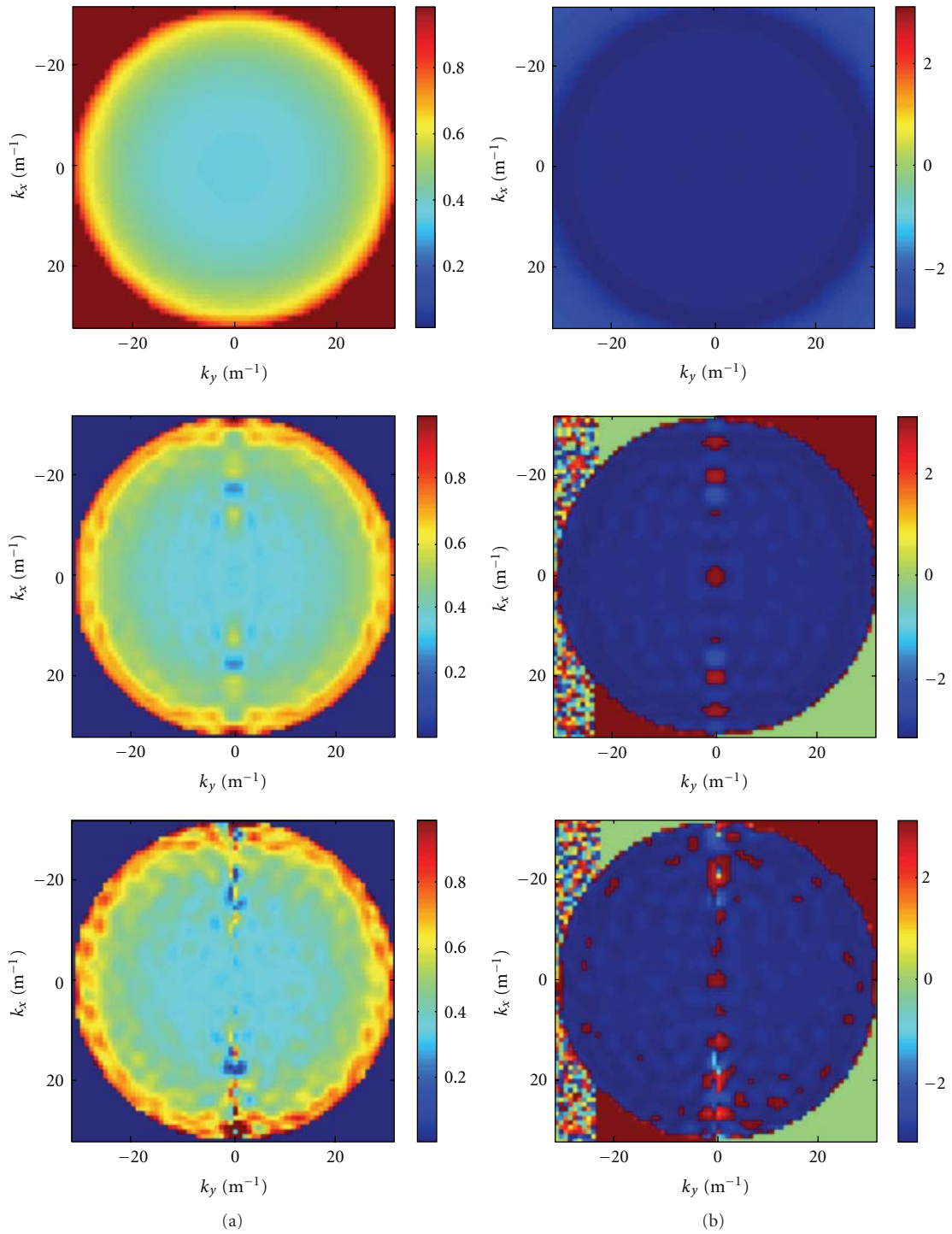


FIGURE 6: Soil 2. Amplitude (a) and phase (b) of Γ_{TE} . Top line: actual values; middle line: noiseless estimation; bottom line: noisy estimation.

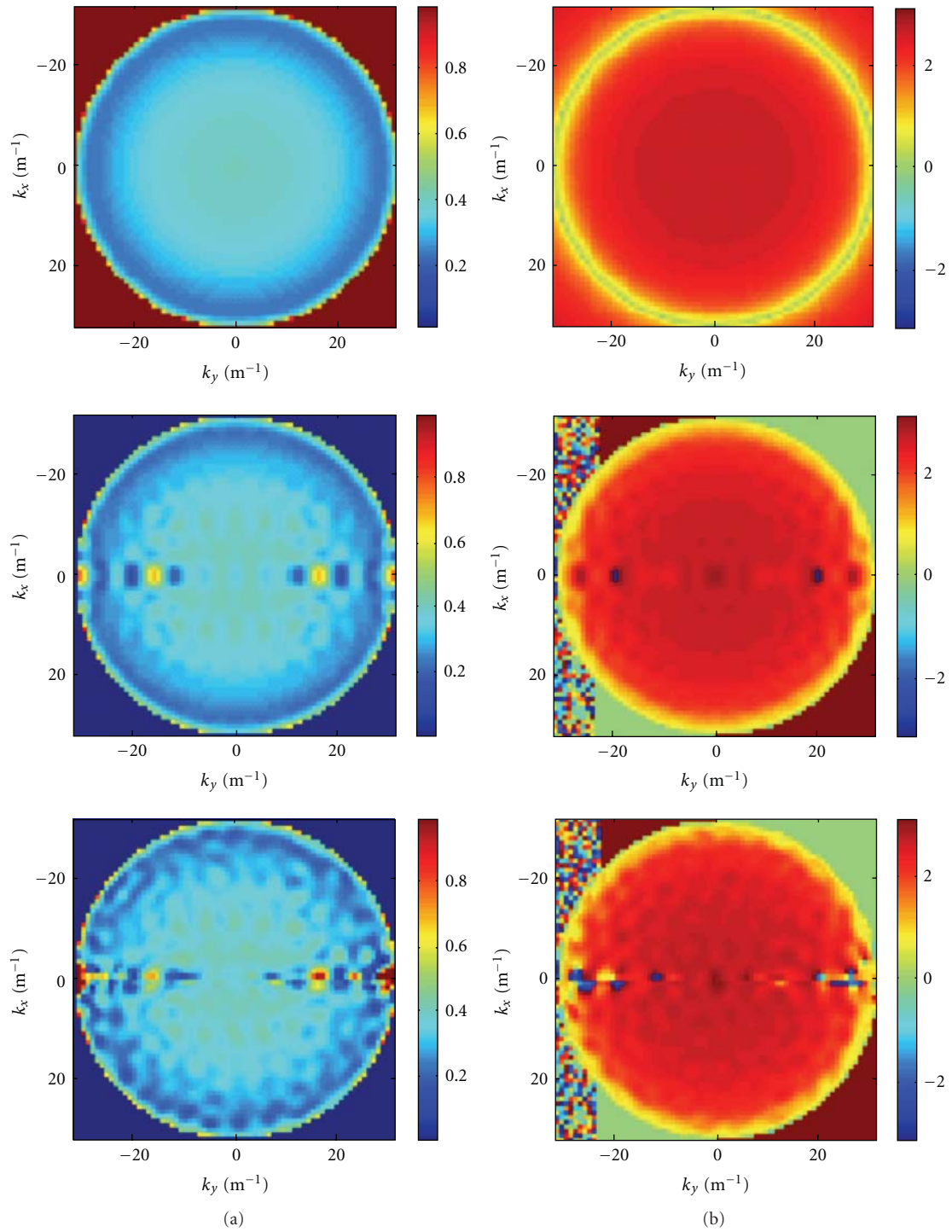


FIGURE 7: Soil 2. Amplitude (a) and phase (b) of Γ_{TM} . Top line: actual values; middle line: noiseless estimation; bottom line: noisy estimation.

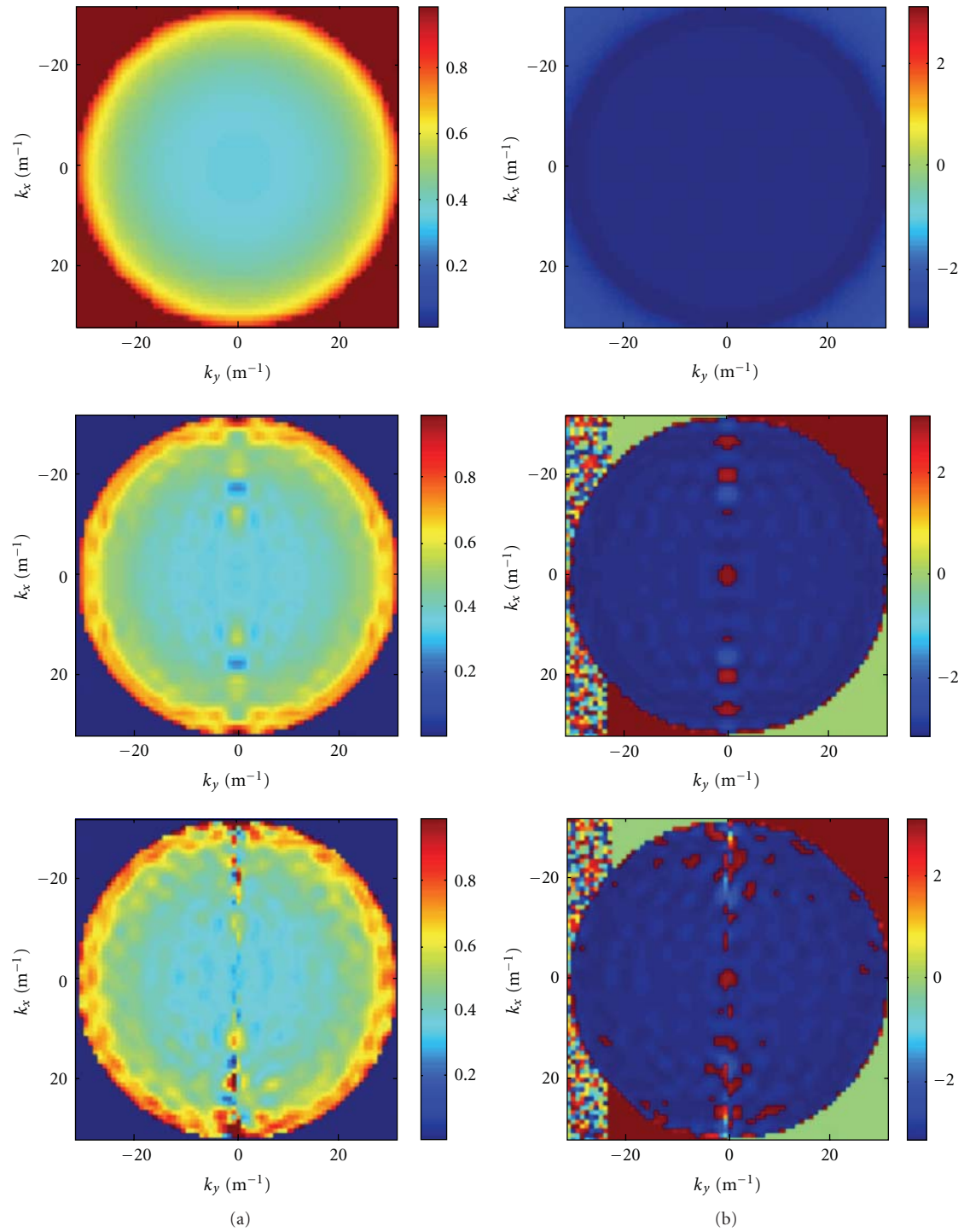


FIGURE 8: Soil 3. Amplitude (a) and phase (b) of Γ_{TE} . Top line: actual values; middle line: noiseless estimation; bottom line: noisy estimation.

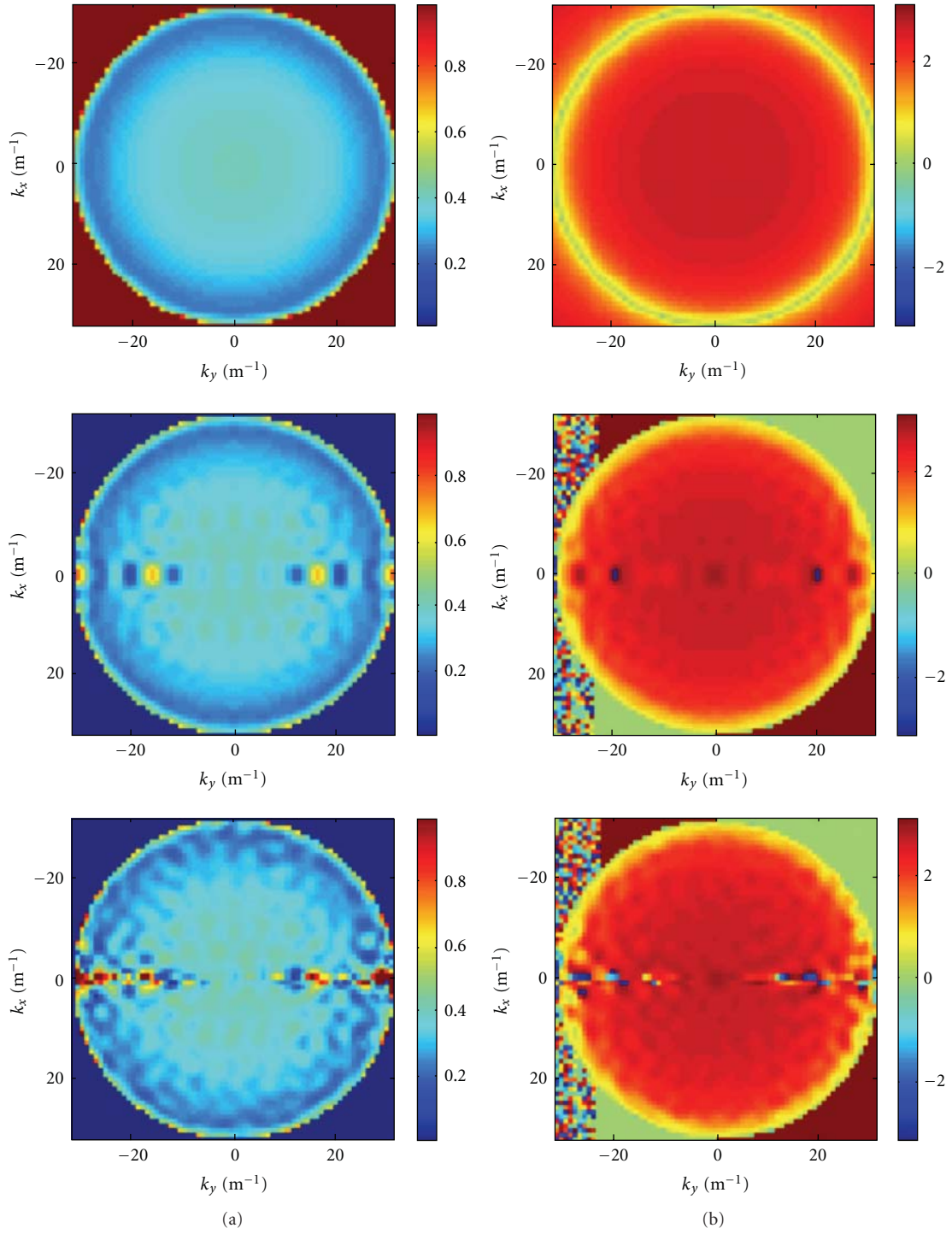


FIGURE 9: Soil 3. Amplitude (a) and phase (b) of Γ_{TM} . Top line: actual values; middle line: noiseless estimation; bottom line: noisy estimation.

By comparing actual and estimated coefficients, it can be noted that in all the cases estimation fails outside the visible domain whereas inside that domain some oscillations appear. This could be expected as they result from regularization, we applied through (9) to invert (6) and (7), which entails retrieving a filtered version of the unknown. By contrast, reconstructions appear rather “stable” against noise. More in detail, estimations fit well actual reflection coefficients expect along the lines at $k_y = 0$ for Γ_{TE} and $k_x = 0$ for Γ_{TM} . This is due to the “numerical” singularities that (8) introduce while passing from the retrieved scattering parameters $\hat{\Gamma}_{11}(\cdot)$ and $\hat{\Gamma}_{21}(\cdot)$ to the Fresnel coefficients. However, this drawback can be circumvented by getting rid estimation along the “singular” lines and replacing such values by some interpolation scheme.

5. Conclusions

In this contribution, we extended our previous work concerning the Fresnel reflection coefficients estimation from reflected field data [13] by including also the role of the receiving antenna.

It is shown that, even in the case of homogeneous soil, the corresponding mathematical problem is rather interesting as it amounts to solving a vector linear integral equation where the unknowns, the Fresnel coefficients, appear embodied within a dyadic term. To solve such a problem a two-step procedure is used. First, a pair of half-space scattering parameters are determined by inverting two integral equations by means of the TSVD scheme. Then, Fresnel reflection coefficients are easily estimated by algebraic equations.

The method allows to retrieve the Fresnel coefficients as function of the angle of incidence (spatial harmonics); therefore it can be used to build up Green’s function which is what is really necessary to obtain focalized subsurface images. The estimation procedure must be run for each adopted frequency. By contrast soil dispersive laws are not required to be a priori known.

Numerical results are used to show the effectiveness of estimation proposed procedure for different and typical kinds of soil. Except for certain numerical singularities, estimation’s fits well the actual reflection coefficient within the visible domain, which in turn generally is prominent contribution with respect to the evanescent waves.

References

- [1] D. Daniels, *Ground Penetrating Radar*, IEE Press, London, UK, 2nd edition, 2004.
- [2] F. Soldovieri and R. Solimene, “Ground penetrating radar subsurface imaging of buried objects,” in *Radar Technology*, G. Kouemou, Ed., In-Tech, 2010.
- [3] D. A. Robinson, “Measurement of the solid dielectric permittivity of clay minerals and granular samples using a time-domain reflectometry immersion method,” *Vadose Zone Journal*, vol. 3, no. 2, pp. 705–713, 2004.
- [4] A. P. Annan, *Ground Penetrating Radar Workshop Notes*, Sensors & Software, Mississauga, Canada, 2001.
- [5] X. Zeng, G. A. McMechan, and T. Xu, “Synthesis of amplitude-versus-offset variations in ground-penetrating radar data,” *Geophysics*, vol. 65, no. 1, pp. 113–125, 2000.
- [6] J. Deparis and S. Garambois, “On the use of dispersive APVO GPR curves for thin-bed properties estimation: theory and application to fracture characterization,” *Geophysics*, vol. 74, no. 1, pp. J1–J12, 2009.
- [7] F. Soldovieri, G. Prisco, and R. Persico, “A strategy for the determination of the dielectric permittivity of a lossy soil exploiting GPR surface measurements and a cooperative target,” *Journal of Applied Geophysics*, vol. 67, no. 4, pp. 288–295, 2009.
- [8] S. Lambot, E. C. Slob, I. van den Bosch, B. Stockbroeckx, B. Scheers, and M. Vanclooster, “Estimating soil electric properties from monostatic ground-penetrating radar signal inversion in the frequency domain,” *Water Resources Research*, vol. 40, no. 4, pp. W042051–W0420512, 2004.
- [9] P. Meincke and T. B. Hansen, “Plane-wave characterization of antennas close to a planar interface,” *IEEE Transactions on Geoscience and Remote Sensing*, vol. 42, no. 6, pp. 1222–1232, 2004.
- [10] R. Solimene, F. Soldovieri, and A. D’Alterio, “Determination of the fresnel reflection coefficient of a half-space for medium estimation purposes,” *Progress in Electromagnetics Research B*, no. 27, pp. 61–82, 2011.
- [11] R. Persico, F. Soldovieri, and G. Leone, “A microwave tomographic imaging approach for multibistatic configuration: the choice of the frequency step,” *IEEE Transactions on Instrumentation and Measurement*, vol. 55, no. 6, pp. 1926–1934, 2006.
- [12] R. Solimene, F. Ahmad, and F. Soldovieri, “A novel CS-TSVD strategy to perform data reduction in linear inverse scattering problems,” *IEEE Geoscience and Remote Sensing Letters*, vol. 9, no. 5, pp. 881–885, 2012.
- [13] R. Solimene, A. D’Alterio, and F. Soldovieri, “Determining Fresnel reflection coefficients in 3D half-space geometry by GPR multistatic data,” *Near Surface Geophysics*, vol. 9, no. 3, pp. 265–275, 2011.
- [14] R. Solimene, A. D’Alterio, and F. Soldovieri, “Half-space estimation by time gating based strategy,” in *Proceedings of the 13th International Conference on Ground Penetrating Radar (GPR ’10)*, pp. 683–687, Lecce, Italy, June 2010.
- [15] R. E. Collin, *Antennas and Radiowave Propagation*, McGraw-Hill, New York, NY, USA, 1985.
- [16] M. Bertero and P. Boccacci, *Introduction to Inverse Problems in Imaging*, IOP, Bristol, UK, 1998.

Research Article

Antipodal Vivaldi Antenna for Water Pipe Sensor and Telemetry

Giuseppe Ruvio, Domenico Gaetano, Max J. Ammann, and Patrick McEvoy

Antenna & High Frequency Research Centre, Dublin Institute of Technology, Kevin Street, Dublin 8, Ireland

Correspondence should be addressed to Giuseppe Ruvio, giuseppe.ruvio@dit.ie

Received 20 March 2012; Accepted 5 May 2012

Academic Editor: Francesco Soldovieri

Copyright © 2012 Giuseppe Ruvio et al. This is an open access article distributed under the Creative Commons Attribution License, which permits unrestricted use, distribution, and reproduction in any medium, provided the original work is properly cited.

An antipodal Vivaldi antenna operates simultaneously for telemetry and sensing when placed conformally onto PVC pipes. Good radiation efficiency is realised and the antenna impedance matching remains stable when a pipe is empty or contains water. The fidelity factor performance based on an input Ultra-Wideband Gaussian pulse is a suitable figure of merit to detect water presence. Different water levels and pipe conditions correspond to fidelity factors between 90% and 96%, which are a suitable dynamic range for sensing and the appropriate quality for pulse communications for remote monitoring.

1. Introduction

Monitoring pipe systems represents a major problem where continuous information on the liquid content must be constantly provided. This is the case for water leakage sensor networks or for stormwater detection in critical drainage system. Several technologies were proposed in the literature for these applications such as tracer gases and thermography [1]. Furthermore, ultrasound sensors have been proposed for accurate detection and localisation of leakages in buried water pipes [2, 3]. Acoustic wave monitoring is widely used in leak detection but they are concerns in terms of time response, robustness, reliability, accuracy, and costs. Radio-frequency telemetry has been more recently introduced to localize leaks and malfunctioning pipelines. In particular, Ground Penetrating Radar (GPR) systems can be efficiently designed to image subsurface scattering leaks by using low-frequency electromagnetic (EM) waves [4, 5]. However, due to their cost and characteristics, GPR is suitable for extraordinary maintenance. EM sensors revealing wave propagation distortion inside metallic pipes have been recently proposed [6]. Although reflections coming from leaks/cracks can be promptly identified by EM propagating mode monitoring, this technique is restricted to a limited number of applications and scenarios.

High data rates and low-power requirements make Ultra-Wideband (UWB) technology largely used for short-range

wireless communication and sensor systems. With a large operating spectrum, short pulses can be generated. UWB sensors can then monitor pulse distortion and identify the associated environmental changes. Operating in the time domain implies the design of novel figures of merit to characterize UWB impulse radio systems. The signal purity in particular can be used to assess the time domain performance of the UWB front-end for antenna and sensor operative scenarios. This can be measured in terms of fidelity factor, which estimates the distortion of the received signal with respect to the original transmitted signal. This paper introduces a conformal antipodal Vivaldi antenna operating in the UWB range to be placed on Polyvinyl Chloride (PVC) pipes. This UWB directional antenna has been designed to fit onto a curved surface of a circular cross-section pipe for communication between flow rate meter devices [7]. The use of wireless monitoring technology to aid fluid flow control can improve reliability, reduce costs, and save space. This was proposed in [8] where an acoustic sensor is combined with to a radiotransmitter which communicates with an external gateway.

In this paper, an innovative UWB antenna for both sensing and data transmission is proposed for pipe telemetry applications. A preliminary study of the pipe proximity effects on a directional UWB antenna in the frequency domain [9] is extended by a thorough time domain analysis. Four standard PVC pipes have been numerically evaluated

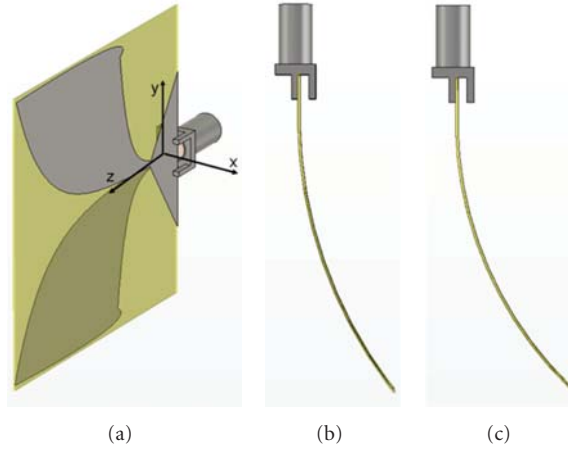


FIGURE 1: Antipodal Vivaldi antenna geometry and coordinate system; (a) flat configuration; (b) bent on 141.2 mm diameter of curvature; bent on 114.3 mm diameter of curvature.

for different water content levels using the finite integration time domain technique (CST Microwave Studio [10]). Numerical results show that the conformal antipodal Vivaldi antenna is suitable for sensing the water level inside the pipe and for simultaneous transmission to an external metering station. These combined operations lead to significant simplification and cost saving for the metering system. In particular, the fidelity factor is shown to be a convenient metric to sense changes in water presence and to assess radiation properties. The time domain performance of the system is assessed by calculating the fidelity of the received pulse at a number of probes circularly distributed around the antenna in the H -plane with a 5° step. The quality of a received pulse through the antenna system and the RF channel can be evaluated by using the following expression [11]:

$$FF = \max_{\tau} \int_{-\infty}^{\infty} L[p_{\text{source}}(t)] p_{\text{output}}(t - \tau) dt, \quad (1)$$

where the source pulse $p_{\text{source}}(t)$ and output pulse $p_{\text{output}}(t)$ are normalised by their energy, respectively. The fidelity factor FF is the maximum integration by varying time delay τ . The linear operator $L[\cdot]$ describes the system transformation occurring in the input signal $p_{\text{source}}(t)$. In this case, as the transmit antenna is a Vivaldi type, a differentiation of the source pulse occurs [12] and the operator $L[\cdot]$ corresponds to $d[\cdot]/dt$.

The operating scenario is envisioned as follows. The pipe mounted antenna/sensor communicates to a UWB IEEE 802.15.4 node which can also be integrated in a Wi-Fi access point (AP). The UWB range is dependent on the data bandwidth, which in this case can be quite small, allowing a range of tens of meters. The position of antennas on the pipe should be considered in relation to the AP location.

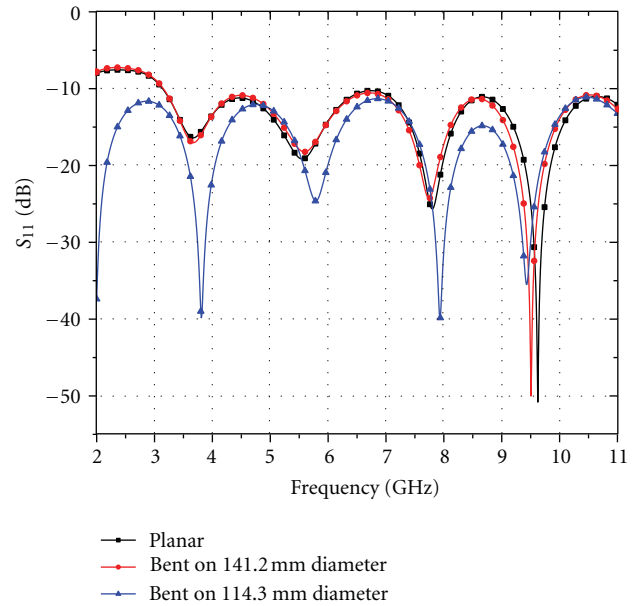


FIGURE 2: S_{11} of free-space planar and conformal antenna.

2. Antipodal Vivaldi Antenna and Testing Environment

An antipodal Vivaldi antenna was designed to operate across the FCC UWB spectrum (3.1–10.6 GHz) when mounted on a pipe surface. The antenna is double-side printed on 0.375 mm thin Duroid 5870 dielectric substrate ($\epsilon_r = 2.33$, loss tangent = 0.0012) with overall dimensions 50×53 mm. This dielectric material was chosen for its stable electrical properties combined with mechanical flexibility that permits the antenna to be curved on a surface of a cylindrical object. Figure 1(a) shows the antenna geometry and the coordinate system. The tapered antenna aperture generates multiple resonances resulting in

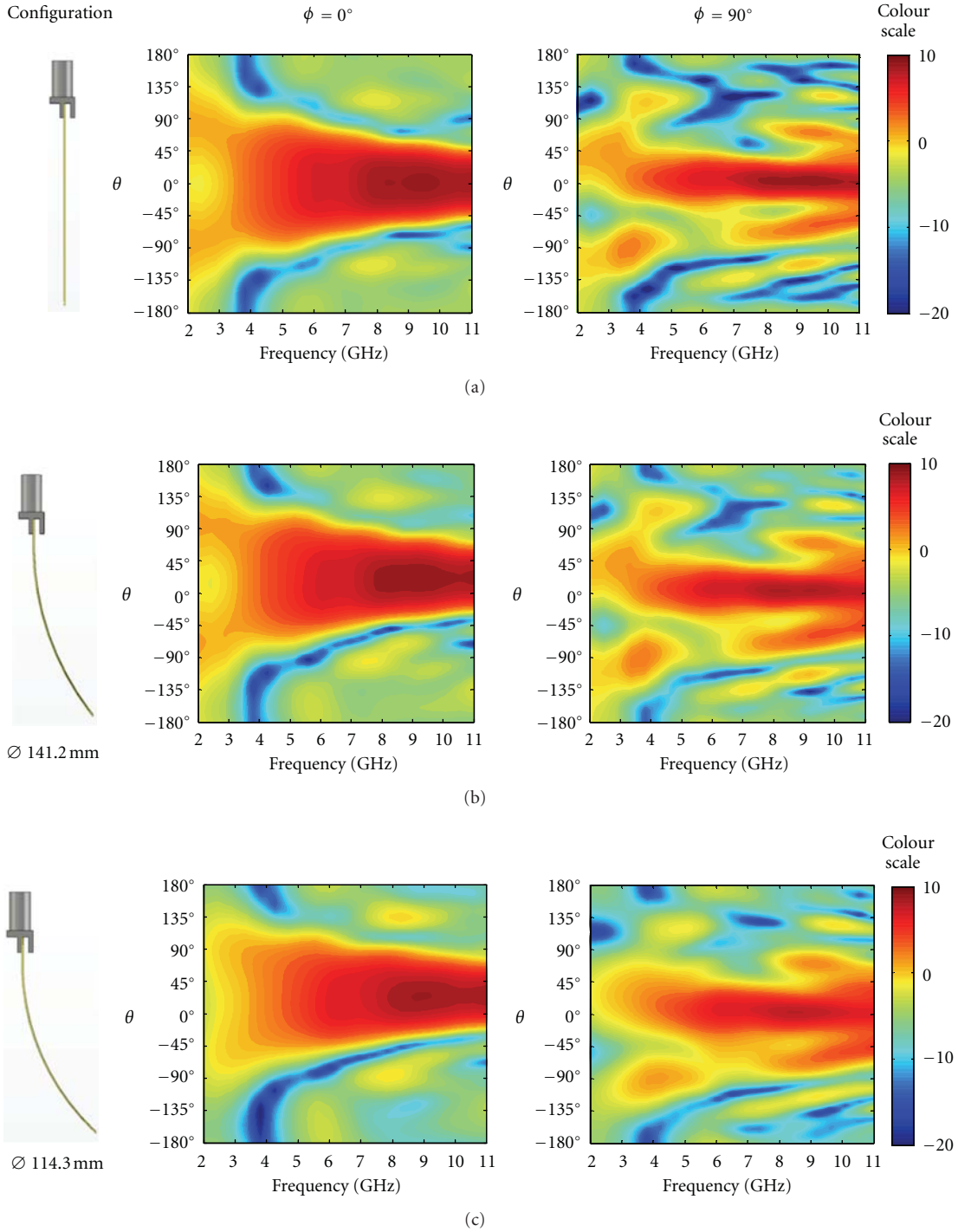


FIGURE 3: 2-D radiation patterns (dBi) of (a) the planar antenna in free space for $\phi = 0^\circ$ (first column) and $\phi = 90^\circ$ (second column); (b) the conformal antenna to a 141.2 mm diameter of curvature in free space for $\phi = 0^\circ$ and $\phi = 90^\circ$; (c) the conformal antenna to a 114.3 mm diameter of curvature in free space for $\phi = 0^\circ$ and $\phi = 90^\circ$.

a continuous operating UWB bandwidth and a uniform end-fire directed radiation pattern. Figures 1(b) and 1(c) show the antenna curvature when the longitudinal axis of the pipe is rotated orthogonally to the antenna end-fire direction on 141.2 mm and 114.3 mm diameters of curvature, respectively.

In particular, the tapered line of the flare shape is described by two exponential curves given by (2) and then mirrored on the opposite side of the dielectric:

$$\begin{aligned}
 y &= 0.125 * e^{0.109z} \quad \text{for } 0 < z < 48.5 \text{ [mm]}, \\
 y &= 0.11 * e^{0.352z} \quad \text{for } 0 < z < 15 \text{ [mm]}
 \end{aligned}
 \tag{2}$$

TABLE 1: Pipe configurations investigated.

Pipe configuration	Diameter [mm]	Thickness [mm]
A	114.3	6.02
B	114.3	8.56
C	141.2	6.55
D	141.2	9.50

for the internal and external tapered profile of each flare, respectively.

In order to reduce the back lobe radiation, the exponential lines were connected with spline shapes [13]. Finally, a tapered microstrip feeding line was designed to secure a broadband $50\ \Omega$ impedance condition in the intersection point [14].

2.1. Free-Space Antenna Characteristics. The performance of this antipodal Vivaldi antenna shows it to be resilient to mechanical bending along the y -axis. Figure 2 shows the free-space S_{11} of the antenna in its flat and both curved configurations. The impedance matching expressed in terms of S_{11} remains stable across all configurations and below -10 dB over the complete UWB bandwidth.

Three-dimensional broadband free-space radiation patterns of the antenna in its flat and both curved configurations are shown in Figure 3. The patterns exhibit the same shape and high gain in the end-fire direction. Due to the antipodal configuration the beam in the $\phi = 90^\circ$ direction is not totally symmetrical. Bending the antenna affects the radiation pattern in its $\phi = 0^\circ$ cut as this corresponds to a rotation of the tapered line termination. As expected, by decreasing the diameter of curvature, the direction of maximum radiation moves from the $\theta = 0^\circ$ direction towards the angular range 20° – 30° . Moreover, significant radiation pattern stability can be observed across the entire FCC UWB band.

2.2. Pipe Characterization. Four different ASTM standard PVC pipes ($\epsilon_r = 2.9$; loss tangent = 0.086 at $f = 2$ GHz and 0.0182 at $f = 11$ GHz [15]) were considered and are summarized in Table 1 [16]. These dimensions are suitable for water and sanitary applications as well as stormwater drainage. The level to be detected has been characterised as “Empty” and “Full” for the pipe without and with water, respectively. The first-order Debye model with $\epsilon_{\text{static}} = 78.4$, $\epsilon_\infty = 3.1$, relaxation time $\tau = 8.27$ ps, and $\mu = 0.99$ has been used to model the dispersive behaviour of water.

2.3. Excitation Signal and Fidelity Factor Measurement. Choosing the excitation signal for the antenna is a very critical aspect of this analysis as the device is designed to operate as both sensor and transmitter. Several design factors need to be considered to select a suitable signal to feed the sensor/antenna:

- (i) antenna dimensions are inversely proportional to the lower edge frequency;

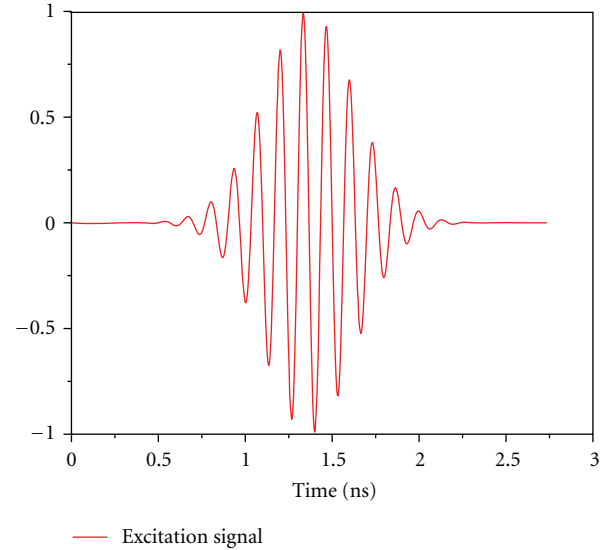


FIGURE 4: Normalised input signal.

- (ii) considering that the antenna is placed close to water, the lower edge frequency must be selected in such a way this remains efficient in the lower part of the operating bandwidth;
- (iii) the system sensitivity to water loading is dependent on the bandwidth over which the fidelity factor is measured.

In Figure 4 the normalised input signal selected for this application is plotted in the time domain. A convenient compromise between antenna efficiency and suitable fidelity factor sensitivity to the testing environment can be reached by using a Gaussian pulse centred at 7.5 GHz. Its frequency spectrum 20 dB bandwidth spans between 6.2 and 8.8 GHz.

3. Frequency Domain Performance

In this section the antenna performance is evaluated in the frequency domain when it is mounted conformally on the pipe configurations given in Table 1. Different diameters of curvature and thickness of the PVC pipes affect the antenna behaviour both in terms of impedance matching and radiation properties. But the presence of water inside the pipe generates the most evident variations. Figure 5 shows the resilience of the antenna impedance matching properties for the different pipe configurations when empty or full of water. It can be observed that the return loss curve drops to lower values when the pipe is filled with water as this introduces more losses. This effect is more evident for configurations A and C due to the thinner PVC layer between the antenna and the water content.

As from simulations the antenna shows stable radiation properties in terms of pattern shape over the operating bandwidth (6.2–8.8 GHz), the H -plane diagrams are only displayed at the centre frequency 7.5 GHz (Figure 6). A significant gain drop occurs when the pipe is filled with water due to increased losses and dielectric loading. However, for

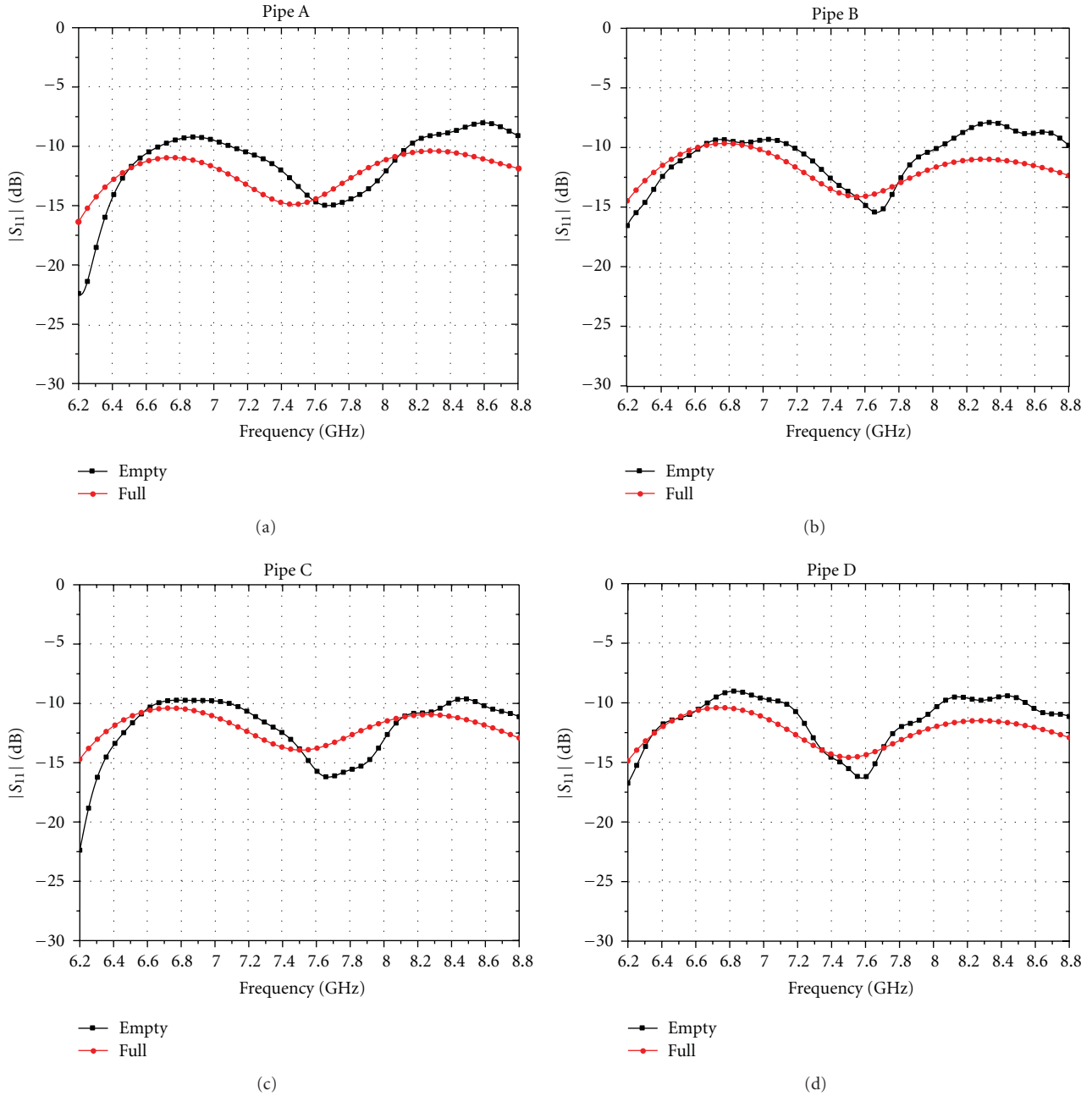


FIGURE 5: S_{11} comparison of antenna conformal to pipe configurations (a)–(d) without water (black trace) and with water (red trace).

all configurations investigated the antenna radiation remains efficient with and without water inside the pipe. Also the direction of maximum radiation changes because of the reflecting behaviour of the water content. In fact, this shifts towards the angular sector 30° – 50° when the pipe is full of water.

4. Time Domain Performance

As the antenna is required to provide simultaneous transmission and sensor function, an angular sector where good

radiation efficiency and sensing characteristics needs to be identified. As shown in Figure 6, for all the configurations investigated, a satisfactory compromise between the gain performance measured in the H -plane with and without water is achieved in the range $60^{\circ} \leq \theta \leq 70^{\circ}$. Moreover, in this spatial region the fidelity factor assumes values above 90% that corresponds to a reliable radio link for pulse communications in all the analysed scenarios. Outside the interval 60° – 70° a combined suitable performance in terms of gain (above 0 dBi) and FF (above 80%) was not found for all the scenarios under investigation. On the other hand, the

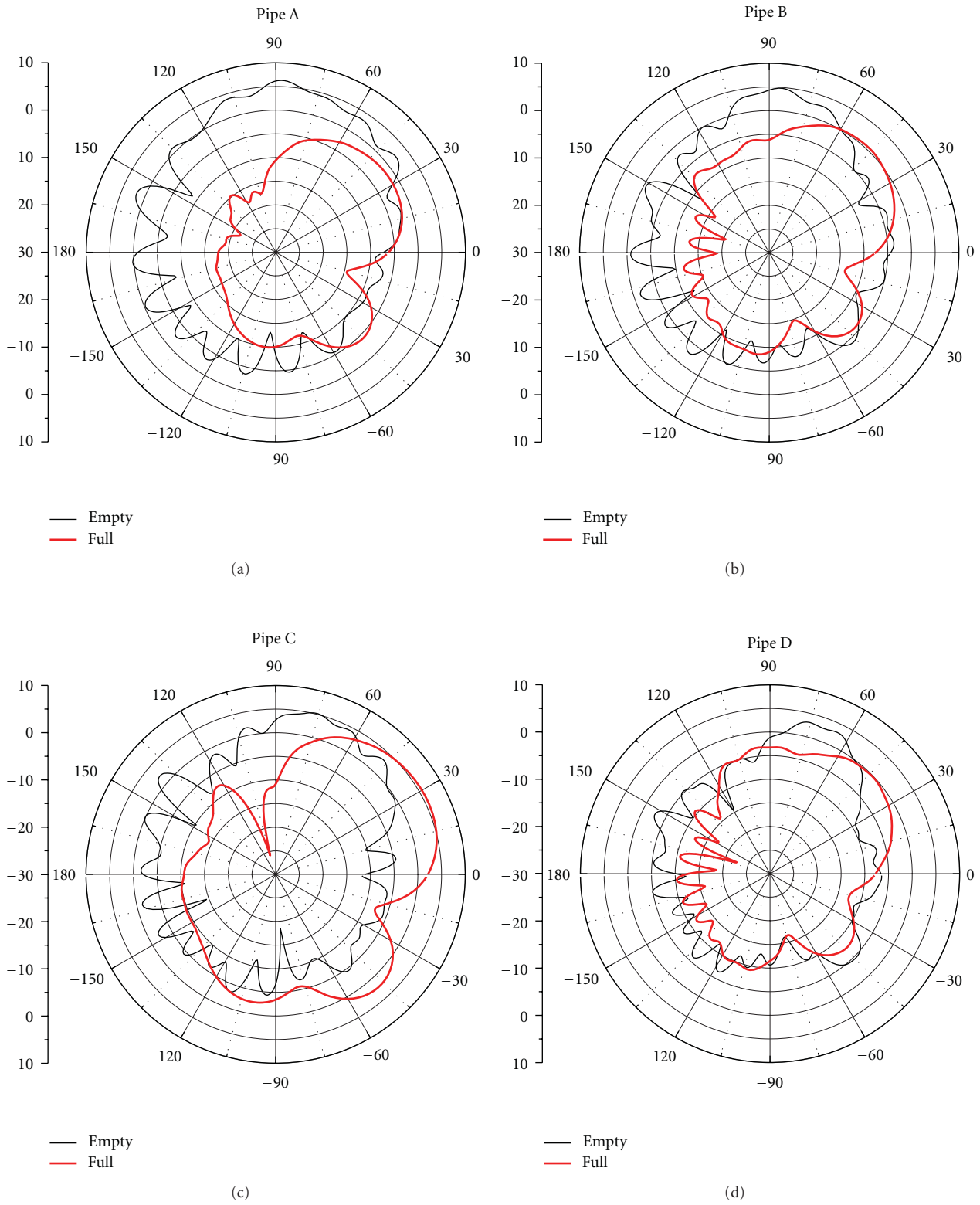


FIGURE 6: *H*-Plane radiation pattern comparison at 7.5 GHz of antenna conformal to pipe configurations (a)–(d) without water (black trace) and with water (red trace).

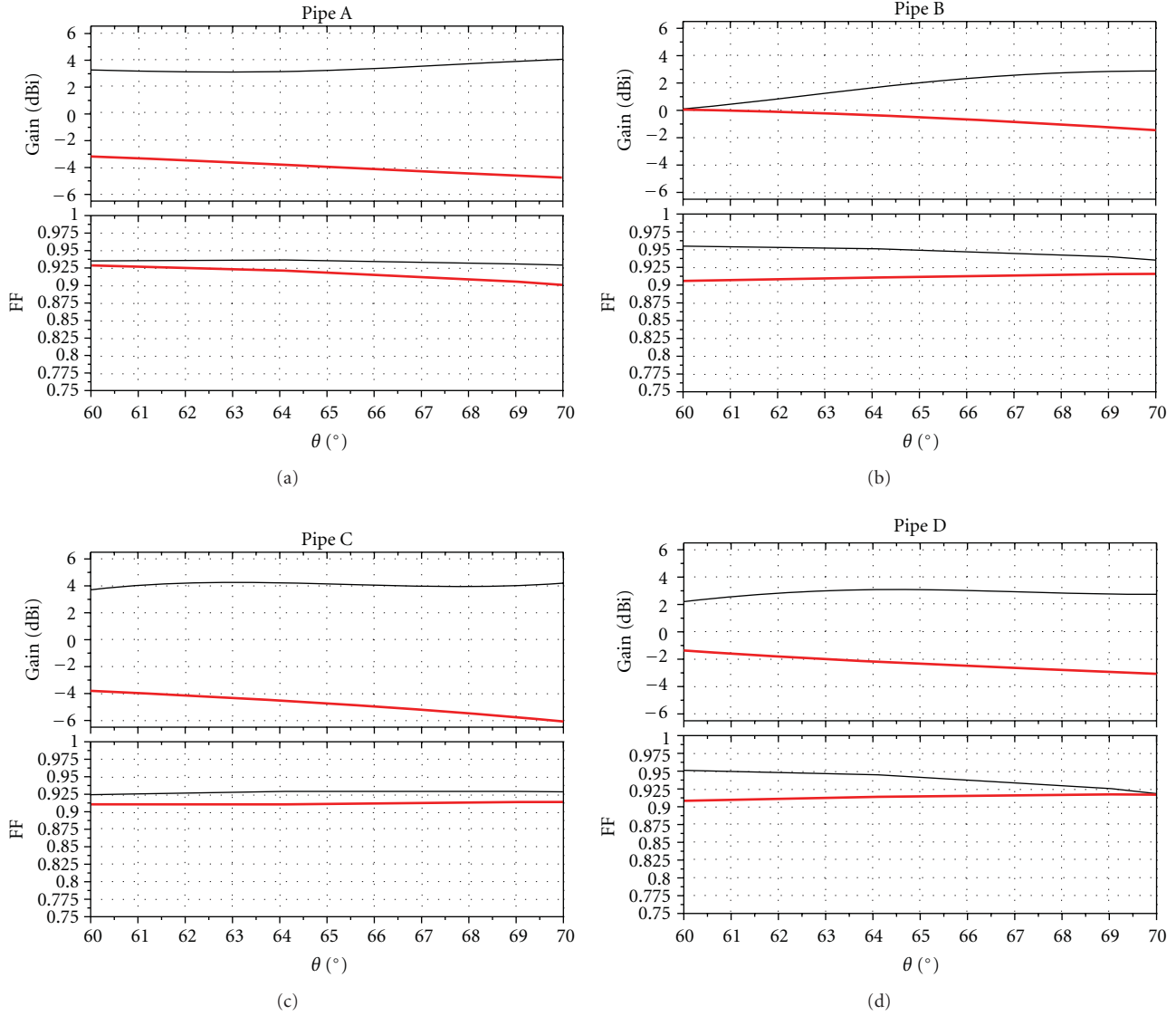


FIGURE 7: Realised gain and fidelity factor comparison at 7.5 GHz in the range $60^\circ \leq \theta \leq 70^\circ$ of antenna conformal to pipe configurations (a)–(d) without water (black trace) and with water (red trace).

fidelity factor can be also used as a valid figure of merit for sensing purposes. By definition, it depends on the variations of the transmitted signal across the entire bandwidth. As the antenna transmitting properties change when water fills the pipe, this effect is promptly expressed as a fidelity factor distortion. Figure 7 shows fidelity factor variations in the order of 6% between the cases “Empty” and “Full.” Once the system is properly characterised, those deviations can be used to monitor the water content inside the PVC pipes and simultaneously transmit the information to an external metering station.

5. Conclusions

A UWB directional antipodal Vivaldi antenna has been designed for water pipe sensing and telemetry. While the antenna impedance remains matched when placed on the

four pipes investigated, gain and fidelity factor undergo a notable reduction with the pipe filled of water. The dispersive property of the pipe material and the water will modify the transfer function of the antenna, distorting the radiated and received signal shape. However, by focusing on the bandwidth between 6.2 and 8.8 GHz and the angular range $60^\circ \leq \theta \leq 70^\circ$ in the H -plane, the antenna radiates efficiently in all the scenarios investigated in terms of gain and fidelity factor figures. These properties suggested using the same antenna for simultaneous sensing and telemetry applications. As the water content causes fidelity factor variations between 90 and 96%, this figure is proposed as a reliable sensing parameter to assess the pipe content status. At the same time, as values above 80% secure good radiolinks for impulse communications, the antenna is able to transmit real-time information to an external telemetry station.

References

- [1] O. Duran, K. Althoefer, and L. D. Seneviratne, "State of the art in sensor technologies for sewer inspection," *IEEE Sensors Journal*, vol. 2, no. 2, pp. 73–81, 2002.
- [2] S. K. Sinha, S. R. Iyer, and M. C. Bhardwaj, "Non-contact ultrasonic sensor and state-of-the-art camera for automated pipe inspection," in *Proceedings of the 2nd International Conference on Sensors*, pp. 493–498, October 2003.
- [3] F. Gomez, K. Althoefer, and L. D. Seneviratne, "Modeling of ultrasound sensor for pipe inspection," in *Proceedings of the IEEE International Conference on Robotics and Automation*, pp. 2555–2560, September 2003.
- [4] O. Hunaidi, "Ground penetrating radar for detection of leaks in buried plastic water distribution pipes," in *Proceedings of the 7th International Conference on Ground Penetrating Radar (GPR'98)*, pp. 783–786, Lawrence, Kan, USA, 1998.
- [5] S.-Y. Hyum, Y.-S. Jo, H.-C. Oh, and S.-Y. Kim, "An experimental study on a ground penetrating radar for detecting water-leaks in buried water transfer pipes," in *Proceedings of the 6th International Symposium on Antennas, Propagation and EM Theory*, pp. 597–599, 2003.
- [6] J. H. Goh, A. Shaw, J. D. Cullen et al., "Water pipe leak detection using electromagnetic wave sensor for the water industry," in *Proceedings of the IEEE Symposium on Computers & Informatics (ISCI '11)*, pp. 290–295, Kuala Lumpur, Malaysia.
- [7] D. Gaetano, M. J. Ammann, P. McEvoy, M. John, L. Keating, and F. Horgan, "A conformal UWB directional antenna," in *Proceedings of the 5th European Conference on Antennas and Propagation (EUCAP'11)*, pp. 1113–1116, April 2011.
- [8] A. Kadri, A. Abu-Dayya, D. Trinchero, and R. Stefanelli, "Design of radio-acoustic sensors for leakage detection in underground water pipes," in *Proceedings of the 12th International Conference on Electromagnetics in Advanced Applications (ICEAA'10)*, pp. 867–870, September 2010.
- [9] A. Dumoulin, M. John, M. J. Ammann, and P. McEvoy, "Optimized monopole and dipole antennas for UWB asset tag location systems," *IEEE Transactions on Antennas and Propagation*, vol. 60, no. 6, Article ID 6192292, pp. 2896–2904, 2012.
- [10] On-line, <http://www.cst.com/>.
- [11] D. Lamensdorf and L. Susman, "Baseband-pulse-antenna techniques," *IEEE Antennas and Propagation Magazine*, vol. 36, no. 1, pp. 20–30, 1994.
- [12] D. Ghosh, A. De, M. C. Taylor, T. K. Sarkar, M. C. Wicks, and E. L. Mokole, "Transmission and reception by ultra-wideband (UWB) antennas," *IEEE Antennas and Propagation Magazine*, vol. 48, no. 5, pp. 67–99, 2006.
- [13] E. Gazit, "Improved design of the vivaldi antenna," *IEE Proceedings Microwaves, Antennas and Propagation*, vol. 135, no. 2, pp. 89–92, 1988.
- [14] K. C. Gupta, R. Garp, I. Bahl, and P. Bhartia, *Microstrip Lines and Slotlines*, Artech House, Dedham, Mass, USA, 2nd edition, 1979.
- [15] M. Adous, P. Quéffelec, and L. Laguerre, "Coaxial/cylindrical transition line for broadband permittivity measurement of civil engineering materials," *Measurement Science and Technology*, vol. 17, no. 8, article no. 026, pp. 2241–2246, 2006.
- [16] ASTM Standard D1785, "ASTM D1785–06 Standard Specification for Polyvinyl Chloride (PVC) plastic pipe, schedules 40, 80, and 120," ASTM International, West Conshohocken, Pa, USA, 2006, <http://www.astm.org/>.

Research Article

Entropy-Based Clutter Rejection for Intrawall Diagnostics

Raffaele Solimene and Antonietta D'Alterio

Dipartimento di Ingegneria dell'Informazione, Seconda Università degli Studi di Napoli, 81031 Aversa, Italy

Correspondence should be addressed to Raffaele Solimene, raffaele.solimene@unina2.it

Received 16 March 2012; Accepted 1 May 2012

Academic Editor: Francesco Soldovieri

Copyright © 2012 R. Solimene and A. D'Alterio. This is an open access article distributed under the Creative Commons Attribution License, which permits unrestricted use, distribution, and reproduction in any medium, provided the original work is properly cited.

The intrawall diagnostic problem of detecting localized inhomogeneities possibly present within the wall is addressed. As well known, clutter arising from masonry structure can impair detection of embedded scatterers due to high amplitude reflections that wall front face introduces. Moreover, internal multiple reflections also can make it difficult ground penetrating radar images (radargramms) interpretation. To counteract these drawbacks, a clutter rejection method, properly tailored on the wall features, is mandatory. To this end, here we employ a windowing strategy based on entropy measures of temporal traces "similarity." Accordingly, instants of time for which radargramms exhibit entropy values greater than a prescribed threshold are "silenced." Numerical results are presented in order to show the effectiveness of the entropy-based clutter rejection algorithm. Moreover, a comparison with the standard average trace subtraction is also included.

1. Introduction

Microwave RADAR imaging is a pervasive research field which finds applications in a number of scenarios where it is mandatory and/or convenient to achieve diagnostics in a nondestructive way. Applicative contexts range from subsurface prospecting to cultural heritage monitoring and preservation [1], from biomedical diagnostics [2] to through-the-wall imaging (TWI) [3], and many others.

Each one of these scenarios characterizes imaging in terms of the challenges to be tackled in order to succeed in target detection and localization. This of course depends on the scatterers' nature and the host medium within which they are embedded.

Indeed, the host medium is the background against which targets have to be discerned.

First, the host medium imposes a suitable trade-off between resolution and electromagnetic wave penetration in order to comply with losses and dispersive effects it introduces. Moreover, host medium also determines that clutter signal against field backscattered from targets must compete.

Literature is extremely reaches imaging algorithms arisen from different scientific areas. Now, it is recognized that wave equation is their common mathematical rationale. Accordingly, they all attempt to solve an electromagnetic

inverse scattering problem by approximating, in different way, the inverse of the relevant scattering operator. The interested reader can refer to [4], where many of these imaging algorithms are compared under the light of inverse scattering theory.

In any case, imaging greatly benefits from a preliminary stage where useful signals (i.e., the ones coming from targets) are "singled out" from cluttered measurements.

Clutter embodies are all those unwanted field contributions which come from background medium heterogeneities and corrupt scattered field data. Indeed, clutter rejection methods are very much welcome as in most practical cases clutter has an amplitude dynamic range much greater than useful signals. The results is that targets tend to be masked and their detection can be strongly impaired.

In order to develop methods for removing/filtering clutter contribution, the key ingredient is to identify features that make targets different from sources of unwanted signals. Accordingly, a filter can be properly designed and tuned on clutter properties with the constraint of preserving as much as possible the useful signal which is needed for imaging purposes.

For example, in many cases, targets move. Here, the so-called moving target indicator (MTI) techniques can be employed to discern a moving target against a strong

stationary clutter. This is possible because clutter and targets have different Doppler spectra. Accordingly, a Doppler filtering is designed to cancel the zero Doppler spectral content [5]. However, there are several cases where scatterers are at rest.

In some further cases, it is known that targets have localized spatial supports, whereas sources of clutter do not. This occurs, for example, when targets are embedded in layered host media, as in subsurface or through-wall imaging. In these cases, clutter contribution mainly arises from medium interfaces whose spatial Fourier spectrum is concentrated around low frequencies. Accordingly, a high-pass filter, that suppresses the data low harmonic spatial content, can be employed to mitigate clutter [6]. Subtraction of the average trace, over sensor number, as well as the difference approach sketched in [7] in the framework of TWI, are examples of this strategy. However, filtering also erases the continuous component of the target spectral content [8]. Therefore, some compensation procedure is required to restore imaging point spread function.

Time gating does not suffer from this drawback as clutter rejection is achieved by nulling the first part of the acquired time traces [1]. Therefore, in principle, it works only in filtering out clutter that arrives before signals to be exploited for imaging.

In these cases, the choice of the time window is crucial and could be difficult if media are dispersive, as time-delayed echoes of the transmitted signal can be distorted and can extend beyond their expected duration. Moreover, multiple reflections between medium interfaces, that may occur after target backscattered field is arrived, are not eliminated. This may be the case of TWI imaging and intrawall diagnostics.

In this paper, we introduce a different time-widening strategy to reject clutter from measurements. The starting point is the observation that the field reflected from interfaces has a strong similarity over different sensor positions, when a multimonostatic configuration is employed. Accordingly, by introducing an entropy-based measure of this similarity, signals at instants of time where entropy exceeds a prescribed threshold are nulled [9]. Note that this allows for clutter reduction also when it does not appear before the target scattered field.

The applicative context within we move is that relevant for intrawall diagnostics. In this case, targets are represented by localized inhomogeneities present within a masonry structure.

The remaining of the paper is organized as follows. In Section 2, we briefly describe the scattering experiment. In Section 3, we introduce the entropy-based clutter rejection method, whereas its numerical assessment is presented in Section 4. Finally, conclusions are drawn at the end the paper.

2. Scattering Layout

The scenario consists of a three-layered medium. The first and the third layers are assumed to be the free space with ϵ_0 and μ_0 being their dielectric permittivity and magnetic permeability, respectively. The second layer is representative

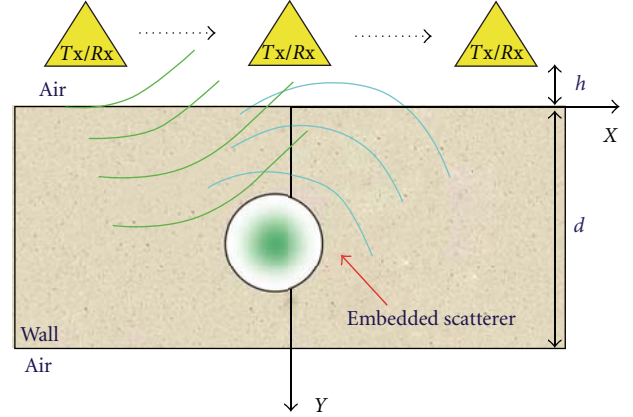


FIGURE 1: Geometry of the scattering problem.

of the wall. It is assumed nonmagnetic (i.e., its magnetic permeability is equal to the one of free space) with thickness d , and laterally homogeneous with relative dielectric permittivity denoted as ϵ_w .

The transmitting antenna is located in the first layer at a distance h from the front face of the wall. We consider a multimonostatic measurement configuration where the reflected field is collected at the same position as the source while the latter moves over a set of M different positions in order to synthesize the measurement line Σ , the latter being parallel to the wall interfaces. In particular, here, a two-dimensional filamentary current directed along the z -axis is considered as source.

Targets to be searched for reside within the wall structure and are represented in terms of spatially localized inhomogeneities. Invariance along the z -axis is assumed so that the problem at hand is two-dimensional and scalar.

The scattering layout is depicted in Figure 1. This configuration can be considered as schematizing a B-scan of the scene.

3. Entropy-Based Clutter Rejection

Let us denote as $e_1(t), e_2(t), \dots, e_n(t), \dots, e_M(t)$ the signals (A-scans) collected over the M observation positions. Each of them accounts for different contribution arising from antenna mismatch, from wall reflections, and from the enclosed targets. In particular, the signal collected at the n th position can be written as

$$e_n(t) = e_{na}(t) + e_{nw}(t) + e_{nt}(t), \quad (1)$$

where $e_{na}(t)$ represents the antenna internal reflection, $e_{nw}(t)$ the wall contribution, and $e_{nt}(t)$ is the field scattered by the targets within the wall (to be used for their detection and localization). Accordingly, $e_{na}(t)$ and $e_{nw}(t)$ are sources of clutter which target signals must compete with. Moreover, clutter is generally much stronger than target returns and this can make scatterer contributions barely visible or can completely mask it. Therefore, in order to “extract” $e_{nt}(t)$ from clutter, a clutter rejection method is indeed necessary.

The key steps in any clutter rejection method is to identify the features which make clutter different from the target signal, and to exploit them to suppress it from the total signal (1). Of course, these features depend on the scattering scene at hand and the nature of scatterers of interest.

When scatters with finite-spatial supports are of concern (hence, no layer interfaces), like in many subsurface or intrawall imaging problems, wall reflections and the field scattered by the targets have different spatial spectral contents. Indeed, the spectral content of the clutter due to the interfaces spans substantially the low-frequency region. Therefore, it can be mitigated by filtering out such a harmonic content [6]. The simplest way to achieve that is to subtract from each total field trace (1) the average (over the number of sensors) trace, that is,

$$e_{AVn}(t) = e_n(t) - \frac{1}{M} \sum_{m=1}^M e_{nw}(t), \quad (2)$$

where the subscript AV on the left side term is a remind of average trace subtraction. However, this filtering also acts on $e_{nt}(t)$ making it necessary for some compensation procedure in order to restore the point spread function if a focusing algorithm is employed [7].

It is observed that $e_{na}(t)$ and $e_{nw}(t)$ “precede” in time $e_{nt}(t)$. Therefore, instead of spatial frequency, difference in the time of arrival can be used to erase clutter. This suggests a time-gating procedure for clutter mitigation which does not introduce unwanted filtering. In this case, the issue to be tackled concerns the automatic selection of the window within which signal must be “silenced.” This could become a difficult task when it is not true that “all” the clutter precedes target signal. The latter circumstance can occur, for example, when targets are embedded in a layered medium like in intrawall diagnostics. In these cases, a suitable windowing function has to be defined in order to remove clutter that appears spread at different instants of time along each A-scan trace.

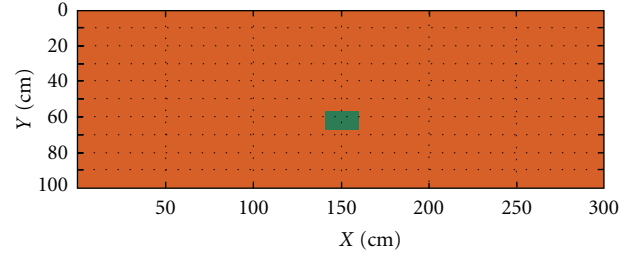
To cover these situations, here, an entropy-based criterion for window selection is exploited.

The starting point is the assumption that clutter has similar behaviour in each timetrace. Note that this assumption is implicitly implied by average subtraction in (2) and even in time gating. Accordingly, the windowing function will be supported over those instants of time where trace “similarity” is “low.” Of course, this statement needs to be properly cast under a “quantitative” point of view. In other words, a suitable metric has to be defined in order to quantify trace “similarity.”

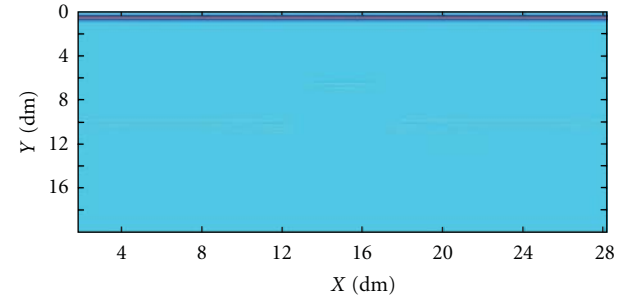
To this end, we first introduce the normalized A-scan as follows:

$$\tilde{e}_n(t) = \frac{|e_n(t)|^2}{\sum_{m=1}^M |e_m(t)|^2}. \quad (3)$$

It is recognized that $\tilde{e}_n(t) \geq 0$ and that $\sum_{n=1}^M \tilde{e}_n(t) = 1$ for all t . Therefore, for each instant of time, the vector of the normalized A-scan can be assimilated as a probability density function. Accordingly, at a given instant of time,



(a)



(b)

FIGURE 2: (a) PEC scatterer located within the wall, (b) corresponding B-scan.

similar signals (over the different sensors’ positions) will translate into a uniform probability density distribution. This observation suggests to adopt an entropy-based metric in order to discriminate between clutter and target signal. Following the Shannon entropy measure, a possible choice is

$$\varepsilon_S(t) = - \sum_{n=1}^M \tilde{e}_n(t) \log[\tilde{e}_n(t)]. \quad (4)$$

As clutter signals are expected to be similar, they result in large values of $\varepsilon_S(t)$. On the contrary, target signals will consist of pulses differently delayed and hence correspond to lower value of $\varepsilon_S(t)$. Accordingly, in order to get rid clutter, a windowing, which eliminates signals for instants of time where $\varepsilon_S(t)$ is high, can be set up. Hence, one obtains the widowed signals as

$$e_{Wn}(t) = W(t)e_n(t), \quad (5)$$

with

$$W(t) = \begin{cases} 0 & \text{if } \varepsilon_S(t) = \log M \\ 1 & \text{elsewhere,} \end{cases} \quad (6)$$

where $\log M$ is the maximum of $\varepsilon_S(t)$ which occurs when all signals are identical.

Instead of Shannon entropy measure, here, we adopt a variant due to Renyi [10]. Accordingly, for quantifying the diversity between signals, we use the Renyi entropy, that is,

$$\varepsilon_{R\beta}(t) = \frac{1}{(1 - \beta) \log \sum_{n=1}^M \tilde{e}_n(t)^\beta}, \quad (7)$$

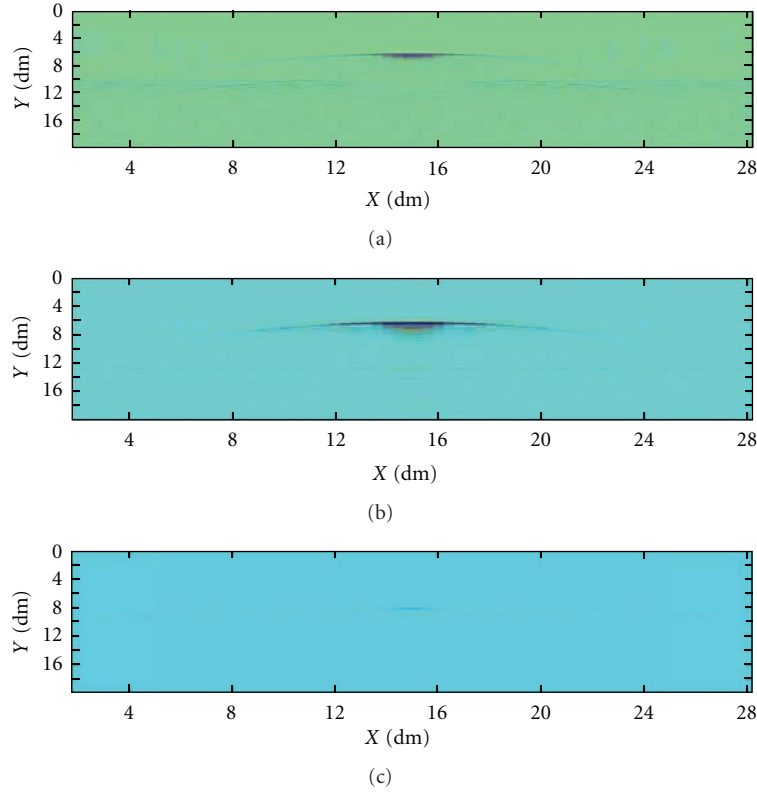


FIGURE 3: Windowed signal for three different values of \tilde{M} . (a) $\tilde{M} = 36$, (b) $\tilde{M} = 10$, (c) $\tilde{M} = 4$.

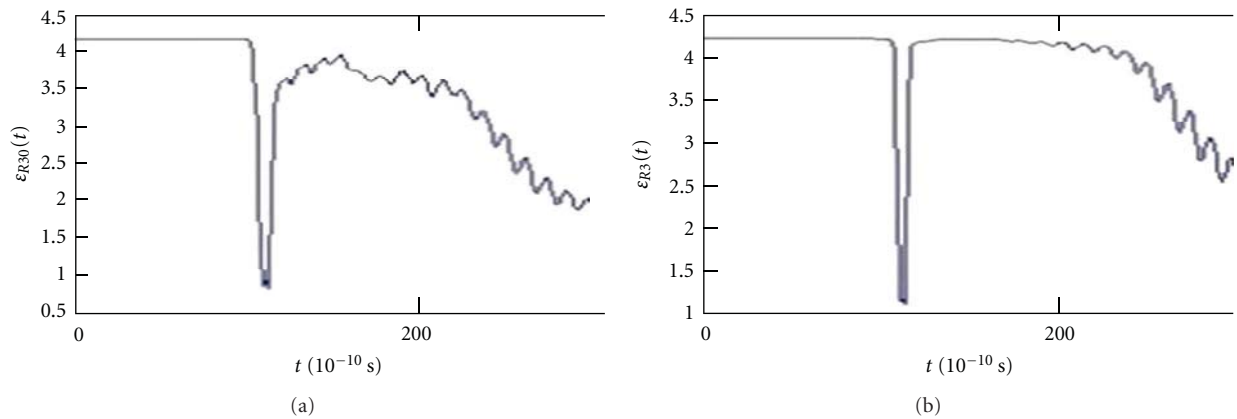


FIGURE 4: Renyi entropy for $\tilde{M} = 10$ and two different values of β . (a) $\beta = 30$, (b) $\beta = 3$.

where $\varepsilon_{R\beta}(t)$ is the Renyi entropy of order β , with β being positive but different from unity. It is easily seen that Renyi entropy maximum is still $\log M$ and that it coincides with Shannon entropy for the case of $\beta = 1$. Therefore, we can conclude that, for clutter arising from antenna internal reflections and the field reflected from the front face of the masonry structure, the two entropy measures are equivalent.

However, Renyi entropy is here preferred because the exponential term β is a one more degree of freedom that can be exploited. In more detail, the contributions arriving

at sensors are weighted in different way during entropy evaluation. In particular, for $\beta > 1$, Renyi entropy mainly depends on the highest “probability events” (highest $\tilde{e}_n(t)$). Therefore, a “sharper” separation between clutter and target signals is expected.

Eventually, the window function to be used is defined as follows:

$$W(t) = \begin{cases} 0 & \text{if } \varepsilon_{R\beta}(t) \geq \alpha \log M \\ 1 & \text{elsewhere,} \end{cases} \quad (8)$$

with $\alpha < 1$. Note that a decision threshold lower than $\log M$ has been introduced this way, it is expected that back wall face reflections and multiple target echoes are mitigated as well. In fact, multiple target echoes appear in the radargramm (B-scan) as hyperbolas whose radii of curvature are greater than the ones of the target signals. This is because they can be regarded as due to scatterers that are more deeply located. On the other hand, their radii of curvature are certainly smaller than the interface reflections which appear as flat curves. Hence, entropy associated to those returns will be greater than that due to the target but lower than the one due to wall interfaces.

4. Numerical Examples

In this section, the ability of the windowing procedure described above to remove clutter is checked. To this end, a series of numerical experiment are conducted with synthetic data obtained by using the FDTD-based GPRMAX forward solver [11].

As source, a filamentary impressed current located over ($h = 0$) the front face of the wall is employed. Sixty-six source positions (i.e., $M = 66$) uniformly taken over a measurement line 3m long are considered. The field is collected at the same position as the source as the latter spans the measurement line. It is worth noting that, in this case, as ideal source is considered, $e_{na}(t) = 0$. Hence, clutter solely arises from the masonry structure.

As to the wall, a slab with thickness $d = 1$ m and dielectric permittivity $\epsilon_w = 7$ is considered. Such a wall resembles to some hancient walls in Italy [12].

4.1. Choice of β and α . The first set of numerical examples have the aim of providing a guide for the choice of the parameters β and α appearing in (7) and (8), respectively.

To this end, we consider a single rectangular perfect electric conducting (PEC) scatterer embedded in the masonry structure, as depicted in Figure 2, and apply different windowing function as β and α vary. For comparison purposes, in Figure 2, it is also reported the radargramm corresponding to the scattering experiment at hand. In particular, depth is provided in terms of $y = vt/2$, where v is wave propagation speed in the wall.

First, for the fixed value of $\beta = 3$, the role of α is studied in Figure 3, where the windowed $e_w(t)$ data are reported for three different values of α . In particular, α is chosen so that $\tilde{M} = \exp(\alpha \log M)$ is equal to 36, 10, and 4, respectively, from the top to the bottom panels. Of course, cases corresponding to $\tilde{M} > M$ do not make any sense as entropy measure would be always lower than the windowing threshold and hence signal would remain unchanged. According to (8), the lower \tilde{M} , the stronger the windowing since the threshold above which signal is silenced is lower. This is clearly shown in Figure 3. In particular, it can be appreciated that, in all the cases, first wall interface contribution is successfully erased. This makes it evident target contribution, which otherwise would be only barely visible in the radargramm (see Figure 2). Moreover, as expected, by decreasing the

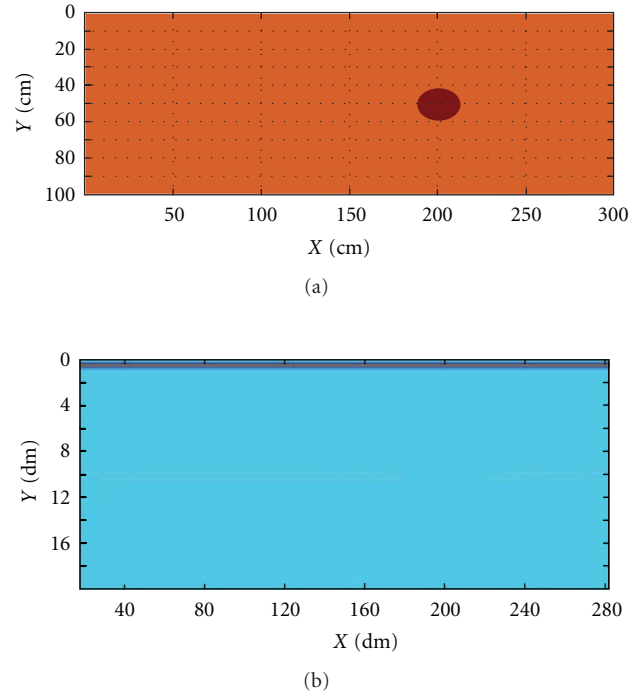


FIGURE 5: (a) Circular dielectric scatterer located within the wall, (b) corresponding B-scan.

windowing threshold, also artifacts due, basically, to the second wall interface, tend to be erased. However, a too low threshold would cancel target contribution as well.

Therefore, according to these results, a judicious choice appears $\tilde{M} = 10$.

With this value of \tilde{M} , we turn now to address the role of β by referring to Figure 4. In such a figure, Renyi entropy is reported for two different values of β ($\beta = 30$ and $\beta = 3$) for a time interval which roughly corresponds to the depth range of Figures 2 and 3. As can be seen, the first part of entropy behavior is rather constant and approximately equal to the maximum value $\log M = 4.2$. This of course could be expected as, in this interval of time, there is a strong similarity between different A-scans which mainly account for front wall reflections. Moreover, it is observed that entropy abruptly drops at around 10.5 ns and stays down roughly for a time interval corresponding to the round-trip delays that signals take to cover antenna/target paths and vice versa. Afterwards, entropy starts to increase once again.

However, entropy measures is a slowly varying function of β as the two entropy behaviors are very similar (as shown in Figure 4).

Therefore, according to this numerical analysis, in the sequel we set $\beta = 3$ and $\tilde{M} = 10$.

5. Numerical Results

In this section, we check the entropy windowing procedure for scattering scenes different from the one reported in Figure 2 which, in turn, guided the choice of β and \tilde{M} . In particular, while the wall structure remains the same as

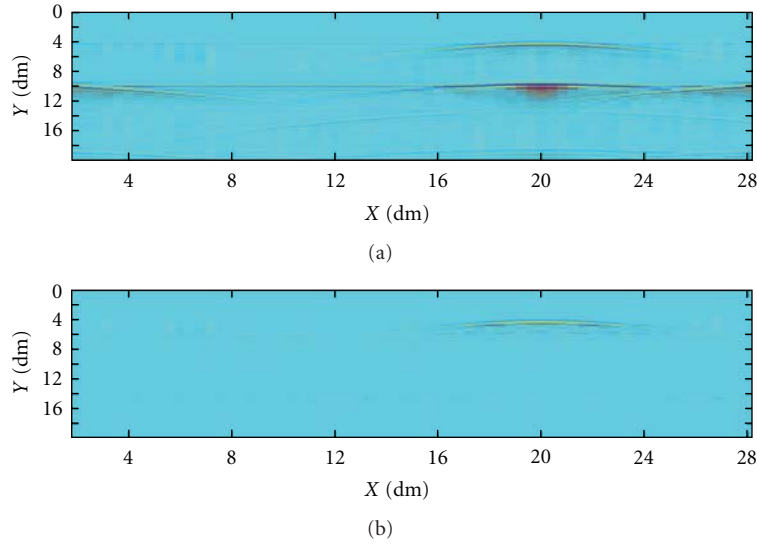


FIGURE 6: The case of Figure 5. (a) Radargramm after average trace subtraction, (b) windowed radargramm.

the previous case, the type of scatterers and their positions are changed.

The first example refers to the scattering scene reported in Figure 5, where a circular dielectric scatterer with relative dielectric permittivity equal to 4 and electric conductivity of 0.1 S/m is considered. Also, its location within the wall, which is different from the case reported in Figure 2, is indicated. In the same figure (Figure 5(b)) the corresponding radargramm is reported as well.

By looking at such a figure, it can be appreciated that target can be hardly discerned from background. Indeed, one could be aware of the presence of a scatterer mainly due to the shadowing that it introduces on the reflection coming from second wall interface. Instead, after windowing (see Figure 6(b)), target contribution turns to be clearly visible.

In the same figure, we also reported, for comparison purposes, the radargramm after average trace subtraction according to (2). By comparing the two methods, it is seen that in both cases, front wall interface clutter is very well cancelled. However, entropy-based windowing outperforms average trace subtraction as a number of spurious artifacts, still affecting radargramm after average trace removing, are almost completely eliminated. This makes the interpretation of the windowed images less ambiguous.

As a second example, the scattering scene depicted in Figure 7 is considered. Now, two scatterers are embedded in the wall. One is circular with relative dielectric permittivity equal to 3 (in order to increase contrast with background) and electric conductivity of 0.1 S/m; the other is a PEC square. Their dimensions and positions within the wall are illustrated in Figure 7(a). In Figure 7(b), the corresponding radargramm is reported. It can be seen that the two scatterers are only barely discernable. After clutter is removed, they turn to be clearly visible, specially by the windowing procedure that, as in the previous case, allows for obtaining a more clear image (see Figure 8).

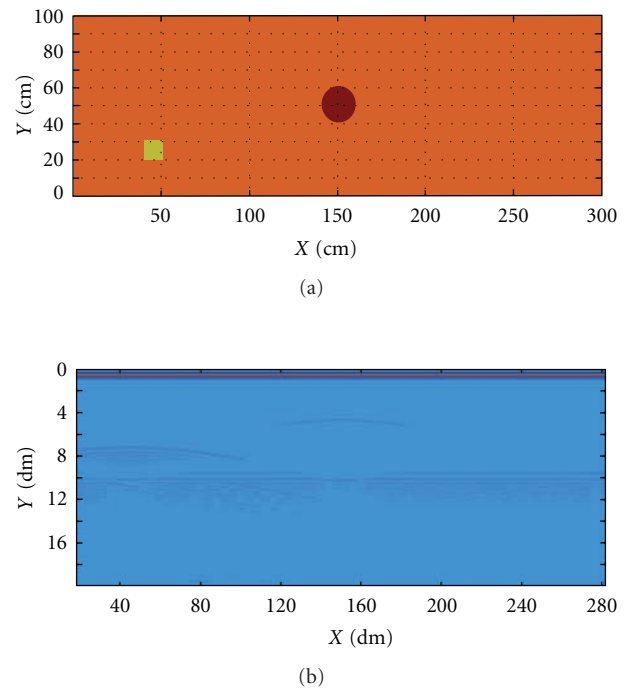


FIGURE 7: (a) Two scatterers are located within the wall, (b) corresponding B-scan.

6. Conclusions

In this paper, we considered intrawall diagnostics of localized scatterers and focused on the problem of clutter mitigation. To this end, we employed an entropy-based time-windowing artifact removal algorithm. In particular, we exploited the fact that wall contributions give rise to signals that have high similarity over different sensors' positions. Therefore, by computing the entropy of time traces at each instant of time, a windowing function was set up so that it takes values

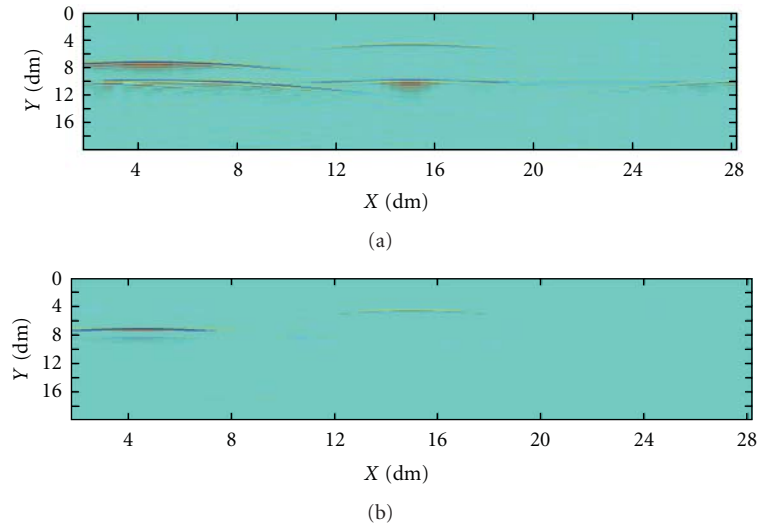


FIGURE 8: The case of Figure 7. (a) Radargram after average trace subtraction, (b) windowed radargram.

of zero for entropy greater than a suitable threshold and values of one when smaller entropy occurs.

Applying the window function to FDTD-simulated data, it was shown the effectiveness of the method. In particular, the windowing strategy proven to be more effective than standard average trace subtraction.

Although the presented results are encouraging, a more deep analysis still has to be performed. This would require a more extensive numerical investigation for different and possibly more realistic scenarios.

It is our commitment to address this study in future works.

References

- [1] D. J. Daniels, *Ground Penetrating Radar*, IET, 2004.
- [2] E. C. Fear, P. M. Meaney, and M. A. Stuchly, "Microwaves for breast cancer detection?" *IEEE Potentials*, vol. 22, no. 1, pp. 12–18, 2003.
- [3] M. Amin and K. Sarabandi, "Special issue on remote sensing of building interior," *IEEE Transactions on Geoscience and Remote Sensing*, vol. 47, no. 5, pp. 1267–1268, 2009.
- [4] F. Soldovieri and R. Solimene, "Ground Penetrating Radar subsurface imaging of buried objects," in *Radar Technology*, G. Kouemou, Ed., In-Tech, 2010.
- [5] N. Levanon, *Radar Principles*, John Wiley & Sons, New York, NY, USA, 1988.
- [6] D. Potin, E. Duflos, and P. Vanheeghe, "Land mines ground-penetrating radar signal enhancement by digital filtering," *IEEE Transactions on Geoscience and Remote Sensing*, vol. 44, no. 9, pp. 2393–2406, 2006.
- [7] M. Dehmollaian, M. Thiel, and K. Sarabandi, "Through-the-wall imaging using differential SAR," *IEEE Transactions on Geoscience and Remote Sensing*, vol. 47, no. 5, pp. 1289–1296, 2009.
- [8] R. Persico and F. Soldovieri, "A microwave tomography approach for a differential configuration in GPR prospecting," *IEEE Transactions on Antennas and Propagation*, vol. 54, no. 11, pp. 3541–3548, 2006.
- [9] W. Zhi and F. Chin, "Entropy-based time window for artifact removal in UWB imaging of breast cancer detection," *IEEE Signal Processing Letters*, vol. 13, no. 10, pp. 585–588, 2006.
- [10] R. G. Baraniuk, P. Flandrin, A. J. E. M. Janssen, and O. J. J. Michel, "Measuring time-frequency information content using the Rényi entropies," *IEEE Transactions on Information Theory*, vol. 47, no. 4, pp. 1391–1409, 2001.
- [11] A. Giannopoulos, *GprMax2D/3D*, Users Guide, 2002, <http://www.xmarks.com/site/www.gprmax.org/>.
- [12] A. Brancaccio, R. Solimene, G. Prisco, G. Leone, and R. Pierri, "Intra-wall diagnostics via a microwave tomographic approach," *Journal of Geophysics and Engineering*, vol. 8, pp. 47–53, 2011.

Research Article

Ground-Penetrating Radar Investigations along Hajipur Fault: Himalayan Frontal Thrust—Attempt to Identify Near Subsurface Displacement, NW Himalaya, India

**Javed N. Malik, Ashutosh Kumar, Sravanthi Satuluri,
Bishuddhakshya Puhan, and Asmita Mohanty**

Department of Civil Engineering, Indian Institute of Technology Kanpur, Kanpur 208016, India

Correspondence should be addressed to Javed N. Malik, javed@iitk.ac.in

Received 3 November 2011; Accepted 25 January 2012

Academic Editor: Raffaele Solimene

Copyright © 2012 Javed N. Malik et al. This is an open access article distributed under the Creative Commons Attribution License, which permits unrestricted use, distribution, and reproduction in any medium, provided the original work is properly cited.

The study area falls in the mesoseismal zone of 1905 Kangra earthquake (Mw 7.8). To identify appropriate trenching site for paleoseismic investigation and to understand the faulting geometry, ground-penetrating radar (GPR) survey was conducted across a Hajipur Fault (HF2) scarp, a branching out fault of Himalayan Frontal Thrust (HFT) in a foot hill zone of NW Himalaya. Several 2D and 3D profiles were collected using 200 MHz antenna with SIR 3000 unit. A 2D GPR profile collected across the HF2 scarp revealed prominent hyperbolas and discontinuous-warped reflections, suggesting a metal pipe and a zone of deformation along a low-angle thrust fault, respectively. The 3D profile revealed remarkable variation in dip of the fault plane and pattern of deformation along the strike of the fault.

1. Introduction

Paleoseismology defines the study of prehistoric earthquakes, especially their location, timing, and size [1–8]. The paleoseismic studies have attained a great pace in seismically active regions of the world [7, 9]. The investigation is mainly emphasized towards identification of surface manifestation of deformation and near subsurface displacements on active fault related to past earthquakes. It has usually been experienced that the preservation of active tectonic landforms along the mountain fronts is difficult because of ongoing dynamic fluvial processes causing high degree of erosion and deposition [10, 11]. Due to the removal of such feature, it becomes difficult to identify appropriate site for trenching to undertake paleoseismic studies. Several geophysical techniques to map the subsurface deformation, for example, seismic reflection and refraction, resistivity survey, ground-penetrating radar (GPR) have been used. The seismic reflection-refraction method has been used to get good resolution subsurface profile up to ≥ 100 m, but submeter resolution is not possible. Since the Ground-penetrating Radar (GPR) technique gives a high-resolution

profile of shallow subsurface succession up to submeter resolution, it has been extensively used for geological studies since the 1990s [12].

Since a decade, the GPR technique has been widely used for different studies for mapping near subsurface displacements in the young Quaternary sediments related to active faulting, for identifying neotectonic faulting activity and liquefaction features like sand-blows (e.g., [10–20]). It has also proved as an important tool in locating archeological sites (e.g., [21–24]). Along with this GPR has been quite useful towards identifying appropriate site to undertake trenching for detailed paleoseismic studies along active faults in an area, where surface manifestation of active faulting is sparsely preserved [10, 11, 16].

The convergence and ongoing collision between Indian and Eurasian plates has kept the Himalayan arc to be one of the most seismically active regions of the world; therefore, seismic hazard assessment is one of the major concern. The built-up strain is released episodically along the active fault systems in Himalaya [20, 25]. This is well justified by the occurrence of large-magnitude earthquakes, namely,

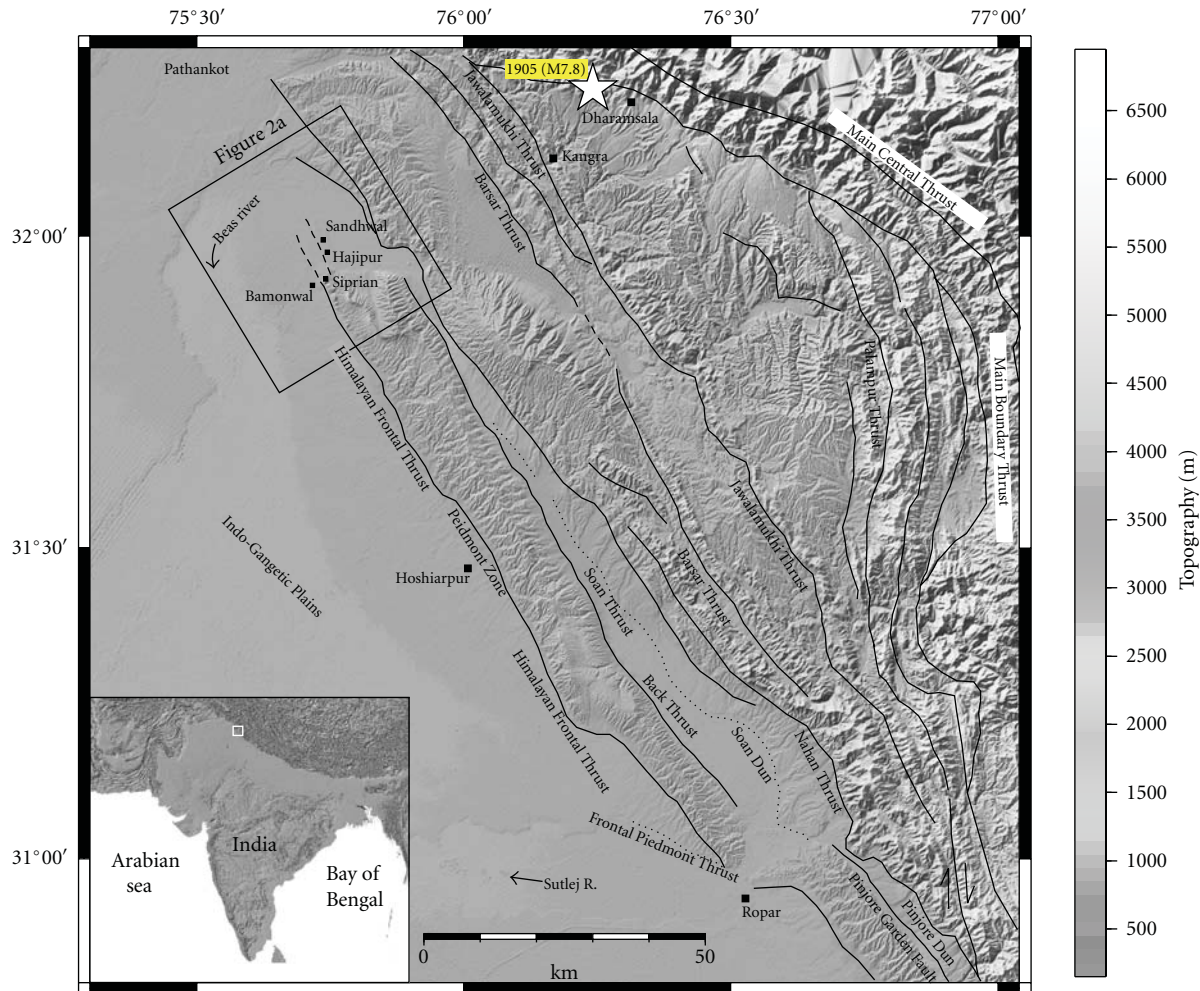


FIGURE 1: SRTM data of study area illustrating major faults marked by continuous lines and major geomorphic divisions around north west Himalaya. Box on top left marks the area of study which was shown in Figure 2. Inset shows DEM of India with location of study area.

1905 Kangra (Mw 7.8), 1934 Bihar (Mw 8.1), 1950 Upper Assam (Mw 8.4), and recent 2005 Muzaffarabad (Mw 7.6) earthquakes [8, 20, 26–28] (Figure 1). A very few studies have been taken up so far in Himalayan region attempting to map the surface manifestation of the past earthquake and to undertake paleoseismic investigation by excavating trenches across active fault scarps. Identification and mapping of such features, understanding the pattern of deformation along with known paleoseismic event are extremely important for proper seismic hazard assessment. In this paper, we discuss GPR studies carried along Hajipur Fault (HF2) a branching out fault of Himalayan Frontal Thrust (HFT) in the foot hill zone of NW Himalaya (Figure 1). To identify the appropriate site for trenching and to understand the geometry of faulting, we collected 2D and 3D GPR profiles.

2. Methodology

Ground-penetrating Radar (GPR) is a noninvasive geophysical technique, where the high-frequency (MHz) electromagnetic wave is transmitted into the ground that detects

the electrical discontinuities in shallow subsurface earth material [12]. The propagation of the georadar waves is dependent on electrical properties of the material such as electric conductivity (σ), magnetic permeability (μ), and dielectric permittivity (ϵ) [12]. When the georadar waves propagate down into the earth surface, they are refracted-reflected back to the surface depending upon the properties of the lithology [29, 30]. The unconsolidated sediments, construction material, and weathered or fractured rocks are porous in nature, hence if filled with water, affect dielectric permittivity or dielectric constant [30]. As the contrast in the subsurface layers is greater, the amount of reflected energy will be greater which is given by the reflection coefficient, R , and can be determined by the contrast in relative velocities and also by the contrast in relative dielectric constants [12]:

$$R = \frac{V1 - V2}{V1 + V2} \quad \text{or} \quad \frac{\sqrt{\epsilon2} - \sqrt{\epsilon1}}{\sqrt{\epsilon2} + \sqrt{\epsilon1}}, \quad (1)$$

where, $V1$ and $V2$ are relative velocities, and $\epsilon1$ and $\epsilon2$ are relative dielectric constants of the adjacent layers. Velocity of

the medium (V) is dependent upon the velocity of light in air (0.3 m/ns) and is given by a simplified equation:

$$V = \frac{c}{\sqrt{\epsilon}}, \quad (2)$$

where c is velocity of light in air. Further, depth of penetration (D) can be determined using two-way travel time (T) and the velocity of the medium, which can be obtained from the graphical interpretation of the GPR signals:

$$D = \frac{T * V}{2}. \quad (3)$$

2.1. Data Acquisition along Hajipur Fault. GPR profiles were collected with SIR-3000 system using 200 MHz-shielded antenna in common-offset continuous mode. Variable settings available in the portable unit were used to determine the best acquisition parameters. For a better vertical resolution, the data was collected with 16-bit format and 512 Sample/scan whereas, 64 Scan/unit (meter) was set for optimum horizontal resolution. Since the data was collected in a distance mode using survey wheel with 512 Sample/scan the rate of 100 Scan/sec was preferred. The floodplain deposits of Beas River is mainly comprised of sand + gravel deposits, with the top surface made up of medium-to-coarse sand with scattered gravels. Keeping in mind the usual dielectric constant of sand ranging from 3–6, higher value was attributed since the area was slightly moist. Finally, after having these parameters GPR profiles were collected, which gave a good resolution with penetration up to 6 m (Table 1). A calibrated odometer fixed on survey wheel was attached to the antenna to get the horizontal distance. Along with this, appropriate gain and IIR filter was applied to the field data to get better resolution and to remove noise with lower and higher frequencies, respectively.

At Sandhwal village, both 2D and 3D GPR profiling was carried out across the active fault scarp along Hajipur Fault (HF2), (Figure 2(a)). The 2D profile was 28 m long and was collected with the acquisition parameters given in Table 1. Out of several profiles taken along this line, the profile shown in Figure 3 was the best one that exhibits ample information about the fault geometry. However, to have further understanding of the fault geometry, a 3D profile was collected for a grid-ABCD with dimensions of 20 m \times 6 m (Figures 2(b) and 4). For 3D profiling, the grid was prepared by taking 20 m along the X -axis and 6 m along the Y -axis and was further divided into smaller grids of 1 m spacing with which we have collected 21 grid lines along X -axis and 07 gridlines along Y -axis. The western corner (A) of the grid was considered as origin (Figure 2(b)). The data acquisition parameters for the 3D grid profile were the same as that of the 2D profile (Table 1). Since the surface across which the profile was collected was not horizontal, topographic profile was collected.

3. Data Processing and Interpretation

The radar profiles collected in the field were processed with RADAN 6.5 software manufactured by Geophysical Survey

TABLE 1: Acquisition parameters used for collection of 2D and 3D profiles across HF2 scarp at Sandhwal village.

Data acquisition parameters	Corresponding values
Sample/scan	512
Bits/sample	16
Scan/sec	100
Scans/m	64
Dielectric constant	6

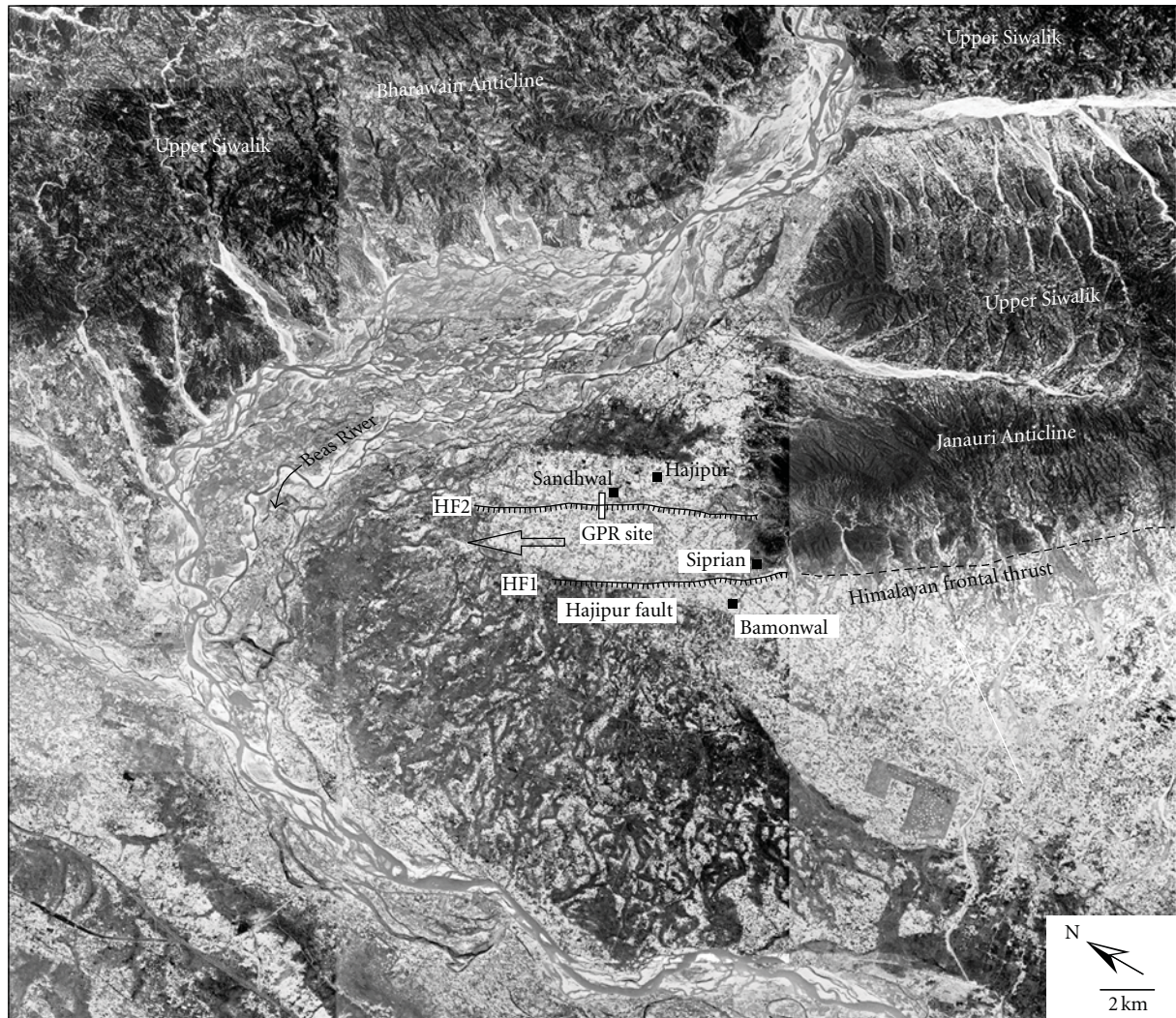
TABLE 2: Data processing parameters used for 2D and 3D GPR profiles across Hajipur Fault (HF2).

Parameters	2D profile	3D grid profile
Time-zero correction	5.86 ns	5.66 ns
FIR filters	Low pass	720 MHz
	High pass	38 MHz
3D grid	x -(start–end)	—
	y -(start–end)	—

Systems, Inc. The 2D profile was processed in the sequence starting from time-zero correction, application of filters, surface normalization, and autogain restoration. The processing parameters for the 2D profiles and 3D grid are given in Table 2. The time-zero correction was applied to remove the uppermost high amplitude reflections obtained from the direct air wave and ground wave (Figure 3(a)) and for the successful realignment of all reflections beneath. The low- and high-pass filters along with background removal were applied to remove noise (interference). Topographic data collected along the same transect was incorporated in the 2D profile, and surface normalization was performed (Figure 3(a)). Automatic gain control (AGC) was applied to enhance the visibility of low-frequency features. The processing of the 3D grid profile was also done following the same steps as for the 2D GPR profiles. To have better view of the variation in fault geometry along the strike, the 3D profiles were vertically sliced.

3.1. Interpretation. Previous studies suggest that for the interpretation of GPR data and for locating near subsurface displacements in young Quaternary deposits, it is necessary to look for the offset of radar reflections on both sides of the fault strand and for the warping of the GPR reflectors or discontinuity in the reflections (e.g., [10, 11, 30, 31]). Keeping the above points into consideration and with the background of the earlier paleoseismic and GPR surveys carried out along the Himalayan Frontal Thrust by Malik et al. [20, 23], attempts were made to interpret the GPR profiles taken for this study.

The 2D profile revealed prominent reflections in the form of hyperbolas between 4 m and 5 m horizontal markers and inclined discontinuities georadar reflections between 10 m and 28 m (Figure 3(a)). The hyperbolic reflections extending up to the depth of 2.5 m are interpreted as a metal pipe. In field, the local villagers informed that this was a main



(a)



(b)

FIGURE 2: (a) CORONA satellite photo showing distribution of active fault traces named as “Hajipur faults”—HF1 and HF2 on the left bank of Beas River near Hajipur village [25]. Box shows the location of trench and GPR profile line across the HF2 fault scarp at Sandhwal village. Empty arrow marks the direction of fault propagation towards NW. Young tectonic movements along HF1 and HF2 faults resulted into uplift of floodplain deposits, responsible for the shifting/deflection of the Beas River channel along its present course. (b) Panoramic view of HF2—Hajipur fault scarp. PQ indicates the 2D scan, and ABCD indicates the 3D grid collected, respectively across the fault which is marked in red arrows.

pipeline that supplies water to a few surrounding villages. Looking the typical characteristic of the multiple inclined radar reflectors marked by discontinuous nature, with warping close to the dipping reflections, it is suggested that

such a pattern was due to displacement of near subsurface young sediment succession caused by faulting (Figures 3(a) and 3(b)). The strong warping observed between 24 m and 28 m horizontal markers extending from 1 m to 5.5 m in

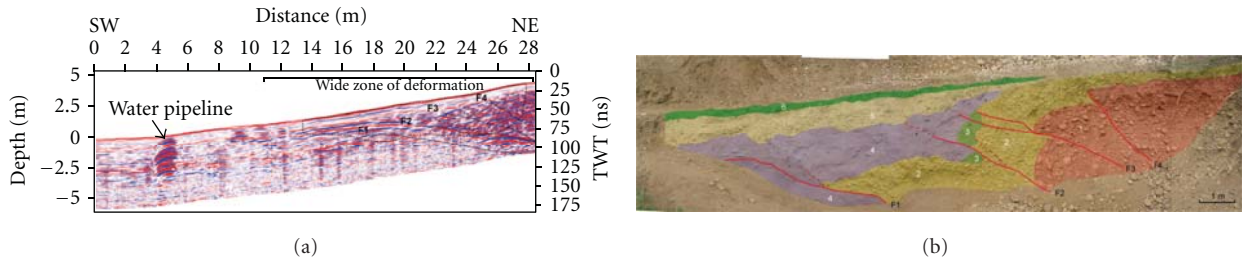


FIGURE 3: (a) Processed 2D GPR profile collected using 200 MHz antenna across the HF2 scarp at Sandhwal Village (refer to Figures 2(a) and 2(b) for location). The profile was about 29 m long showing the processed profile after topographic correction. Reflections at 4-5 m indicate water pipeline, whereas the reflections from 14-28 m show the fault traces. Box with dotted line shows approximate area of a trench. (b) Interpretation with fault traces and stratigraphic units on north wall of trench excavated across HF2 fault scarp. F1, F2, F3, and F4 are the thrust faults dipping in NE direction. Latest event has been observed along F1, F2, and F3 displacing the units 1, 2, 3, and 4.

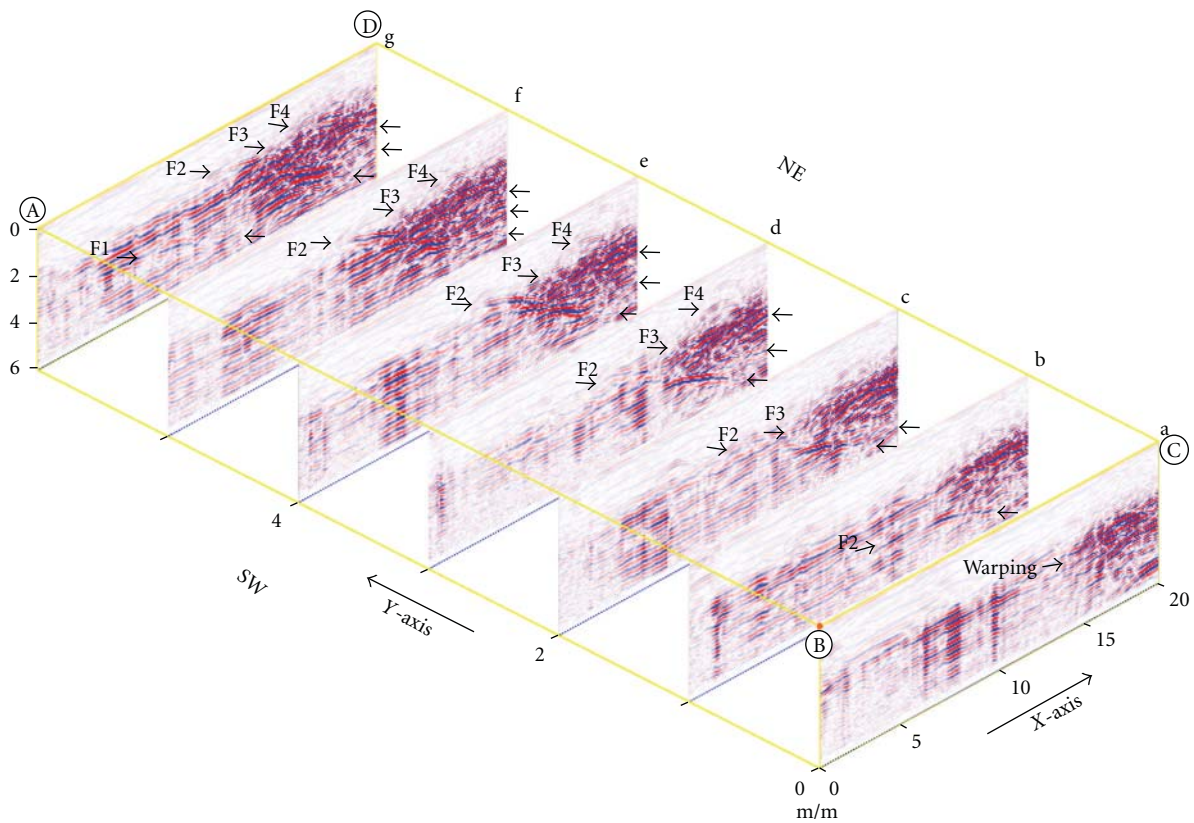


FIGURE 4: Sliced 3D grid profile across the HF2 scarp at Sandhwal Village collected with 200 MHz antenna (refer to Figures 2(a) and 2(b) for location). The profile was collected for a grid-ABCD with dimensions of 20 m × 6 m. The dashed lines and arrowheads represent the faults. The grid was sliced along the Y-axis along the strike of the scarp at 1 m interval (seven slices from a-g). Changes in the pattern of deformation along the strike can be noticed from the slices. For location of the grid, refer to Figure 2.

depth is related to the deformation on hanging wall side (Figures 3(a) and 3(b)). Considering the angle of dip in the 2D profile, it can be suggested that the deformation is due to movement from NE to SW along a major low-angle thrust fault (Figures 3(a) and 3(b)). Discontinuity and warping of the reflectors along more than one inclined reflection suggest splay of branching faults from the main fault.

To have proper understanding of the fault geometry along the strike, 3D profile collected was vertically sliced at

an interval of 1 m (Figure 4). The grid was sliced along the Y-axis (i.e., along the strike of the fault scarp) into seven layers with 1 m spacing, namely a, b, c, d, e, f, and g (Figure 4). Each layer represents the line scan profile at 1 m interval. After close analysis, four low-angle fault strands were identified in slices (a-g) which were named as F1, F2, F3, and F4. The F2 strand was identified in all slices, where in slices a, b, and c, it is marked by low-angle dipping towards NE between 10 m and 20 m horizontal markers and clearly traceable from

surface up to 6 m of depth (Figure 4). Prominent warping of georadar reflections was observed on the northeast side of the fault plane, which represents the hanging wall. A change in dip of F2 strand was observed in slice *b* (Figure 4). In addition to this other fault, strands F3 and F4 were seen in slices *d–g*. These strands are also dipping in NE direction with slightly higher angle. Strand F1 was observed between 3 m and 10 m horizontal markers in slice *g* only. It is marked by slightly steeper angle in basal part and becomes almost subhorizontal towards the surface (Figure 4).

Based on the multiple fault strands identified in 2D and 3D profiles, it is suggested that the F1 is probably the main fault propagating towards foreland and F2, F3, and F4 are the branching out faults. The 3D slice *g* and 2D profile collected gave similar features; hence, with this information for detailed paleoseismic investigation a trench with dimension—16 m long, 4–5 m wide 1–3 m deep was excavated across the HF2 fault scarp in NE-SW direction [20] (Figure 3(b)). The trench wall matched the fault strands identified in GPR profiles (Figures 3(a) and 3(b)).

The splays, namely, F1, F2, F3, and F4 identified in GPR profiles were comparable with the exposed trench section (Figures 3(a) and 3(b)). Trench section revealed five sedimentary units 1–6. Units 1 and 2 are rounded to sub-rounded gravel-poorly sorted cobble-pebble with sandy matrix. These units are marked by high-prominent geo-radar reflections observed on the NE part of the profiles. The warping reflection can well be justified by the preferred orientation of gravel clasts, suggestive of folding related to faulting along the F1–F4 faults. The southern part of the trench is comprised of finer deposits as compare to the northern. These deposits are comprised of medium-to-fine sand (units 3–4). Unit 5 is made up of medium-to-coarse sand with scattered gravel finally caps the sequence. It is suggested that F1, F2, F3, and F4 are the thrust faults dipping in NE direction, and the latest event occurred along F1, F2, and F3 displacing the units 1, 2, 3, and 4. Because of the instability of trench wall due to coarser gravel clasts, we were not able to excavate the trench to see deeper section. However, the GPR profiles (2D and 3D) helped us tracing the fault at greater depth.

4. Conclusion

The GPR survey, 2D and 3D helped us in identifying the suitable location for trenching. The 3D profiling with slicing at 1 m interval gave a complete picture of variation in deformation in terms of the geometry of the fault and related deformation along the strike of the active fault (HF2). The 2D profile and slice *g* of 3D profile were considered to open a trench for paleoseismic investigations. The prominent georadar reflections marked with discontinuities on either side of the inclined planes, warping suggested faulting along thrust faults. Also with the limitation to excavate trench up to greater depth, GPR profiles provide information on deformation and structure of greater depth. It is, therefore, suggested that GPR is one of the important tools which can be used for mapping the near subsurface displacements and variation in deformation along the strike of the active fault.

Acknowledgments

Financial support provided to the research project sponsored by DST, New Delhi, (vide project no. SR/S4/ES-417/2009) is duly acknowledged. We are grateful to two anonymous referees for providing valuable suggestions and comments, this helped us in improving the paper and brought more clarity to our findings. We are also thankful to our institute IIT Kanpur for providing support to our students.

References

- [1] V. P. Solonenko, "Paleoseismogeology," *Izvestiya, Academy of Sciences, USSR, Physics of the Solid Earth*, vol. 9, pp. 3–16, 1973.
- [2] K. Sieh, "Pre-historic large earthquakes produced by slip on the San Andreas Fault at Pallett Creek," *Journal of Geophysical Research*, vol. 83, pp. 3907–3939, 1978.
- [3] R. E. Wallace, "Active faults, Palaeoseismology, and earthquake hazards in the Western United States," in *Earthquake Prediction. An International Review*, D. W. Simpson and P. G. Richards, Eds., pp. 209–216, American Geophysical Union, Washington, DC, USA, 1981.
- [4] R. E. Wallace, "Variations in slip rates, migration, and grouping of slip events on faults in the Great Basin Province," *Bulletin of Seismological Society of America*, vol. 77, pp. 868–876, 1987.
- [5] D. P. Schwartz and K. J. Coppersmith, "Fault behavior and characteristic earthquakes: examples from the Wasatch and San Andreas fault zones (USA)," *Journal of Geophysical Research*, vol. 89, no. 7, pp. 5681–5698, 1984.
- [6] C. R. Allen, "Seismological and paleoseismological techniques of research in active tectonics," in *Active Tectonics*, R. E. Wallace, Ed., pp. 148–154, National Academy Press, Washington, DC, USA, 1986.
- [7] J. P. Mc Calpin, Ed., *Paleoseismology*, Academic Press, San Diego, Calif, USA, 1996.
- [8] R. S. Yeats, K. Sieh, and C. R. Allen, *Geology of Earthquakes*, Oxford University Press, 1997.
- [9] R. S. Yeats and V. C. Thakur, "Reassessment of earthquake hazard based on a fault-bend fold model of the Himalayan plate-boundary fault," *Current Science*, vol. 74, no. 3, pp. 230–233, 1998.
- [10] K. B. Anderson, J. A. Spotila, and J. A. Hole, "Application of geomorphic analysis and ground-penetrating radar to characterization of paleoseismic sites in dynamic alluvial environments: an example from southern California," *Tectonophysics*, vol. 368, no. 1–4, pp. 25–32, 2003.
- [11] J. N. Malik and C. Mohanty, "Active tectonic influence on the evolution of drainage and landscape: geomorphic signatures from frontal and hinterland areas along the Northwestern Himalaya, India," *Journal of Asian Earth Sciences*, vol. 29, no. 5–6, pp. 604–618, 2007.
- [12] A. Neal, "Ground-penetrating radar and its use in sedimentology: principles, problems and progress," *Earth-Science Reviews*, vol. 66, no. 3–4, pp. 261–330, 2004.
- [13] J. P. Busby and J. W. Merritt, "Quaternary deformation mapping with ground penetrating radar," *Journal of Applied Geophysics*, vol. 41, no. 1, pp. 75–91, 1999.
- [14] L. Liu and Y. Li, "Identification of liquefaction and deformation features using ground penetrating radar in the New Madrid seismic zone, USA," *Journal of Applied Geophysics*, vol. 47, no. 3–4, pp. 199–215, 2001.

- [15] J. C. Audru, M. Bano, J. Begg, K. Berryman, S. Henryys, and B. Niviere, "GPR investigations on active faults in urban areas: the Georisc-NZ project in Wellington, New Zealand," *Comptes Rendus de l'Académie des Sciences-Series IIA- Earth and Planetary Science*, vol. 333, no. 8, pp. 447–454, 2001.
- [16] R. Gross, A. Green, K. Holliger, H. Horstmeyer, and J. Baldwin, "Shallow geometry and displacements on the San Andreas fault near Point Arena based on trenching and 3-D georadar surveying," *Geophysical Research Letters*, vol. 29, no. 20, pp. 34–1, 2002.
- [17] A. Green, R. Gross, K. Holliger, H. Horstmeyer, and J. Baldwin, "Results of 3-D georadar surveying and trenching the San Andreas fault near its northern landward limit," *Tectonophysics*, vol. 368, no. 1–4, pp. 7–23, 2003.
- [18] L. Slater and T. M. Niemi, "Ground-penetrating radar investigation of active faults along the Dead Sea Transform and implications for seismic hazards within the city of Aqaba, Jordan," *Tectonophysics*, vol. 368, no. 1–4, pp. 33–50, 2003.
- [19] P. J. Alasset and M. Meghraoui, "Active faulting in the western Pyrénées (France): paleoseismic evidence for late Holocene ruptures," *Tectonophysics*, vol. 409, no. 1–4, pp. 39–54, 2005.
- [20] J. N. Malik, A. A. Shah, A. K. Sahoo et al., "Active fault, fault growth and segment linkage along the Janauri anticline (frontal foreland fold), NW Himalaya, India," *Tectonophysics*, vol. 483, no. 3–4, pp. 327–343, 2010.
- [21] B. K. Sternberg and J. W. McGill, "Archaeology studies in southern Arizona using ground penetrating radar," *Journal of Applied Geophysics*, vol. 33, no. 1–3, pp. 209–225, 1995.
- [22] B. M. Whiting, D. P. McFarland, and S. Hackenberger, "Three-dimensional GPR study of a prehistoric site in Barbados, West Indies," *Journal of Applied Geophysics*, vol. 47, no. 3–4, pp. 217–226, 2001.
- [23] J. N. Malik, A. K. Sahoo, and A. A. Shah, "Ground-penetrating radar investigation along Pinjore Garden Fault: implication toward identification of shallow subsurface deformation along active fault, NW Himalaya," *Current Science*, vol. 93, no. 10, pp. 1422–1427, 2007.
- [24] S. Satuluri, "Ground penetrating radar application in archaeological investigations at ahichhatra, bareilly (Distt)," M.Tech Dissertation Report, Department of Civil Engineering, Indian Institute of Technology, Kanpur, India, 2009.
- [25] J. N. Malik, A. K. Sahoo, A. A. Shah, D. P. Shinde, N. Juyal, and A. K. Singhvi, "Paleoseismic evidence from trench investigation along Hajipur fault, Himalayan Frontal Thrust, NW Himalaya: implications of the faulting pattern on landscape evolution and seismic hazard," *Journal of Structural Geology*, vol. 32, no. 3, pp. 350–361, 2010.
- [26] L. Seeber and J. G. Armbruster, "Great detachment earthquakes along the Himalayan arc and long-term forecasting," in *Earthquake Prediction. An International Review*, D. W. Simpson and P. G. Richards, Eds., vol. 4 of *Maurice Ewing Series*, pp. 259–279, AGU, 1981.
- [27] N. Ambraseys and R. Bilham, "A note on the Kangra $M_s = 7.8$ earthquake of 4 April 1905," *Current Science*, vol. 79, no. 1, pp. 45–50, 2000.
- [28] N. N. Ambraseys and J. Douglas, "Magnitude calibration of north Indian earthquakes," *Geophysical Journal International*, vol. 159, no. 1, pp. 165–206, 2004.
- [29] C. S. Bristow and H. M. Jol, *Ground Penetrating Radar in Sediments*, NO. 211, Geological Society, London, UK, 2003.
- [30] Jol H. M., *Ground Penetrating Radar: Theory and Applications*, Elsevier Scientific, Oxford, UK, 2009.
- [31] J. Chow, J. Angelier, J. J. Hua, J. C. Lee, and R. Sun, "Paleoseismic event and active faulting: from ground penetrating radar and high-resolution seismic reflection profiles across the Chihshang Fault, eastern Taiwan," *Tectonophysics*, vol. 333, no. 1–2, pp. 241–259, 2001.

Review Article

Analysis and Interpretation of the Field and Laboratory Geophysical Measurements of Black-Sand Beach Deposits, East Rosetta, Egypt

Mohamed A. El-Sadek, Ahmed A. Ammar, and Sayed A. Elkhateeb

Exploration Division, Nuclear Materials Authority, P.O. Box 530, Maadi, Cairo, Egypt

Correspondence should be addressed to Mohamed A. El-Sadek, elsadek_eg@yahoo.com

Received 13 November 2011; Accepted 3 February 2012

Academic Editor: Francesco Soldovieri

Copyright © 2012 Mohamed A. El-Sadek et al. This is an open access article distributed under the Creative Commons Attribution License, which permits unrestricted use, distribution, and reproduction in any medium, provided the original work is properly cited.

The present study deals with the analysis and interpretation of the results of field geophysical survey and laboratory geophysical measurements. The study of the magnetic and electrical methods was selected because the beach sands contain many minerals that have magnetic and electric properties. Analysis and interpretation of the field and laboratory magnetic and geoelectric maps demonstrated that the investigated beach-alluvial deposits can be subdivided according to their magnetic and geoelectric properties into three main zones striking nearly parallel to the shoreline of the Mediterranean Sea at the study area. The northern zone is more enriched in black sands than the central or southern zones. Field and laboratory magnetic susceptibility measurements provided very useful maps for the concentration of heavy minerals. The deep-seated magnetic response was calculated at an average depth of 239.6 m, while the near-surface magnetic responses were computed at average depths of 9.1, 57.9, and 81.8 m, respectively. The correlation between the geophysical features, recorded on the total magnetic field intensity, the electric resistivity, the IP chargeability, and the calculated metal factor, was found to agree to a great extent. The heavy mineral concentration was found to decrease with depth. However, the heavy minerals show parallel zones below the surface, suggesting similar sedimentation environments.

1. Introduction

The alluvial-beach placer deposits, East Rosetta, Mediterranean Sea Coast, Northern Egypt, are known for their enhanced natural radiation environment, due to the presence of radiogenic heavy minerals, such as monazite and zircon, which contain Th and U in their chemical composition [1]. The placer deposits are well known as sources for economic heavy minerals and nuclear raw materials, in addition to their importance in many of the strategic, metallurgical, and engineering industries. The mineralogical analyses identified six main heavy mineral sands accompanied by traces of cassiterite and gold as well as some minerals of rare earth elements (REEs). According to their relative frequencies, the six heavy minerals include ilmenite, magnetite, zircon, monazite, garnet, and rutile. The study area ($30^{\circ}32'10''$ E and $30^{\circ}34'08''$ E long.; $31^{\circ}26'59''$ N and $31^{\circ}27'59''$ N lat.) extends

over a length of 3.0 km, trending in an E-W direction along the Mediterranean Sea Coast, with an average width of more than 1.8 km (Figure 1).

The main objectives of the present study are

- (1) evaluation of surface extensions of the beach-alluvial deposits, using field magnetic and susceptibilities survey, as well as laboratory magnetic and geoelectric measurements;
- (2) mapping the spatial distribution patterns of zones of heavy mineral concentrations;
- (3) identification of the depositional phases;
- (4) delineation of the subsurface (shallow and deep seated) magnetic sources.

Figure 2 shows the schematic diagram for all techniques employed in the study area.

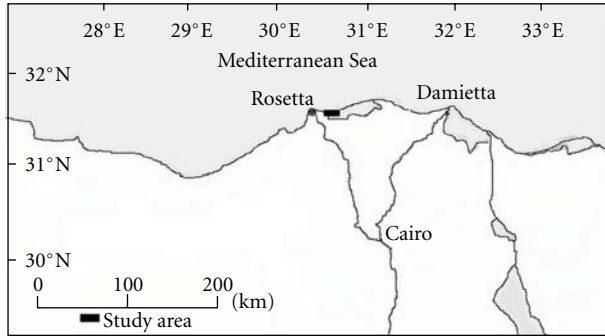


FIGURE 1: Map of Northern Egypt showing the location of the study area.

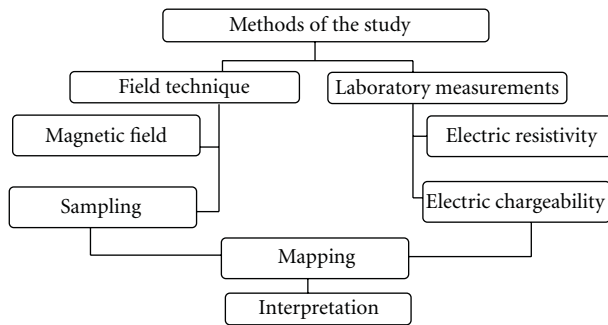


FIGURE 2: Schematic diagram for all the techniques in the study area.

Placer sand deposits in the northern Nile Delta, especially in Koam Mashaal area, have received the attention of several researchers since the early years of the 20th century. The most recent researches that carried out studies on these placer sands include Hedrick and Waked [2], Elhadary [3], Abu-Diab [4], El-Sadek and Elkhateeb [5], Bakheit [6], Ammar et al. [1], and Moustafa [7]. The study area is a part of the semiarid coastal region which is characterized by its wide plain covered by placer sand deposits.

The placer deposits, East Rosetta, have high mineral productivity, which can be easily mined. El Askary and Frihy [8] identified three depositional phases in the upper 30 m at Rosetta and Damietta promontories. These are from base to top: transgression, regression, and erosional transgression phases. The beach is generally flat in the Rosetta area, where seawater crosses the beach during winter stormy conditions and high-tide periods [9].

2. Materials and Methods

2.1. Ground Magnetic Survey. The ground magnetic survey was conducted along a set of equally spaced (100 m) parallel traverses oriented N-S, a direction that is perpendicular to the general extension of the Mediterranean Sea Coast in the study area. The general strike of the lithological units in the study area was determined according to the general elongation of the black-sand lenses occurring along the Mediterranean Sea Coast, which approximately extends in

an E-W direction. Magnetic measurements were made at regular intervals of 10 m. The survey data were tied along one tie line perpendicular to the direction of the survey traverses. A base station was placed at a reference point, selected far from artificial magnetic disturbances within the surveyed area. The total magnetic-intensity measurements, collected at the survey stations, were regarded as positive or negative deviations from the ones at the reference point (base station).

The ground raw magnetic survey measurements were subjected to essential corrections, including diurnal as well as tie-line corrections. On the other hand, the terrain correction was not applied to the magnetic data, since the surveyed area is characterized by its smooth terrain and insignificant elevation differences between survey stations. The geomagnetic correction was calculated at the central point of the study area, where the International Geomagnetic Reference Field (IGRF) reaches 43,519.12 nT, the inclination angle attains 45.89°, and the declination angle equals 2.78° at 31°27'05''N lat. and 30°33'00''E long. in October 30, 2001 [10]. The IGRF value was subtracted from the readings of the whole survey stations. The survey data were transformed from the field magnetometer to a desktop computer, where data reduction was performed by using a set of computer softwares (Microsoft Excel, MDA1-Ver.1.97 and MDA2-Ver.1.97).

The total magnetic-field intensity measurements were carried out using a portable proton-precession magnetometer, model PMG-1, Geofyzika Brno, Czech Republic, having a sensitivity of 0.1 nT and a measuring range from 25,000 to 100,000 nT (PGM-1 Manual, 1997). Another magnetometer of the same type was used as a base station for automatic monitoring and recording of diurnal variations in the Earth's magnetic field. The measuring time was set for one minute at the base station as a matter of diurnal variation and storage capacity of the instrument.

The ground magnetic survey data, including spectral frequency analysis and isolation of magnetic anomalies, were carried out using the software of Magnetic Data Analysis (MDA2-Ver 1.97; [11]), which is based on Filon Fourier Transform. This software designs the suitable filter and separates the regional and residual magnetic components.

2.2. Field and Laboratory Magnetic Susceptibility Measurements. The pocket susceptibility meter, type KT-6, Geofyzika Brno, Czech Republic, is designed for quick-field measurements of magnetic susceptibility of outcropping rocks, drill cores, and larger pieces of rocks. The sensitivity of the equipment is 1×10^{-5} SI units, and the measuring range varies from -999 to 9,999 SI units, with automatically switched accuracies: 9.99, 99.9, and 999 [12]. It was used to determine the magnetic susceptibility both in field and laboratory. The samples were friable with size about 234 grams. The black-sand samples were put in plastic cylindrical containers of 11.0 cm in diameter and 6.0 cm in height. The magnetic susceptibility measurements were applied to surface field measurements and quartered 966 representative samples, taken from large samples, collected from the field up to 50 cm in depth. The collected samples were taken along

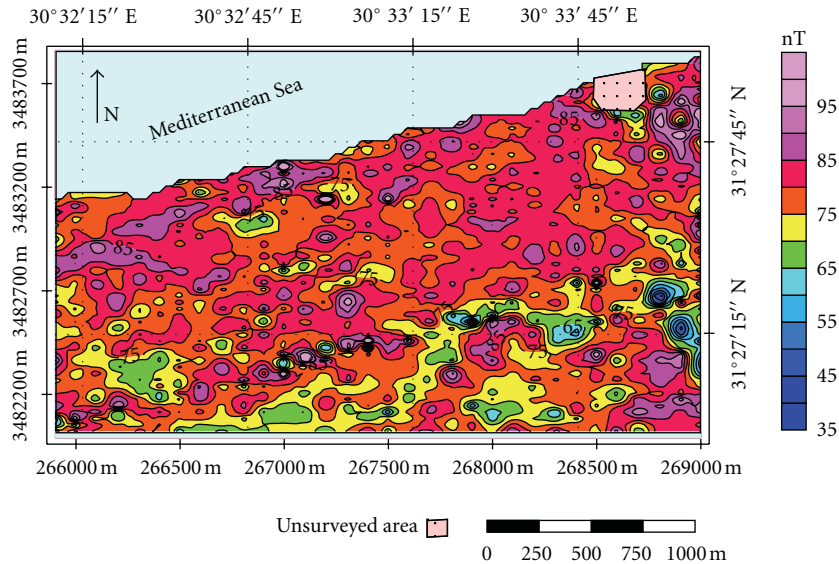


FIGURE 3: Filled colour contour map of the total magnetic intensity of Koam Mashaal area, East Rosetta, Mediterranean Sea Coast, Northern Egypt.

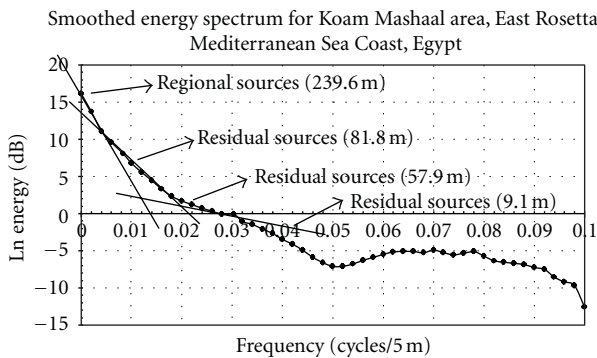


FIGURE 4: The local power spectrum of the ground magnetic data for the study area.

equally spaced stations, 50 m apart, at 32 parallel equally spaced (100 m) profiles. These profiles were oriented in an N-S direction and spaced at 100 m intervals, covering an area of about 5.4 km².

A 12-channel global positioning system (GPS) instrument was used to set up the survey grid with a Universal Transverse Mercator (UTM) coordinate system, using World Grid (WG84) as datum. All samples were put in plastic bags and labelled by their UTM positions.

2.3. Laboratory Geoelectric Measurements. The laboratory geoelectric (resistivity and chargeability) measurements were applied to the 966 quartered representative samples, taken from large samples collected in the field at depths up to 50 cm. The large samples were taken along 32 equally spaced (100 m apart) profiles, at equally spaced (50 m apart) stations. These profiles were oriented in an N-S direction, covering about 5.4 km². The samples were taken by pushing a rigid plastic tube (5 cm in diameter and 70 cm in length)

into the ground up to 70 cm in depth. The collected samples were quartered using John’s splitter.

The ELREC-2 instrument, induced polarization of low power system (IP-L system), manufactured by IRIS Instruments, France, was used in this study to measure the electric resistivity and induced polarization (IP) parameters on the 966 quartered representative samples collected from the field as previously mentioned. The measuring system consists of three units: a sample holder frame, an IP-L low-power time domain transmitter, and an ELREC-2 as a time-domain IP receiver [13]. The sample holder was modified to be compatible with friable sand samples. The new holder is a rigid plastic tube, with a plastic piston to compress the friable sand. This plastic tube possesses four-minute holes at equal distances of 4.0 cm, as a Wenner array, and four-electrode terminals for connecting the electric current. The two current electrodes are connected to the external holes and the two potential electrodes to the central holes.

3. Results and Discussion

3.1. Magnetic Survey. Environmental magnetism deals with the magnetic properties of natural iron oxides as a tool for understanding and interpreting the processes in sedimentary systems [14–16]. It was applied successfully in modelling sediment loads in fluvial systems [17, 18]. The intensity of magnetization of a rock is largely dependent upon the amount, size, shape, and distribution of its content of ferromagnetic minerals that usually represent only a small proportion of its mineral composition. Much qualitative information may be derived from magnetic contour maps. Such qualitative interpretation may be greatly facilitated by the use of digital image-processing techniques, similar to those used in the display of remotely sensed data [19]. The corrected ground magnetic data were subjected to various

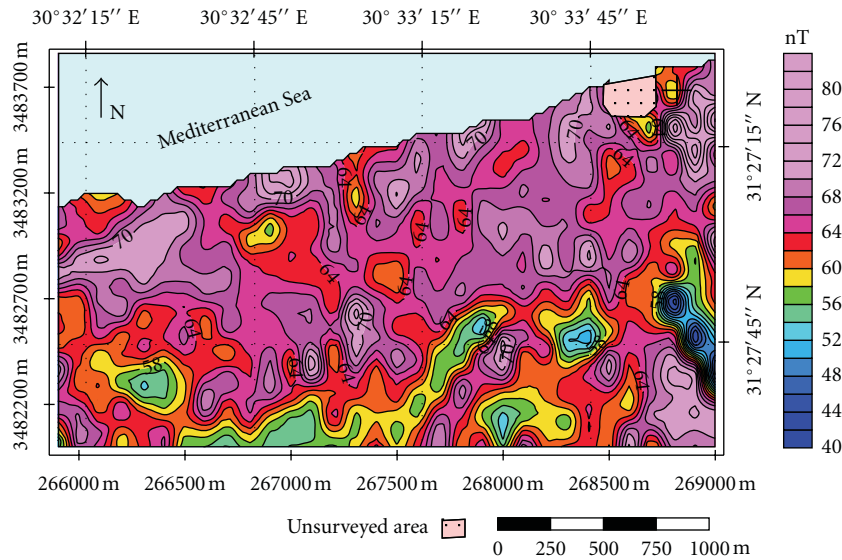


FIGURE 5: Filled colour contour map of the regional component of magnetic-field intensity of Koam Mashaal area, East Rosetta, Mediterranean Sea Coast, Northern Egypt at an average depth (h) of 239.6 m, contour interval = 2 nT.

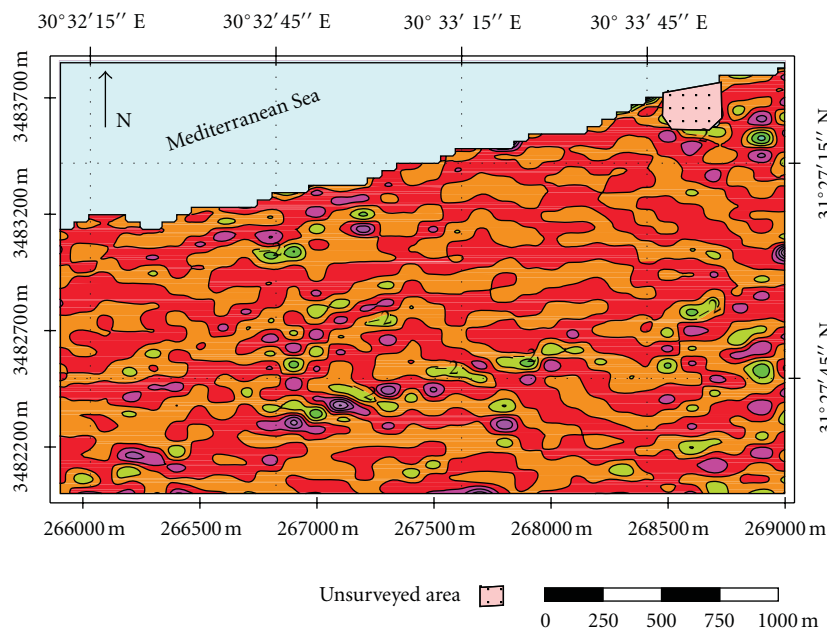


FIGURE 6: Filled colour contour map of the residual component of magnetic-field intensity of Koam Mashaal area, East Rosetta, Mediterranean Sea Coast, Northern Egypt at an average depth (h) of 9.1 m, contour interval = 2 nT.

techniques of analysis in order to get qualitative and quantitative parameters that can well describe the subsurface magnetic sources and consequently guide the exploratory drilling for the buried heavy mineral lenses in the study area. These techniques involved the application of spectral analysis and matched filtering.

3.2. *Spectral Analysis of the Ground Magnetic Survey Data.* Frequency analysis of the potential field data using the

computer software that implements the fast Fourier transform (FFT) has now become a routine practice. The fast Fourier transform is a computational tool which facilitates signal analysis such as power spectrum analysis and filter simulation by means of digital computers. It is a method for efficiently computing the discrete Fourier transform of a series of data samples. It has become a widely used tool for interpretation of potential field data, especially for depth estimation. This approach has been developed by many workers (e.g., [20–22]). However, it was proved that the

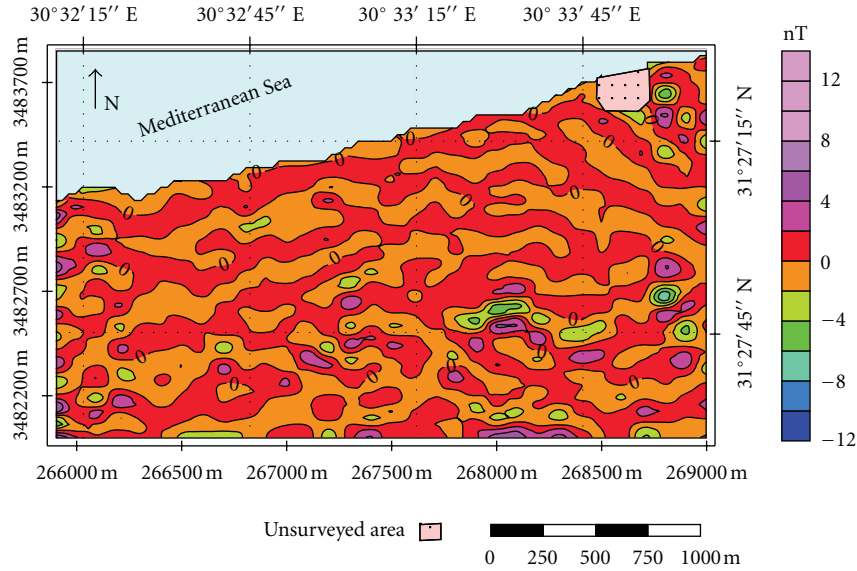


FIGURE 7: Filled colour contour map of the residual component of magnetic-field intensity of Koam Mashaal area, East Rosetta, Mediterranean Sea Coast, Northern Egypt at an average depth (h) of 57.9 m, contour interval = 2 nT.

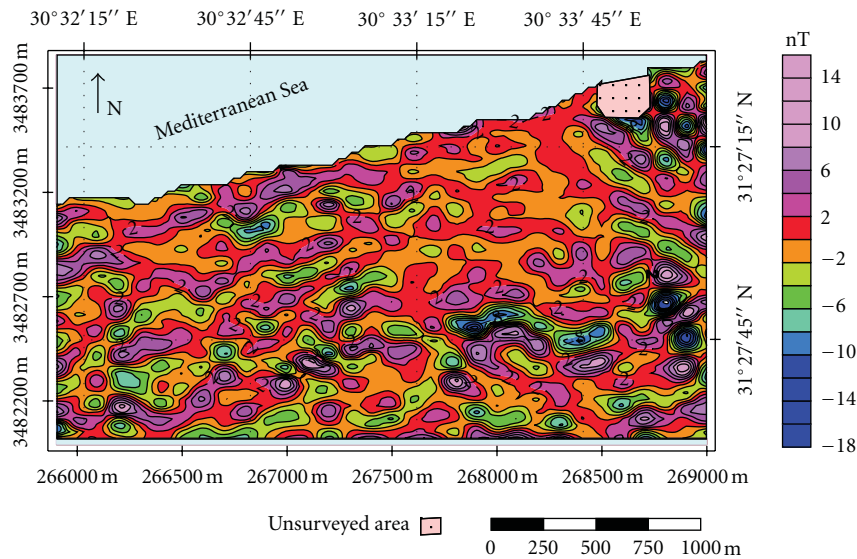


FIGURE 8: Filled colour contour map of the residual component of magnetic-field intensity of Koam Mashaal area, East Rosetta, Mediterranean Sea Coast, Northern Egypt at an average depth (h) of 81.8 m, contour interval = 2 nT.

FFT introduces unacceptable distortions at high frequencies, which describe the response of shallow sources. Accordingly, the interpretation of such sources using FFT is not very reliable [23]. The use of the filon Fourier transform in the spectral analysis of potential field data decreases the distortions in the high-frequency range and thus enables reasonable depth estimates to shallow sources, which are of considerable interest in mineral exploration. Figure 4 shows the local power spectrum of the ground magnetic data for the study area using the magnetic Data Analysis (MDA) software [11].

3.3. Total Magnetic-Field Intensity Map. The recorded total magnetic-field intensity measurements in the study area

ranges from 35 to 115 nT. The magnetic intensities are roughly arranged in two zones parallel to the shoreline, orienting in an NW-SE direction (Figure 3). The northern part is mainly characterized by relatively higher values of the total-field magnetic intensity measurements. It is mainly enriched in black sands of a beach lens as well as old sand dunes. The magnetic response is mainly due to the existence of magnetite and other magnetic minerals either on the surface or at very shallow depths. The southern part is mainly magnetically lower in intensity values.

3.3.1. Regional Magnetic-Field Intensity Map. Frequencies of magnetic anomalies could reveal the depths of their magnetic sources. The regional magnetic-field intensity map

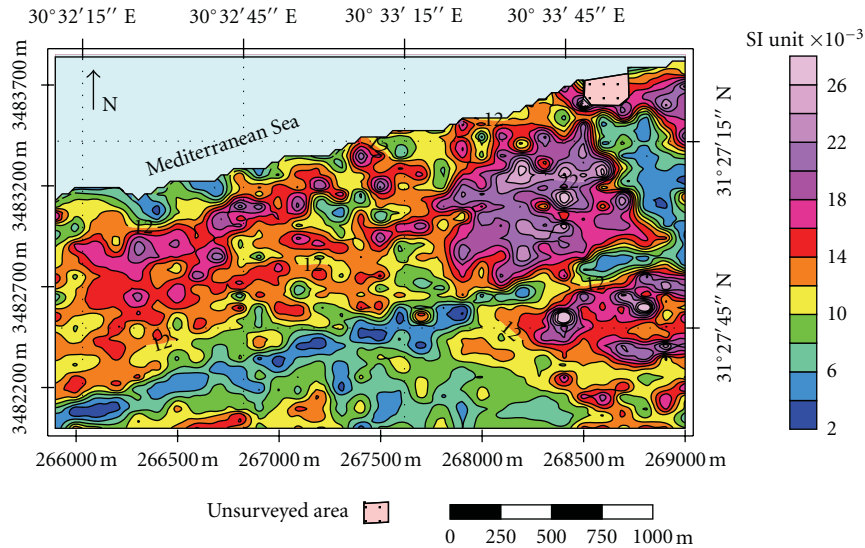


FIGURE 9: Filled colour contour map of field magnetic susceptibility (k_F) measurements, Koam Mashaal area, East Rosetta, Mediterranean Sea Coast, Northern Egypt. Contour interval = 2×10^{-3} SI unit.

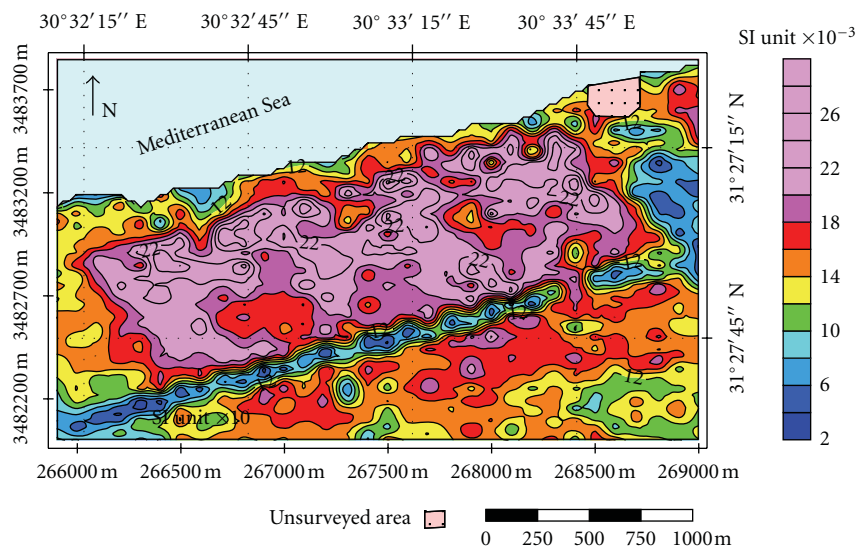


FIGURE 10: Filled colour contour map of laboratory magnetic susceptibility (k_L) measurements on samples, Koam Mashaal area, East Rosetta, Mediterranean Sea Coast, Northern Egypt. Contour interval = 2×10^{-3} SI unit.

(Figure 5) represents the relatively deep-seated magnetic response of the black-sand beach and dune deposits, at an average depth of 239.6 m (Figure 4). Figure 5 shows that the study area could be also divided into two main zones according to magnetic causative sources. The first zone, located in the northern part of the study area, is characterized by its high magnetic-amplitude anomalies, with low frequencies and long wavelengths, which refer to deep-seated lenses of black-sand deposits. It is also characterized by high to very high magnetic response, ranging in amplitude from 76 nT to 88 nT. The other zone, located in the southern part of the study area, is characterized by variations in magnetic responses from low to very high (64 nT to 88 nT), with higher frequencies and shorter wavelengths. The high and

low magnetic bands, within the second zone, are arranged into elongated stripes oriented in the NE-SW direction.

3.3.2. Residual Magnetic-Field Intensity Map. An important interpreting technique in geophysical exploration is the residual mapping, in which local anomalies are separated from regional ones. According to Burger [24], the definition of residual depends on the exploration target. The residual magnetic intensity contour maps (Figures 6, 7, and 8) represent the magnetic responses of the black-sand deposits at various depths of 9.1, 57.9, and 81.8 m, respectively (Figure 4). The magnetic-field intensity ranges from 25 nT to 45 nT, -40 to 30 nT, and -16 to 12 nT at the three depths,

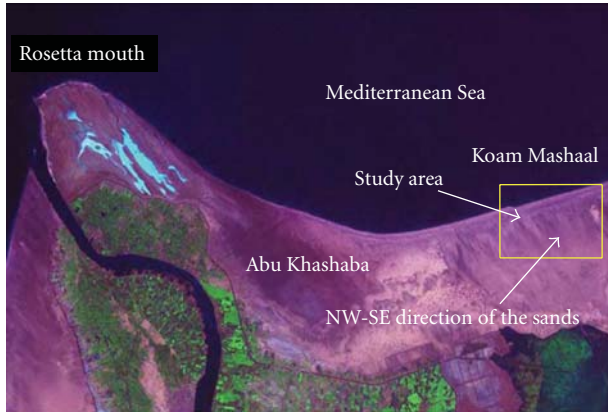


FIGURE 11: Northern Egypt Landsat colour composite image showing the location of the studied Koam Mashaal beach area, East Rosetta, Mediterranean Sea Coast.

respectively. The magnetic zones are elongated and roughly parallel to the shoreline. The magnetic zones are almost similar at the three depths, suggesting similar sedimentation environment. The magnetic intensity at 81.8 m depth is much lower than the shallower depths (9.1 m and 57.9 m).

3.4. Magnetic Susceptibility Measurements. As a result of the presence of the earth's magnetic field, rocks containing magnetic minerals show induced magnetizations. The constant of proportionality between the inducing field and the magnetization is known as the magnetic susceptibility (k). The intensity of magnetization (I) is related to the inducing magnetic field (H) through a constant of proportionality (k):

$$I = kH. \quad (1)$$

The magnetic susceptibility (k) is a measure of the ease by which the material can be magnetized. It is a dimensionless quantity. Magnetic susceptibility can take on positive or negative values. Positive values imply that the induced magnetic field (I) is in the same direction as the inducing field (H). Negative values imply that the induced magnetic field is in the opposite direction as the inducing field. The magnetic susceptibilities of paramagnetic and diamagnetic materials are generally extremely small. Although susceptibility is unitless, its values differ depending on the unit system used to quantify H and I . The international system of units (SI), based on the meter, kilogram, second, and ampere (mksa), was used in the present study [19, 25]. Based on the magnetic susceptibility, the solid materials can be classified into diamagnetic, paramagnetic, and ferromagnetic. In diamagnetic, k has low and negative values. Paramagnetic materials have low and positive k values. Ferromagnetism is a cooperative phenomenon observed in metals like iron, nickel, and cobalt. Ferromagnetic behaviour is characterized by high positive susceptibilities and strong magnetic properties [26]. The intensity of magnetization of rocks can be determined in two different ways: by measuring the magnetic field produced either by a rock sample or by measuring the effect of the sample on the inductance of an electromagnetic circuit [27].

3.4.1. Field Magnetic Susceptibility (k_F) Measurements. Magnetic susceptibility (k_F) can be measured easily, fast, and with high sensitivity in the field by using pocket susceptibility meter, type KT-6. The measurements of field magnetic susceptibility attain their maximum values reaching about 38.0×10^{-3} SI units in the northeastern part of the study area, in the form of a great anomaly running parallel to the shoreline. The minimum k_F value reaching 1.52×10^{-3} SI units forms an elongated narrow zone, parallel to the shoreline, roughly in the centre of the study area, where an old dry excavated drainage channel is existing (Figure 9). The mean value of k_F in the study area reaches 12.2×10^{-3} SI units. Interestingly, Figures 8 and 9 clearly demonstrate that some of the relatively high residual magnetic anomalies correspond to the relatively low magnetic susceptibility measurements; this indicates that the heavy minerals increase with depth.

3.4.2. Laboratory Magnetic Susceptibility (k_L) Measurements. The measurements of laboratory magnetic susceptibility (k_L) attain their maximum value reaching about 28.6×10^{-3} SI units in the central northeastern part of the area under study in the form of a great anomaly running parallel to the shoreline (Figure 10). The minimum k_L value reaching 2.16×10^{-3} SI units is situated in the central southern part of the study area, which represents an old dry excavated drainage channel. The mean value of k_L in the study area reaches 15.67×10^{-3} SI units.

The filled colour contour maps for field and laboratory magnetic susceptibility measurements (Figures 9 and 10, resp.) show great similarity between each other, especially for the positions of the black-sand lenses. Some of the delineated high magnetic susceptibility anomalies are circular in shape and others are elongated, either parallel to the shoreline or perpendicular to it. The highest levels of magnetic susceptibility are located nearly in the central part and in the north-eastern corner of the study area. These levels are associated with the eastern side of the major lens and the old sand dunes. The lowest levels of magnetic susceptibility are located in different places: close to the shoreline, southwards, and along the dry man-excavated drainage channel. The intermediate magnetic susceptibility level is distributed all over the remaining surface of the study area.

From the visual examination of all geophysical magnetic contour maps, it is noticed that the contours are elongated in two main directions, one parallel to the seashore, that is, in the N 75°E direction, and the other is oriented in the NW-SE direction. The values always point to low concentrations of heavy minerals towards the shore line and to the south of the study area. These observations could be interpreted as follows.

When the area is covered by standing sea water and its slow motion in winter seasons, the denser heavy minerals go down and the light ones float up by gravity. In the summer seasons when the seawater retreats, and the wind blows in an NW-SE direction; the light sand minerals are transported away from the shore to the south of the study area. Hence, the heavy minerals are concentrated by this way in an NW-SE

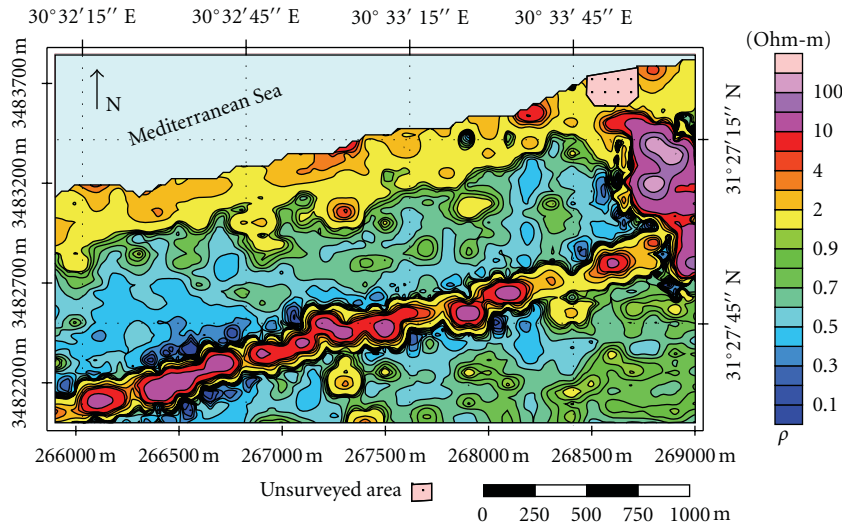


FIGURE 12: Filled colour contour map of the electric resistivity (ρ) laboratory measurements, Koam Mashaal area, East Rosetta, Mediterranean Sea Coast, Northern Egypt. Contour interval = 0.1 Ohm·m.

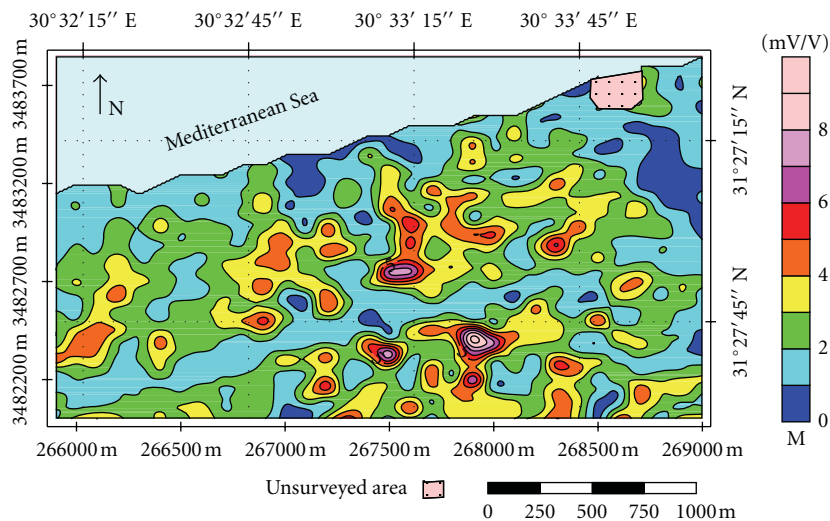


FIGURE 13: Filled colour contour map of the electric chargeability (M) laboratory measurements, Koam Mashaal area, East Rosetta, Mediterranean Sea Coast, Northern Egypt. Logarithmic contour interval = 1 MV/V.

direction, beside the main action of the sea waves (which act similarly to the action of a Wilfley table on the concentration of the heavy minerals) in a direction parallel to the sea shore (N 75°E direction). There are two other evidences for these two directions. The first one is the satellite image of the Rosetta area (Figure 11), which shows the NW-SE direction of the sands. The second evidence is concerned with the nonsurveyed area, located around the study area, which is occupied by a building that acts as a guard protecting the southeastern part from the wind action and consequently the concentration of heavy minerals.

3.5. Geoelectric Measurements. Electrical measurements are among the most difficult of all geophysical methods to interpret quantitatively, because of the complex theoretical

bases of the technique. Electric IP quantitative interpretation is considerably more complex than the electric resistivity method. Much electric IP interpretation is, however, only qualitative [19].

3.5.1. Laboratory Electric Resistivity Measurements. The recorded electric resistivity measurements range from 0.1 to 200 Ohm·m. The electric resistivity map (Figure 12) shows a prominent broad zone of low resistivity values, occupying most of the study area. A central high-resistivity zone, parallel to the shoreline, separates this prominent low-resistivity zone into two subzones. This central zone takes the form of a narrow strip of an elongated shape, trending to the NNW direction. It shows very high electric resistivity values (>100 Ohm·m), especially in its eastern part, where

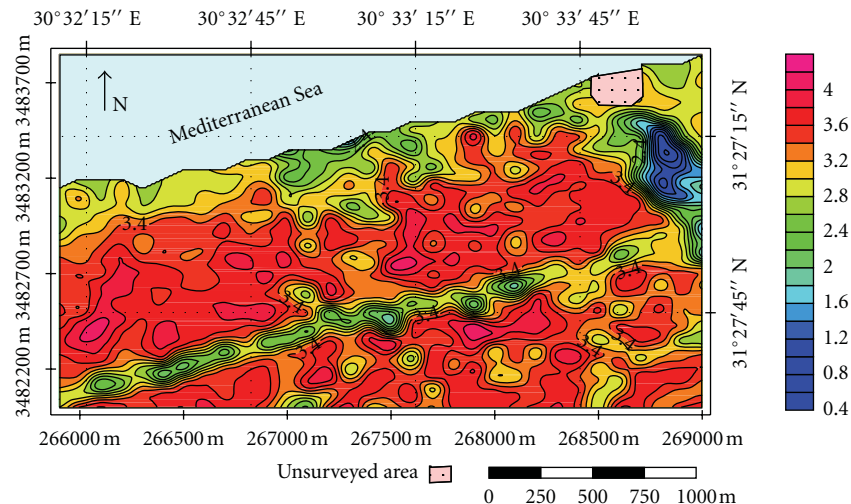


FIGURE 14: Filled colour contour map of the calculated metal factor (MF) values from laboratory measurements, Koam Mashaal area, East Rosetta, Mediterranean Sea Coast, Northern Egypt. Logarithmic contour interval = 0.2.

the old excavated drainage channel exists, as well as in the western part of some old sand dunes. There is also a relatively moderate- to high-electric-resistivity zone (from 1.0 to 10.0 Ohm.m.) delimiting the northern part of the study area, running parallel to the shoreline (Figure 12).

3.5.2. Laboratory Electric (IP) Chargeability Measurements. The low electric IP chargeability values agree well with the high electric resistivity values at the narrow zone, located in both central and eastern parts of the study area as well as its northern part (Figure 13). The intermediate- and high-electric-IP-chargeability zones also correspond well with the intermediate- and low-electric-resistivity zones, where the economic heavy mineral deposits occur. Two relatively high-electric-IP-chargeability zones were distinguished at the central northern, and southern parts of the study area, with electric IP chargeability values exceeding 11 mV/V, and they coincide well with the zones of very high concentrations of heavy minerals.

3.5.3. The Calculated Metal Factor. Similar to the distribution of the IP chargeability, and electric resistivity values, the high values of the calculated metal factor (Figure 14) coincide well with high electric IP chargeability and low electric resistivity values. Moreover, they indicate the existence of anomalous zones that occur at the central, northern, and southern parts of the study area, which also agree well with the zones of anomalous concentrations of economic heavy minerals.

4. Conclusions

The correlation between the geophysical features recorded on the maps of total magnetic field intensity, magnetic susceptibility, electric resistivity, IP chargeability and calculated metal factor of the study area was found to agree to a great extent. Field and laboratory magnetic and geoelectric maps

demonstrate that the investigated beach-alluvial deposits of Koam Mashaal area can be subdivided into three main zones striking nearly parallel to the shoreline of the Mediterranean Sea, Northern Egypt. The northern zone is more enriched in black sands than the central or southern zones. The heavy mineral concentration was found to decrease with depth. However, the heavy minerals also show some parallel zones below the surface, suggesting similar sedimentation environments. The deep-seated magnetic response was interpreted to lie at an average depth of 239.6 m, while the near-surface magnetic responses were interpreted to lie at average depths of 9.1, 57.9, and 81.8 m, respectively. The recorded electric resistivity measurements range from 0.1 to 200 Ohm·m. The high electric IP chargeability values coincide well with the high values of the calculated metal factor, low electric resistivity values, and high magnetic susceptibility values. These tools are very useful and are recommended for the study and investigation of black-sand beach deposits everywhere.

References

- [1] A. A. Ammar, A. S. Sharaaky, A. N. Shahein, M. A. El-Sadek, and S. A. Elkhateeb, "Radiolithologic studies on beach and alluvial black-sand deposits, Koam Mashaal area, Egypt, using ground radiospectrometry," in *Proceedings of the 1st International Conference on the Geology of Tethys*, vol. 1, pp. 125–136, Cairo University, 2005.
- [2] J. B. Hedrick and L. Waked, "Heavy minerals, including monazite, in Egypt's black sand deposits," *Journal of The Less-Common Metals*, vol. 148, no. 1-2, pp. 79–84, 1989.
- [3] A. F. Elhadary, *Geological, sedimentological and radiometric studies on the black-sand deposits, west Rosetta beach, with emphasis on the heavy economic minerals*, Ph.D. thesis, Faculty of Science, Cairo University, Geiza, Egypt, 1998.
- [4] A. A. Abu-Diab, *Sedimentological studies and economic evaluation of the coastal sand dunes between Elgadia and Idko, Rosetta, Egypt*, Ph.D. thesis, Faculty of Science, Mansuora University, Mansuora, Egypt, 2001.

- [5] M. A. El-Sadek and S. A. Elkhateeb, "Magnetic susceptibility of black-sand beach deposits," Koam Mashaal area, east Rosetta, Egypt, Internal Report Series, NMA-IRS-3/2002, Cairo, Egypt, 2002.
- [6] A. F. Bakheit, *Mineralogy and concentration of economic heavy minerals, northern Delta, Egypt*, Ph.D. thesis, Cairo University, Geiza, Egypt, 2004.
- [7] M. I. Moustafa, "Chemistry and origin of enigmatic monazite and chevkinite/perrierite in the egyptian black beach sand," *Resource Geology*, vol. 60, no. 3, pp. 271–287, 2010.
- [8] M. A. El Askary and O. E. Frihy, "Depositional phases of rosetta and damietta promontories on the Nile Delta coast," *Journal of African Earth Sciences*, vol. 5, no. 6, pp. 627–633, 1986.
- [9] A. F. Elhadary, *Geologic and radiometric investigations on Abu-Khashaba deposits, east Rosetta, Egypt*, Ph.D. thesis, Geology Department, Faculty of Science, Cairo University, Geiza, Egypt, 1988.
- [10] GM. SYS. Program, "Definitive International Geomagnetic Reference Field, Version 1.5," Computation Routines by Mike Gemperle and Rowland B. French, Interface by Pierre Doguin, Northwest Geophysical Associates Inc., 1997.
- [11] F. O. Badokhon, *Geophysical exploration for oolitic iron deposit extensions in the northern part of Wadi Ash-Shumaysi, Saudi Arabia*, Ph.D. thesis, King Abdulazeiz University, Jeddah, Saudi Arabia, 1998.
- [12] G. Brno, *Instruction Manual of Kappa Meter KT6*, Geofyzika Brno, Brno, Czech Republic, 1998.
- [13] IRIS Instruments, "ELREC 2 Operating manual, Revised. BRGM & OYO Joint Venture," IRIS Instruments, Orleans, Cedex 2, France 1993.
- [14] R. Thompson and F. Oldfield, *Environmental Magnetism*, Allen and Unwin, London, UK, 1986.
- [15] B. A. Maher, R. Thompson, and M. W. Hounslow, "Introduction," in *Quaternary Climates, Environments and Magnetism*, B. A. Maher and R. Thompson, Eds., pp. 1–48, Cambridge University Press, Cambridge, UK, 1999.
- [16] M. E. Evans and F. Heller, *Environmental Magnetism: Principles and Applications of Enviromagnetics*, Academic Press, London, UK, 2003.
- [17] J. Lees, "Evaluating magnetic parameters for use in source identification, classification and modelling for natural and environmental materials," in *Environmental Magnetism: A Practical Guide*, J. Walden, F. Oldfield, and J. P. Smith, Eds., pp. 113–138, Quaternary Research Association, Cambridge, UK, 1999.
- [18] J. A. Dearing, "Natural magnetic tracers in fluvial geomorphology," in *Tracers in Geomorphology*, I. D. L. Foster, Ed., pp. 57–82, John Wiley & Sons, London, UK, 2000.
- [19] P. Kearey and M. Brooks, *An Introduction to Geophysical Exploration. Geoscience Texts*, Blackwell Science, London, UK, 2nd edition, 1998.
- [20] S. Treittle, W. C. Clement, and R. K. Kaul, "Spectral determination of depth to buried magnetic basement rocks," *Geophysical Journal of the Royal Astronomical Society*, vol. 24, no. 4, pp. 415–428, 1971.
- [21] M. Muniruzzaman and R. J. Banks, "Basement magnetization estimates by wavenumber domain analysis of magnetic and gravity maps," *Geophysical Journal*, vol. 97, no. 1, pp. 103–117, 1989.
- [22] A. Spector and F. S. Grant, "Statistical models for interpreting aeromagnetic data," *Geophysics*, vol. 34, no. 1, pp. 193–302, 1970.
- [23] H. S. Sadek, "Profile frequency analysis of potential field data using filon fourier transform, with basic software," in *Proceedings of the 5th International Seminar on Model optimization in Exploration Geophysics*, Free University of Berlin, 1987.
- [24] H. R. Burger, *Exploration Geophysics of the Shallow Subsurface*, Prentice Hall International, London, UK, 1992.
- [25] D. H. Griffiths and R. F. King, *Applied Geophysics for Geologists and Engineers. The Elements of Geophysical Prospecting*, Pergamon Press Ltd., Headington Hill Hall, Oxford OX30BW, England, UK, 1981.
- [26] W. Lowrie, *Fundamentals of Geophysics*, Cambridge University press, 1997.
- [27] D. S. Parasnis, *Principles of Applied Geophysics*, Chapman and Hall, A Halsted Press Book, London, UK, 3rd edition, 1979.